

**AEDC-TR-80-57**  
**AFWAL-TR-81-2110**



# **An Investigation of F-16 Nozzle-Afterbody Forces at Transonic Mach Numbers with Emphasis on Model Scale Effects**

Earl A. Price, Jr.  
ARO, Inc.

September 1981

Final Report for Period October 1979 — September 1980

Approved for public release; distribution unlimited.

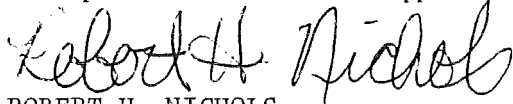
**ARNOLD ENGINEERING DEVELOPMENT CENTER  
ARNOLD AIR FORCE STATION, TENNESSEE  
AIR FORCE SYSTEMS COMMAND  
UNITED STATES AIR FORCE**

NOTICES
When U. S. Government drawings, specifications, or other data are used for any purpose other than a definitely related Government procurement operation, the Government thereby incurs no responsibility nor any obligation whatsoever, and the fact that the Government may have formulated, furnished, or in any way supplied the said drawings, specifications, or other data, is not to be regarded by implication or otherwise, or in any manner licensing the holder or any other person or corporation, or conveying any rights or permission to manufacture, use, or sell any patented invention that may in any way be related thereto.
Qualified users may obtain copies of this report from the Defense Technical Information Center.
References to named commercial products in this report are not to be considered in any sense as an indorsement of the product by the United States Air Force or the Government.

This report has been reviewed by the Office of Public Affairs (PA) and is releasable to the National Technical Information Service (NTIS). At NTIS, it will be available to the general public, including foreign nations.

**APPROVAL STATEMENT**

This report has been reviewed and approved.



ROBERT H. NICHOLS  
Directorate of Technology  
Deputy for Operations

Approved for publication:

FOR THE COMMANDER



MARION L. LASTER  
Director of Technology  
Deputy for Operations

SECURITY CLASSIFICATION OF THIS PAGE (When Data Entered)

DD FORM 1473  
1 JAN 73

EDITION OF 1 NOV 65 IS OBSOLETE

SECURITY CLASSIFICATION OF THIS PAGE (When Data Entered)

UNCLASSIFIED

SECURITY CLASSIFICATION OF THIS PAGE(When Data Entered)

20. ABSTRACT, Concluded.

in coefficients of nozzle-afterbody axial and normal forces obtained from integrating pressure data. High-pressure air at ambient temperature was utilized for exhaust plume simulation. The results indicate close agreement in axial-force coefficient between configurations having full and annular nozzles at design pressure ratio. Very little effect of Reynolds number was found on the nozzle-afterbody axial force. Wave interference adversely affected axial-force data from the 0.25-scale model at Mach numbers between 1.0 and 1.1, producing lower axial force on the model afterbody. Large differences were determined in both the magnitude and the sign of strut interference from the two model installations.

UNCLASSIFIED

SECURITY CLASSIFICATION OF THIS PAGE(When Data Entered)

## **PREFACE**

The work reported herein was conducted by the Arnold Engineering Development Center (AEDC), Air Force Systems Command (AFSC), for the Directorate of Technology (AEDC/DOT). The results were obtained by ARO, Inc., AEDC Group (a Sverdrup Corporation Company), operating contractor for the AEDC, AFSC, Arnold Air Force Station, Tennessee. Testing was conducted under ARO Project Number P41T-44, and analysis of the data was conducted under ARO Project Number P32G-23E. The Air Force project manager for this program was Mr. Elton R. Thompson, AEDC/DOT. Data analysis was completed on September 1, 1980, and the manuscript was submitted for publication on October 7, 1980.

Mr. Earl A. Price is currently employed by Calspan Field Services, Inc., AEDC Division.

## CONTENTS

	<u>Page</u>
1.0 INTRODUCTION .....	7
2.0 APPARATUS .....	7
2.1 Test Facility .....	7
2.2 Model and Support Systems .....	8
2.3 Instrumentation .....	9
3.0 PROCEDURE .....	10
3.1 Test Conditions and Procedures .....	10
3.2 Data Reduction .....	11
3.3 Uncertainty of Measurements .....	11
4.0 RESULTS AND DISCUSSION .....	12
4.1 0.25-Scale Model Data .....	13
4.2 Comparison of 0.11- and 0.25-Scale Model Data .....	19
5.0 CONCLUDING REMARKS .....	22
REFERENCES .....	23

## ILLUSTRATIONS

### Figure

1. General Arrangement of F-16A Model .....	25
2. Model Support Systems .....	26
3. Bay Purge External Details .....	29
4. Nozzle Geometry .....	31
5. Strut Installation .....	34
6. Internal Structure and Airflow System for Strut-Mounted Model .....	35
7. Strut-Mounted Model with Large Dummy Sting .....	37
8. Sting Support Systems .....	38
9. Model Internal Structure and Airflow System; Sting Supports .....	39
10. Forebody Static Pressure Instrumentation .....	40
11. Afterbody Static Pressure Instrumentation .....	41
12. Nozzle Static Pressure Instrumentation .....	42
13. Nozzle-Afterbody Static Pressure Instrumentation .....	44
14. Aft Air Supply Tube Internal Instrumentation .....	45
15. Estimated Uncertainties in Wind Tunnel Parameters .....	46

<u>Figure</u>	<u>Page</u>
16. Effect of Nozzle Configuration on Axial-Force Coefficient, Sting Support System, $\alpha = 0$ .....	47
17. Effect of Angle of Attack on the Nozzle-Afterbody Axial-Force Coefficient for Various Nozzle Configurations, Sting Support System .....	49
18. Effect of Angle of Attack on the Nozzle-Afterbody Normal-Force Coefficient for Various Nozzle Configurations, Sting Support System .....	53
19. Effect of Horizontal Tail Deflection on the Nozzle-Afterbody Axial-Force Coefficients for Various Nozzle Configurations, Sting Support System, $\alpha = 0$ .....	57
20. Effect of Horizontal Tail Deflection on the Nozzle-Afterbody Normal-Force Coefficients for Various Nozzle Configurations, Sting Support System, $\alpha = 0$ .....	60
21. Influence of Horizontal Tail Deflection on the Nozzle-Afterbody Pressure Distribution, Sting Support System, Cruise 3.4 Nozzle, $\text{NPR} = 3.3$ , $M_\infty = 0.9$ , $\alpha = 0$ , $\text{RE} \approx 3.4 \times 10^6$ .....	62
22. Variation of Nozzle-Afterbody Axial-Force Coefficient with NPR for Various Nozzle Configurations, Strut Support System, $\alpha = 0$ .....	64
23. Effect of Nozzle Pressure Ratio on the Nozzle-Afterbody Pressure Distributions, Max A/B 6.6 Nozzle, Strut Support System, $\alpha = 0$ , $\text{RE} \approx 3.4 \times 10^6$ .....	69
24. Comparison of Afterbody Axial-Force Data from Full and Annular Jet Configurations, Strut Support System, $\alpha = 0$ .....	73
25. Summary of Annular Jet Axial-Force Comparison at Design NPR, Strut Support System, $\alpha = 0$ .....	78
26. Effect of Bay Purge System Flow on the Nozzle-Afterbody Axial-Force Coefficient, Sting Support System, Design NPR .....	79
27. Effect of Bay Purge System Flow on the Nozzle-Afterbody Normal-Force Coefficient, Sting Support System, Design NPR .....	80
28. Effect of Bay Purge System Flow on the Nozzle-Afterbody Pressure Distributions, Sting Support System, Cruise 3.4 Nozzle, Design NPR, $M_\infty = 0.9$ , $\text{RE} \approx 3.4 \times 10^6$ .....	81

<u>Figure</u>	<u>Page</u>
29. Effects of Bay Purge System Flow on the Nozzle-Afterbody Pressure Distributions, Sting Support System, Cruise 3.4 Nozzle, Design NPR, $M_\infty = 1.1$ , $RE \approx 3.4 \times 10^6$ .....	85
30. Strut Interference on Nozzle-Afterbody Axial-Force Coefficient .....	89
31. Strut Interference on Nozzle-Afterbody Normal-Force Coefficient .....	91
32. Effect of Strut Interference on the Nozzle-Afterbody Pressure Distributions, Max A/B 6.6 Nozzle, Design NPR, $\alpha = 0$ , $RE \approx 3.4 \times 10^6$ .....	92
33. The Effect of Strut Interference on the Variation of Afterbody Axial Force with NPR, Max A/B 6.6 Nozzle, $\alpha = 0$ .....	102
34. Relative Size of 0.11-Scale and 0.25-Scale Models Installed in Tunnel 16T .....	104
35. Effect of Reynolds Number on Axial-Force Coefficient for the Sting-Supported F-16 Models, Max A/B 6.6 Nozzle, NPR = 4.8, $\alpha = 0$ .....	105
36. Effect of Model Scale on the Nozzle-Afterbody Axial-Force Coefficients, Sting Support System Max A/B 6.6 Nozzle, NPR = 4.8, $RE = 3.4 \times 10^6$ .....	106
37. Comparison of Primary Model Shock Interactions for the 0.11- and 0.25-Scale Models .....	108
38. Effect of Model Scale on the Nozzle-Afterbody Normal-Force Coefficients, Sting Support System, Max A/B 0.6 Nozzle, NPR = 4.8, $RE = 3.4 \times 10^6$ .....	109
39. Effect of Model Scale on the Sensitivity of the Nozzle-Afterbody Normal-Force Coefficient to Angle of Attack, Sting Support System, Max A/B 6.6 Nozzle, NPR = 4.8, $RE = 3.4 \times 10^6$ .....	110
40. Effect of Model Scale on the Nozzle-Afterbody Pressure Distributions, Sting Support System, Max A/B 6.6 Nozzle, NPR = 4.8, $RE = 3.4 \times 10^6$ .....	114
41. Effect of Model Scale on the Sensitivity of Nozzle-Afterbody Axial-Force Coefficients to Nozzle Closure, Sting Support System, Design NPR, $\alpha = 0$ .....	132
42. Effect of Model Scale on the Sensitivity of Nozzle-Afterbody Axial-Force Coefficients to Horizontal Tail Deflection, Sting Support System, Cruise Nozzle, NPR = 3.4, $\alpha = 0$ .....	133
43. Comparison of Strut Planforms Utilized with the 0.11- and 0.25-Scale Models .....	134
44. Comparison of Strut Interference on Nozzle-Afterbody Axial-Force Coefficient from the 0.11-and 0.25-Scale Models, Max A/B 6.6 Nozzle, NPR = 4.8 .....	136

**TABLES**

1. Configuration Identification ..... 137

2. Location of Pressure Instrumentation ..... 138

3. Test Condition Matrix ..... 143

4. Configuration Identification ..... 144

NOMENCLATURE ..... 146

## 1.0 INTRODUCTION

The design of propulsion system installations in high-speed aircraft typically requires wind tunnel tests to define the effects of the complex flow field on the afterbody aerodynamic forces throughout the transonic Mach number regime. The requirement for providing full exhaust jet simulation for such tests has resulted in the use of model support systems which produce significant interference effects in the measured data quantities. Use of such support systems is typically justified by using only increments in force coefficients between two configurations or test conditions on the same support system and assuming that support interference is the same for both sets of data. However, as was shown in Ref. 1, this is not always a valid assumption.

The purposes of the tests reported herein were as follows: (1) to obtain data on the F-16 afterbody with the most interference-free installation possible; (2) to evaluate the support system interference from strut and sting installations; and (3) to obtain data with a 0.25-scale F-16 model which could be compared with previously obtained 0.11-scale model data (Ref. 1) and with flight test data when it becomes available.

The test program reported herein was conducted on a 0.25-scale F-16 nozzle-afterbody with three different support systems: a strut attached to the canopy region of the model, a 5.4-in.-diam sting, and a 6.5-in.-diam sting. The strut-supported model was used to obtain the data required to evaluate exhaust jet effects from a full and an annular jet. Results in Ref. 1 indicated that a sting-supported model with annular jet provided a minimum interference support system for nozzle-afterbody tests. Therefore, the sting-supported model was utilized to evaluate the effects of some of the basic test parameters such as angle of attack and horizontal tail deflection. The effects of engine bay purge system flow were also evaluated with the model sting-supported.

Afterbody and nozzle surface pressures were measured over the Mach number range from 0.6 to 1.5. The basic data matrix was obtained at a unit Reynolds number of  $3.4 \times 10^6/\text{ft}$ ; however, Reynolds number effects were evaluated over a range from 2.0 to  $6.0 \times 10^6/\text{ft}$ . High-pressure air at ambient temperature was utilized for exhaust plume simulation. Model angle of attack and horizontal tail deflection angles were varied in the ranges from 0 to 9 deg and 0 to -8 deg, respectively.

## 2.0 APPARATUS

### 2.1 TEST FACILITY

The Arnold Engineering Development Center (AEDC) Propulsion Wind Tunnel (16T) is a variable density, continuous flow tunnel capable of operation at Mach numbers from 0.20

to 1.60 and stagnation pressures from 120 to 4,000 psfa. The maximum attainable Mach number can vary slightly depending upon the tunnel pressure ratio requirements with a particular test installation. The maximum stagnation pressure attainable is a function of Mach number and available electrical power. The tunnel stagnation temperature can be varied from about 80 to 160°F depending upon the available cooling water temperature. The test section is 16 ft square by 40 ft long and is enclosed by 60-deg-inclined-hole perforated walls of 6-percent porosity. Additional information about the tunnel, its capabilities and operating characteristics is presented in Ref. 2.

## 2.2 MODEL AND SUPPORT SYSTEMS

The test article was a 1/4-scale model of the F-16A fighter aircraft with overall dimensions as shown in Fig. 1. Since one of the purposes of this test program was to investigate the effects of support system interference on the aft portion of a jet effects model, tunnel entries on different support systems were required. The three support systems utilized consisted of a strut (Fig. 2a), a 5.4-in.-diam sting (Fig. 2b), and a 6.5-in.-diam sting (Fig. 2c).

The aircraft model was designed for jet effects testing by incorporating an aerodynamic fairing over the inlet and internal high-pressure air passages through the support systems to the nozzle exit region of the model. High-pressure air at ambient temperature was used to simulate the exhaust nozzle flow.

The simulated bay purge system included two inlets located on the lower fuselage ahead of the horizontal stabilizers as shown in Fig. 3a. These inlets supplied air to an internal plenum ducted to the three exits located on the base of the vertical and horizontal stabilizers (Fig. 3b). Two nozzle configurations were tested with the inlets removed and the inlet area sealed to compare data with the 0.11-scale model, which did not have the bay purge system.

The model was configured with the basic F-16A wing and wingtip missiles. The horizontal stabilizers could be remotely positioned individually from 1 to -9 deg. Nozzles corresponding to four engine power settings, cruise (3.4), partially augmented (5.1), max augmented-low mode (6.6), and max augmented-high mode (7.75), were used during this test. (The numerals after each nozzle indicate the nozzle full-scale exit area in square feet.) The cross sections of each of the four nozzles are shown in Fig. 4 for conventional jet (Fig. 4a), annular jet with small sting (Fig. 4b), and annular jet with large sting (Fig. 4c). Each nozzle was split longitudinally to facilitate nozzle changes with the sting installation. Nozzle construction consisted of aluminum external shells with an epoxy internal casting. The same basic set of nozzles was used for each support system, with the internal geometry

being recast and machined as required for each support system. The throat diameter and axial location of the throat were different for each support system to provide the same internal area ratio and nozzle divergence angle. The size of the cruise nozzle precluded testing it with the large (6.5-in. diam) sting. A list of all configurations tested is presented in Table 1.

### **2.2.1 Strut Support System Installation**

The test article was mounted in an inverted position on a strut (Fig. 5) attached to a pitch table below the test section floor. High-pressure air was routed through a pipe in the strut leading-edge fairing, and instrumentation leads were routed through the strut trailing-edge fairing. The model internal structure and the airflow system of the strut-mounted configuration are shown in Fig. 6a for the conventional full jet nozzles and in Fig. 6b for the annular jet configurations with dummy stings. Dummy stings simulating both the small and large real stings to a point past the sting maximum diameter were used. The small dummy sting installation is illustrated in Fig. 7.

### **2.2.2 Sting Support System Installations**

Tests were conducted during two tunnel entries on stings of different diameters. The sketch in Fig. 8 shows the pertinent dimensions for each of the two stings. Each sting supported the model through the exhaust nozzle, which was operated in the annular jet mode during these test phases. The basic differences between the two stings were the diameter and the taper angle. The small sting (5.4-in. diam) was used for testing the cruise nozzle configuration only and was required since the size of the cruise nozzle exit diameter was smaller than the large sting. Structural loads at the maximum model attitudes and Reynolds numbers required a larger sting be used where possible. Therefore, the large sting (6.5-in. diam) was used for testing each of the other three air-vehicle nozzles. The model internal structure and airflow passages for the sting-supported configurations are shown in Fig. 9. Instrumentation leads to the model were contained in a tube installed in the center of the sting. High-pressure air for exhaust plume simulation was supplied through the sting annulus around the instrumentation tube.

## **2.3 INSTRUMENTATION**

Model surface pressures, obtained from 202 surface pressure orifices located on the forebody (28), afterbody (108), horizontal tail-shelf (6), and boattail (60), were measured using five 48-port Scanivalves® equipped with  $\pm 15$ -psid transducers. The reference and calibrate pressures of each valve were recorded at the beginning and end of each valve cycle. These pressures, measured by precision facility transducers, were used to calculate the

transducer sensitivities for each data point. Pressure orifice locations are indicated in Figs. 10 through 13 and are defined in Tables 2a-f. Exhaust nozzle flow rate was determined from facility-supplied critical flow venturis. Standard facility pressure transducers of the appropriate ranges were used to measure the pressures on the model flow duct (Fig. 14). Two thermocouples were also located on the flow duct rake for measuring air temperature in the flow duct. Strain-gaged transducers were used to measure venturi pressures.

The primary angle-of-attack measurement was made with a model-mounted angular position indicator. During the two sting installations angle of attack was also calculated using the sting support system pitch angle and the angle resulting from the deflection of the sting with load. The stings were instrumented with two strain gages and calibrated to determine deflection versus load.

The horizontal tails were remotely positioned over the range from 0 to -8 deg by electric motors. Angular position of each tail was determined from the output of a potentiometer in each drive mechanism.

All steady-state measurements were recorded by an online computer system in which the data were reduced to engineering units and tabulated in the control room. Sting strain gage-measured loads and deflections, model attitude, and high-pressure air system parameters were paralleled to a real-time digital data acquisition system which permitted monitoring of the parameters during test conditions. Strain gage-measured loads were also monitored on an electrostatic strip chart recorder.

### **3.0 PROCEDURE**

#### **3.1 TEST CONDITIONS AND PROCEDURE**

Data were obtained over a Mach number range from 0.6 to 1.5 at a nominal unit Reynolds number of  $3.4 \times 10^6$  on each of the three support systems, and unit Reynolds number excursions within the range from  $2.0$  to  $6.0 \times 10^6$  were made at selected Mach numbers. Model angle of attack was varied from 0 to 9 deg, and nozzle pressure ratio was varied from 1.0 (jet-off) to 19.3 depending on nozzle configuration and support system. When testing was conducted with annular jet configurations, the nozzle was operated at pressure ratios which would produce the same maximum plume diameter (based on isentropic flow area relations) as a corresponding full jet nozzle. The full jet NPR being simulated in such cases is defined as NP<sub>RE</sub>. A discussion of this method of jet simulation is presented in Ref. 3. Data were recorded at various horizontal tail deflection angles between 0 and -8 deg. The test matrix was devised to obtain data for evaluation of support system

interference (strut interference and annular jet simulation) and for obtaining data to be used for wind tunnel to flight correlation. A matrix of test conditions containing Mach number, Reynolds number, and configuration number is presented in Table 3.

The test procedure with a given geometric configuration and horizontal tail angle consisted either of setting a constant angle of attack and varying nozzle pressure ratio or setting a constant nozzle pressure ratio and varying angle of attack. In either mode of data acquisition, nozzle pressure ratio and angle of attack were controlled by the facility computer. Real-time calculation of angle of attack, nozzle pressure ratio, and horizontal tail deflection angle were displayed in the control room to aid in conducting the test.

### **3.2 DATA REDUCTION**

Pressure coefficients were calculated from the static pressure measured at each orifice. Each pressure was associated with a given projected area in the axial- and normal-force directions so that axial and normal pressure forces on the afterbody and nozzle could be obtained from a pressure-area integration. The pressure forces determined from pressure measurements on the right side of the model were multiplied by two and nondimensionalized by free-stream dynamic pressure and model reference area. When a pressure orifice was determined to be bad (plugged or leaking), the projected areas associated with that orifice were assigned to the adjacent orifices. Wing and empennage forces were not included in the calculated forces since no pressure instrumentation was located on these surfaces. The calculated pressure-integrated axial and normal forces were converted to coefficient form on the basis of the wing reference area (18.75 ft<sup>2</sup>).

Nozzle total pressure was based upon the average of the seven total pressures in the aft air supply tube for the full jet configurations and the average of three total pressures for the annular jet configurations.

### **3.3 UNCERTAINTY OF MEASUREMENTS**

Uncertainties (bands which include 95 percent of the calibration data) of the basic tunnel parameters shown in Fig. 15 were estimated from repeat calibrations of the instrumentation and uniformity of the test section flow during tunnel calibration. Uncertainties of the instrumentation systems were estimated from repeat calibrations of the systems against secondary standards whose precisions are traceable to the National Bureau of Standards calibration equipment. The instrument uncertainties are combined using the Taylor series method of error propagation described in Ref. 4 to determine the uncertainties of the data parameters shown below.

UNCERTAINTIES

<u>Parameter</u>	<u>Mach Number</u>			
	<u>0.6</u>	<u>0.9</u>	<u>1.2</u>	<u>1.5</u>
UALPHA	±0.10	±0.10	±0.10	±0.10
UNPR	±0.008	±0.013	±0.019	±0.027
UC <sub>P</sub>	±0.0127	±0.0091	±0.0066	±0.0060
UCA <sub>A</sub>	±0.00030	±0.00018	±0.00015	±0.00013
UCN <sub>A</sub>	±0.0027	±0.0016	±0.0013	±0.0012

The uncertainties in the axial- and normal-force coefficients were calculated by integrating the uncertainty in pressure coefficient over the respective projected areas. The uncertainty in angle of attack is based upon average differences in angle of attack as determined from the redundant systems. Data repeatability is also a useful parameter to consider for the type test documented in this report when differences between two configurations are of primary interest.

The data presented in the following table illustrate the repeatability in the integrated coefficients.

<u>M<sub>∞</sub></u>	<u>REPEATABILITY</u>				<u>Number of Repeat Conditions</u>
	<u>Average ΔCA<sub>A</sub></u>	<u>Maximum ΔCA<sub>A</sub></u>	<u>Average ΔCN<sub>A</sub></u>	<u>Maximum ΔCN<sub>A</sub></u>	
0.6	0.00011	0.00055	0.00030	0.00125	23
0.9	0.00009	0.00059	0.00025	0.00063	18
1.2	0.00015	0.00099	0.00038	0.00170	17
1.5	0.00005	0.00010	0.00028	0.00078	11

**4.0 RESULTS AND DISCUSSION**

The results in this report are presented in two major subsections. Subsection 4.1 contains data obtained on the 0.25-scale F-16 model. Data are shown which illustrate the effects of parameters typically encountered in nozzle-afterbody testing: nozzle closure, angle of attack, horizontal tail deflection, and nozzle pressure ratio. Support interference effects from stings (annular jet comparison) and the strut are also presented along with effects of flow from the bay purge system. Subsection 4.2 contains comparisons of 0.25-scale model data with those from a 0.11-scale model presented in Ref. 1. The majority of the data in this

report are presented in terms of integrated normal- and axial-force coefficients; however, interference effects are generally presented in terms of increments in these coefficients between two configurations. Except where specific exceptions are noted, data are presented for the horizontal tail at zero deflection angle and at a free-stream unit Reynolds number of  $3.4 \times 10^6$  per foot.

## 4.1 0.25-SCALE MODEL DATA

Data to determine the effects of nozzle closure, angle of attack, horizontal tail deflection and bay purge system flow were obtained with the sting-supported model using annular flow through the nozzle around the sting to simulate jet effects. The effects of nozzle pressure ratio and the annular jet-full jet comparison were obtained with the strut-supported model since full plume nozzle flow was desired. Strut interference was obtained by calculating increments between coefficients from the strut-supported model with a dummy sting and from the sting-supported model.

### 4.1.1 Effects of Nozzle Closure

Axial-force coefficients as a function of free-stream Mach number are presented in Fig. 16 for each nozzle configuration. Data were obtained with an annular jet plume operating at the design pressure ratio of each nozzle. For each of the nozzles tested, the nozzle portion of the model experienced a thrust force (negative axial-force coefficient) at subsonic Mach numbers, Fig. 16a. At Mach numbers of 0.9 and below, the magnitude of the force increased as nozzle closure (axial projected area) increased. At supersonic Mach numbers, however, this trend was reversed, with a drag force acting on all nozzles, which increased with increasing closure. The afterbody portion of the model experienced a decreasing axial force with decreasing nozzle closure for all Mach numbers below 1.5. The effect of nozzle closure on the afterbody force is significant at the subsonic Mach numbers but is relatively small at the supersonic Mach numbers, decreasing to essentially zero at  $M_\infty = 1.5$ . When coefficients from the two model components are combined (Fig. 16b), the large effects of nozzle closure on the two portions of the model tend to cancel at Mach numbers below 0.95, resulting in a relatively small positive axial force. The model component forces are additive at supersonic Mach numbers, resulting in a large, systematic effect of closure, with the largest closure having the highest axial force.

An anomaly in the data at  $M_\infty = 1.1$ , which consists of a significant decrease in axial force, is present with each of the three nozzles. The anomaly is believed to be associated with model shocks being reflected from the tunnel wall. Additional discussion of this anomaly is included in Subsection 4.2.

#### 4.1.2 Effects of Angle of Attack

The effects of angle of attack on the nozzle-afterbody axial-force coefficients are presented in Fig. 17 for the sting-mounted model. With the exception of the two max A/B nozzle configurations at  $M_\infty = 1.1$ , there was generally a decrease in axial force with increasing angle of attack. The variations with angle of attack are generally similar for each of the nozzle configurations, the cruise nozzle being slightly more sensitive to angle of attack at  $M_\infty = 0.95$  and  $1.0$ . In general, the effects of angle of attack on  $CA_A$  are similar enough for each nozzle that it would be sufficient for configuration optimization studies to determine the effects of angle of attack on only one nozzle configuration, thereby reducing the required test matrix.

The effect of angle of attack on the nozzle-afterbody normal-force coefficient is presented in Fig. 18. In general, a linear increase in  $CN_A$  with angle of attack was found for each nozzle configuration. One notable exception is the data at  $M_\infty = 0.9$ , where the  $CN_A$  variation with  $\alpha$  is nonlinear and indicates a decrease in  $CN_A$  between  $\alpha = 7$  and  $9$  deg. A similar variation in  $CN_A$  at  $M_\infty = 0.9$  was found in the 0.11-scale model data in Ref. 1. The similarity in the  $CN_A$  characteristics of each of the nozzle configurations would also allow determination of angle of attack effects with a single configuration when conducting configuration optimization studies.

#### 4.1.3 Effects of Horizontal Tail Deflection

The nominal horizontal tail deflection angle for most of the effects evaluated during this investigation was zero. However, since one objective of this investigation was to obtain data for comparison with flight test data at various trimmed flight conditions, a study of the sensitivity of the afterbody forces to tail deflection was conducted.

Data are presented in Figs. 19 and 20 which illustrate the effects of horizontal tail deflection on nozzle-afterbody axial- and normal-force coefficients, respectively. Data are presented for each of the four nozzles at both subsonic and supersonic Mach numbers. In general, increasing negative tail deflection resulted in increased axial force. The rate of increase is generally higher at subsonic than at supersonic Mach numbers. The largest effect of tail deflection on axial force was at  $M_\infty = 0.9$ , where the 8-deg change in tail angle produced an increase in axial-force coefficient of 0.0016 on the cruise nozzle. Normal force decreased approximately linearly as the horizontal tail was deflected negative. As with axial force, the normal force is more sensitive to changes in tail deflection at the subsonic Mach numbers than at the supersonic Mach numbers.

An example of the effects of horizontal tail deflection on the afterbody pressure distributions is shown in Fig. 21. The data were obtained with the cruise nozzle at  $M_\infty = 0.9$ , which was the Mach number at which the maximum sensitivity to tail deflection was found. The data indicate that as the horizontal tails are deflected in the negative direction, the compression on the upper tail surface and the expansion on the lower surface have an influence over a significant portion of the afterbody. In general, the variation of both the upper and lower surface pressures is in the direction to decrease normal force with increasing negative tail deflection. The upper and lower surface pressure variations tend to have a compensating effect as far as axial force is concerned; however, the magnitude of the expansion on the lower surface is generally greater than that of the compression on the upper surface, and the result is the increase in  $CA_A$  shown in Fig. 19. Because of the sensitivity of the afterbody pressures to tail deflection, it is concluded that tail deflection must be duplicated as closely as possible when pressure distribution comparisons are made between any two sets of data.

#### 4.1.4 Effects of Nozzle Pressure Ratio

The data presented in this section were obtained with the strut-supported model with full jet plume simulation. It is shown in Section 4.1.7 that strut interference can have a significant influence on the absolute value of nozzle-afterbody axial force at Mach numbers between 0.9 and 1.2. In spite of this, it is also shown in Section 4.1.7 that for a given nozzle configuration the variation in axial force with NPR will provide valid jet effects increments even in the presence of strut interference. Total nozzle and afterbody axial-force coefficients are presented in Fig. 22 as a function of nozzle pressure ratio for each of the four nozzles. The data obtained at the design pressure ratio for each nozzle are identified by a solid symbol. Jet-off ( $NPR \approx 1.0$ ) data are also shown for each nozzle configuration.

The variation of the data with NPR is typical of the data shown in Ref. 1 on the 0.11-scale F-16 model. As with the sting-supported, annular jet model at design pressure ratio (Fig. 16), the nozzle configuration has relatively minor effects on the magnitude or the sensitivity of the total afterbody drag to NPR at subsonic Mach numbers. In general, the difference in  $CA_A$  between all the nozzle configurations is within 0.0003 at any given NPR. At supersonic Mach numbers there are large increases in total afterbody drag as nozzle closure is increased. The sensitivity of  $CA_A$  to NPR also increases with increased nozzle closure.

Typical effects of nozzle pressure ratio on the afterbody pressure distributions are presented in Fig. 23 for Mach numbers of 0.8 and 1.2. The data obtained with the max A/B 6.6 nozzle configuration are presented for jet-off and a range of nozzle pressure ratios which

spans the design value. At supersonic Mach numbers, the effects of NPR are restricted to the nozzle, whereas at the subsonic Mach numbers the effects of NPR are propagated over significant portions of the afterbody as well.

#### 4.1.5 Annular and Full Jet Comparison

The requirements associated with providing exhaust plume simulation and a properly contoured aircraft aft end have typically led to supporting nozzle-afterbody models by struts or wingtip support arrangements. The results of Ref. 1 indicated that introducing a sting into the nozzle flow and creating an annular jet resulted in significantly less interference than that from a strut or wingtip support system. The data in Refs. 1 and 3 indicate that reasonable agreement in afterbody drag can be obtained between full and annular jet configurations at underexpanded jet pressure ratios by comparing results obtained with the same maximum plume diameter. The support system arrangement for this test provided another opportunity to obtain such a comparison by obtaining data with the model strut supported with a full-flowing jet and with a dummy sting installed through the nozzle to create an annular nozzle configuration. In the change from full nozzle to annular nozzle configurations the diameter and axial location of the nozzle throat were changed to maintain a constant exit diameter, divergence angle, and area ratio between full and annular nozzle configurations.

Presented in Fig. 24 are comparisons of the nozzle-afterbody axial-force coefficients from each of the four nozzle configurations obtained with full and annular jets. The annular jet configurations encompass a range of sting-to-nozzle exit diameter ratios ( $D_S/D_E$ ) from 0.621 to 0.865. Data obtained at the design pressure ratio for each nozzle are denoted by the solid symbols. The annular jet data are presented as a function of both NPR and the effective nozzle pressure ratio parameter NP<sub>RE</sub> (dashed fairing). The parameter NP<sub>RE</sub> corresponds to the NPR of a full jet which has the same maximum isentropic plume diameter as the annular jet.

Of primary interest is the agreement between the annular and full jet data near the nozzle design pressure ratio as well as the slope of the axial-force curve in the region of the design NPR. The slope is important if the correct axial force at off-design conditions is to be defined. At the design pressure ratio, agreement between the two test techniques varies from exact ( $M_\infty = 1.5$ , Part A/B 5.1 nozzle) to a maximum difference in  $CA_A$  of 0.0004 ( $M_\infty = 1.2$ , Part A/B 5.1 nozzle). For nozzle pressure ratios greater than the design value, the annular jet data as a function of NP<sub>RE</sub> are in reasonably good agreement with the full jet data for each configuration except the Part A/B 5.1 nozzle. For this configuration the annular jet data versus NP<sub>RE</sub> result in axial-force curves that are steeper in slope than the

full jet data. The disagreement becomes larger as pressure ratio is increased and as  $D_S/D_E$  is increased. The data obtained with the Part A/B 5.1 nozzle have more disagreement than that obtained with the cruise nozzle even though the cruise nozzle configuration had a larger sting-to-nozzle exit diameter ratio (0.865). This indicates that there are other parameters or combinations of parameters such as internal nozzle divergence angle and external nozzle contour which influence the correlation procedure. In matching the maximum plume diameter at underexpanded jet pressure ratios, the initial jet expansion angle for the annular jet nozzle is higher than that for the full jet case. It is possible that the Part A/B 5.1 external boattail contour is more sensitive to this mismatch than the other nozzle contours. Although as yet unpublished, similar differences in the full jet and annular jet data at underexpanded jet pressure ratios were measured with the 0.11-scale F-16 model of Ref. 1.

The comparison between the full jet and annular jet data is most important at design pressure ratio. Therefore, these data are summarized in Fig. 25 for all nozzle and sting combinations over the complete Mach number range of this investigation. All of the differences in axial-force coefficients are equal to or less than 0.0005. The average of the absolute magnitude of all  $\Delta C_{A_A}$ 's is 0.00015. In general, the variations with nozzle configuration and with Mach number are similar to those shown in Ref. 1 for the 0.11-scale F-16 model.

#### 4.1.6 Effects of Bay Purge System Flow

To duplicate as closely as possible the details of the aircraft, a system which simulated the engine bay purge system of the F-16 was included on the 0.25-scale model. The system was composed of two inlet scoops on the lower fuselage ahead of the instrumented afterbody (Fig. 3), which captured ram air, and exit ducts at the base of the vertical and horizontal stabilizers. The 0.11-scale model did not have a bay purge system; therefore, so that data would be available for comparison with the 0.11-scale model data, two nozzle configurations were tested both with and without the bay purge system. The effects of the bay purge system flow on afterbody axial- and normal-force coefficients are presented in Figs. 26 and 27, respectively. The effect of the bay purge flow is to decrease axial force with slightly larger effects at the transonic and supersonic Mach numbers than at the subsonic Mach numbers. The largest effects were on the cruise nozzle, where at  $\alpha = 7$  deg the bay purge flow resulted in a decrease in axial force of 0.0008 at  $M_\infty = 1.1$ . The effect of bay purge flow on normal force was small but generally produced slightly lower values. This result is an indication of higher pressure on the upper surface of the nozzle, which would be caused by the flow through the exit at the base of the vertical tail. Examples of the effects of bay purge flow on the pressure distributions are shown in Figs. 28 and 29 for Mach numbers 0.9 and 1.1, respectively. The data indicate that higher pressure is present on the afterbody

immediately downstream of the bay purge exit when bay purge flow is present; however, the pressure near the nozzle exit generally recompresses to a higher value without bay purge flow.

#### 4.1.7 Effects of Strut Interference

The effects of the strut on the afterbody axial-force coefficients are presented in Fig. 30. Strut interference data were obtained by taking increments in coefficients between the strut-supported model with a dummy sting and the model supported by a sting. These data demonstrate a large variation in interference as a function of Mach number with both positive and negative increments in axial force occurring over the Mach number range. Although the data show relatively minimal interference at Mach numbers up through the transonic and supersonic Mach number range to  $M_\infty = 1.5$ , where relatively low interference may be a fortuitous consequence of the strut afterbody geometric relationship. The maximum measured interference on axial-force coefficient was 0.0038 at  $M_\infty = 1.05$  at  $\alpha = 7$  deg. While the variation of interference with Mach number is similar for each nozzle, there is a notable configuration dependency at some of the higher interference conditions wherein the higher closure nozzle configurations experienced the larger interference. Increasing angle of attack to 7 deg (Fig. 30b) had little effect at the low interference conditions but shifted the value of the maximum interference such that the magnitude of the interference was increased at  $M_\infty = 1.05$  and decreased at  $M_\infty = 1.2$ .

The interference effects from the strut on afterbody normal force are presented in Fig. 31. The magnitude and direction of the strut interference are functions of both Mach number and angle of attack. The most pronounced effect of the strut was to induce a negative normal-force increment on the afterbody over a significant portion of the Mach number range. Since the strut was mounted through the canopy region of the forebody the normal-force increment is indicative of a force in the direction away from the strut. The largest interference increment was  $\Delta C_{N_A} = -0.018$ , which occurred at  $M_\infty = 0.9$  at  $\alpha = 7$  deg. Examples of the effects of the strut on the surface pressure distributions at Mach numbers which displayed small effects ( $M_\infty = 0.6$  and  $0.8$ ) and those which had the largest effect ( $M_\infty = 1.05$  and  $1.2$ ) are presented in Fig. 32. These pressure distributions illustrate that for the subsonic Mach numbers the effects of the strut are small and primarily confined to the top of the model where the strut is installed, whereas at  $M_\infty = 1.05$  and  $1.2$  significant effects of the strut are seen on both sides of the model. The fact that the interference appears symmetrical indicates that at supersonic Mach numbers the strut alters the flow around both upper and lower surfaces of the model in the same manner.

The effects of nozzle pressure ratio which were shown in Section 4.1.4 were obtained with the strut-supported model. The effect of the strut on the variation of axial force with NPR is shown in Fig. 33 for the max A/B 6.6 nozzle. The data indicate that essentially constant increments in axial-force coefficient are present at both jet-off and jet-on conditions between the two configurations. This indicates that although the absolute level of axial force may be affected significantly (i.e.,  $M_\infty = 1.2$ ), the increments that result from varying NPR on a given nozzle configuration are valid even in the presence of strut interference. Data for variations in NPR are not available to evaluate this effect at the Mach numbers between 0.9 and 1.2 where large interference increments from the strut were shown in Fig. 30. Therefore, caution should be exercised in assuming that this is a general conclusion that is applicable at all Mach numbers.

## 4.2 COMPARISON OF 0.11- AND 0.25-SCALE MODEL DATA

Data obtained with the two sting-supported models were used to evaluate Reynolds number effects and the basic aerodynamic characteristics because the sting support is considered to produce the least support interference. Relative sizes and blockage of each model installed in Tunnel 16T are illustrated in Fig. 34.

### 4.2.1 Effects of Reynolds Number

The range of unit Reynolds numbers over which each model was tested varied with Mach number but was within the range of 2.0 to  $6.0 \times 10^6$  per foot. The characteristic Reynolds number ranged from 11 to  $70 \times 10^6$ . For Mach numbers below 1.0 this range of Reynolds numbers provides overlap between data from the 0.25-scale model and the full-scale aircraft. The effects of varying characteristic Reynolds number on the afterbody-nozzle axial-force coefficient are presented in Fig. 35. The data were obtained with the max A/B 6.6 nozzle configuration with an annular jet flowing at design pressure ratio. The Reynolds number variation tests with the 0.25-scale model were conducted with the bay purge system installed while the 0.11-scale model data were obtained without bay purge flow. Therefore, comparison of  $CA_A$  between the two models is not completely valid; however, the effect of bay purge flow on axial-force coefficient was only 0.0004, as shown in Fig. 26. The disagreement between the two data sets is discussed in Section 4.2.2.

The data for either model indicate very little effect of Reynolds number at any Mach number. For each of the model sizes, the largest axial-force coefficient change over the unit Reynolds number range investigated was 0.0003. It is concluded, therefore, that for the configuration tested, little error would be introduced as a result of a Reynolds number mismatch between either model and the full-scale vehicle.

#### 4.2.2 Basic Aerodynamic Characteristics

A comparison of afterbody axial-force coefficients for the two models without bay purge flow is presented in Fig. 36. The data were obtained at a constant unit Reynolds number of  $3.4 \times 10^6$  per foot with the max A/B 6.6 nozzle configuration. At  $\alpha = 0$  the axial-force data from the two models exhibit relatively consistent variations up through  $M_\infty = 1.0$  and for Mach numbers of 1.2 and 1.5. At each of these Mach numbers  $CA_A$  for the 0.25-scale model is greater than that for the 0.11-scale model. The largest apparent discrepancy in the two sets of data is the atypical variation of axial-force coefficient which occurs at Mach numbers 1.05 and 1.10. Shock reflections from the tunnel wall to the model are most likely to occur between Mach numbers 1.0 and 1.15, which are typically avoided in test programs for which high quality aerodynamic data are required. Presented in Fig. 37 are sketches of the two models relative to the size of the tunnel with some of the primary model shocks shown at the Mach angle for free-stream flow along with reflections from the tunnel walls as they would appear if incomplete cancellation occurred at the wall. The sketches are a very simple representation in one plane of the very complex three-dimensional wave structure. They illustrate, however, that if incomplete shock or expansion wave cancellation at the tunnel wall does occur, then the flow on the 0.25-scale model afterbody is influenced by reflected waves at  $M_\infty = 1.05$  to 1.2 which the flow on the 0.11-scale model does not experience. The presence of these reflected waves in the flow field could alter the strength and location of the model shock system, resulting in the altered axial force. Similar interference effects were found on the large size models in the study reported in Ref. 5. At  $\alpha = 7$  deg (Fig. 36b) there is significant disagreement ( $\Delta CA_A = 0.0037$ ) in the value of the axial-force coefficient at  $M_\infty = 1.0$  in addition to the atypical variation with Mach number which was found at  $\alpha = 0$ .

Comparisons of afterbody normal-force coefficients on the 0.11- and 0.25-scale models are presented in Fig. 38 for  $\alpha = 0$ . The variation in normal force with Mach number is similar for each model. Comparison of the two data sets indicates that an unknown bias exists in one or both sets. The effect of angle of attack on the afterbody normal force for the two models is presented in Fig. 39. The two sets of data typically agree within their respective uncertainty limits at subsonic Mach number conditions. However, the apparent bias exhibited at  $\alpha = 0$  persists at supersonic Mach numbers.

Surface pressure distributions on the two models from which the data in Figs. 36 and 38 were computed are presented in Fig. 40. The pressure variations substantiate the interpretation of the axial-force data which was shown in Fig. 36. For example, pressure data at subsonic Mach numbers, such as 0.8, show a relatively consistent variation of pressure along the surface for the two models. For Mach numbers 1.05 and 1.1, however, at

which the axial force was atypical on the 0.25-scale model, there are significant differences in the pressure distributions, the 0.25-scale model generally having higher pressure, which is indicative of shock disturbances. At Mach numbers 1.2 and 1.5 the nozzle region indicates an expansion disturbance on the 0.25-scale model. At certain Mach numbers (0.9, for example) there are pressure variation differences between the two models which are typical of Reynolds number effects. For example, the pressures on the 0.25-scale model in row AB134, Fig. 40c, expand to a lower value near  $X/L = 0.88$  and then recompress to a higher value at the trailing edge of the nozzle than do the pressures on the 0.11-scale model. This variation in pressure, which is typically deemed a Reynolds number effect, has a compensating effect on afterbody drag since the drag on the afterbody increases and nozzle drag decreases. Thus, while comparison of the pressure distributions indicates there may be Reynolds number effects between the two data sets, the net effect on drag is small.

In conducting nozzle-afterbody tests, the most common geometric variable is nozzle contour. The sensitivity of afterbody drag to nozzle closure may be obtained from tests on nozzles with different exit areas. Presented in Fig. 41 is a comparison of the afterbody axial force as a function of nozzle closure. The data were obtained on the sting-supported models with annular exhaust plumes flowing at design pressure ratio. The comparisons illustrate small effects of changes in nozzle closure at the subsonic Mach numbers and relatively large effects at the supersonic Mach numbers. However, a comparison of the slopes of the data from the two models indicates excellent agreement at all Mach numbers except  $M_\infty = 1.2$ . At  $M_\infty = 1.2$ , the difference in the closure increment for the two models between the maximum and minimum closure is only 0.0007, which is greater than the estimated data uncertainty. At this Mach number the occurrence of reflected waves was shown (Fig. 37) to be probable. Thus, the extraction of the increments caused by the effects of different closures from either data set appears valid except where the flow field is disturbed by support interference or spurious waves.

The sensitivity levels of axial force from each of the models to horizontal tail deflection are compared in Fig. 42. The increment in  $CA_A$  which results from a  $-4^\circ$  tail deflection is small. There is excellent agreement between the two sets of data.

#### 4.2.3 Strut Interference

A comparison of the strut interference on nozzle-afterbody axial-force coefficients determined with the 0.11-scale and 0.25-scale models, is presented in Fig. 43. It is readily apparent that there are large differences not only in the magnitude but also in the sign of the interference increments at Mach numbers between 0.95 and 1.2. For Mach numbers between 0.6 and 0.9 and  $M_\infty = 1.5$ , at which strut interference was relatively small on both models,

the agreement between the strut interference effects with the two models is good. The thickness of the two struts was scaled in the vicinity of the model attachment line in the same relation as the models; however, neither the chord nor strut height was scaled, as may be seen in Fig. 44. In terms of percent of model length the 0.11-scale model strut had a longer chord and greater height from the tunnel floor than the 0.25-scale model strut. It is apparent therefore that any conclusions regarding the magnitude and sign of strut interference must be evaluated for each installation.

## 5.0 CONCLUDING REMARKS

An investigation was conducted with a 0.25-scale F-16 nozzle-afterbody model to obtain (1) data on the most interference-free installation, (2) a data base for evaluating support system interference from a strut and sting, and (3) data for evaluating model scale effects by comparison with data obtained on a 0.11-scale model.

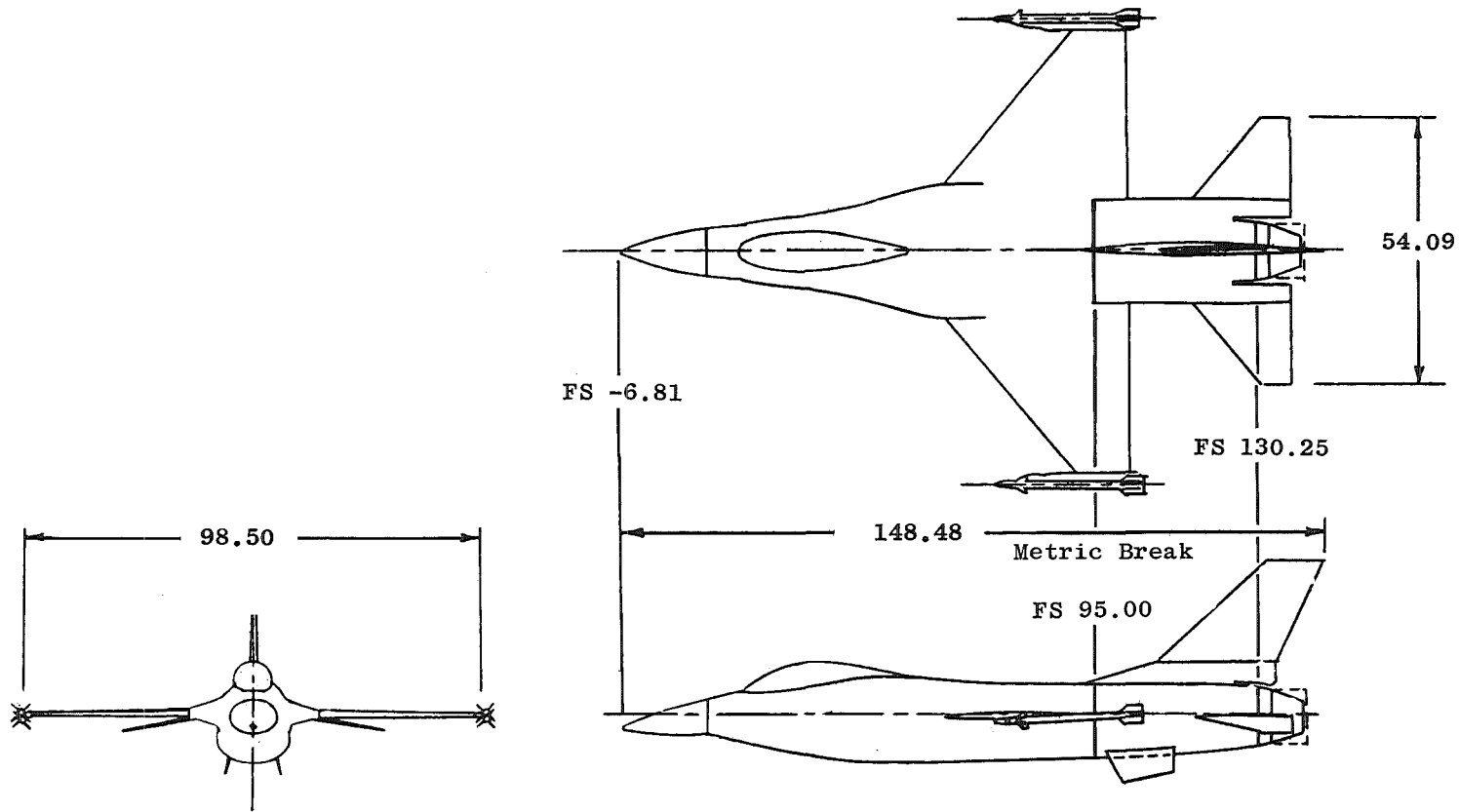
The significant results and conclusions are summarized as follows:

1. Excellent agreement was obtained in axial-force coefficient between the 0.11-scale and 0.25-scale models at Mach numbers from 0.6 to 0.95. Compression wave interference adversely affected axial-force data from the 0.25-scale model at Mach numbers from 1.0 to 1.1. Expansion wave disturbances produced higher axial force on the 0.25-scale model at Mach numbers 1.2 and 1.5. The agreement in normal-force coefficient for the two models was within the estimated data uncertainty at subsonic Mach numbers.
2. Very little effect of Reynolds number was evident on either the 0.11- or 0.25-scale models. It is concluded that little error as a result of Reynolds number would be introduced in making full-scale afterbody pressure force predictions from the data obtained on either model.
3. At Mach numbers of 0.95 through 1.2 there were significant interference effects from the model support strut with both models. Large differences in both magnitude and sign of the strut interference were shown for the two model sizes. Therefore, strut support interference must be evaluated for each model/strut combination. For Mach numbers at which data were available, the effects of nozzle pressure ratio were the same with or without strut interference.

4. The average difference in axial-force coefficient obtained with annular and full jet configurations at design pressure ratio was within 0.00015 for all nozzles at all Mach numbers. The maximum disagreement was  $\pm 0.0005$ .
5. Bay purge flow through the root of the vertical and horizontal tails produced a decrease in axial force. The magnitude of the decrease was generally greater at supersonic Mach numbers and reached a maximum increment of 0.0008 in axial-force coefficient.

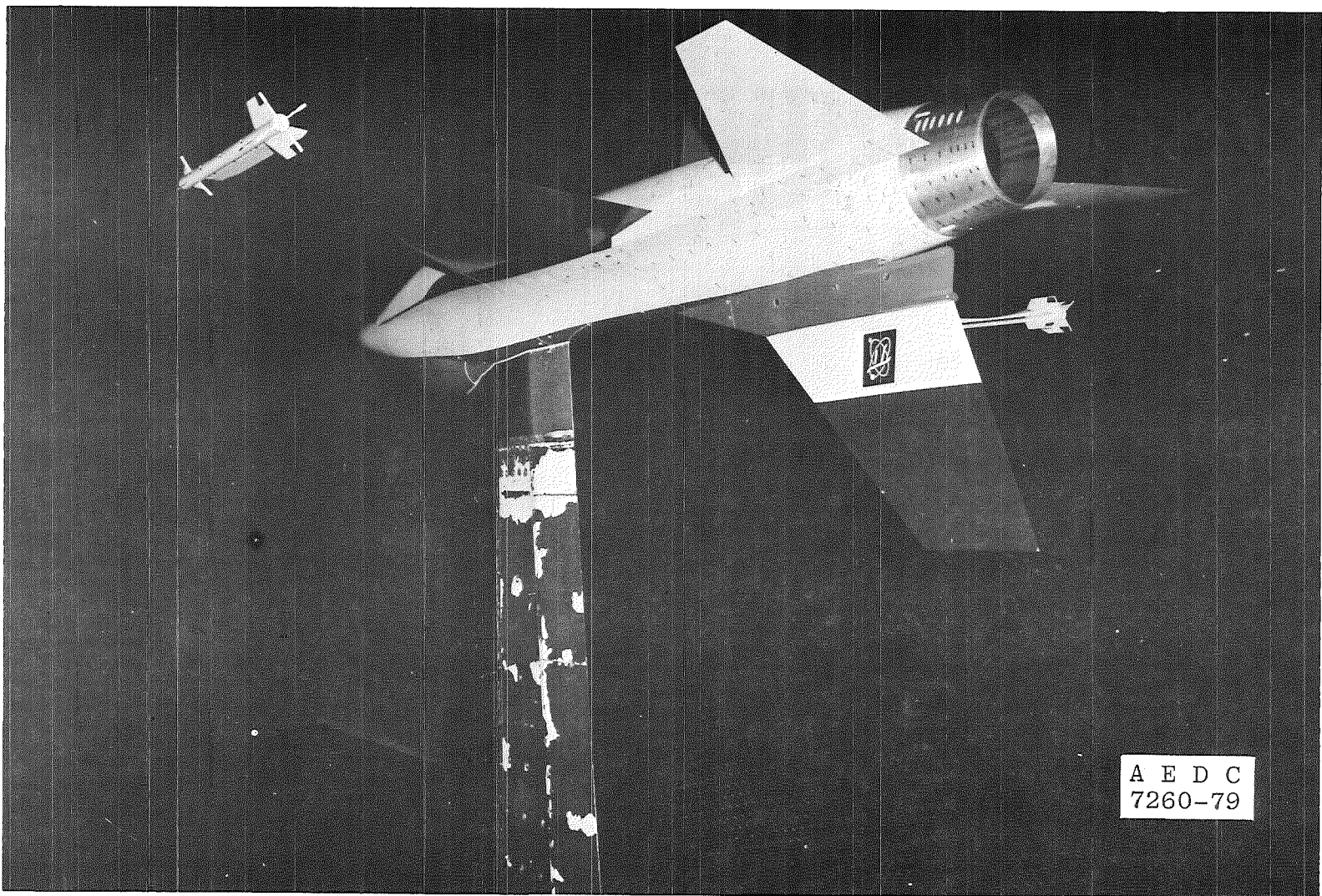
### REFERENCES

1. Price, Earl A., Jr. "An Investigation of F-16 Nozzle-Afterbody Forces at Transonic Mach Numbers with Emphasis on Support System Interference." AEDC-TR-79-56 (AD-A078693), December 1979.
2. *Test Facilities Handbook* (Eleventh Edition). "Propulsion Wind Tunnel Facility, Vol. 4." Arnold Engineering Development Center, June 1979.
3. Price, Earl A., Jr. "A Parametric Investigation of the Annular Jet Concept for Obtaining Afterbody Drag Data at Transonic Mach Numbers." AEDC-TR-77-104 (AD-A050891), February 1978.
4. Abernethy, R. B., Thompson, J. W., Jr., et al. "Handbook — Uncertainty in Gas Turbine Measurements." AEDC-TR-73-5 (AD755356), February 1973.
5. Reichenau, David E. A. "An Investigation of Model Scaling Effects at Mach Numbers from 0.60 to 1.40." AEDC-TR-73-202 (AD915551L), December 1973.



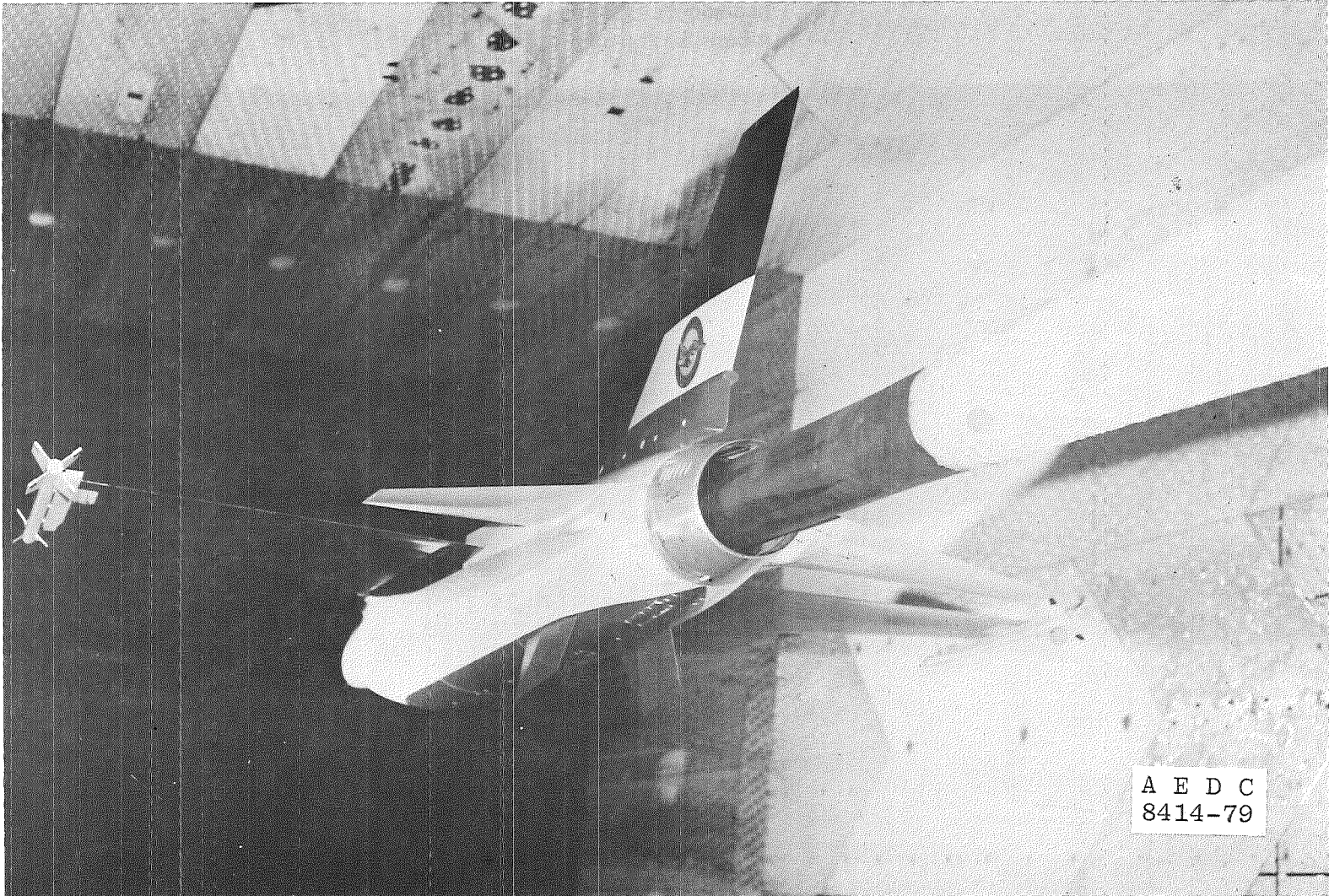
Stations and Dimensions in Inches

Figure 1. General arrangement of F-16A model.

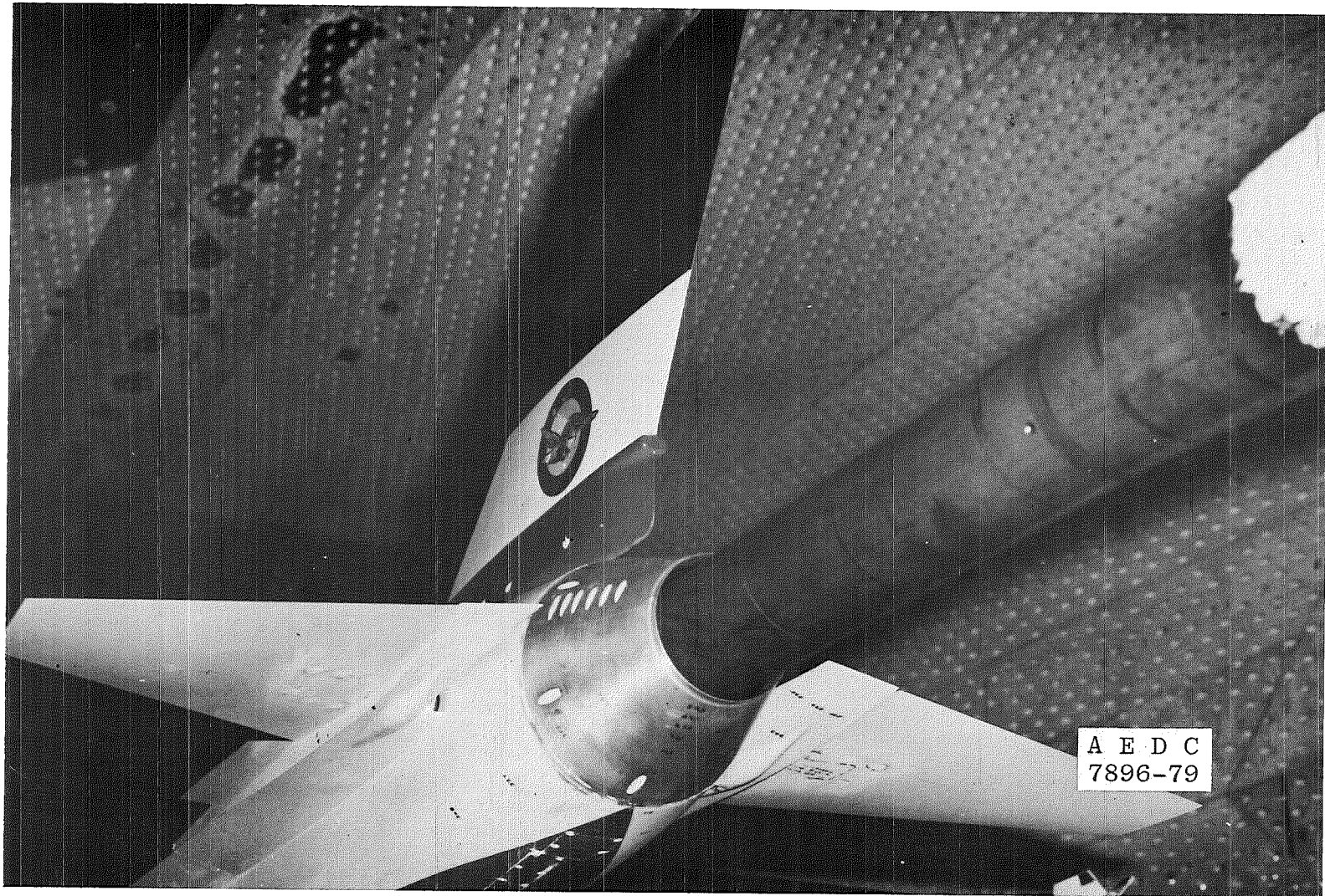


a. Strut support

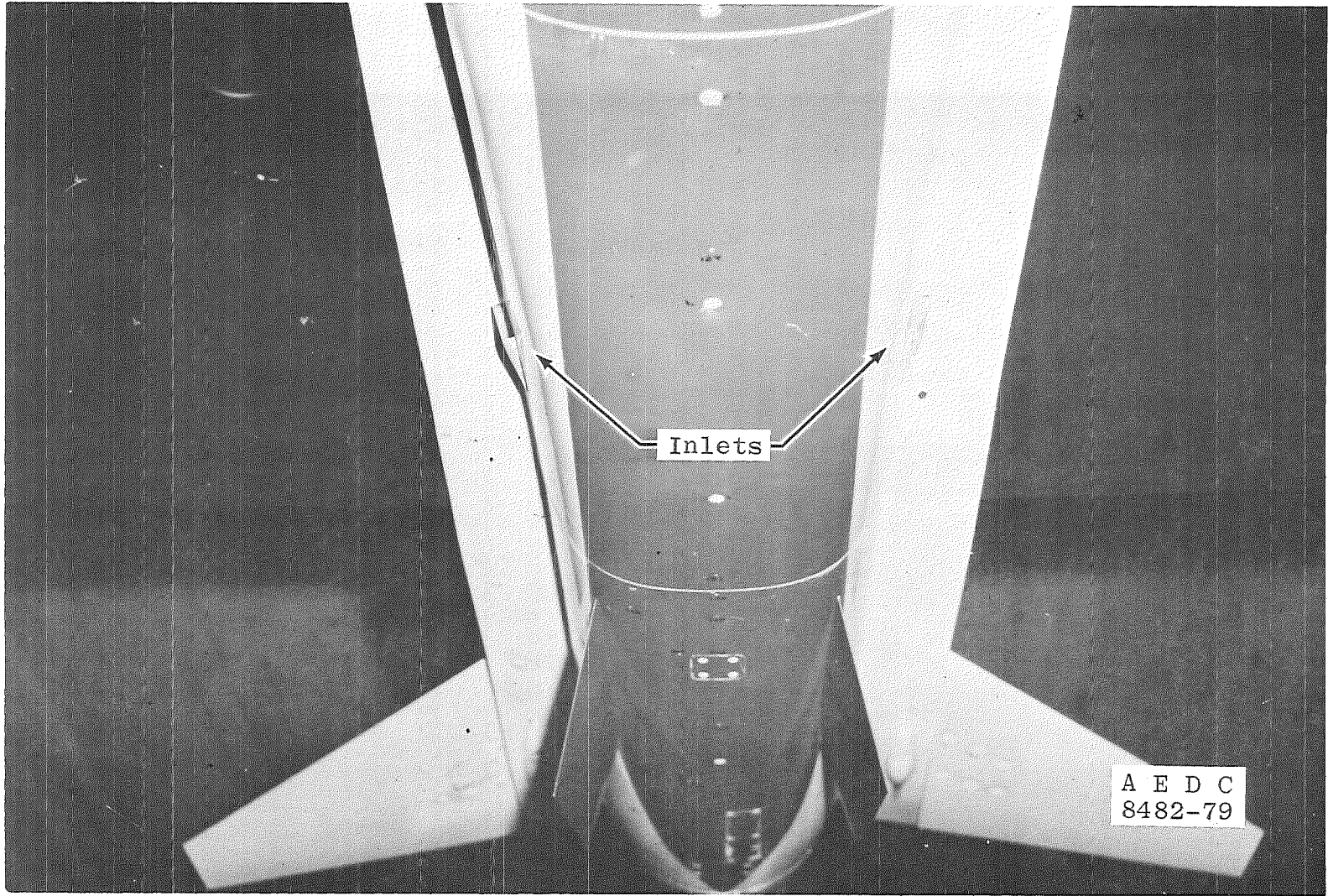
Figure 2. Model support systems.



b. Large sting support  
Figure 2. Continued.



c. Small sting support  
Figure 2. Concluded.



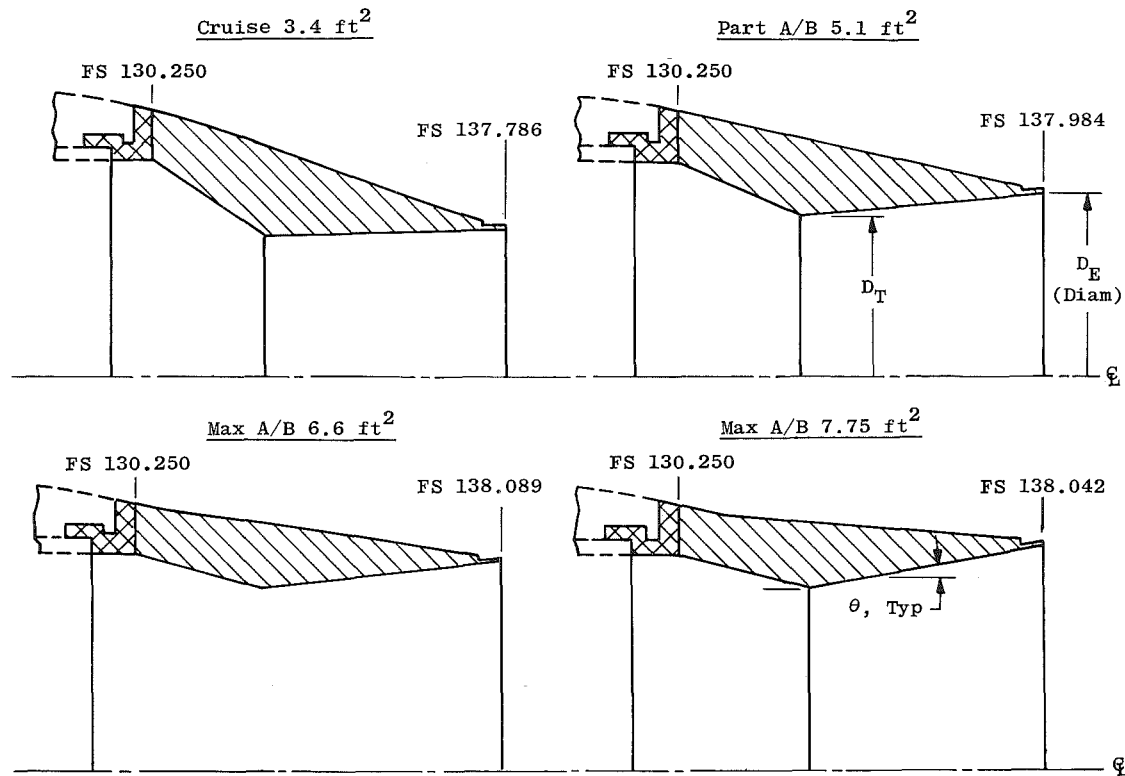
a. Inlets

Figure 3. Bay purge external details



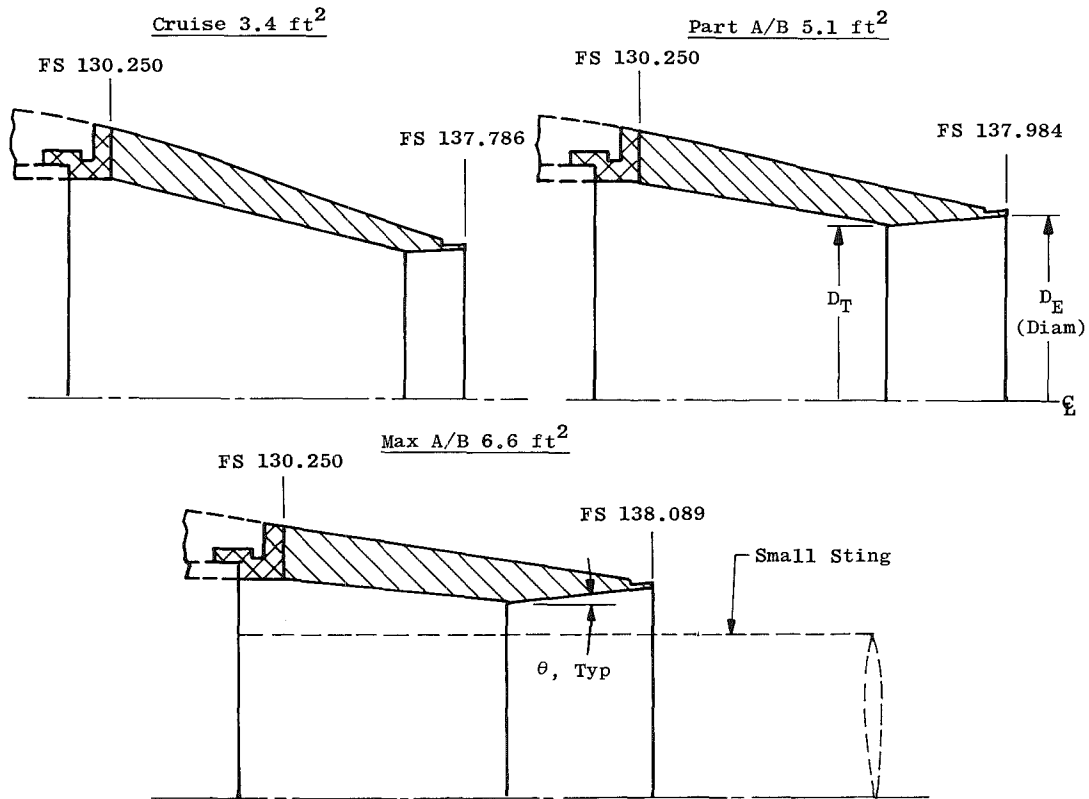
b. Exits  
Figure 3. Concluded.

Nozzle	$A_e, \text{ft}^2$ (Full Scale)	$D_T, \text{in.}$	$D_E, \text{in.}$	$(A_E/A_T)$	$\theta$
Cruise	3.4	5.867	6.252	1.136	$2^\circ 7' 10''$
Part A/B	5.1	6.778	7.657	1.276	$4^\circ 50' 28''$
Max A/B	6.6	7.574	8.695	1.318	$6^\circ 16' 4''$
Max A/B	7.75	7.582	9.450	1.553	$10^\circ 20' 15''$



a. Strut support used with full plume configurations  
Figure 4. Nozzle geometry.

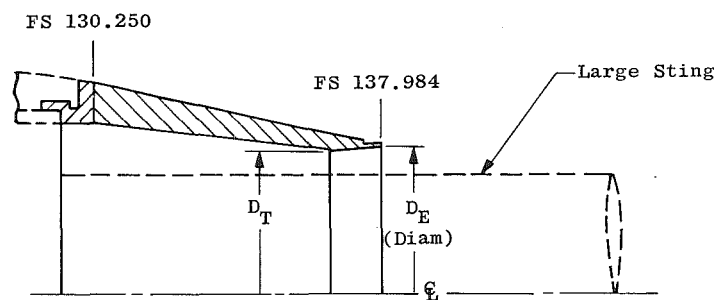
Nozzle	$A_e, \text{ft}^2$ (Full Scale)	$D_T, \text{in.}$	$D_E, \text{in.}$	$(A_E/A_T)$	$\theta$
Cruise	3.4	6.153	6.252	1.141	$2^\circ 7' 10''$
Part A/B	5.1	7.228	7.657	1.277	$4^\circ 50' 28''$
Max A/B	6.6	8.024	8.695	1.318	$6^\circ 16' 4''$



b. Configurations used with small sting  
Figure 4. Continued.

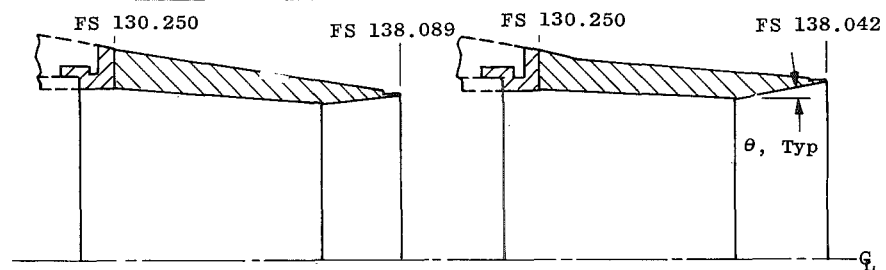
Nozzle	$A_e, \text{ft}^2$ (Full Scale)	$D_T, \text{in.}$	$D_E, \text{in.}$	$(A_E/A_T)$	$\theta$
Part A/B	5.1	7.416	7.657	1.284	$4^\circ 50' 28''$
Max A/B	6.6	8.215	8.695	1.321	$6^\circ 16' 4''$
Max A/B	7.75	8.501	9.450	1.567	$10^\circ 20' 15''$

Part A/B 5.1 ft<sup>2</sup>



Max A/B 6.6 ft<sup>2</sup>

Max A/B 7.75 ft<sup>2</sup>



c. Configurations used with large sting  
Figure 4. Concluded.

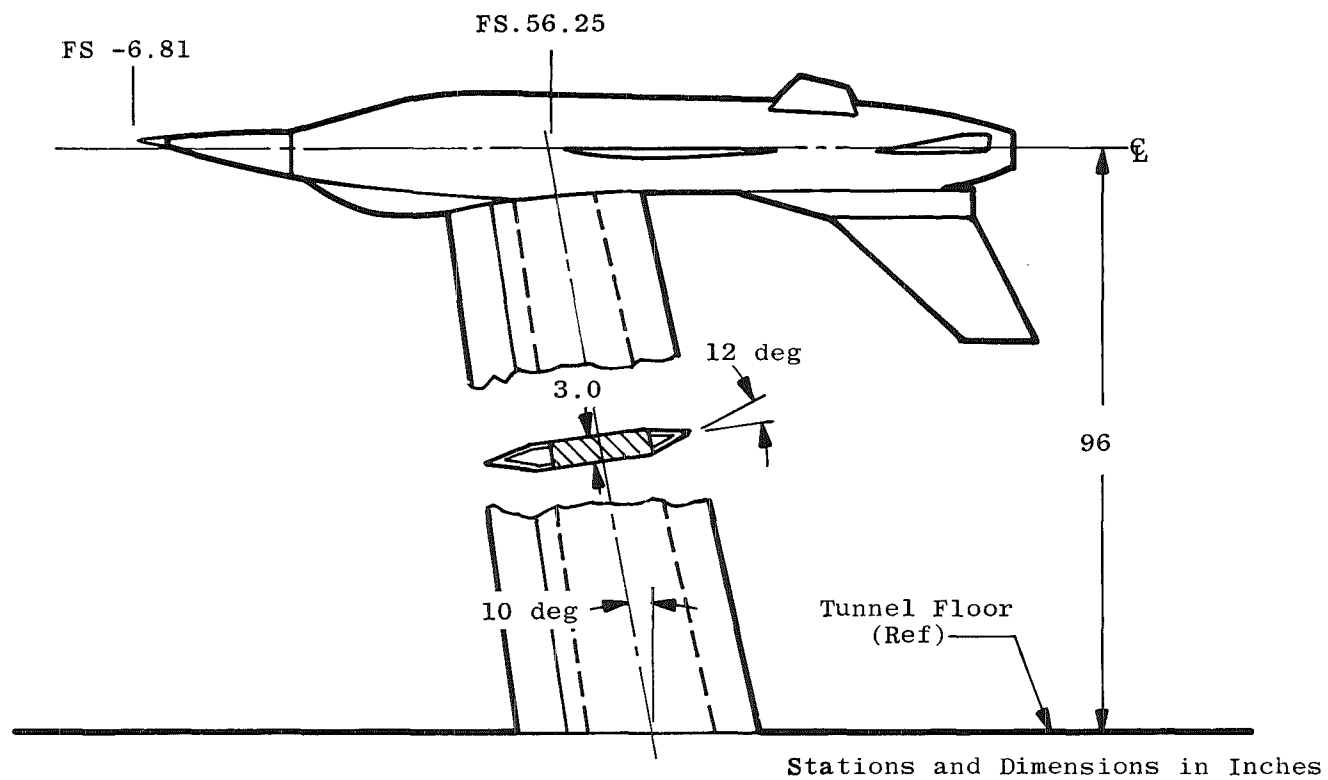
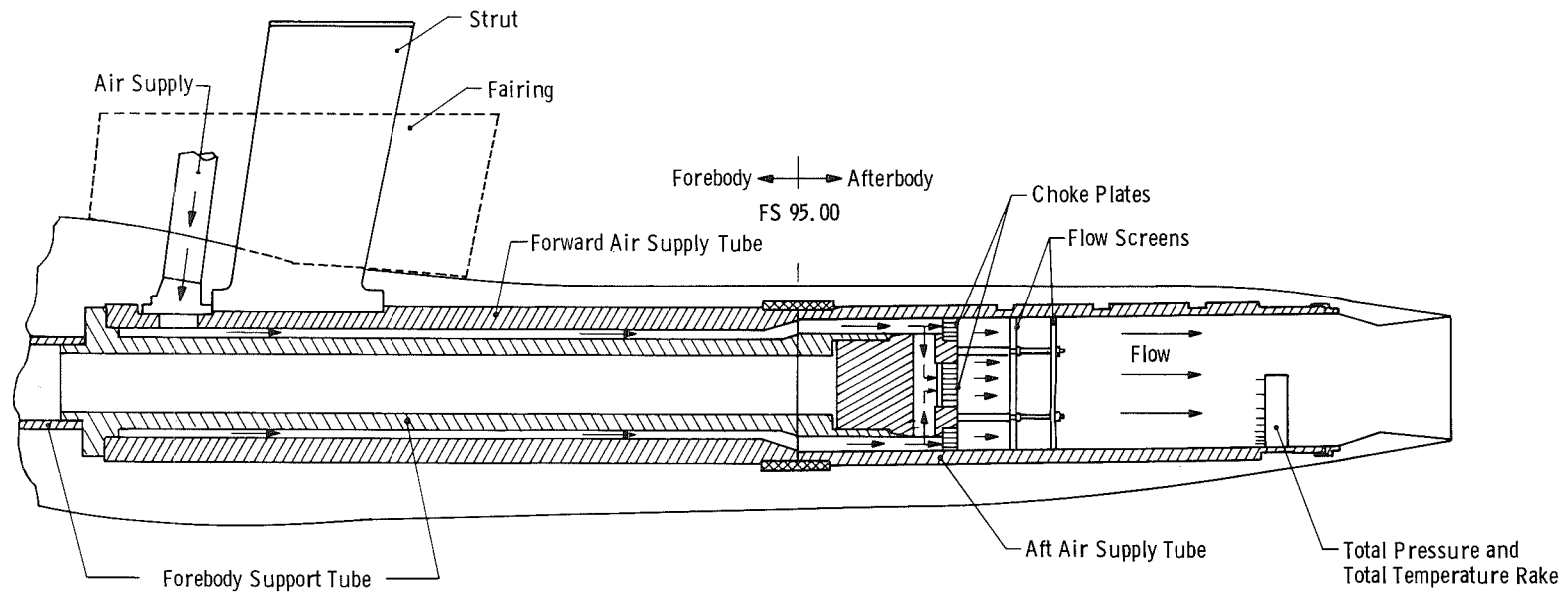
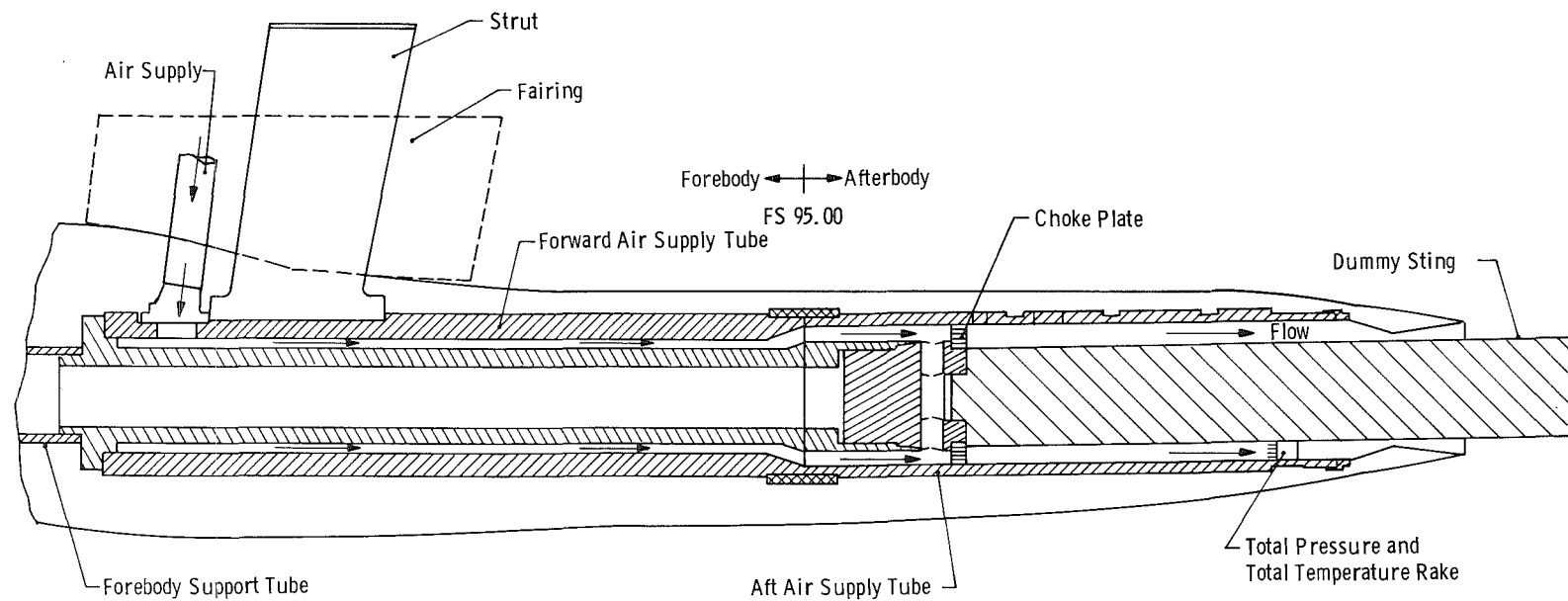


Figure 5. Strut installation.



a. Full jet nozzles

Figure 6. Internal structure and airflow system for strut-mounted model.



b. Annular jet nozzles  
Figure 6. Concluded.

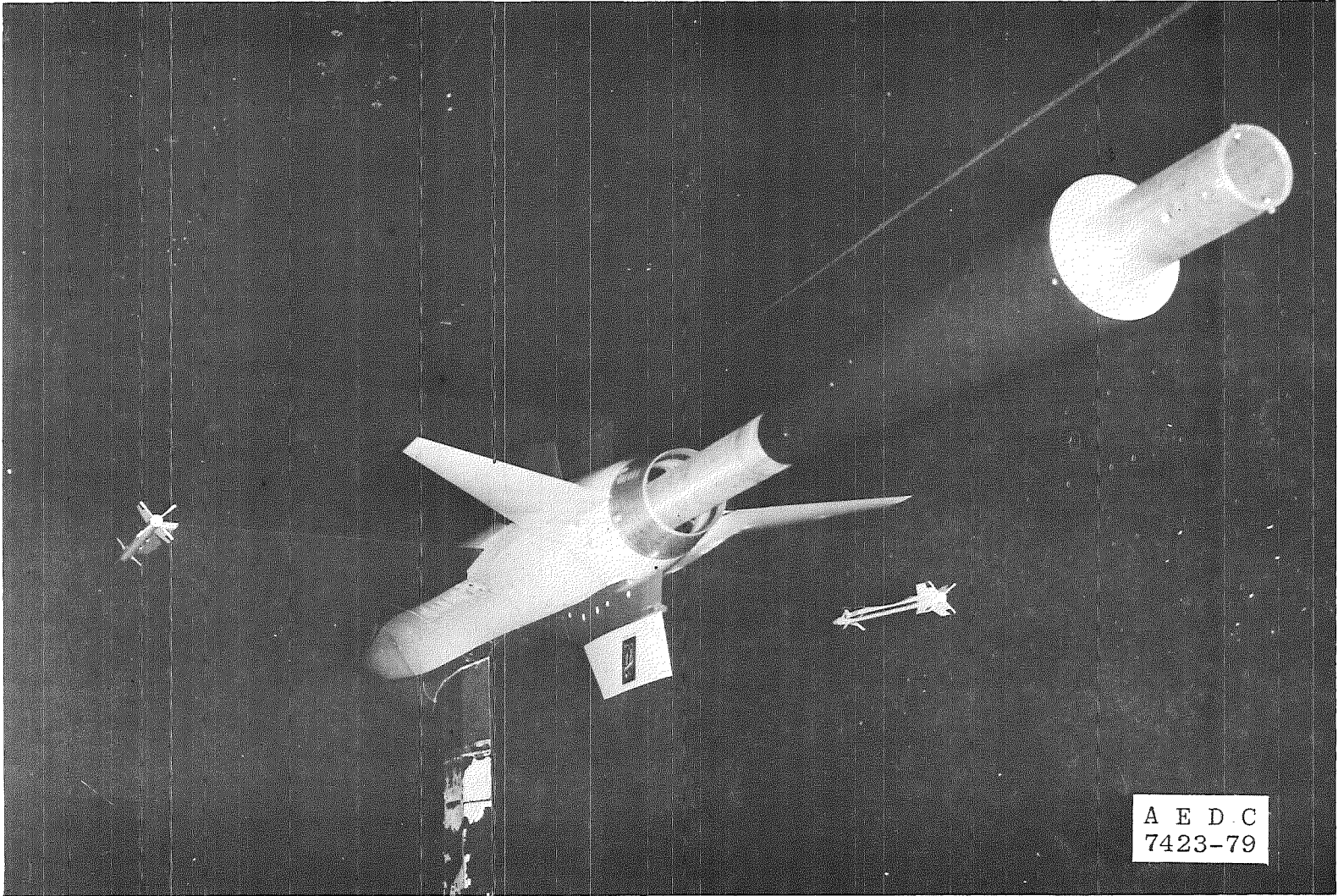


**Figure 7. Strut-mounted model with small dummy sting.**

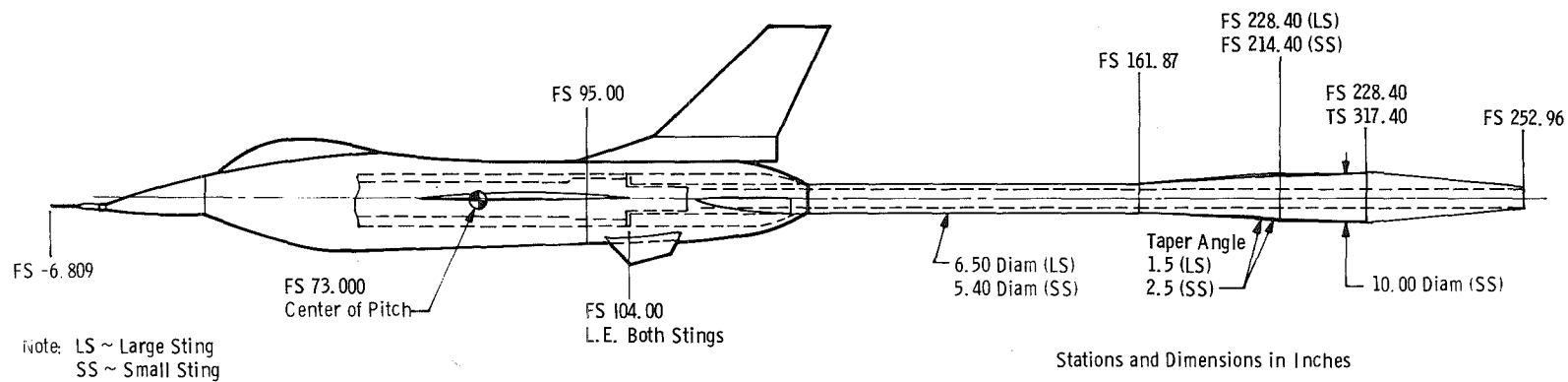


Figure 8. Sting support systems.

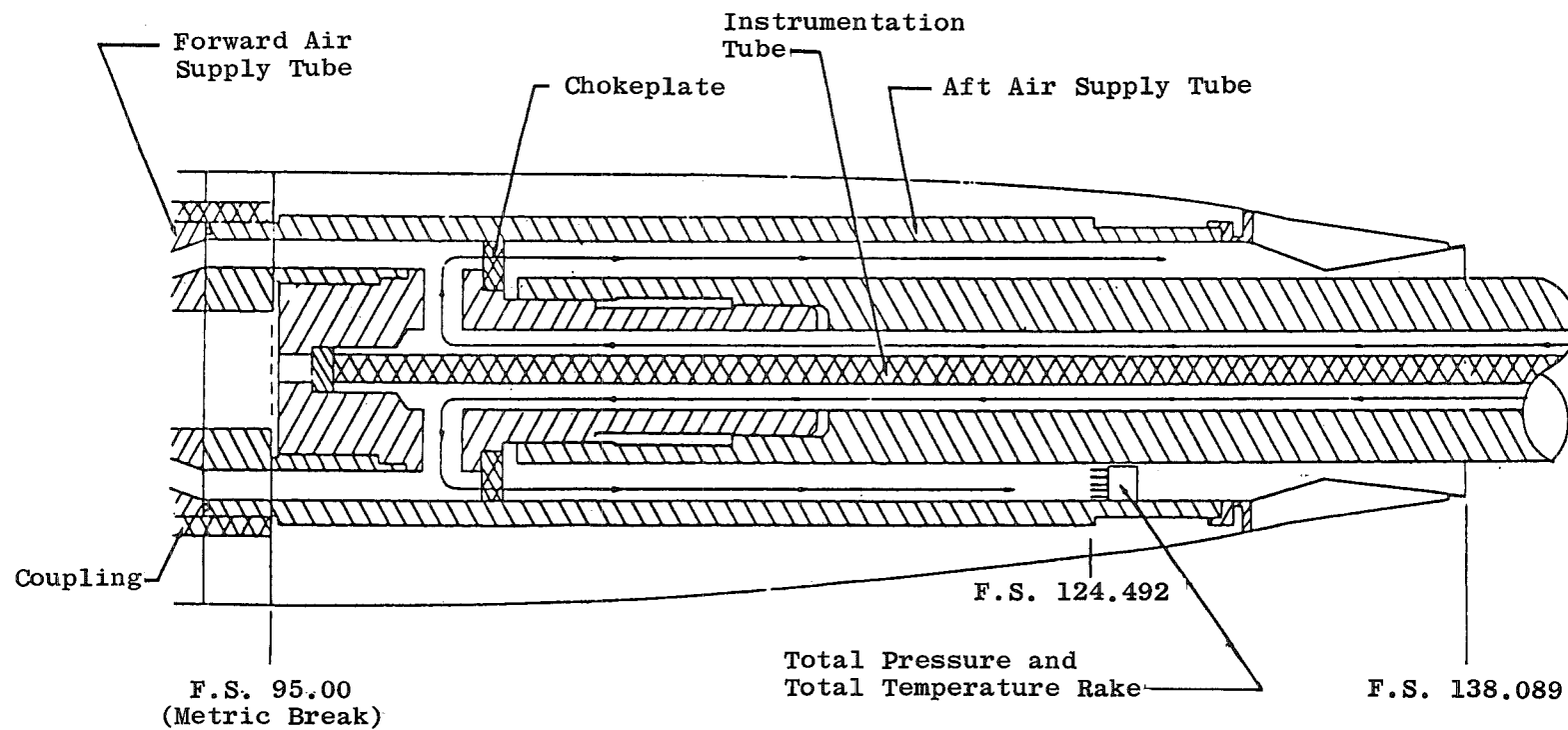


Figure 9. Model internal structure and airflow system; sting supports.

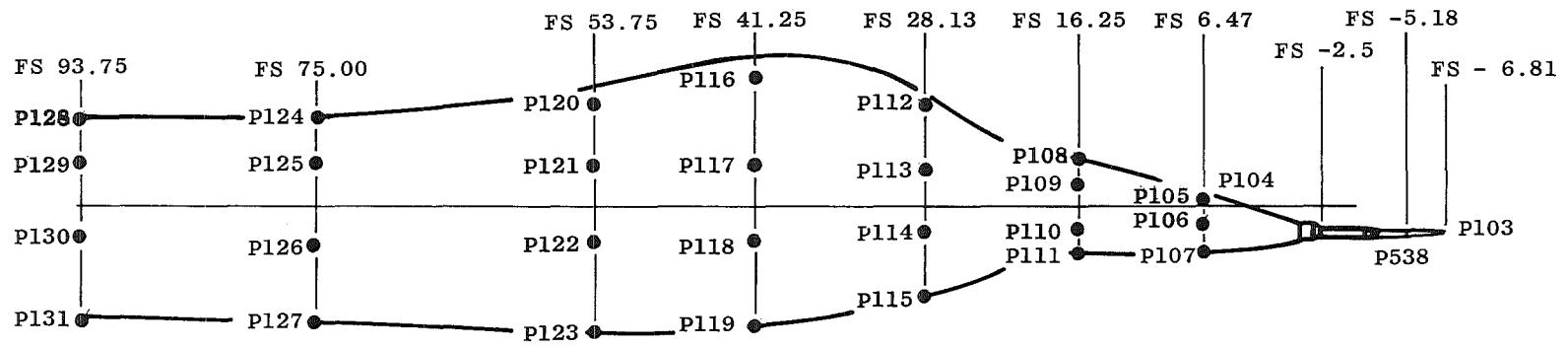
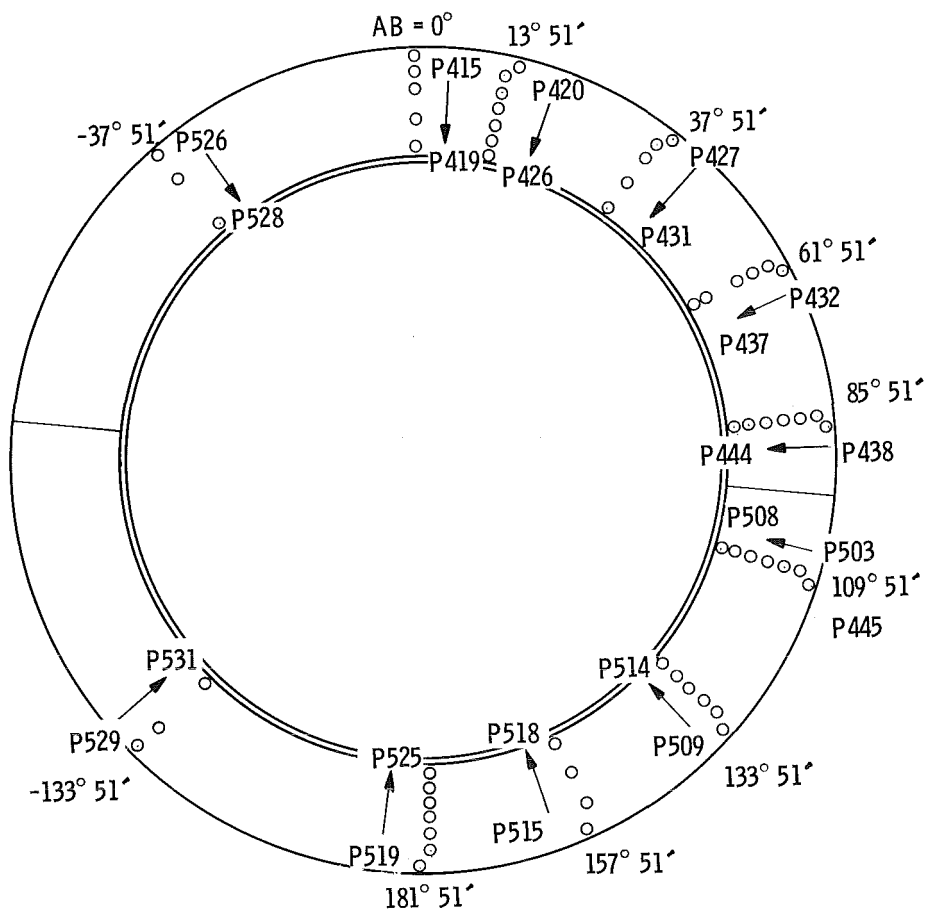


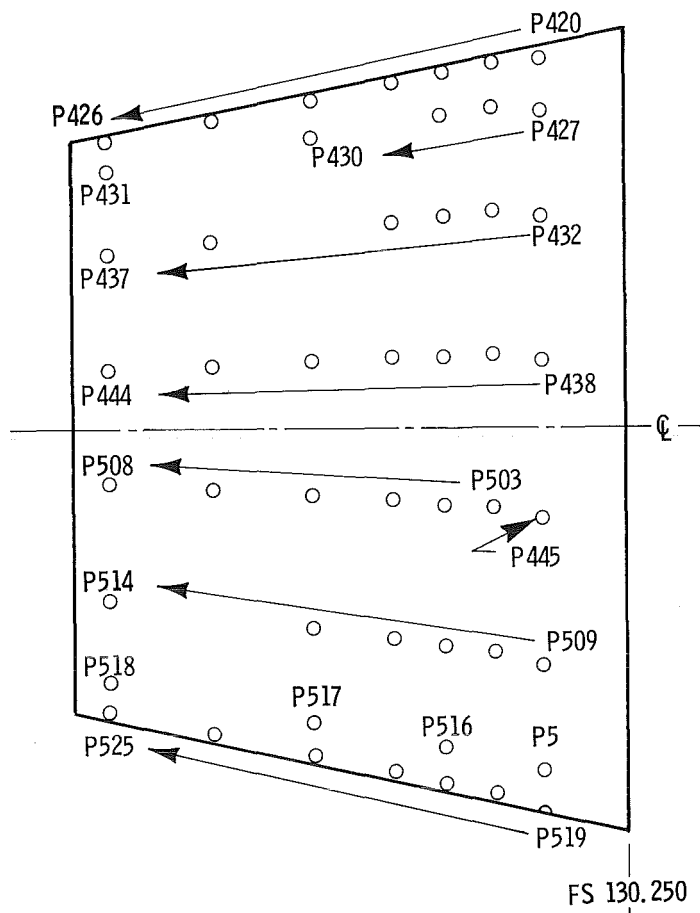
Figure 10. Forebody static pressure instrumentation.

**Figure 11. Afterbody static pressure instrumentation.**



a. Upstream view

Figure 12. Nozzle static pressure instrumentation.



b. Nozzle right-hand side view  
Figure 12. Concluded.

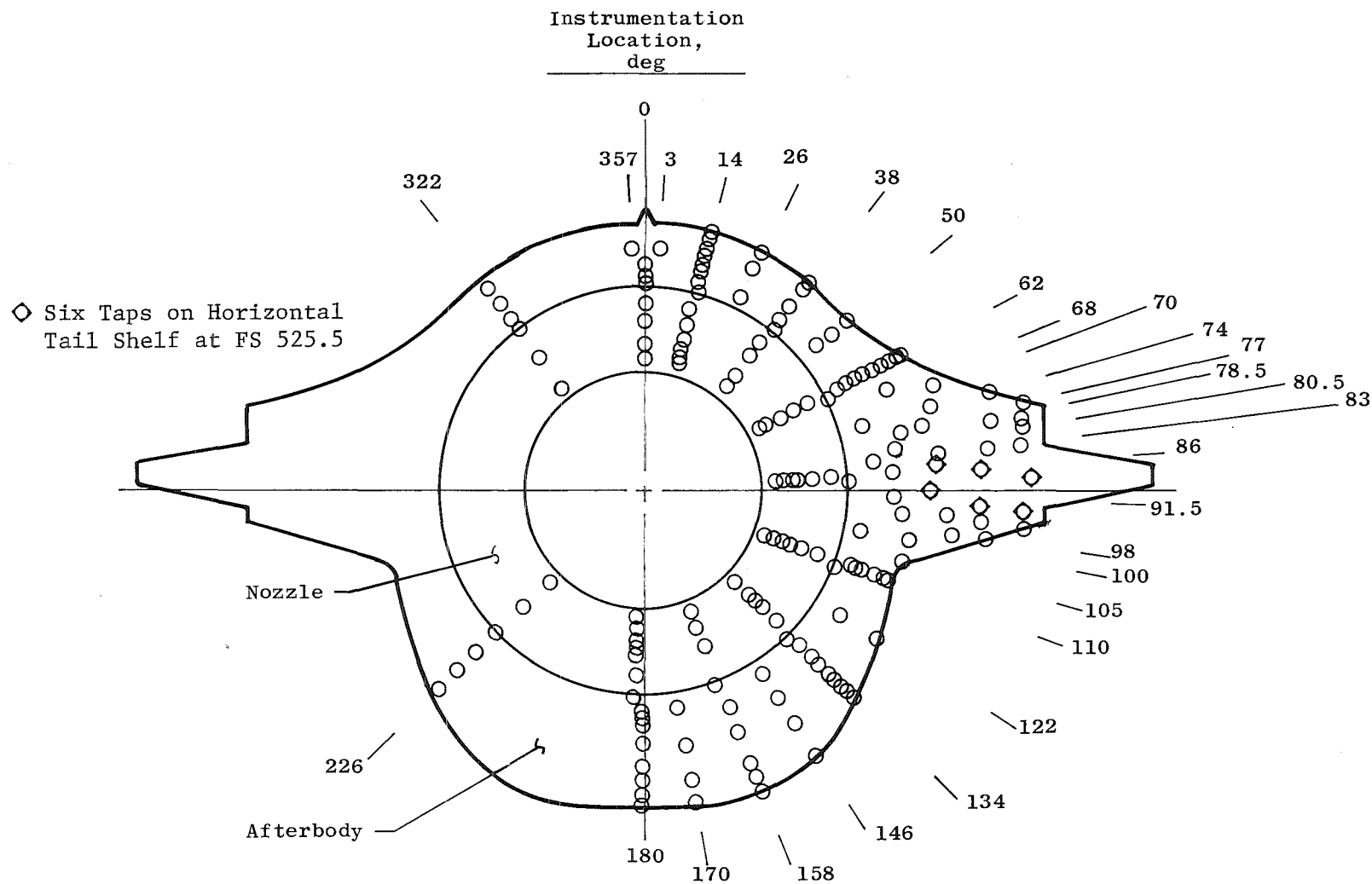


Figure 13. Nozzle-afterbody static pressure instrumentation.

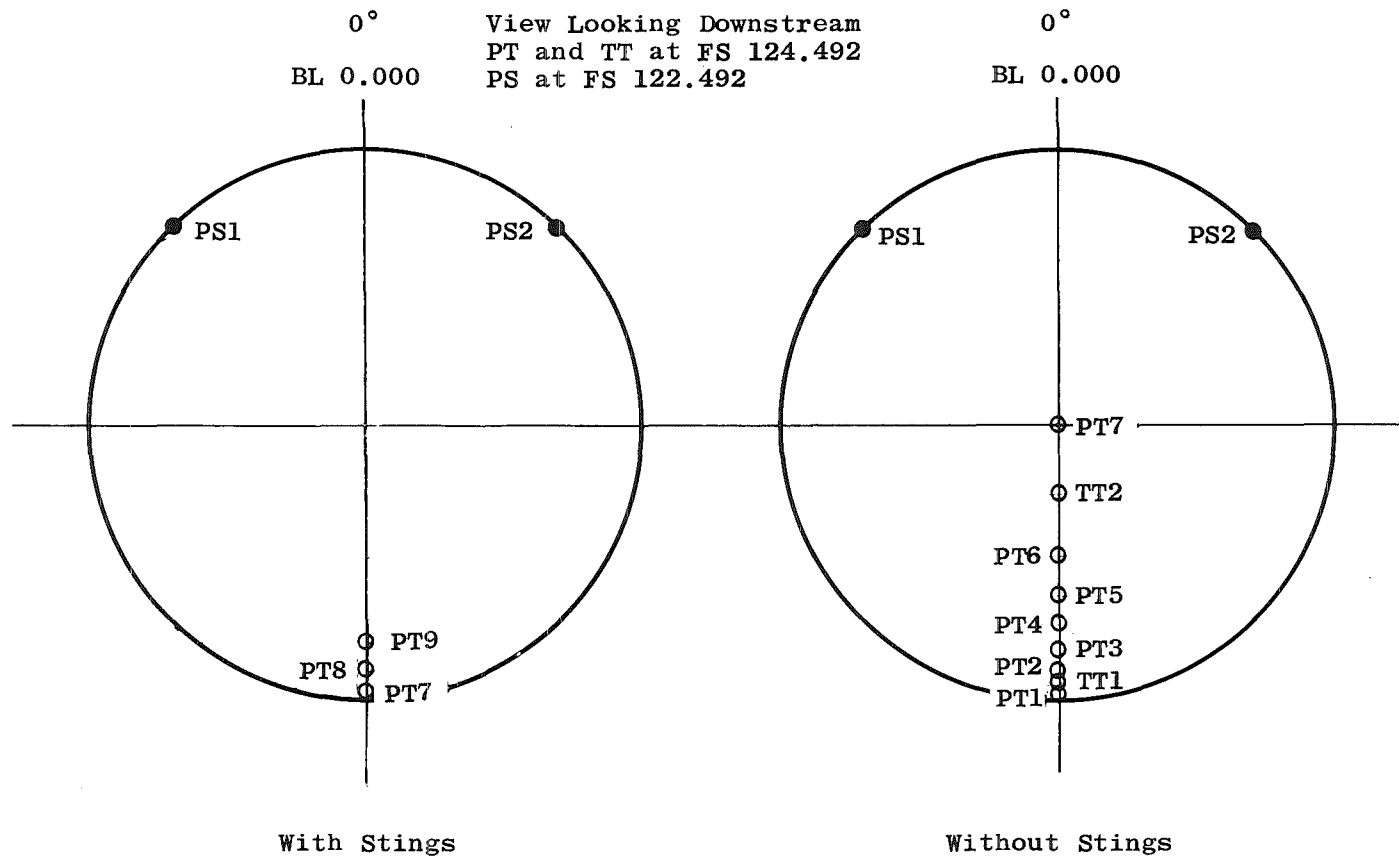


Figure 14. Aft air supply tube internal instrumentation.

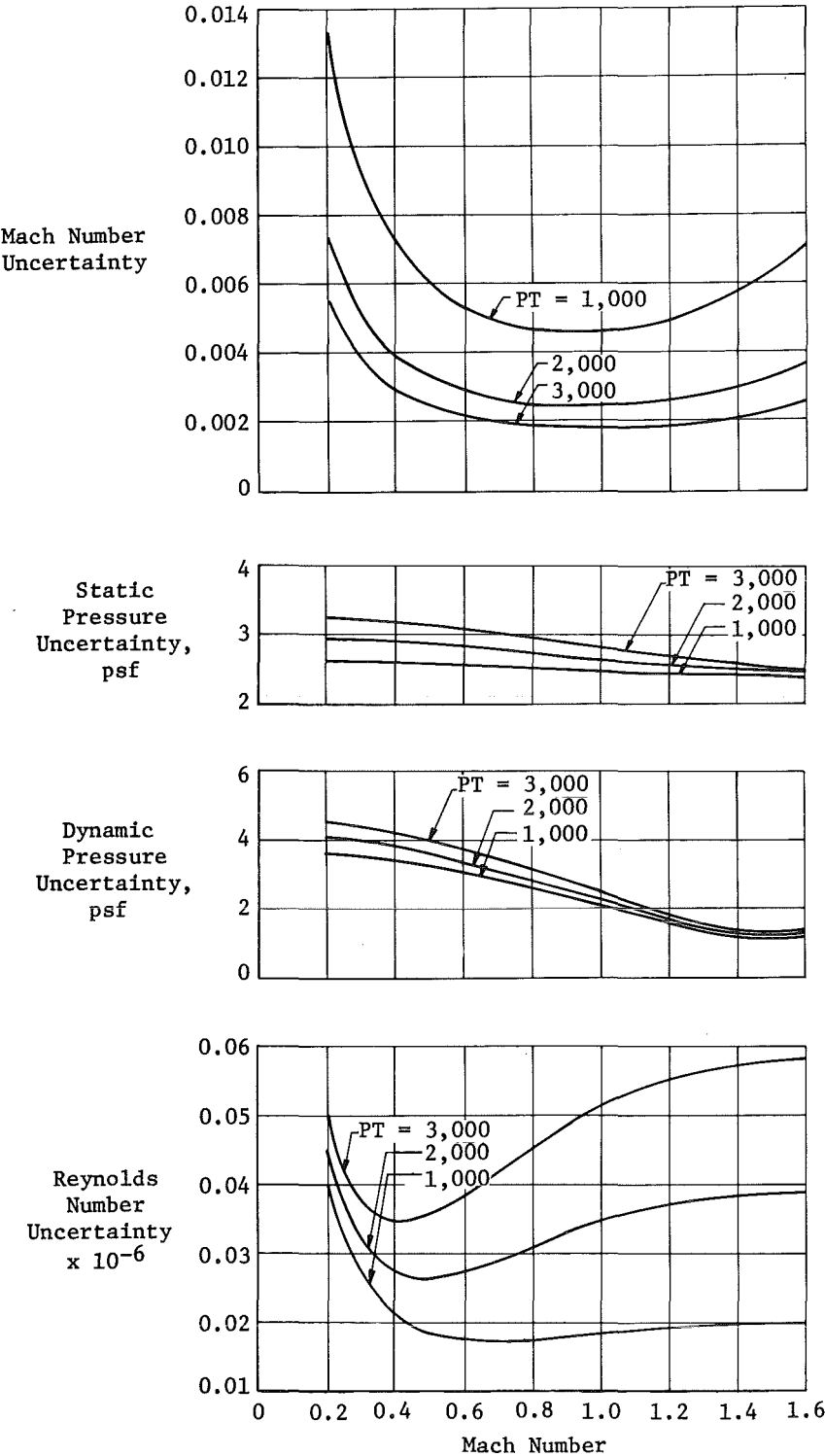
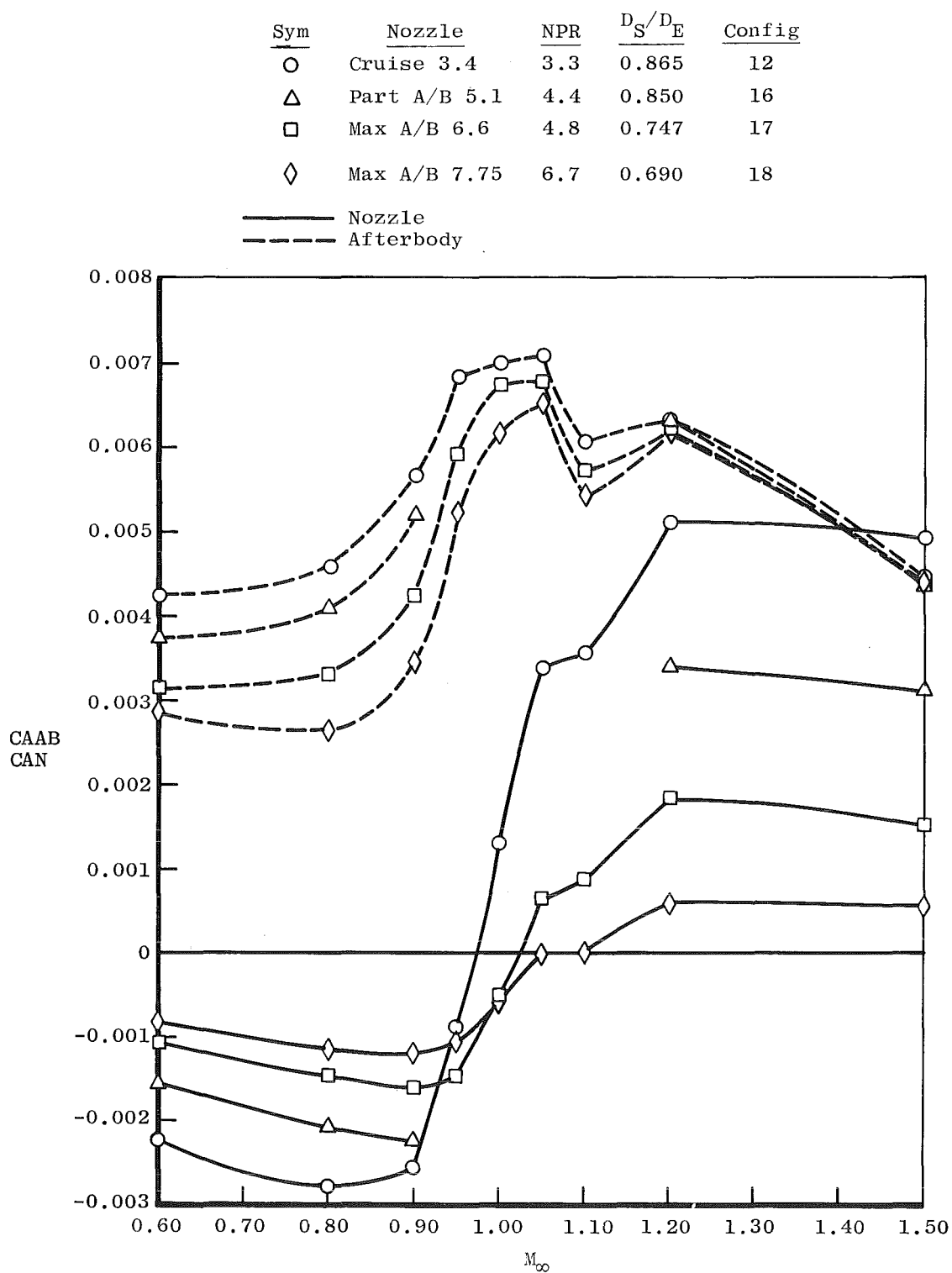


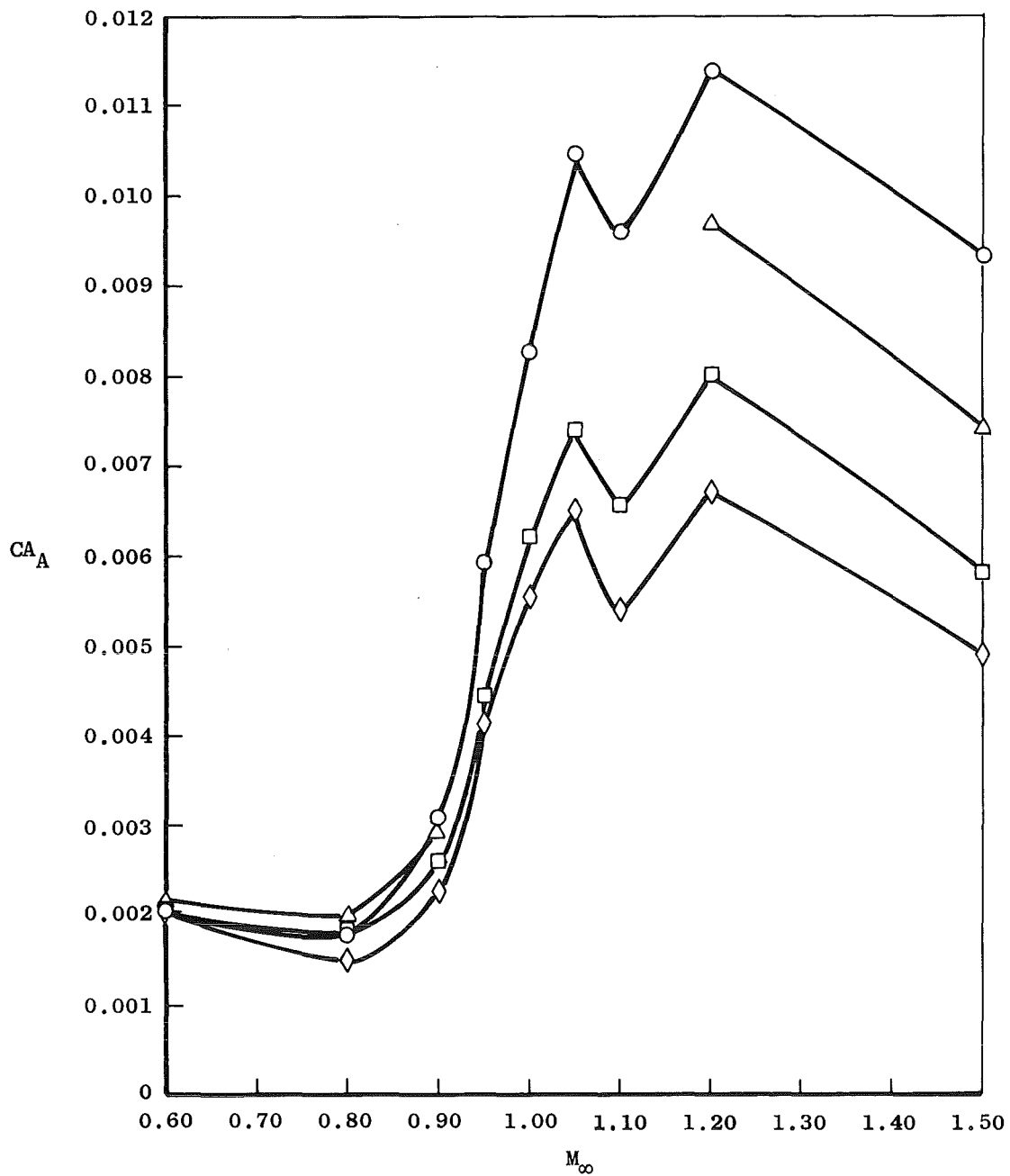
Figure 15. Estimated uncertainties in wind tunnel parameters.



a. Afterbody and nozzle

Figure 16. Effect of nozzle configuration on axial-force coefficient, sting support system,  $\alpha = 0$ .

<u>Sym</u>	<u>Nozzle</u>	<u>NPR</u>	<u><math>D_S/D_E</math></u>	<u>Config</u>
○	Cruise 3.4	3.3	0.865	12
△	Part A/B 5.1	4.4	0.850	16
□	Max A/B 6.6	4.8	0.747	17
◇	Max A/B 7.75	6.7	0.690	18



b. Complete aft nacelle  
Figure 16. Concluded.

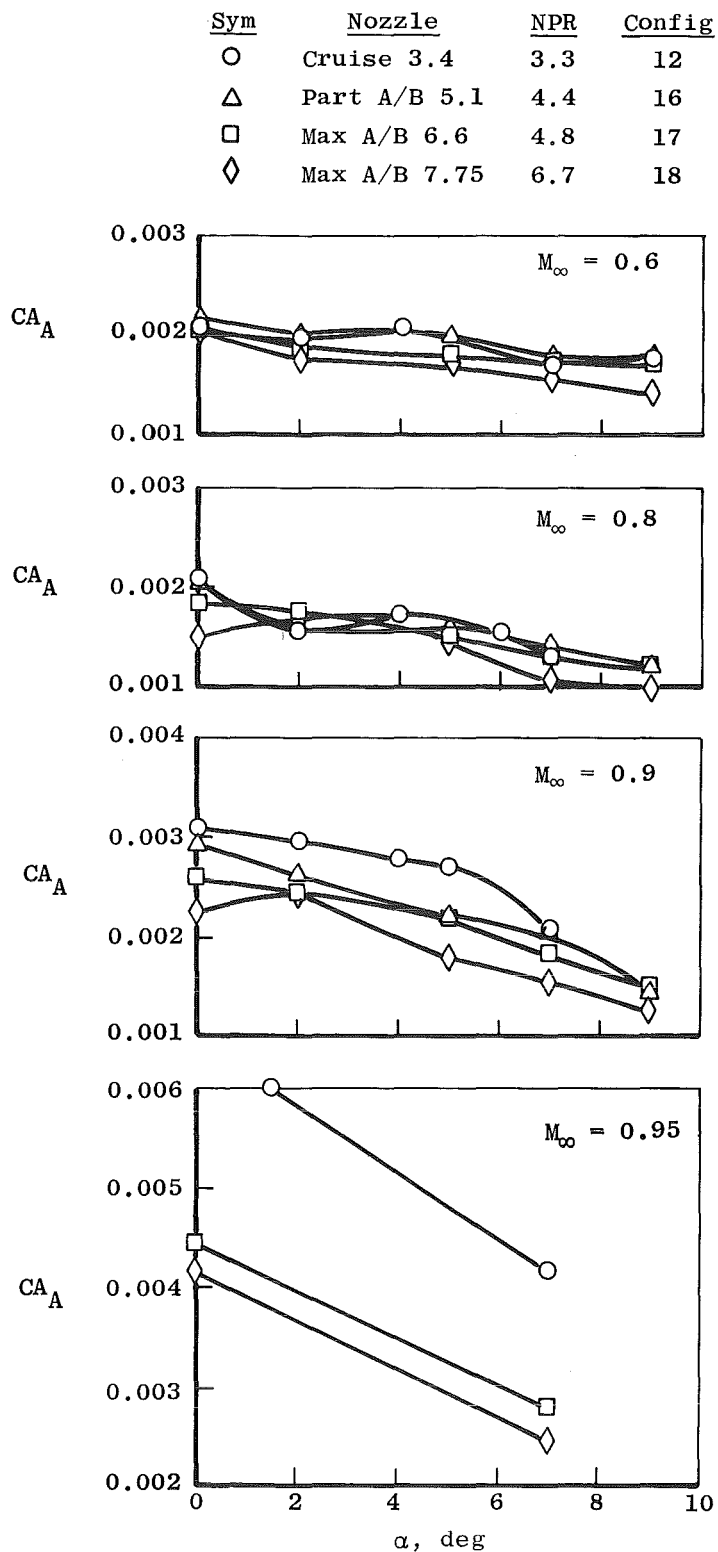


Figure 17. Effect of angle of attack on the nozzle-afterbody axial-force coefficient for various nozzle configurations, sting support system.

<u>Sym</u>	<u>Nozzle</u>	<u>NPR</u>	<u>Config</u>
○	Cruise 3.4	3.3	12
△	Part A/B 5.1	4.4	16
□	Max A/B 6.6	4.8	17
◇	Max A/B 7.75	6.7	18

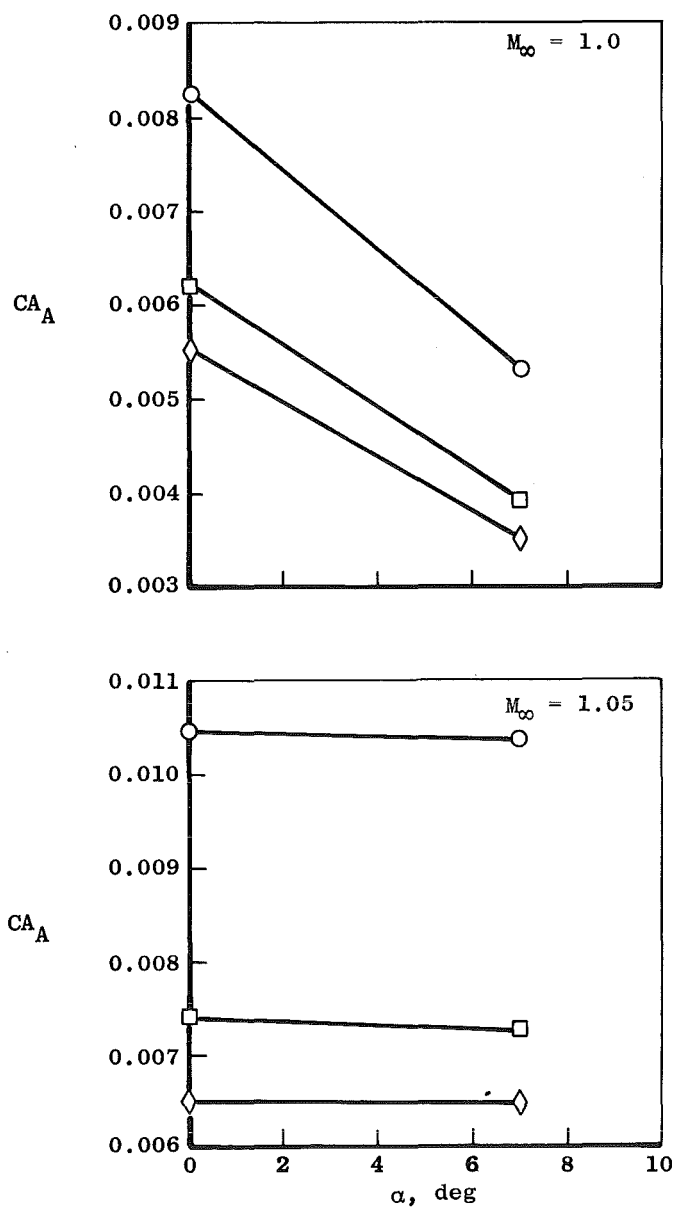


Figure 17. Continued.

Sym	Nozzle	NPR	Config
○	Cruise 3.4	3.3	12
△	Part A/B 5.1	4.4	16
□	Max A/B 6.6	4.8	17
◇	Max A/B 7.75	6.7	18

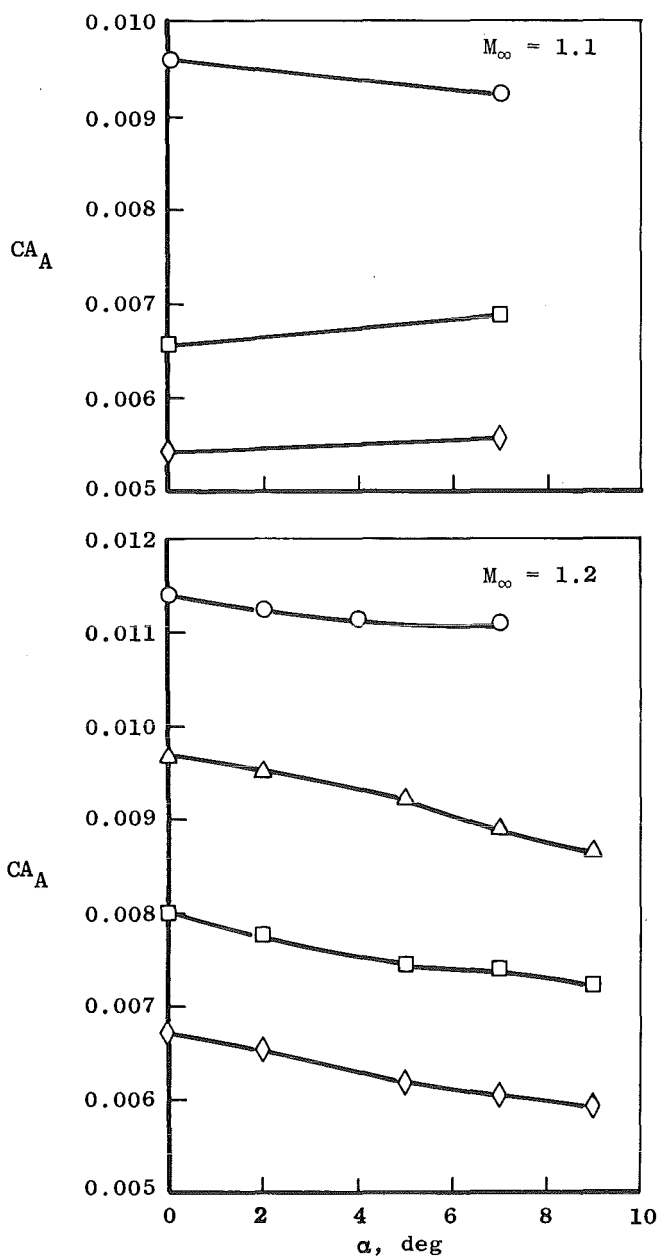


Figure 17. Continued.

<u>Sym</u>	<u>Nozzle</u>	<u>NPR</u>	<u>Config</u>
○	Cruise 3.4	3.3	12
△	Part A/B 5.1	4.4	16
□	Max A/B 6.6	4.8	17
◇	Max A/B 7.75	6.7	18

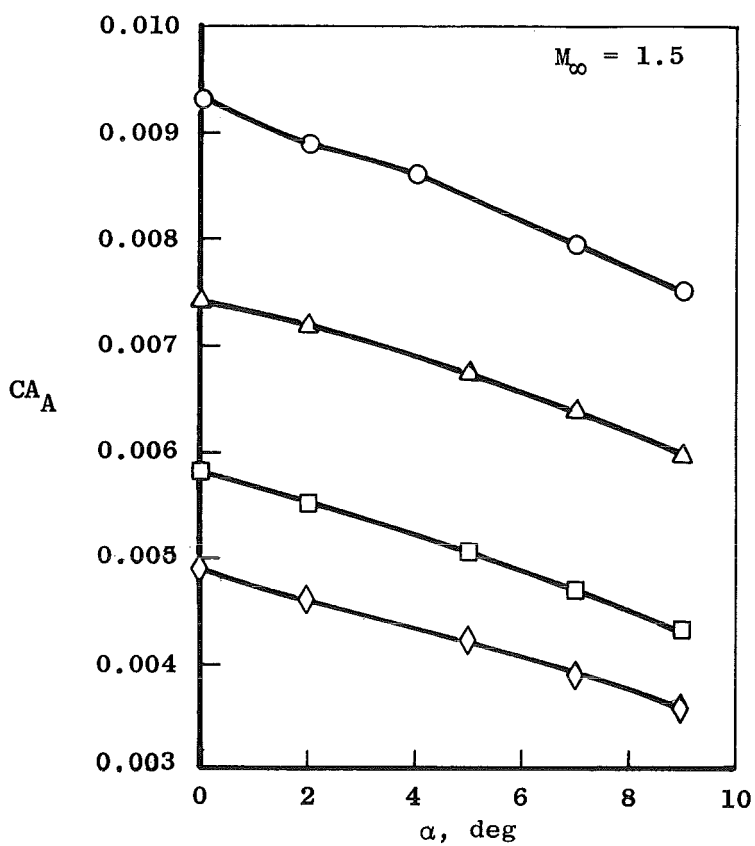


Figure 17. Concluded.

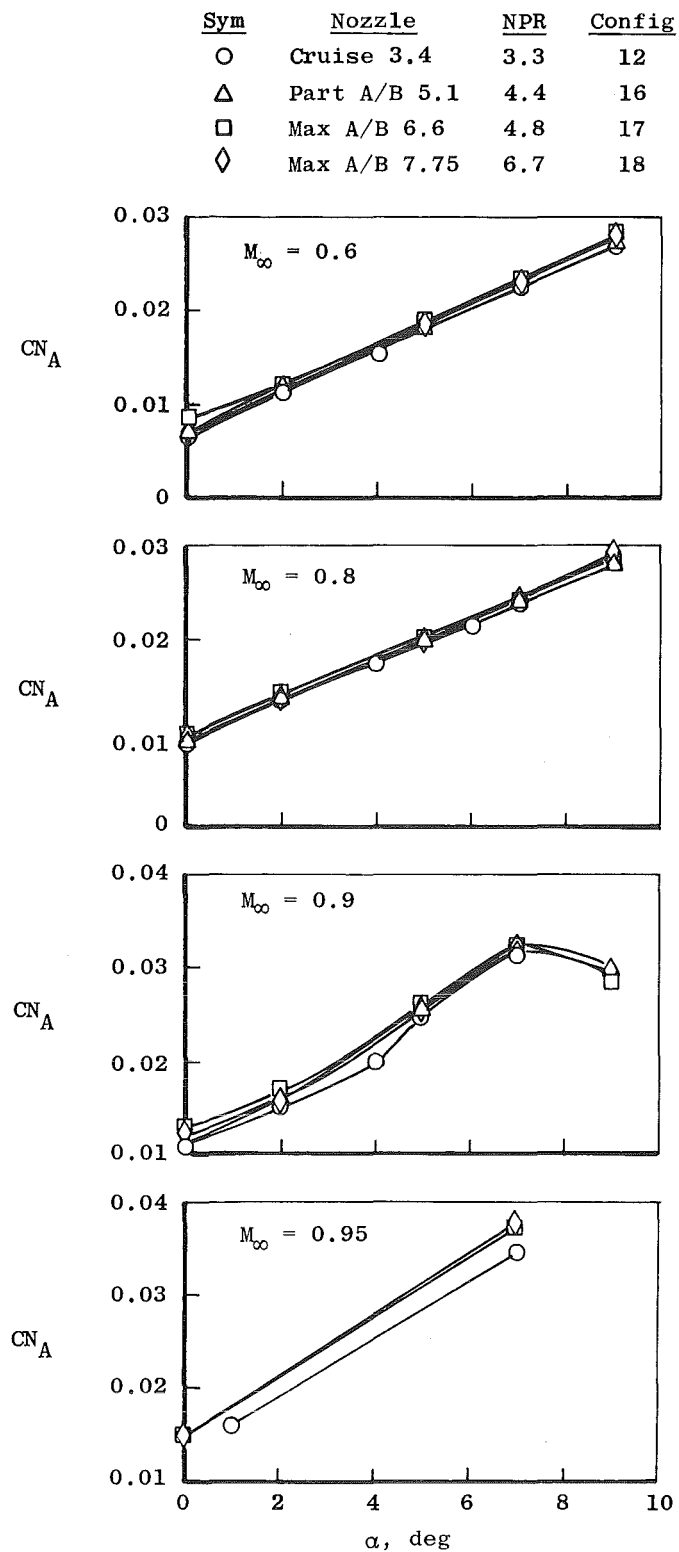
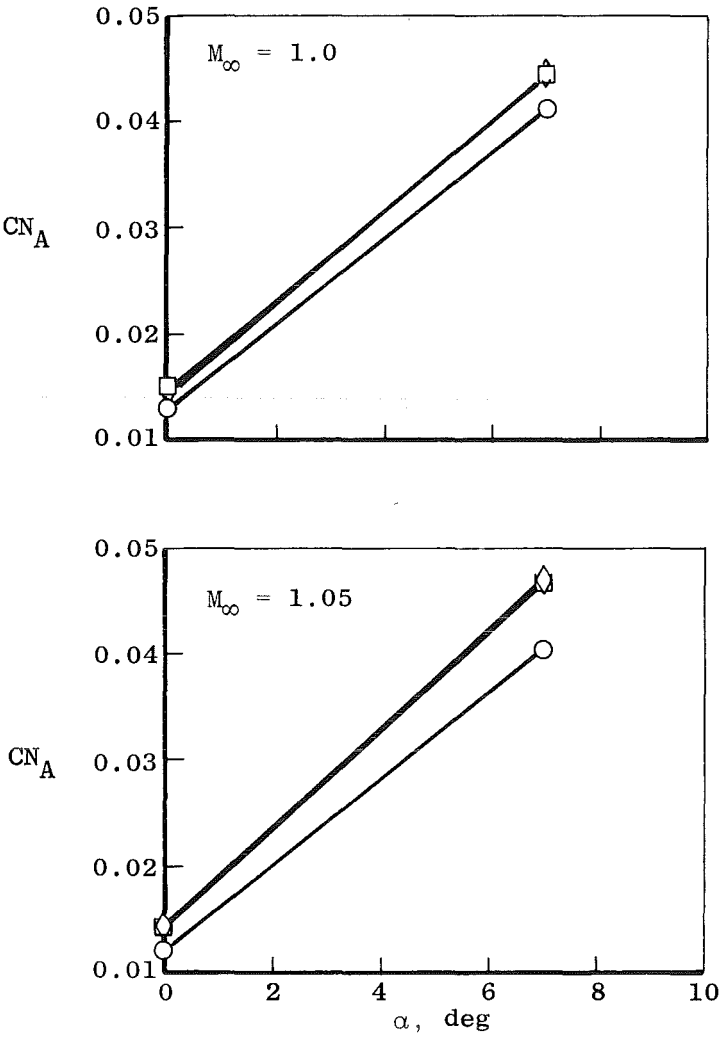


Figure 18. Effect of angle of attack on the nozzle-afterbody normal-force coefficient for various nozzle configurations, sting support system.

Sym	Nozzle	NPR	Config
○	Cruise 3.4	3.3	12
△	Part A/B 5.1	4.4	16
□	Max A/B 6.6	4.8	17
◇	Max A/B 7.75	6.7	18



<u>Sym</u>	<u>Nozzle</u>	<u>NPR</u>	<u>Config</u>
○	Cruise 3.4	3.3	12
△	Part A/B 5.1	4.4	16
□	Max A/B 6.6	4.8	17
◇	Max A/B 7.75	6.7	18

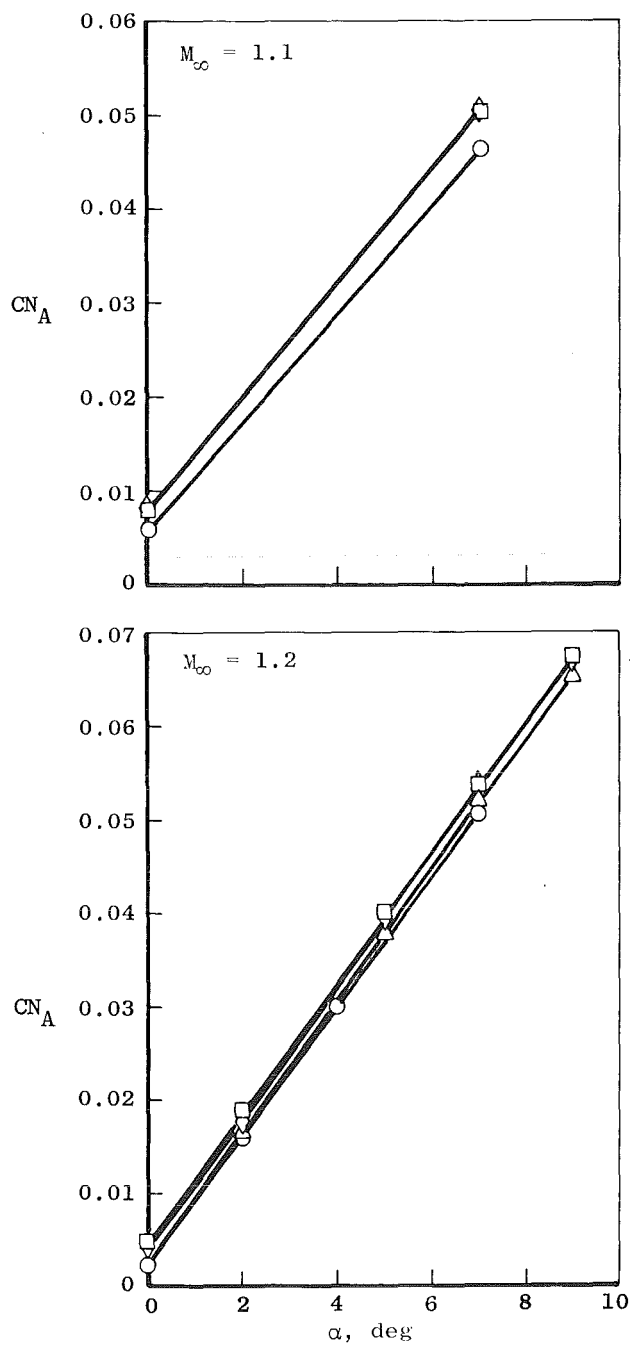


Figure 18. Continued.

Sym	Nozzle	NPR	Config
○	Cruise 3.4	3.3	12
△	Part A/B 5.1	4.4	16
□	Max A/B 6.6	4.8	17
◇	Max A/B 7.75	6.7	18

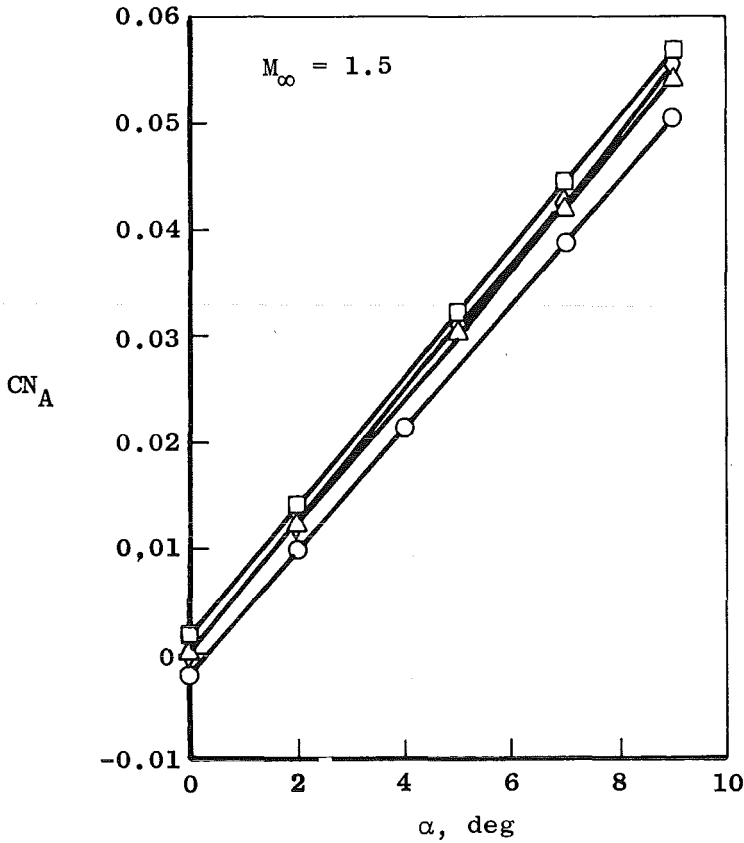


Figure 18. Concluded.

Sym	Nozzle	NPR	Config
○	Cruise 3.4	3.3	12
△	Part A/B 5.1	4.4	16
□	Max A/B 6.6	4.8	17
◇	Max A/B 7.75	6.7	18

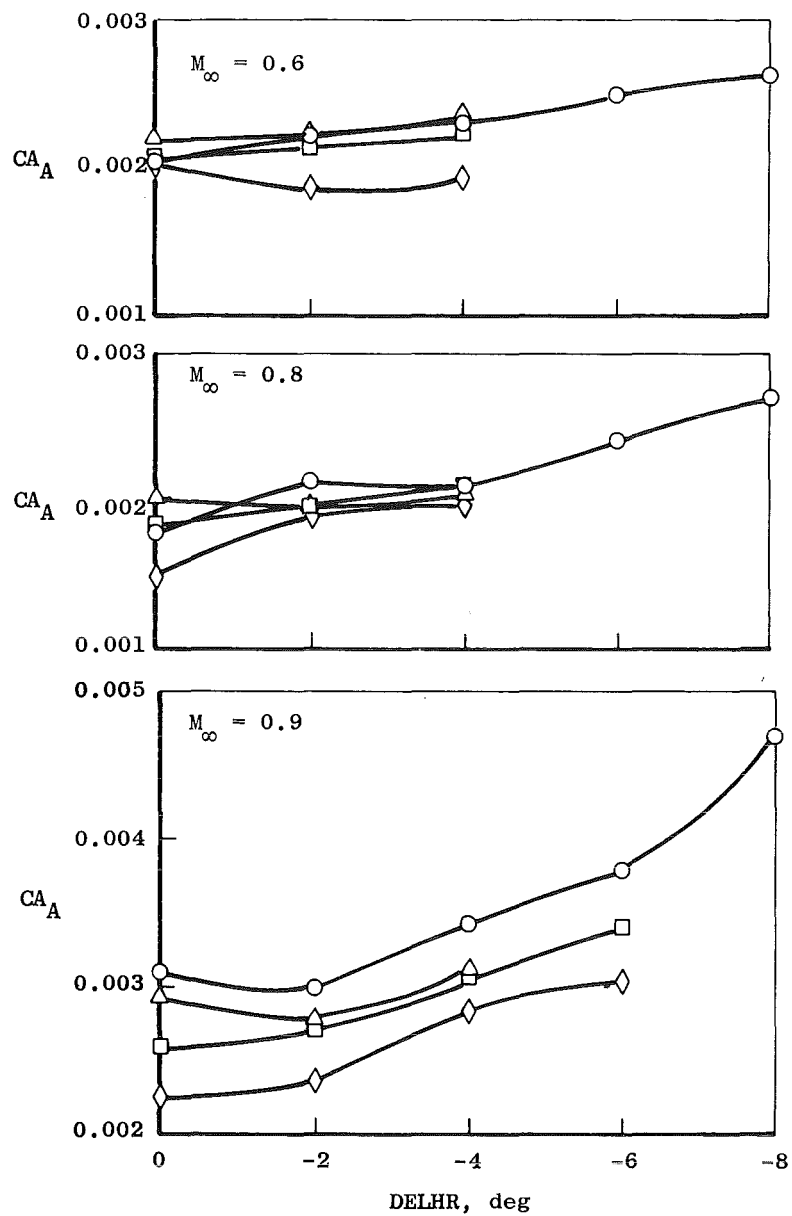


Figure 19. Effect of horizontal tail deflection on the nozzle-afterbody axial-force coefficients for various nozzle configurations, sting support system,  $\alpha = 0$ .

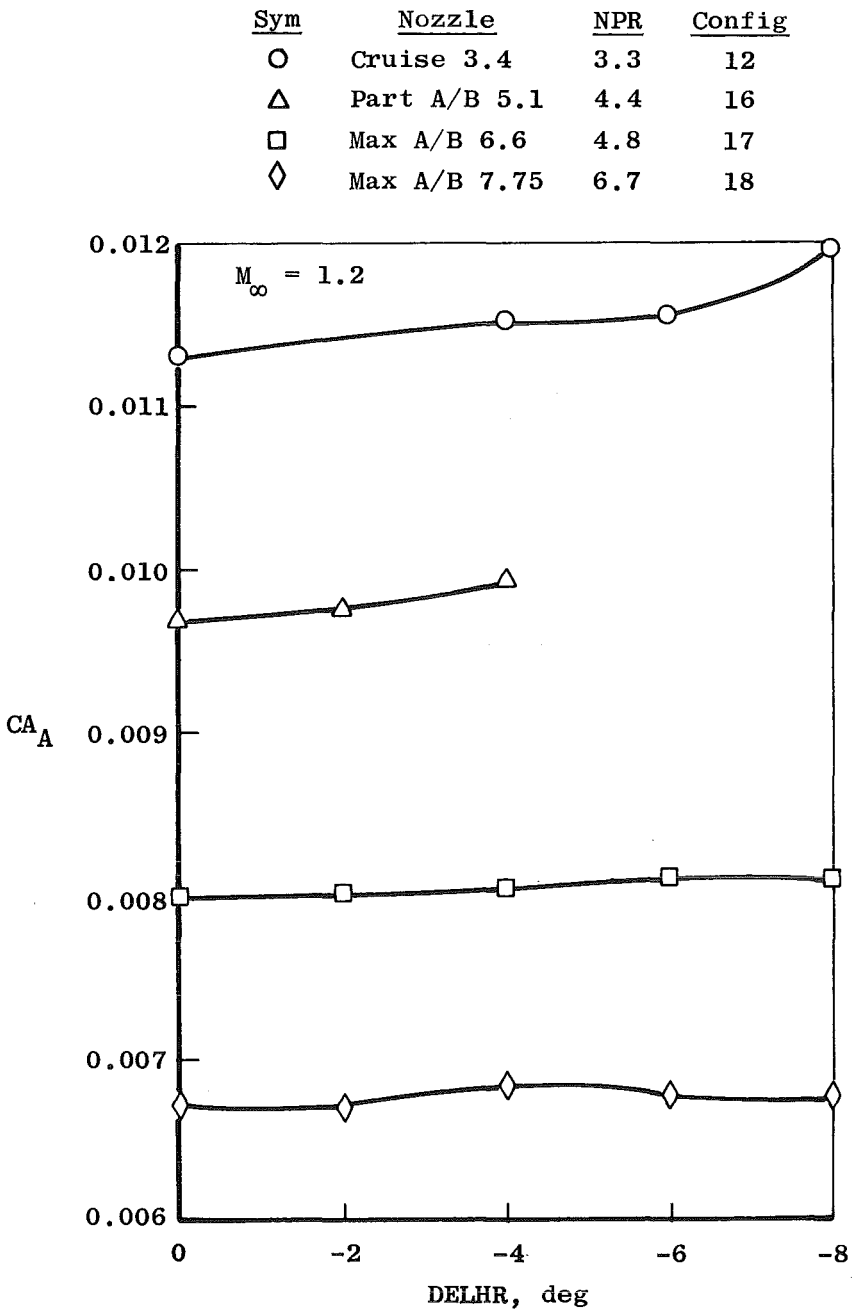


Figure 19. Continued.

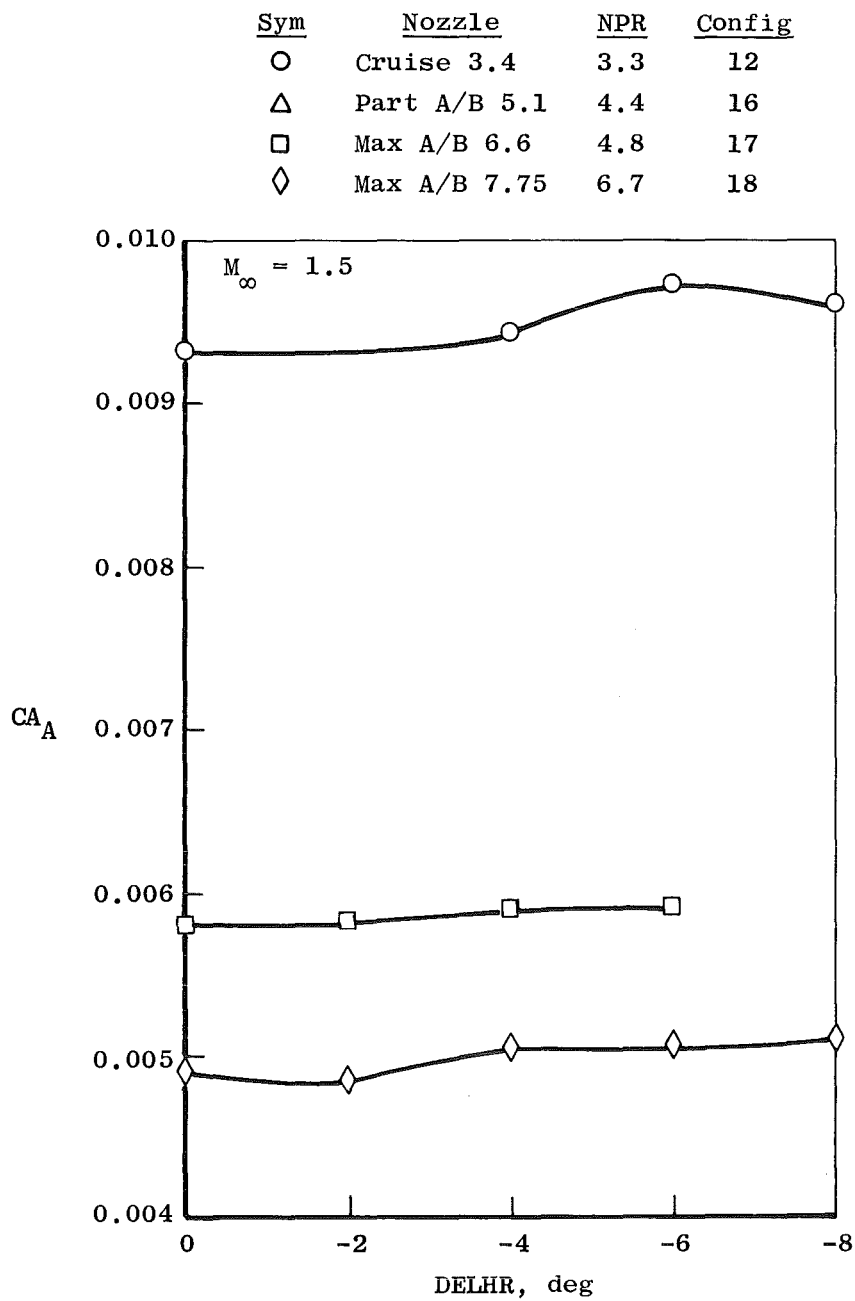


Figure 19. Concluded.

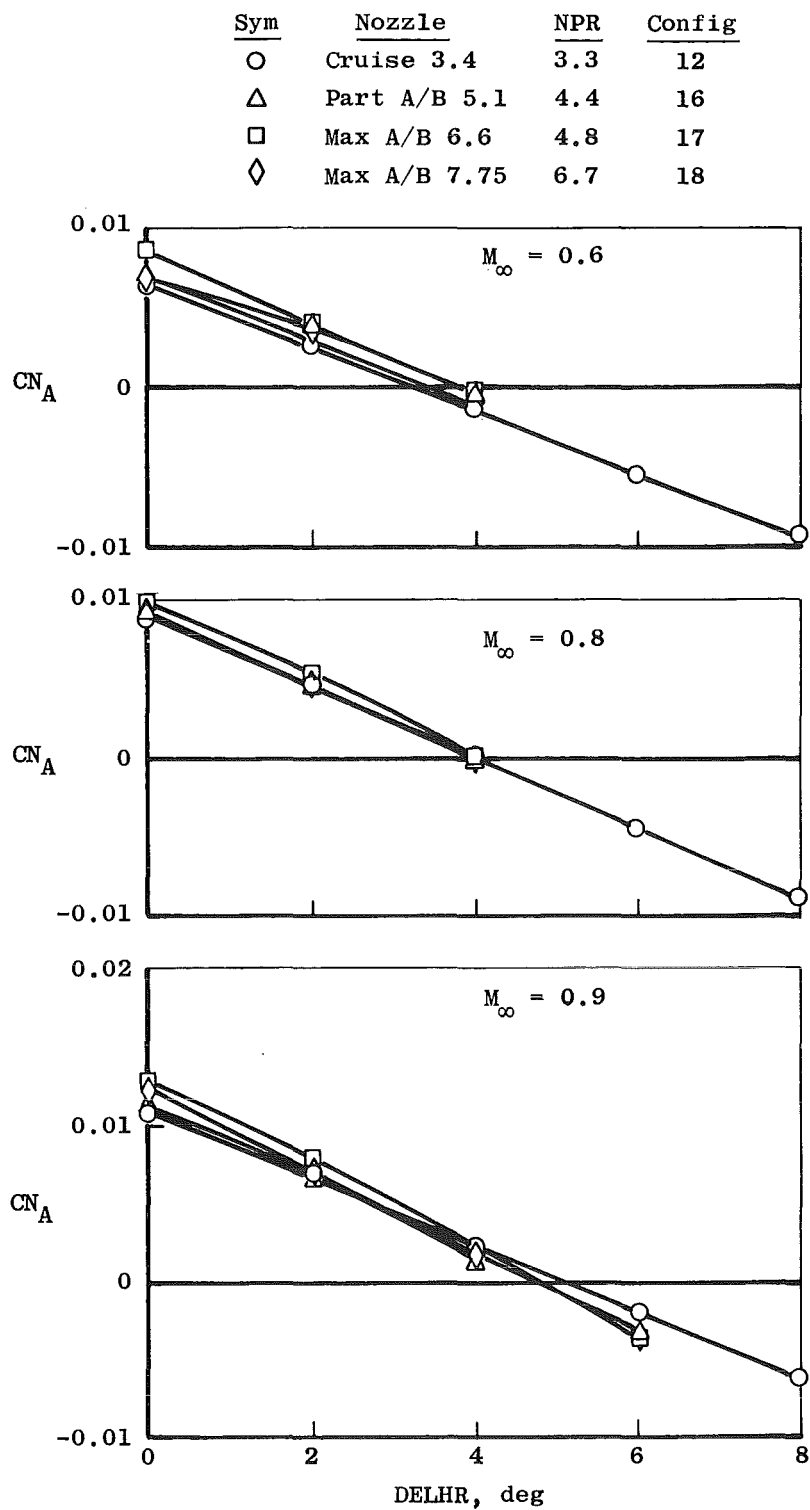


Figure 20. Effect of horizontal tail deflection on the nozzle-afterbody normal-force coefficients for various nozzle configurations, sting support system,  $\alpha = 0$ .

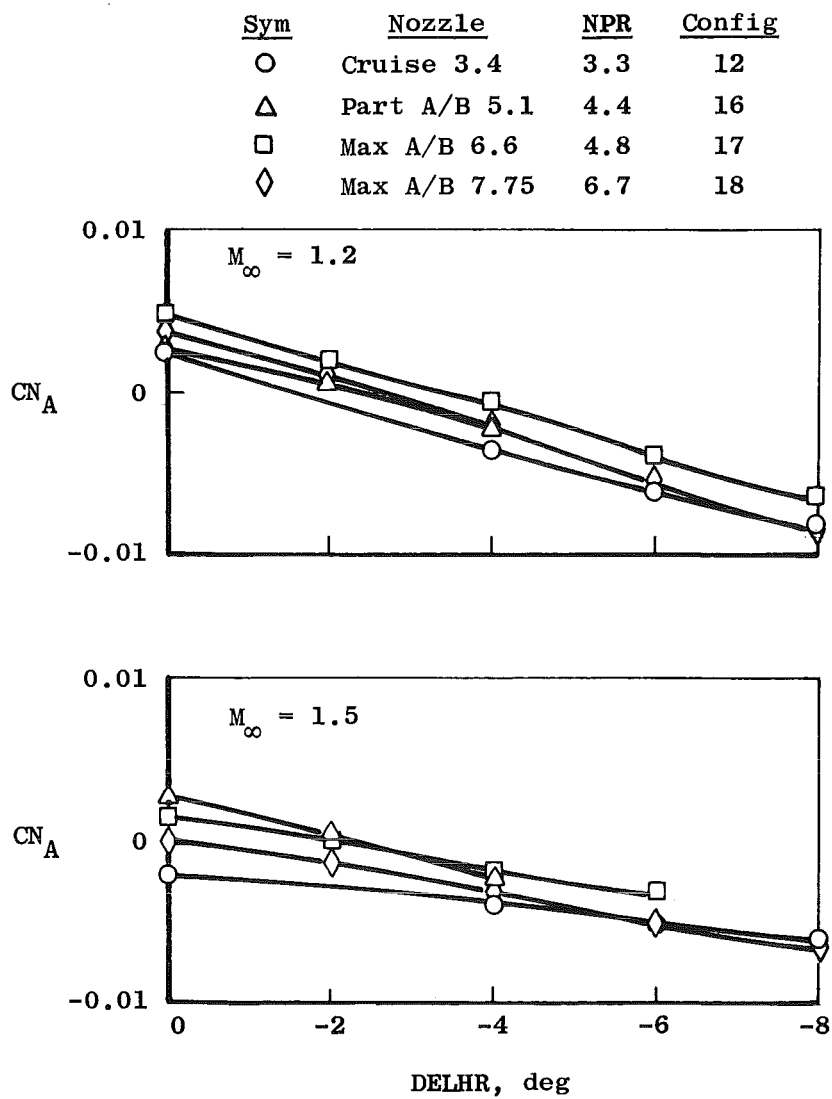


Figure 20. Concluded.

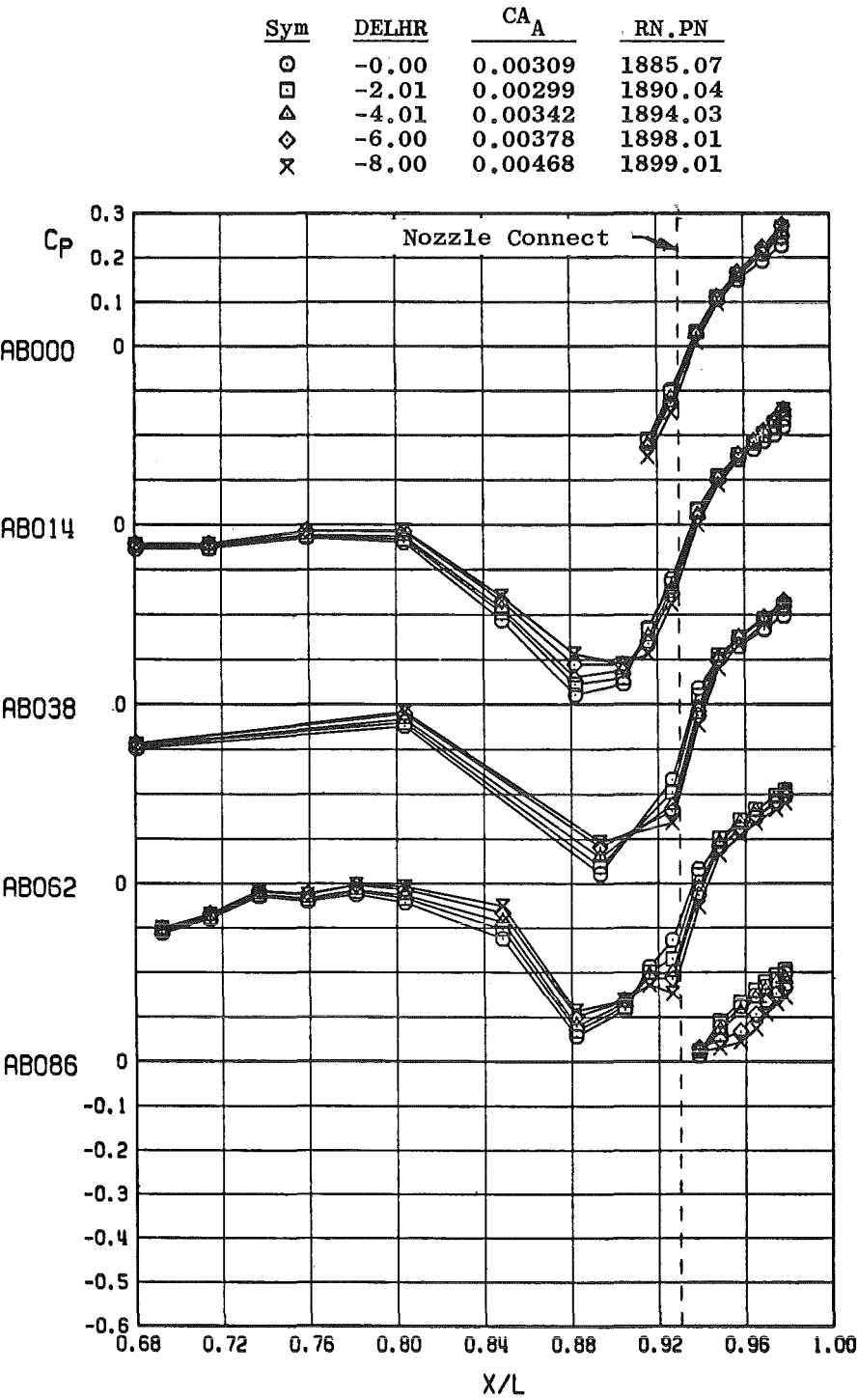


Figure 21. Influence of horizontal tail deflection on the nozzle-afterbody pressure distribution, sting support system, cruise 3.4 nozzle, NPR = 3.3,  $M_\infty = 0.9$ ,  $\alpha = 0$ ,  $RE \approx 3.40 \times 10^{-6}$ .

<u>Sym</u>	<u>DELHR</u>	<u>CA<sub>A</sub></u>	<u>RN.PN</u>
○	-0.00	0.00309	1885.07
□	-2.01	0.00299	1890.04
△	-4.01	0.00342	1894.03
◇	-6.00	0.00378	1898.01
×	-8.00	0.00468	1899.01

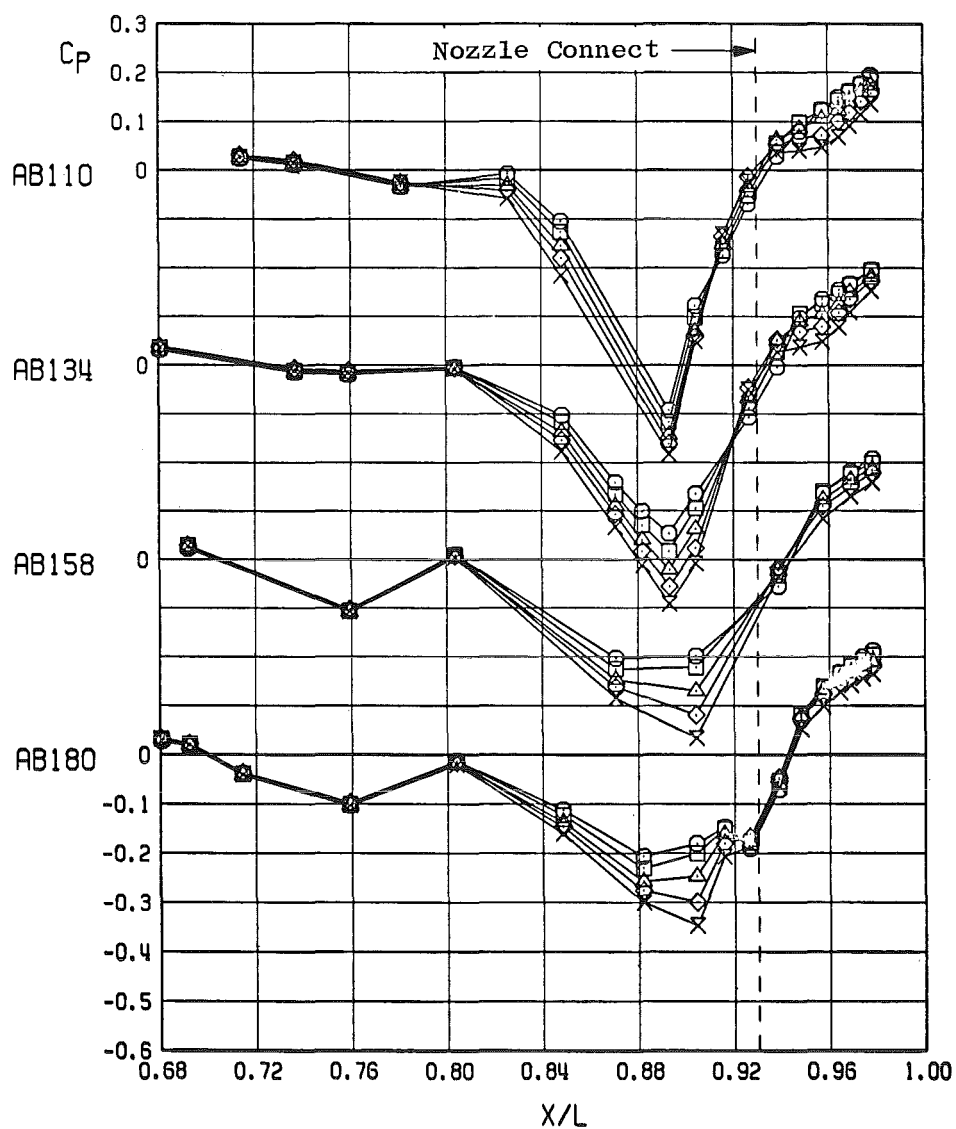
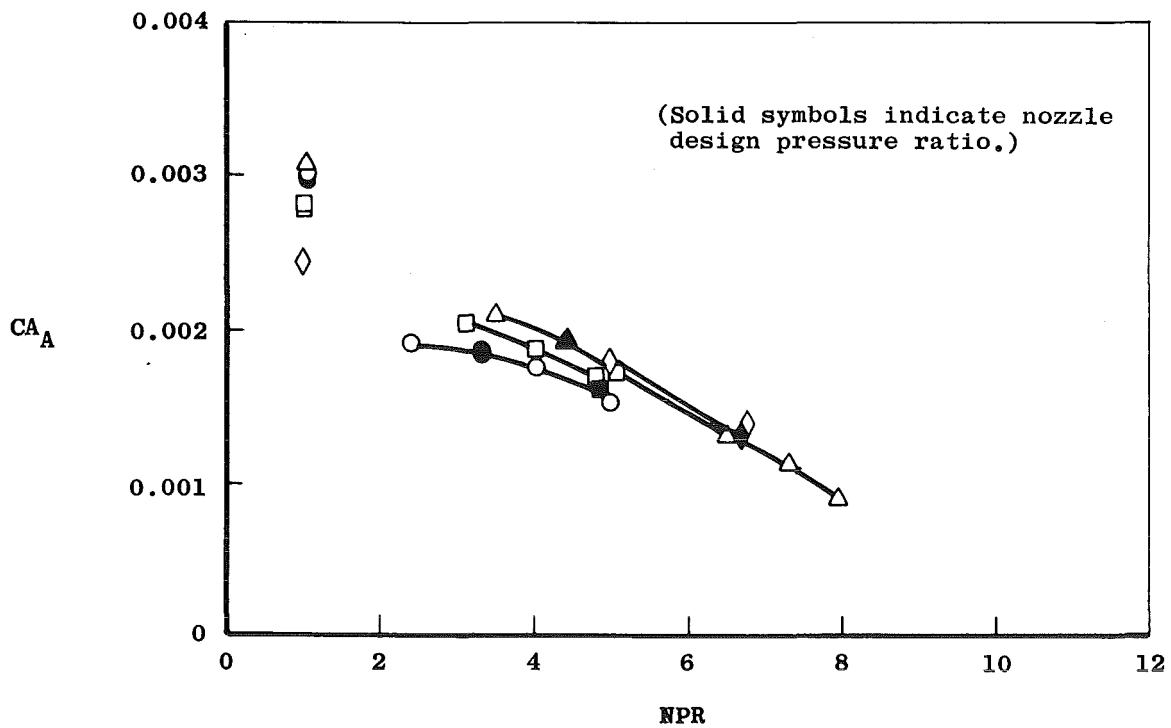


Figure 21. Concluded.

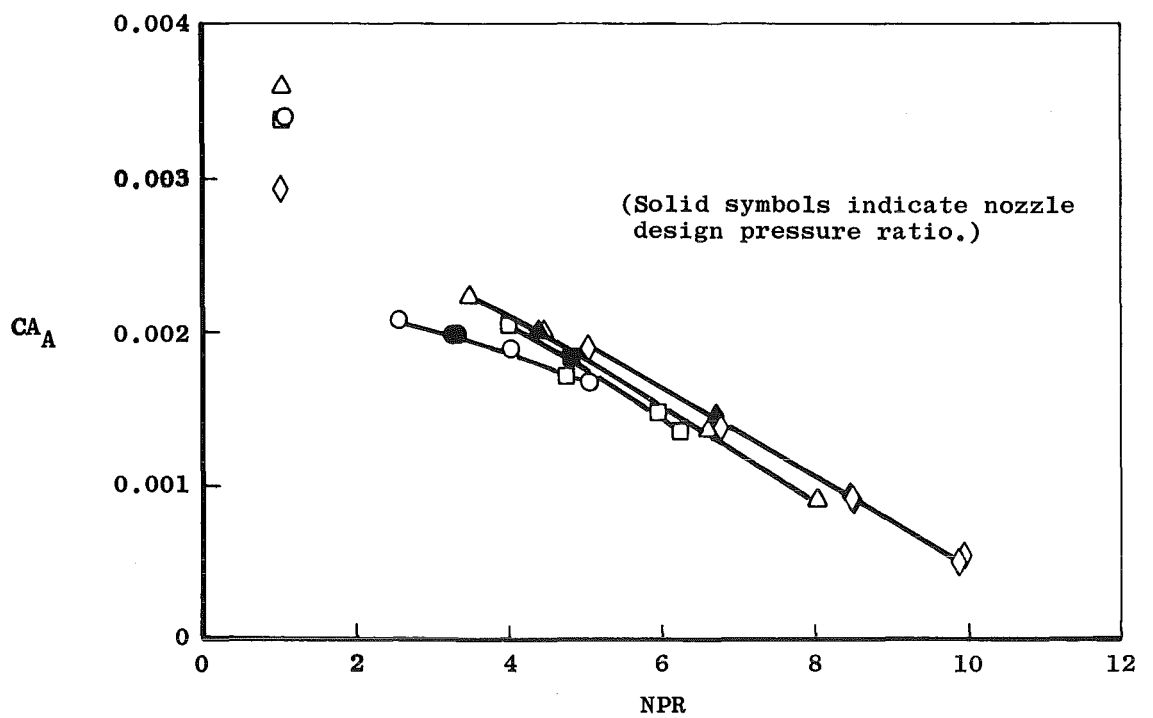
Sym	Nozzle	Config
○	Cruise 3.4	1
△	Part A/B 5.1	2
□	Max A/B 6.6	3
◇	Max A/B 7.75	4



a.  $M_\infty = 0.6$

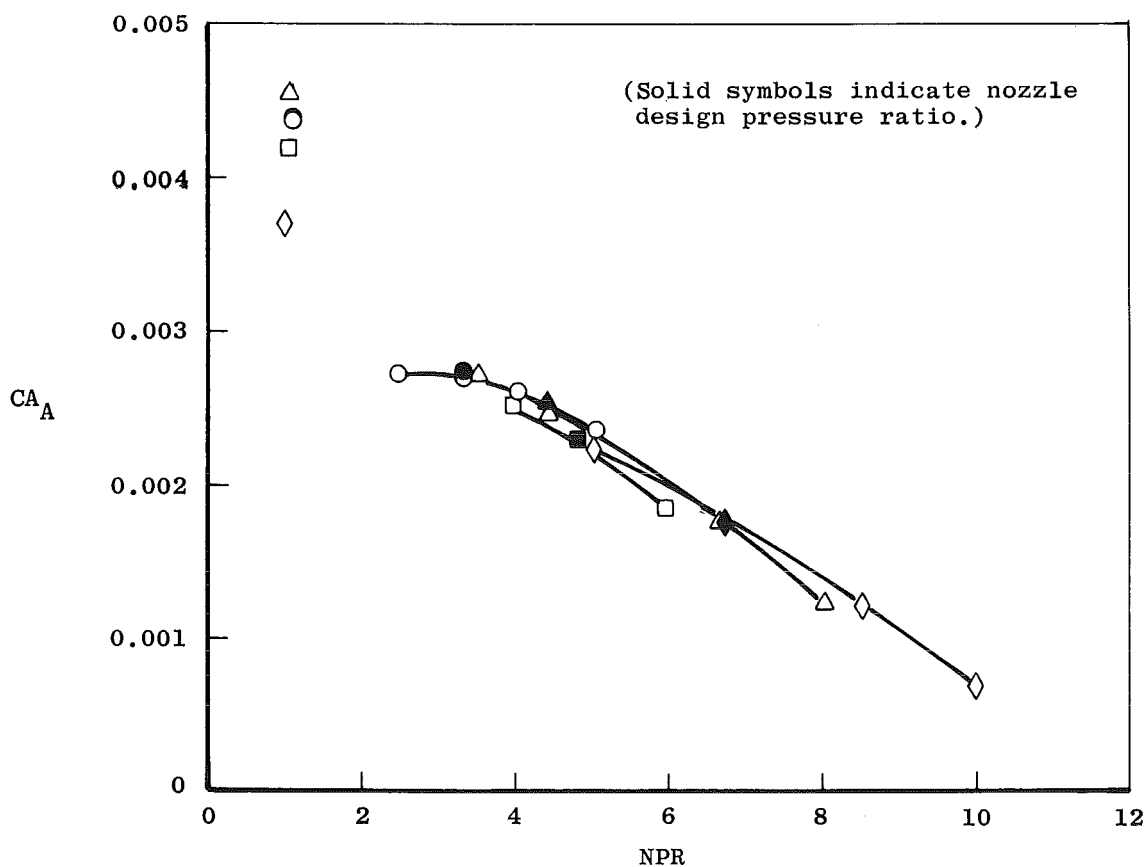
Figure 22. Variation of nozzle-afterbody axial-force coefficient with NPR for various nozzle configurations, strut support system,  $\alpha = 0$ .

Sym	Nozzle	Config
○	Cruise 3.4	1
△	Part A/B 5.1	2
□	Max A/B 6.6	3
◇	Max A/B 7.75	4



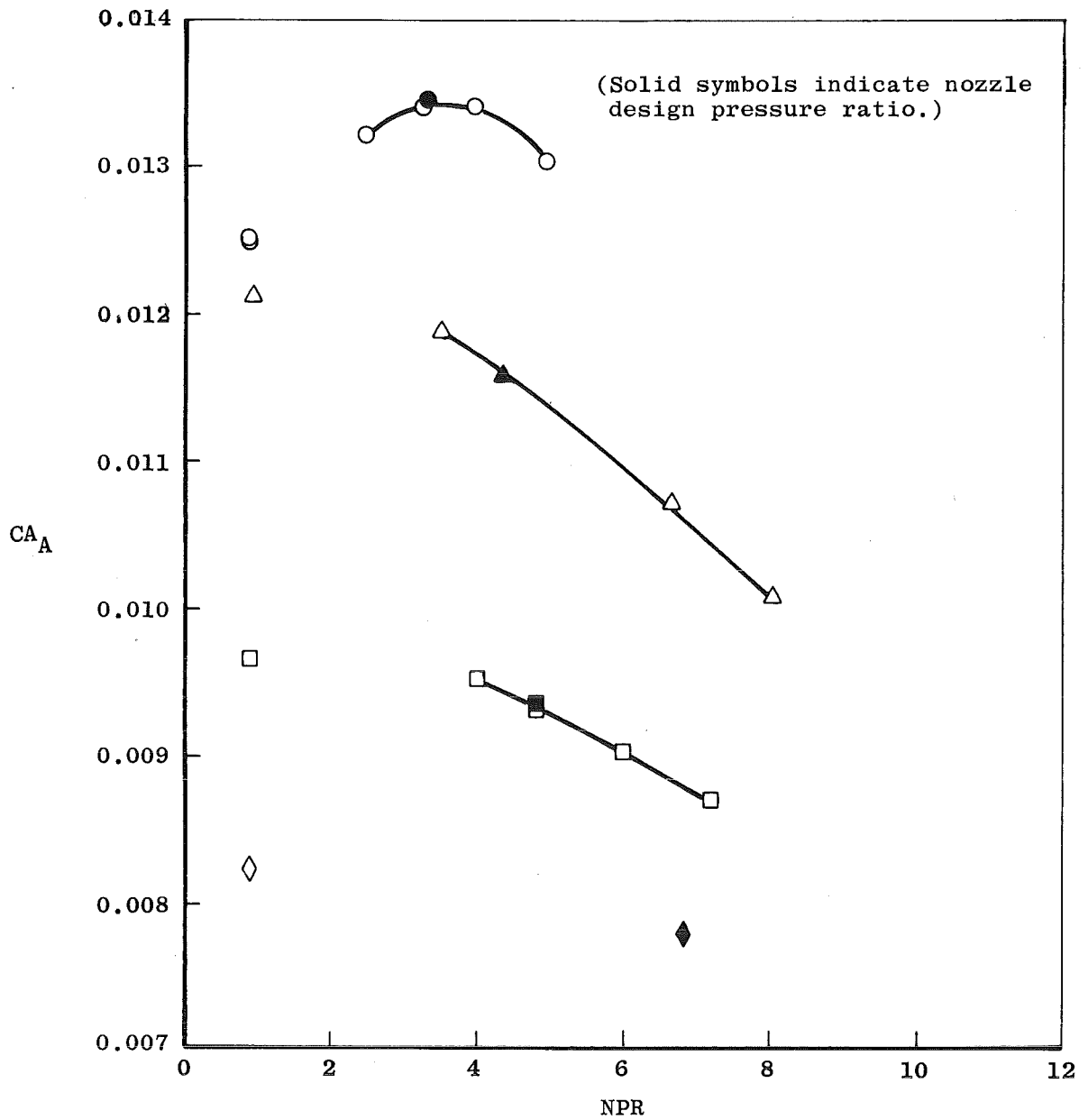
b.  $M_\infty = 0.8$   
Figure 22. Continued.

Sym	Nozzle	Config
○	Cruise 3.4	1
△	Part A/B 5.1	2
□	Max A/B 6.6	3
◇	Max A/B 7.75	4



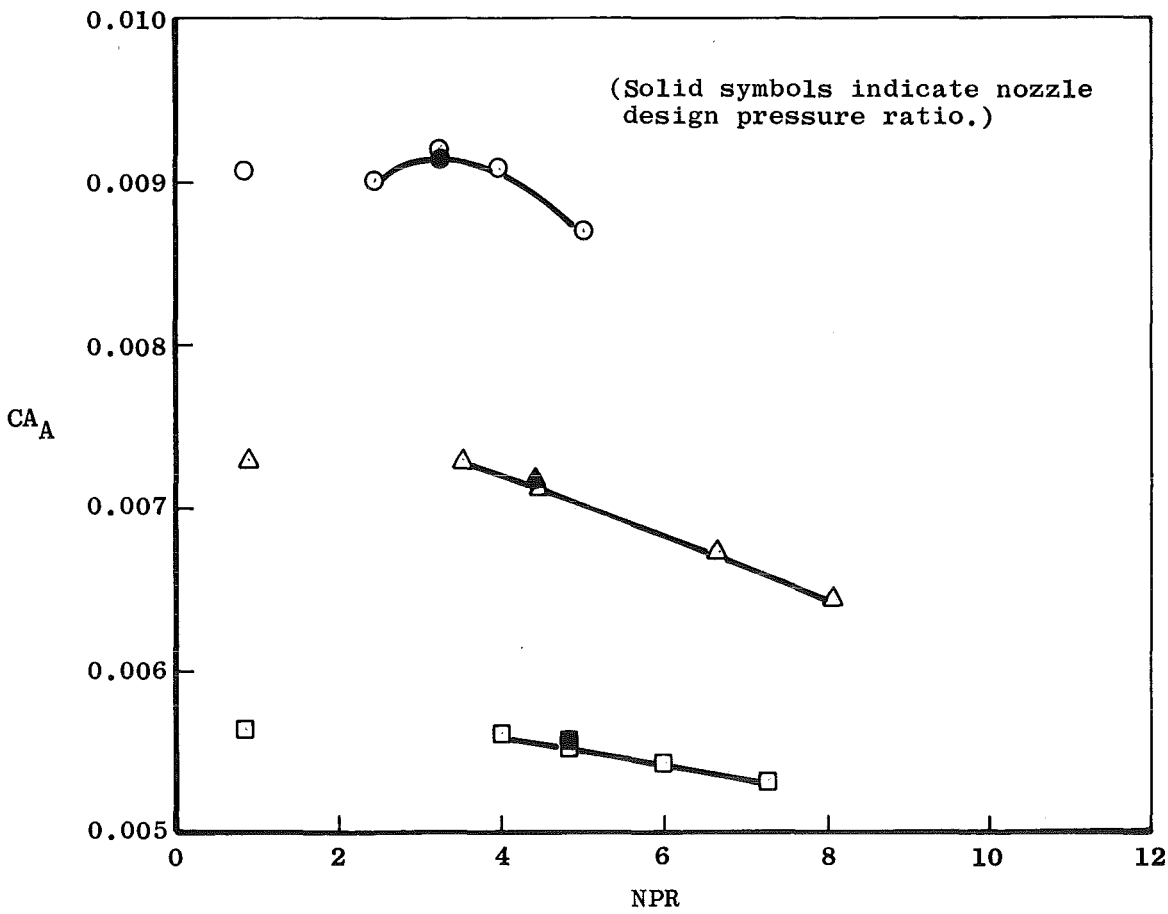
c.  $M_\infty = 0.9$   
Figure 22. Continued.

Sym	Nozzle	Config
○	Cruise 3.4	1
△	Part A/B 5.1	2
□	Max A/B 6.6	3
◇	Max A/B 7.75	4



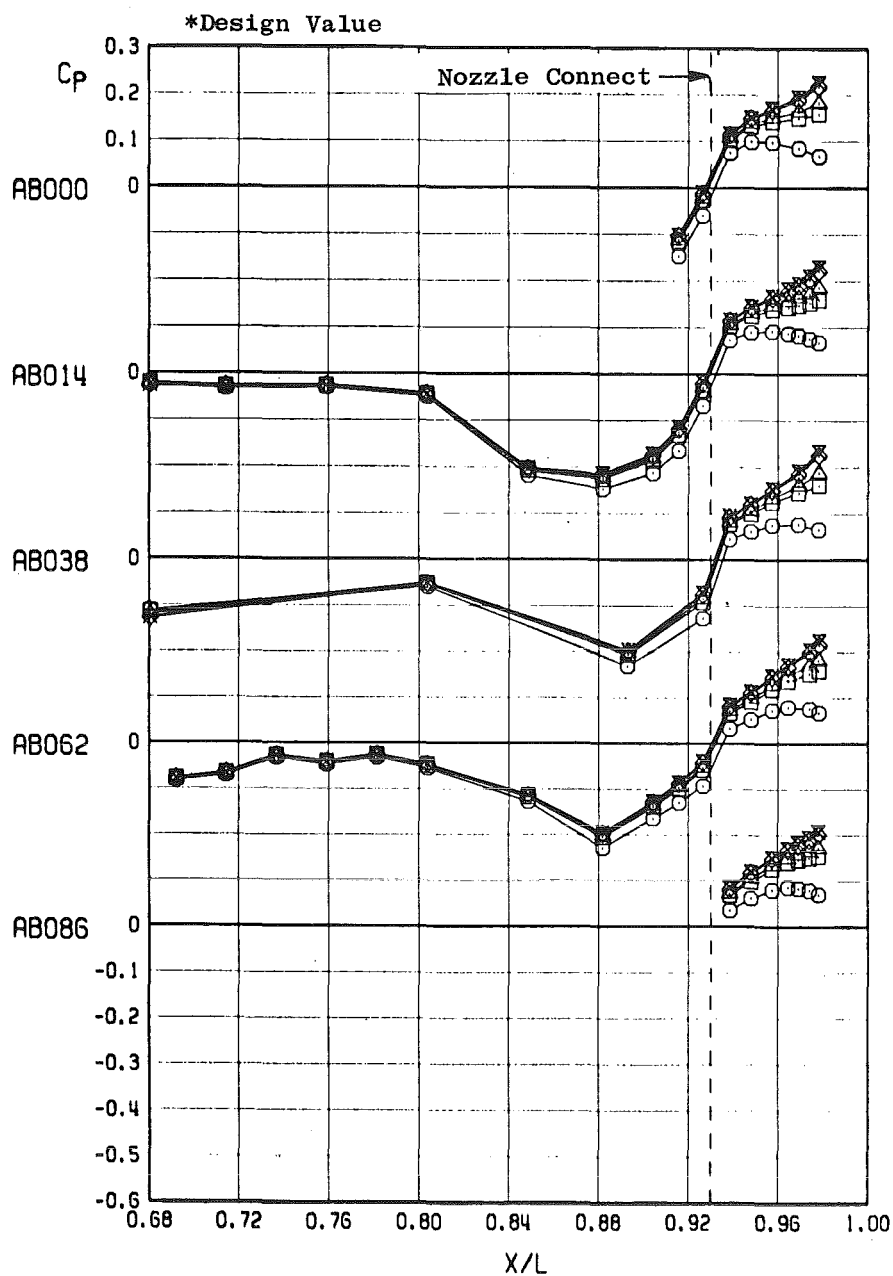
d.  $M_{\infty} = 1.2$   
Figure 22. Continued.

Sym	Nozzle	Config
○	Cruise 3.4	1
△	Part A/B 5.1	2
□	Max A/B 6.6	3
◇	Max A/B 7.75	4



e.  $M_\infty = 1.5$   
Figure 22. Concluded.

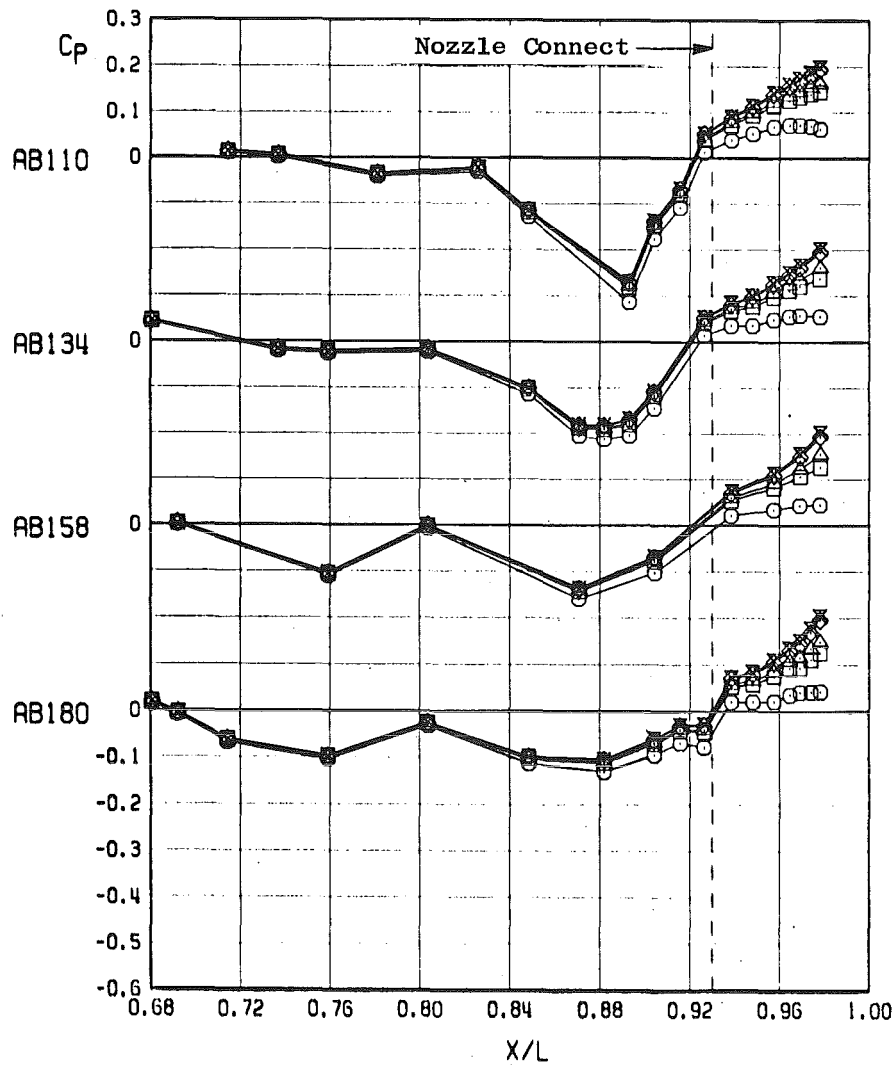
Sym	NPR	NPREFF	CA <sub>A</sub>
□	4.00	4.00	0.00203
△	4.80*	4.80	0.00183
◇	5.96	5.96	0.00146
×	6.24	6.24	0.00134
○	1.03	1.03	0.00336



a.  $M_\infty = 0.8$

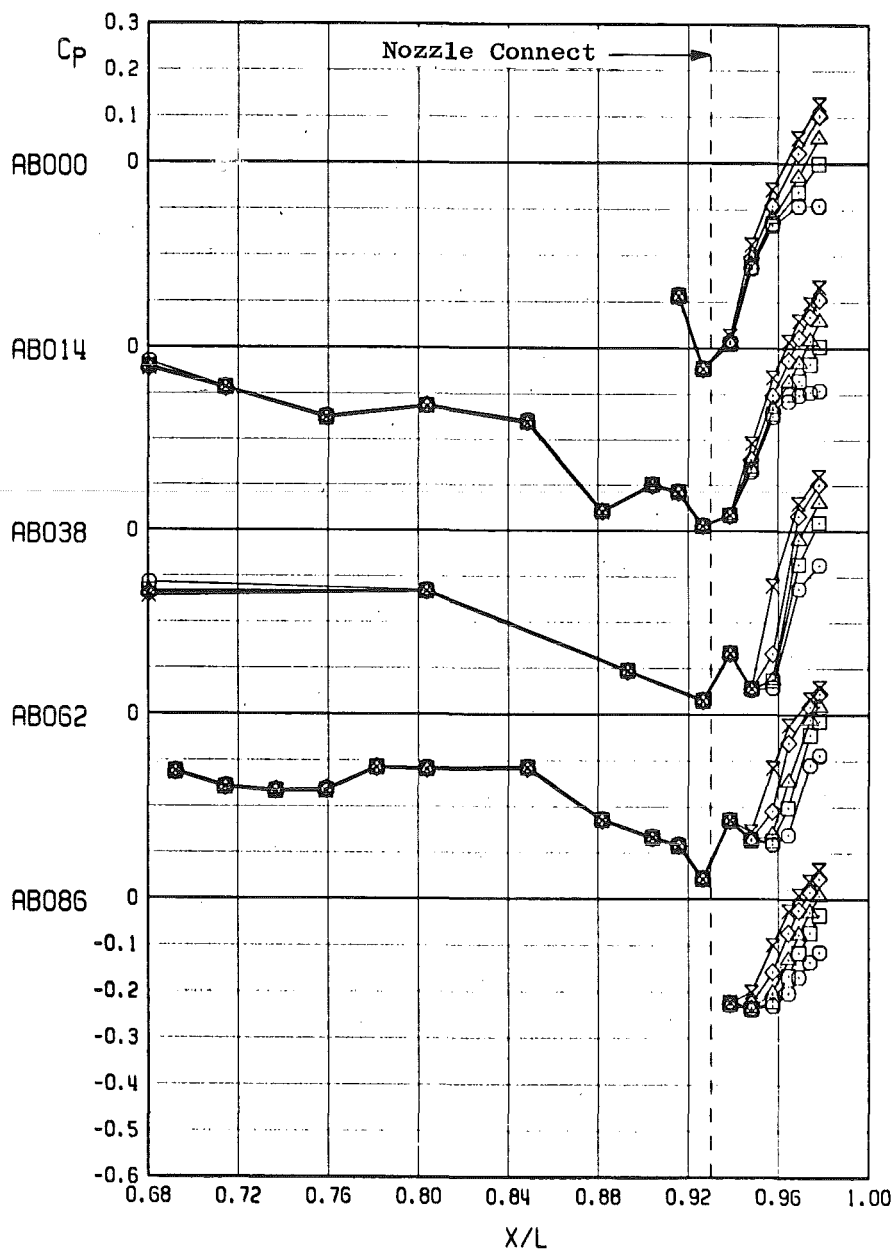
Figure 23. Effect of nozzle pressure ratio on the nozzle-afterbody pressure distributions, max A/B 6.6 nozzle, strut support system,  $\alpha = 0$ ,  $RE \approx 3.4 \times 10^6$ .

Sym	NPR	NPREF	$CA_A$	RN.PN
□	4.00	4.00	0.00203	1643.03
△	4.80	4.80	0.00183	1643.05
◇	5.96	5.96	0.00146	1643.10
×	6.24	6.24	0.00134	1643.11
○	1.03	1.03	0.00336	1644.06



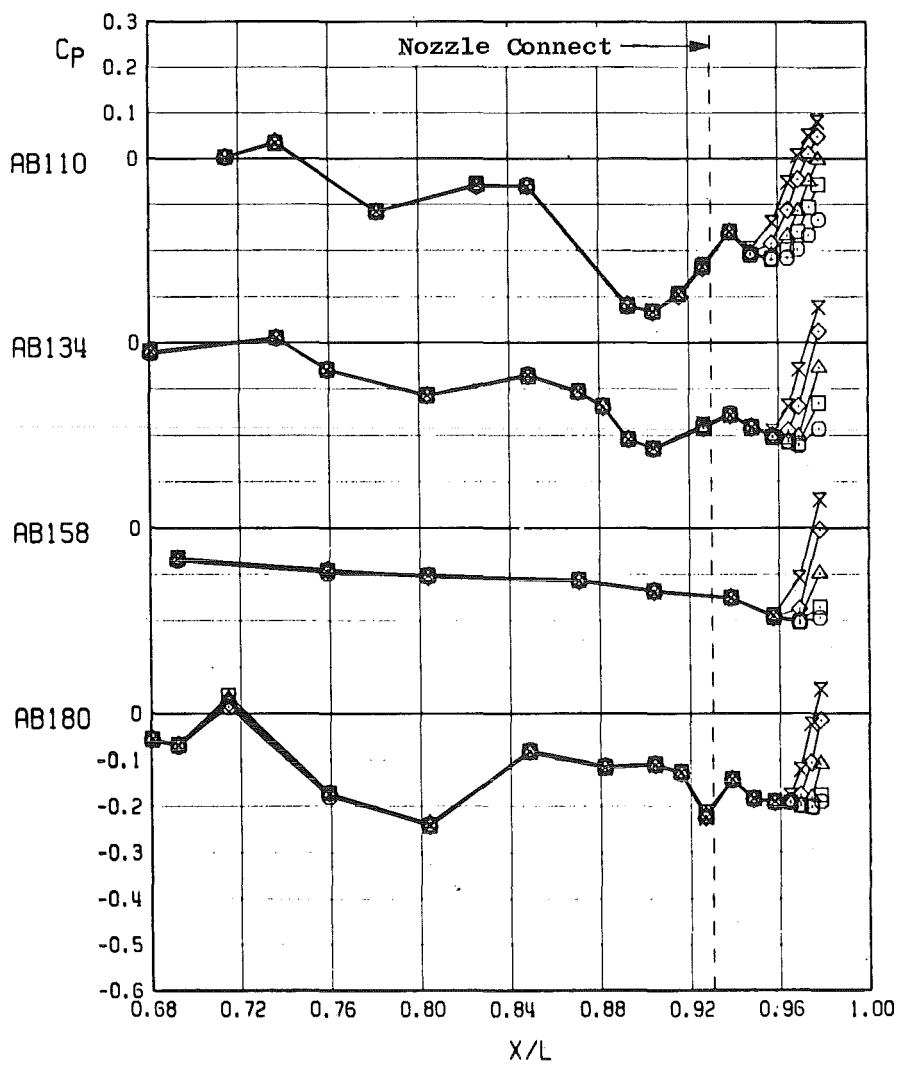
a. Concluded  
Figure 23. Continued.

Sym	NPR	NPREFF	DELHR	$CA_A$	RN, PN
○	0.90	0.90	-0.03	0.00965	1667.03
□	3.99	3.99	-0.03	0.00950	1669.04
△	4.81	4.81	-0.03	0.00934	1669.06
◇	5.98	5.98	-0.03	0.00903	1669.08
×	7.21	7.21	-0.03	0.00869	1669.12

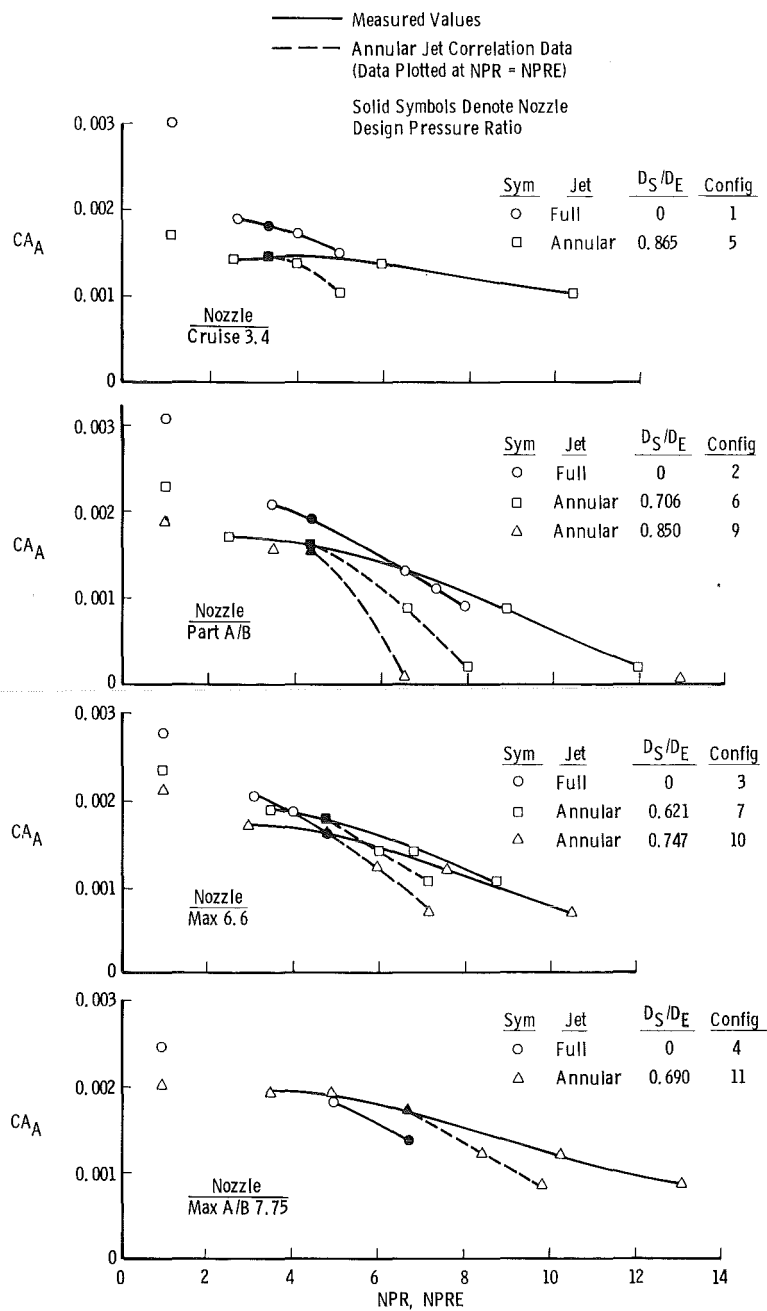


b.  $M_\infty = 1.2$   
Figure 23. Continued.

Sym	NPR	NPREF	DELHR	CA <sub>A</sub>	RN.PN
○	0.90	0.90	-0.03	0.00965	1667.03
□	3.99	3.99	-0.03	0.00950	1669.04
△	4.81	4.81	-0.03	0.00934	1669.06
◇	5.98	5.98	-0.03	0.00903	1669.08
×	7.21	7.21	-0.03	0.00869	1669.12

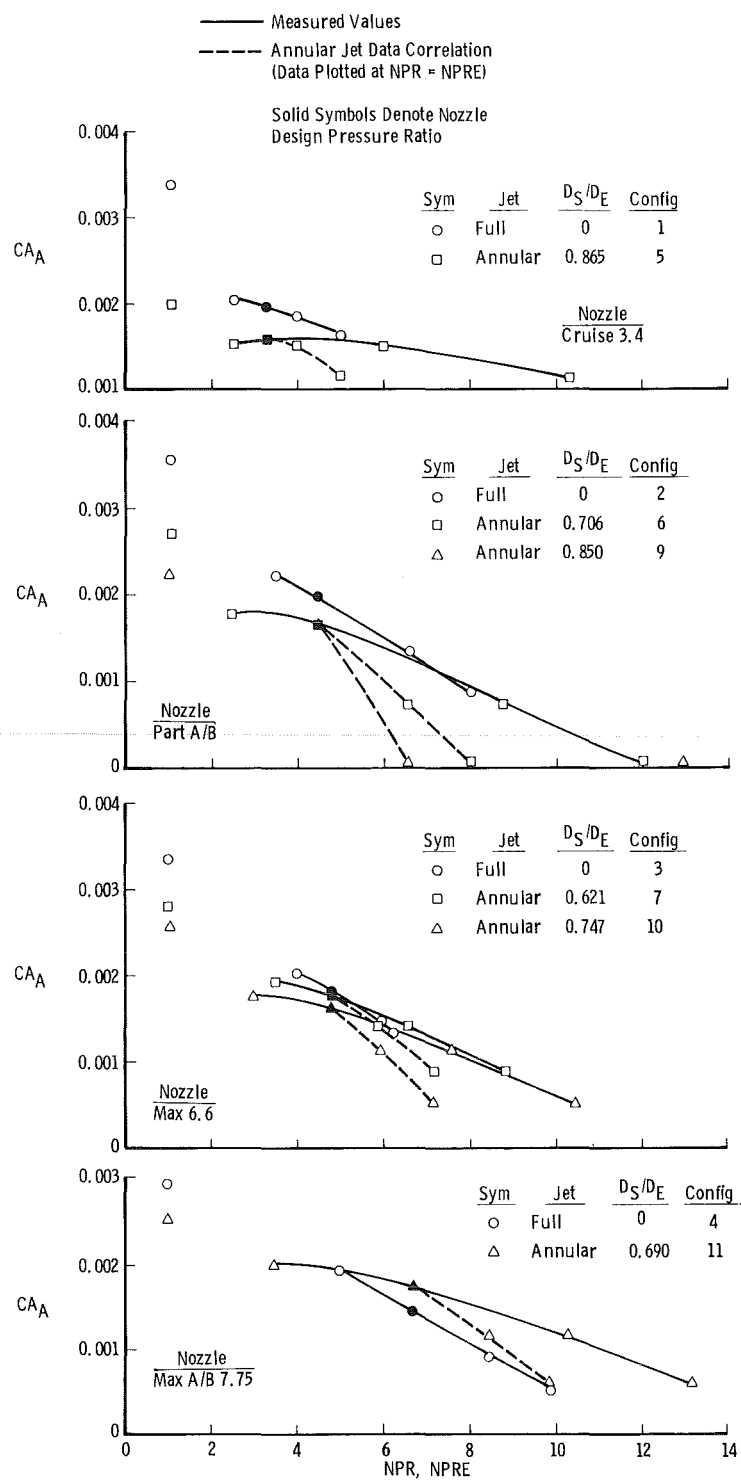


b. Concluded  
Figure 23. Concluded.



a.  $M_\infty = 0.6$

Figure 24. Comparison of afterbody axial-force data from full and annular jet configurations, strut support system,  $\alpha = 0$ .



b.  $M_\infty = 0.8$   
Figure 24. Continued.

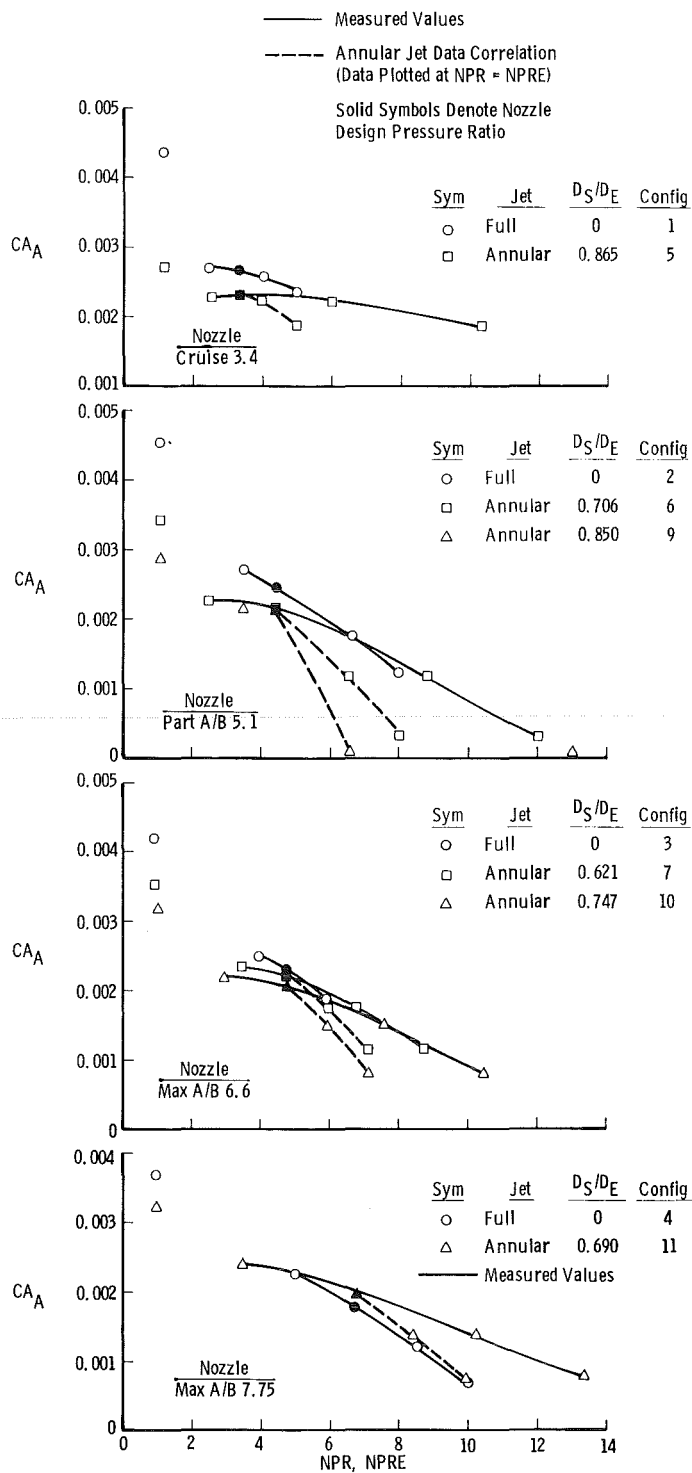
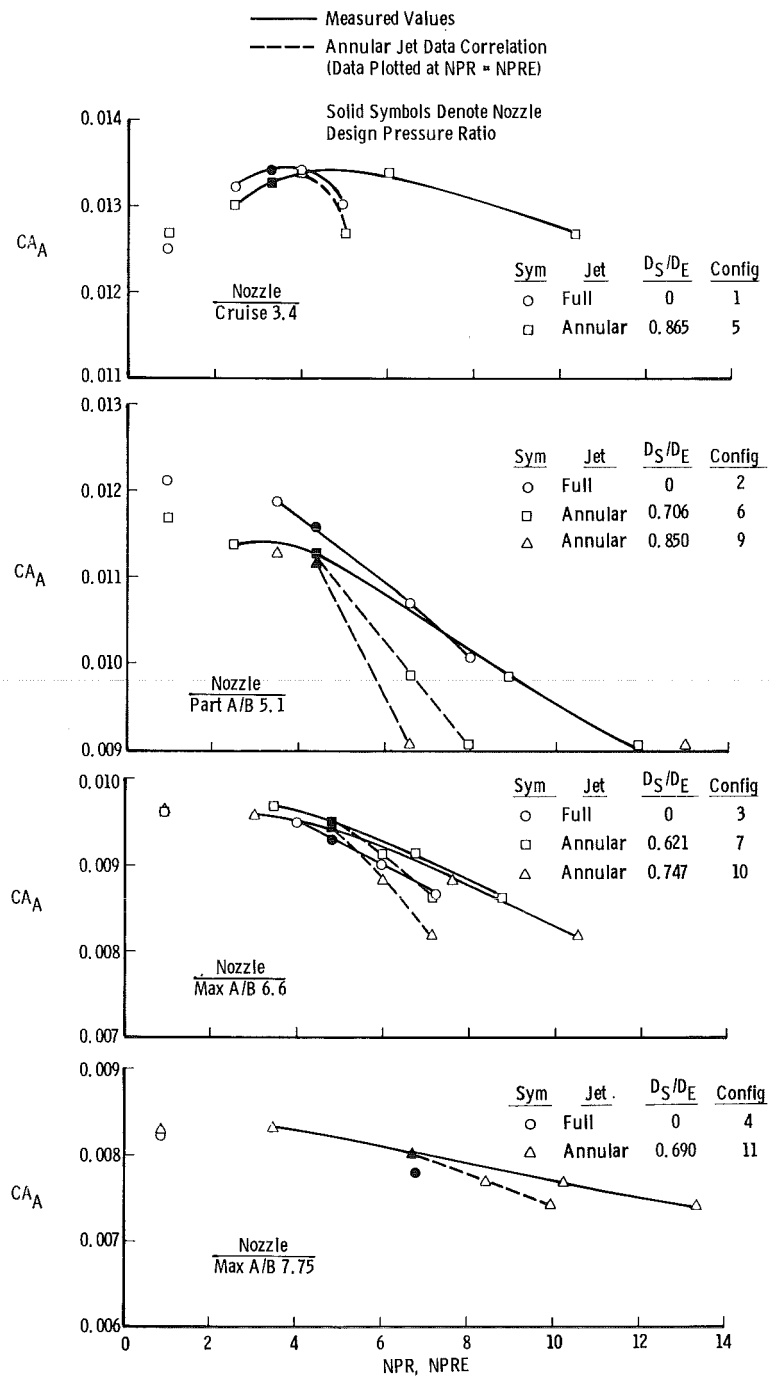
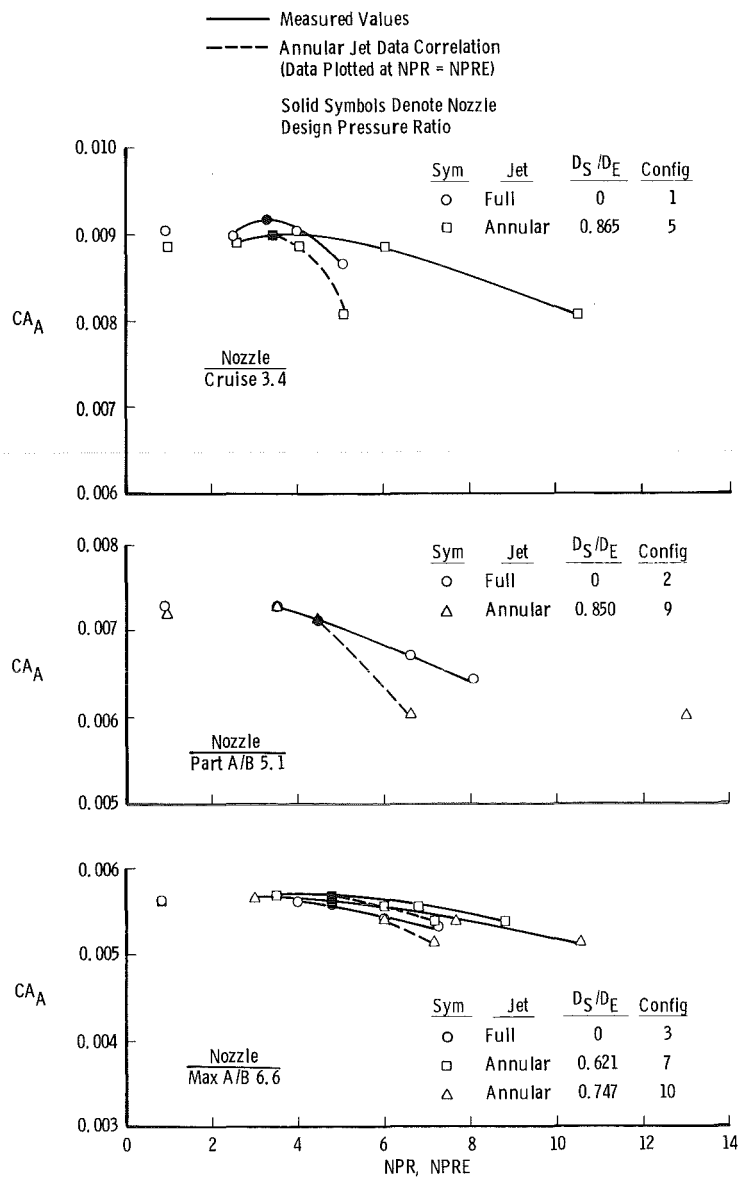
c.  $M_\infty = 0.9$ 

Figure 24 Continued.



d.  $M_\infty = 1.2$   
Figure 24. Continued.



e.  $M_\infty = 1.5$   
Figure 24. Concluded.

Sym	Nozzle	$D_S$	$D_S/D_E$	Config
○	Cruise 3.4	5.4	0.865	(5) - (1)
△	Part A/B 5.1	5.4	0.706	(6) - (2)
▲	Part A/B 5.1	6.5	0.850	(9) - (2)
□	Max A/B 6.6	5.4	0.621	(7) - (3)
■	Max A/B 6.6	6.5	0.747	(10) - (3)
◇	Max A/B 7.75	6.5	0.690	(11) - (4)

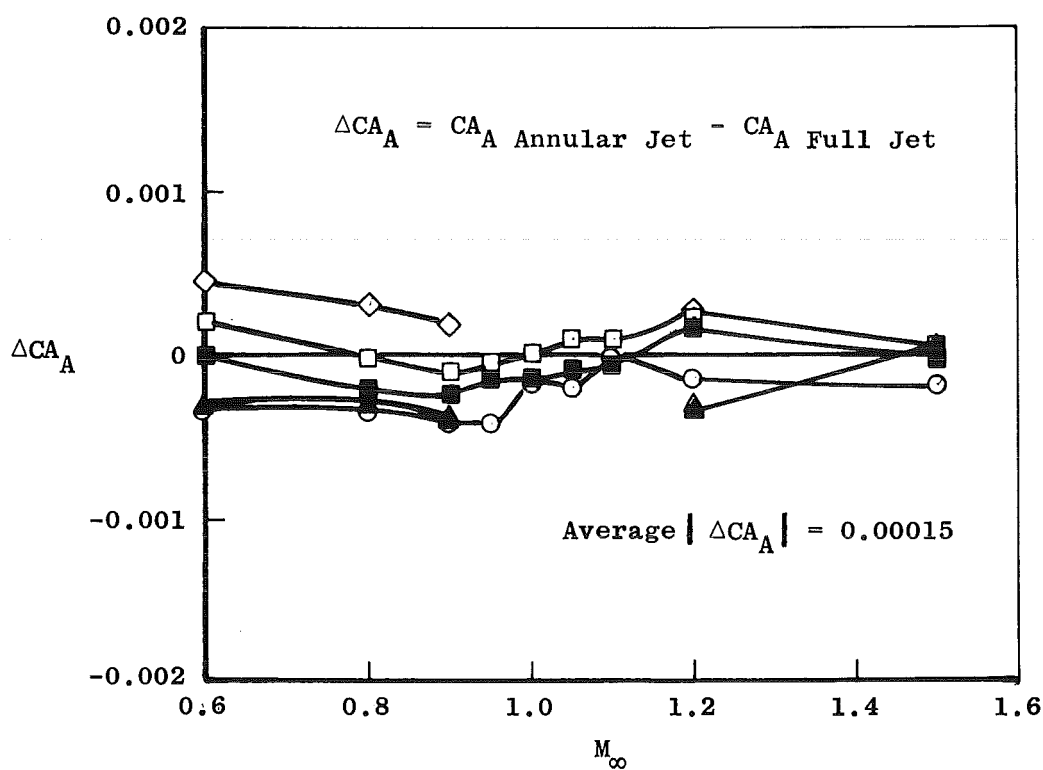


Figure 25. Summary of annular jet axial-force comparison at design NPR, strut support system,  $\alpha = 0$ .

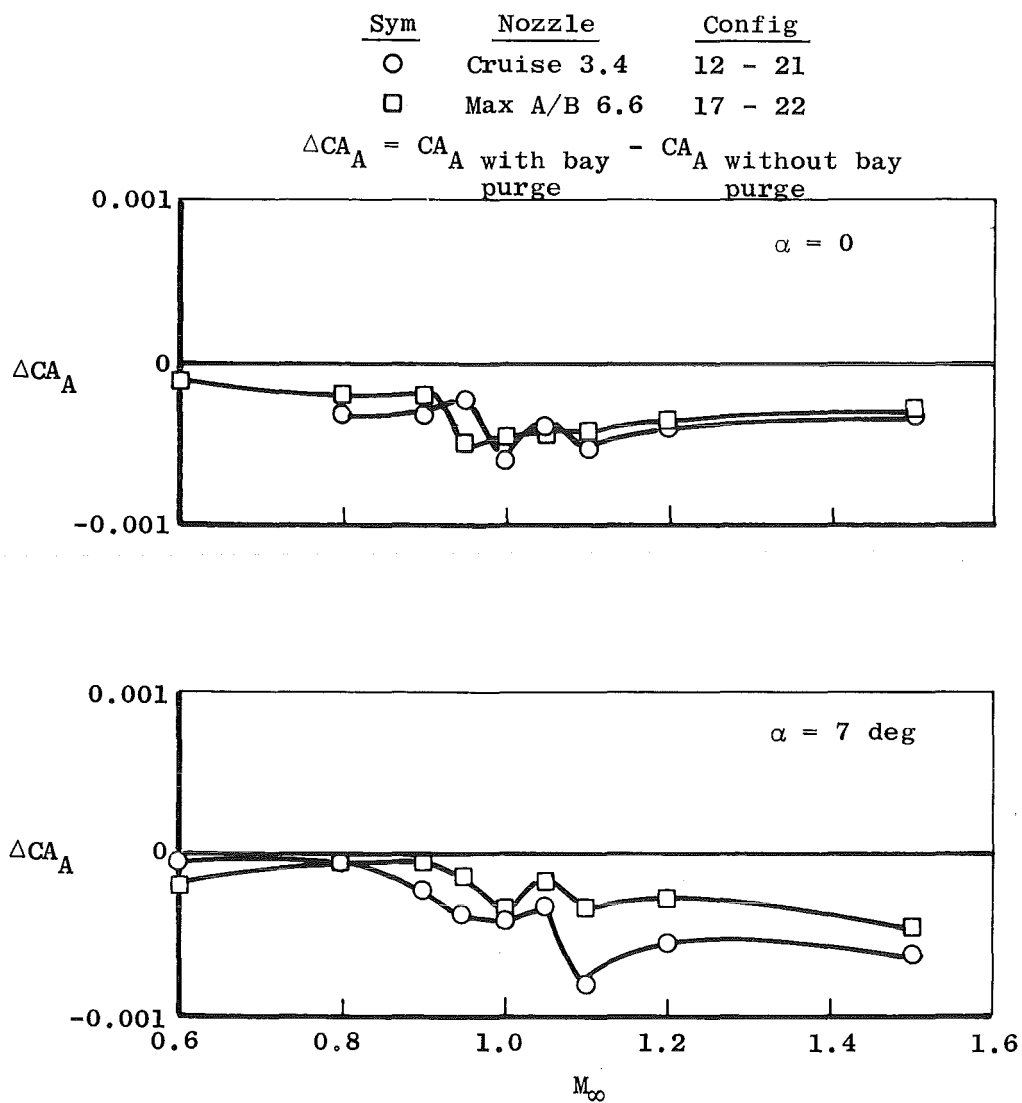


Figure 26. Effect of bay purge system flow on the nozzle-afterbody axial-force coefficient, sting support system, design NPR.

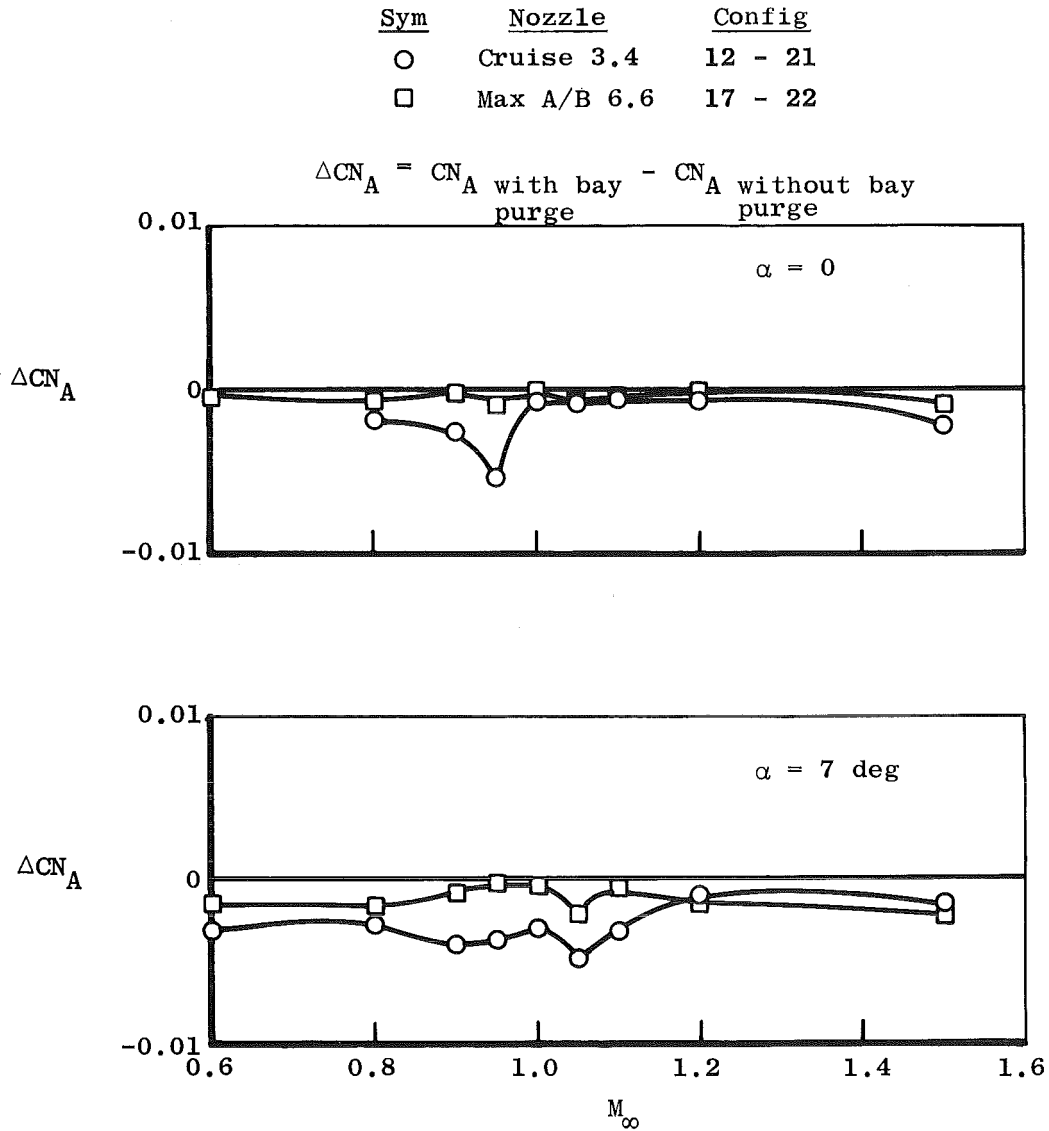
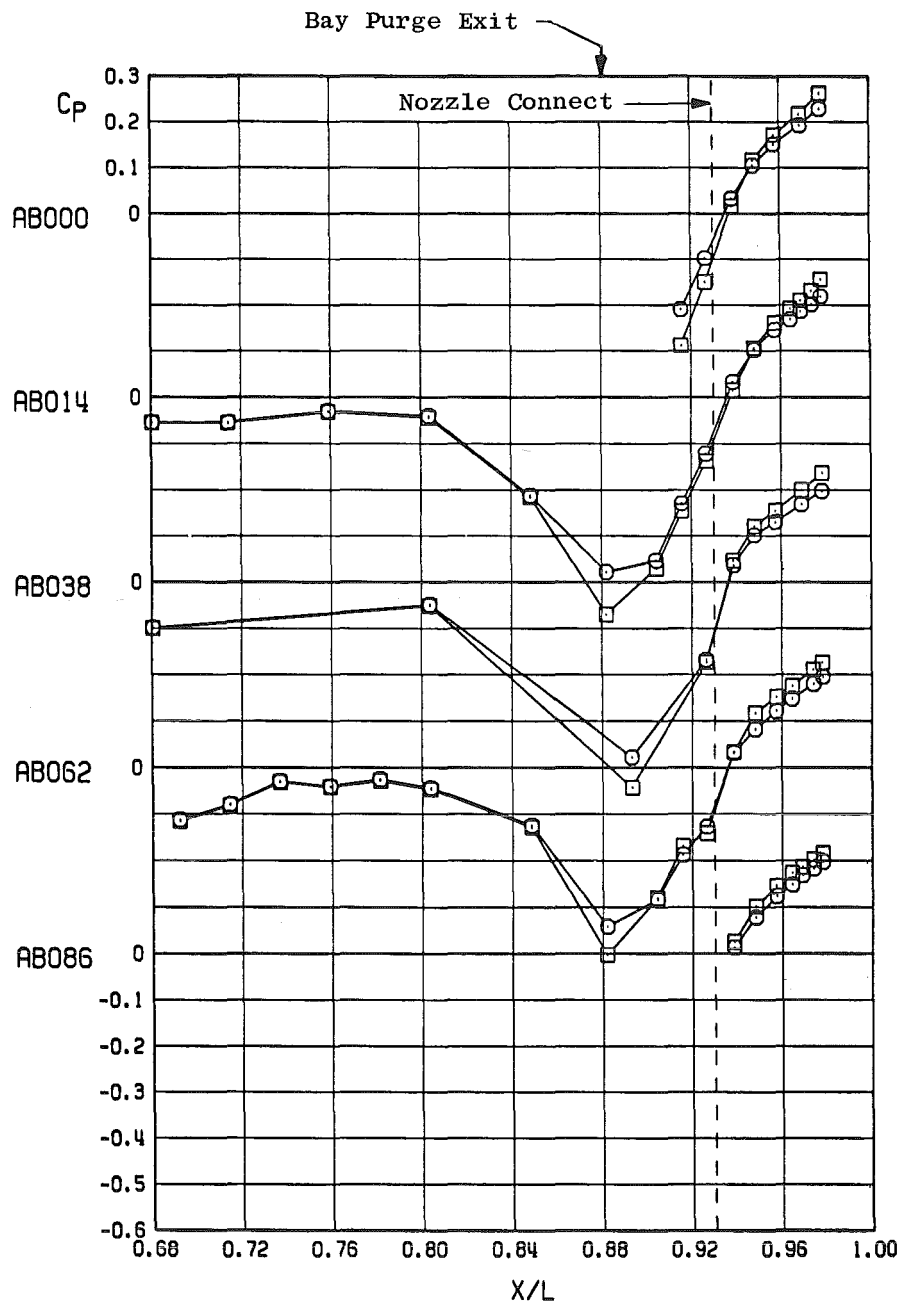


Figure 27. Effect of bay purge system flow on the nozzle-afterbody normal-force coefficient, sting support system, design NPR.

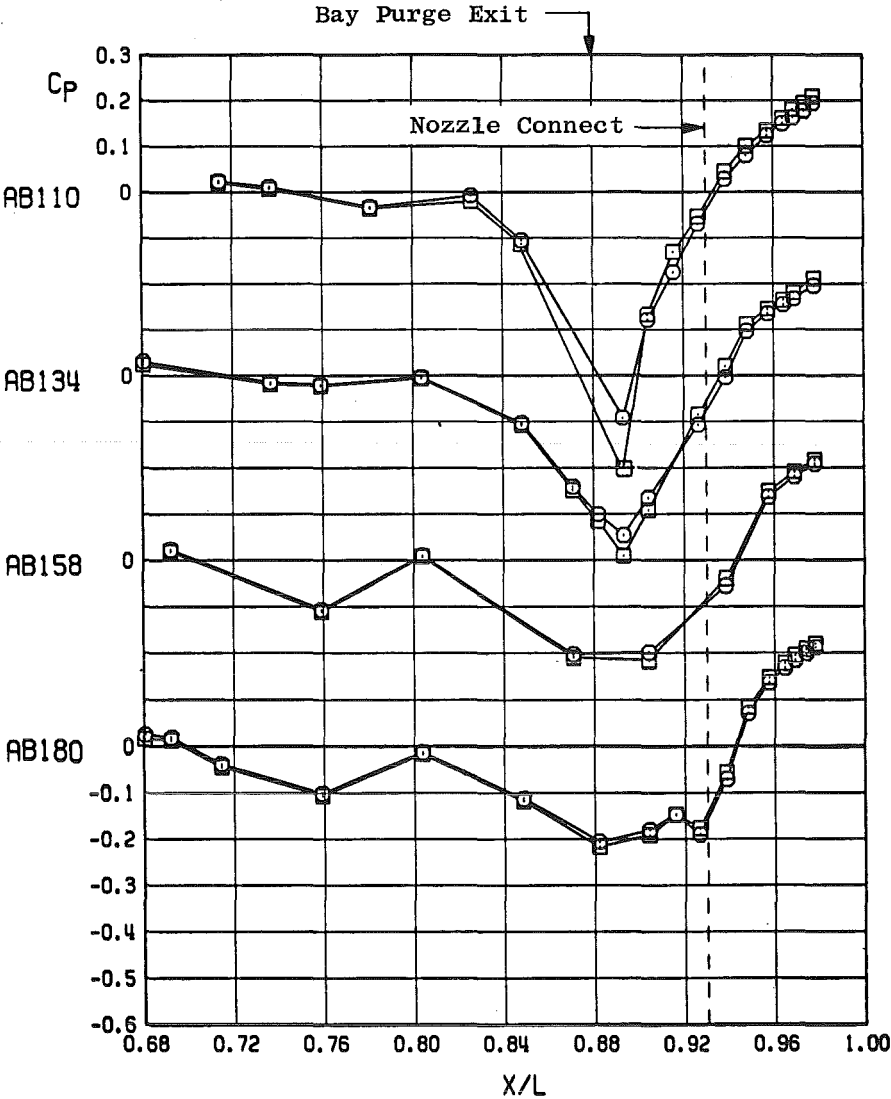
Sym	Conf	$CA_A$	Bay Purge	RN.PN
○	12	0.00309	On	1885.07
□	21	0.00341	Off	1998.03



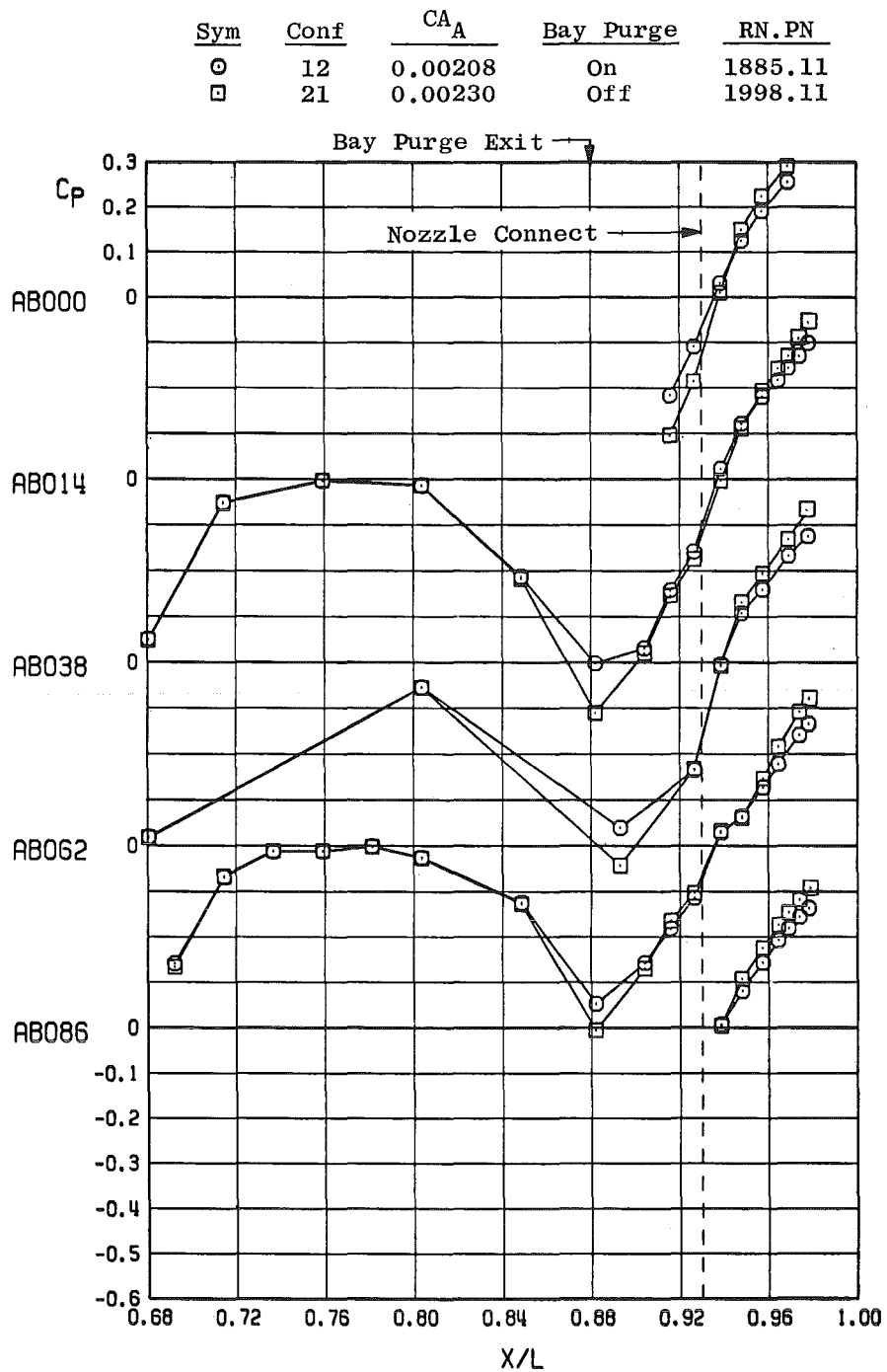
a.  $\alpha = 0$

Figure 28. Effect of bay purge system flow on the nozzle-afterbody pressure distributions, sting support system, cruise 3.4 nozzle, design NPR,  $M_\infty = 0.9$ ,  $RE \approx 3.4 \times 10^6$ .

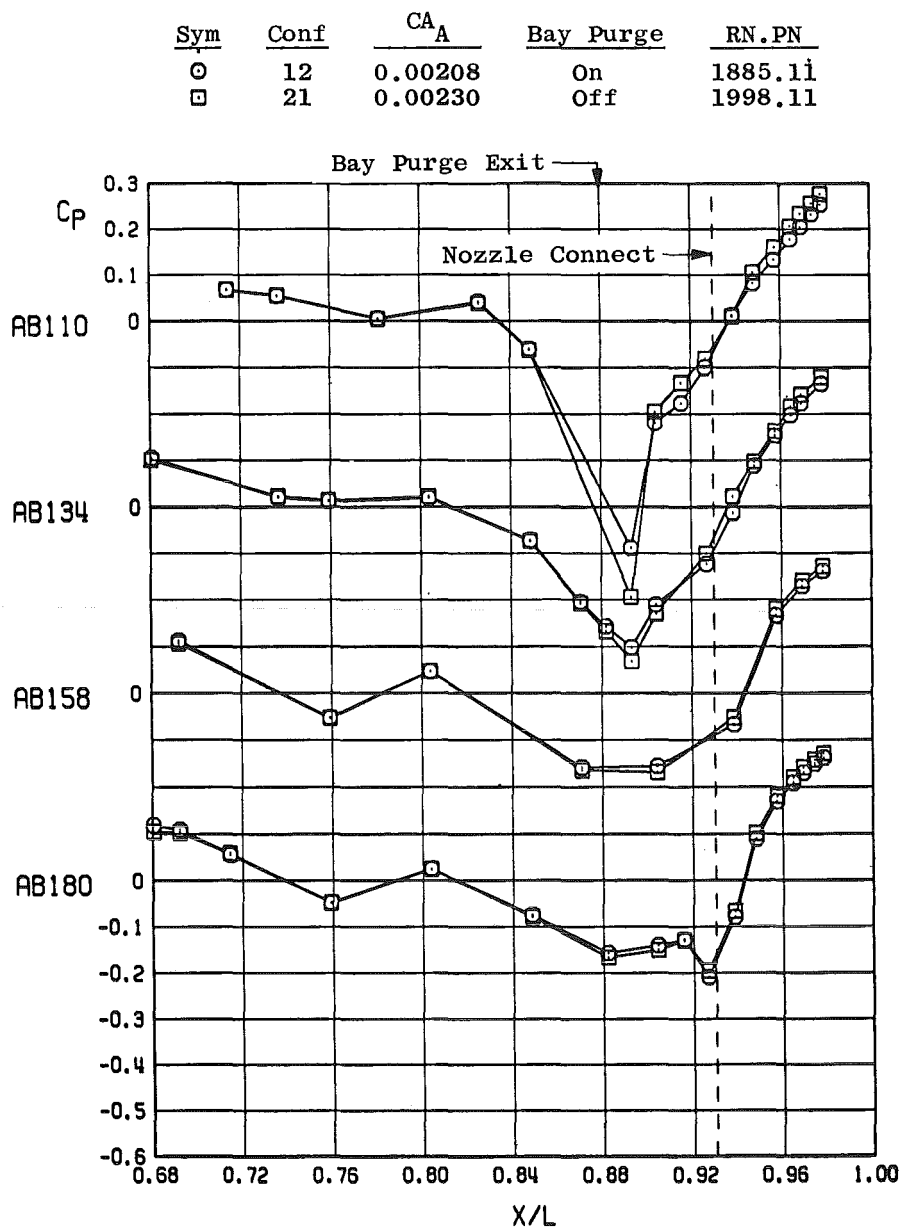
Sym	Conf	CA <sub>A</sub>	Bay Purge	RN.PN
⊙	12	0.00309	On	1885.07
⊠	21	0.00341	Off	1998.03



a. Concluded  
Figure 28. Continued.

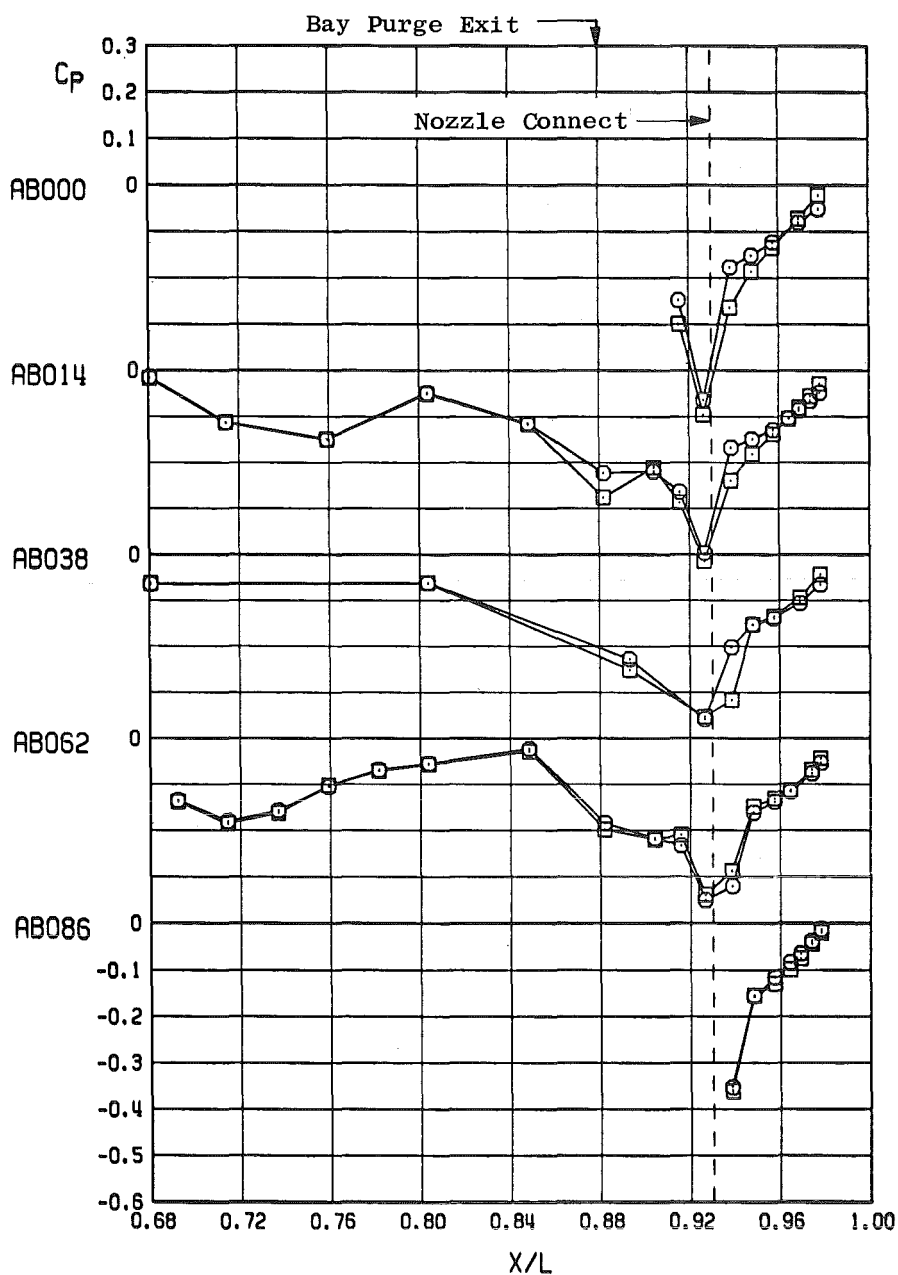


b.  $\alpha = 7$  deg  
Figure 28. Continued.



b. Concluded  
Figure 28. Concluded.

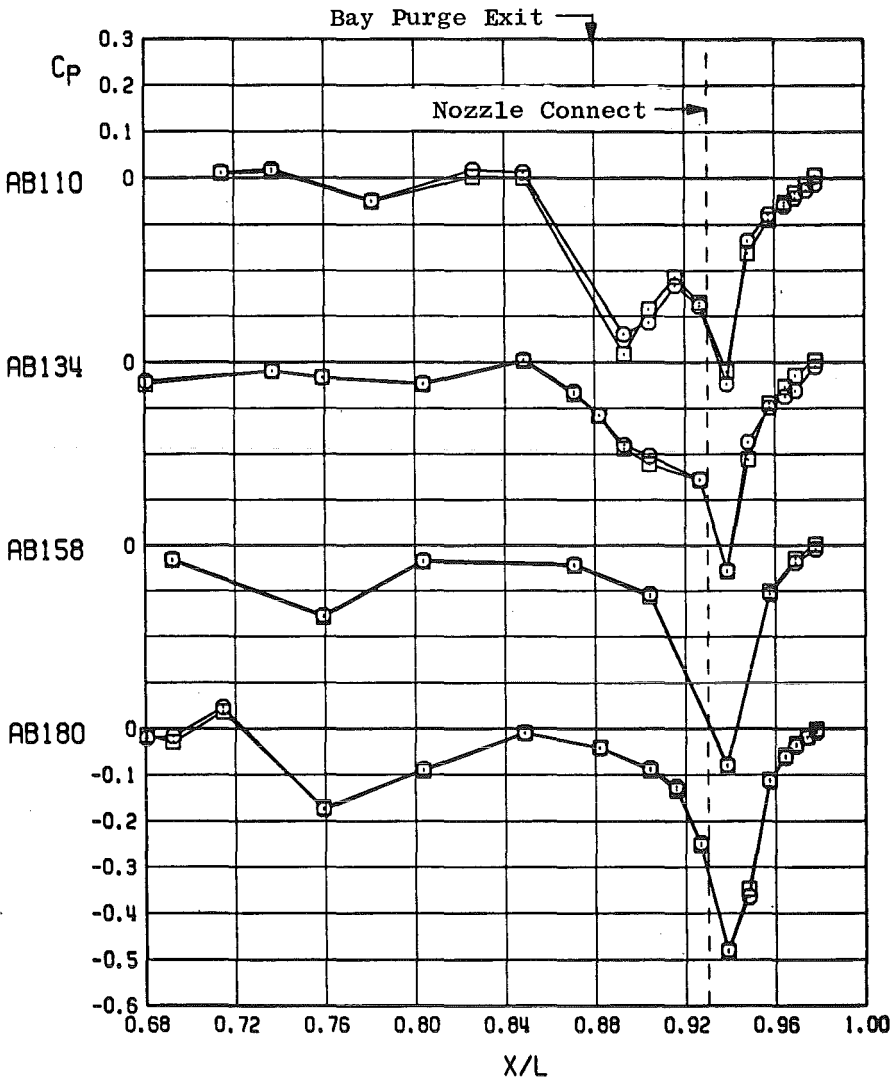
Sym	Conf	$CA_A$	Bay Purge	RN.PN
○	12	0.00958	On	1903.01
□	21	0.01011	Off	2013.03



a.  $\alpha = 0$

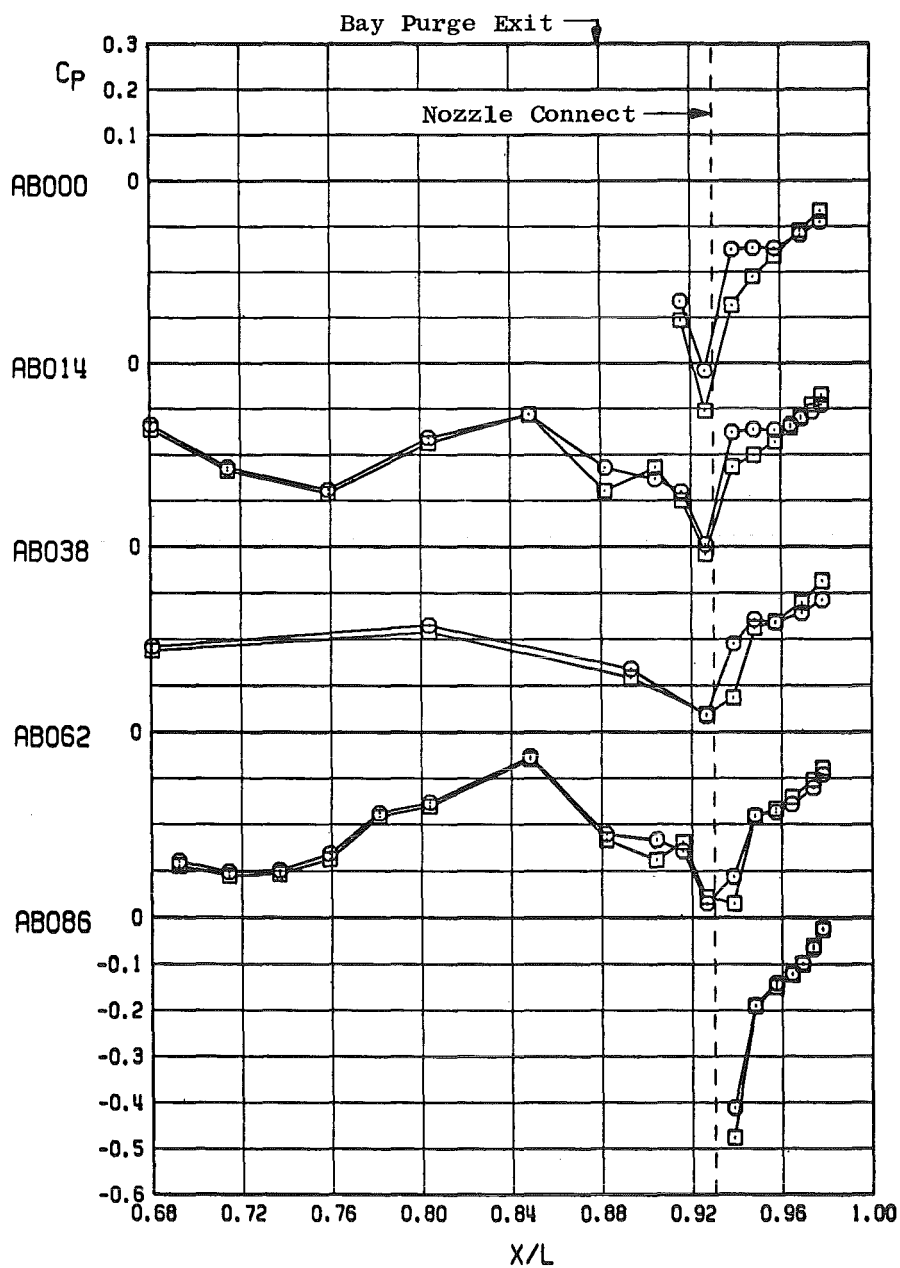
Figure 29. Effects of bay purge system flow on the nozzle-afterbody pressure distributions, sting support system, cruise 3.4 nozzle, design NPR,  $M_\infty = 1.1$ ,  $RE \approx 3.4 \times 10^6$ .

Sym	Conf	CA <sub>A</sub>	Bay Purge	RN.PN
○	12	0.00958	On	1903.01
□	21	0.01011	Off	2013.03



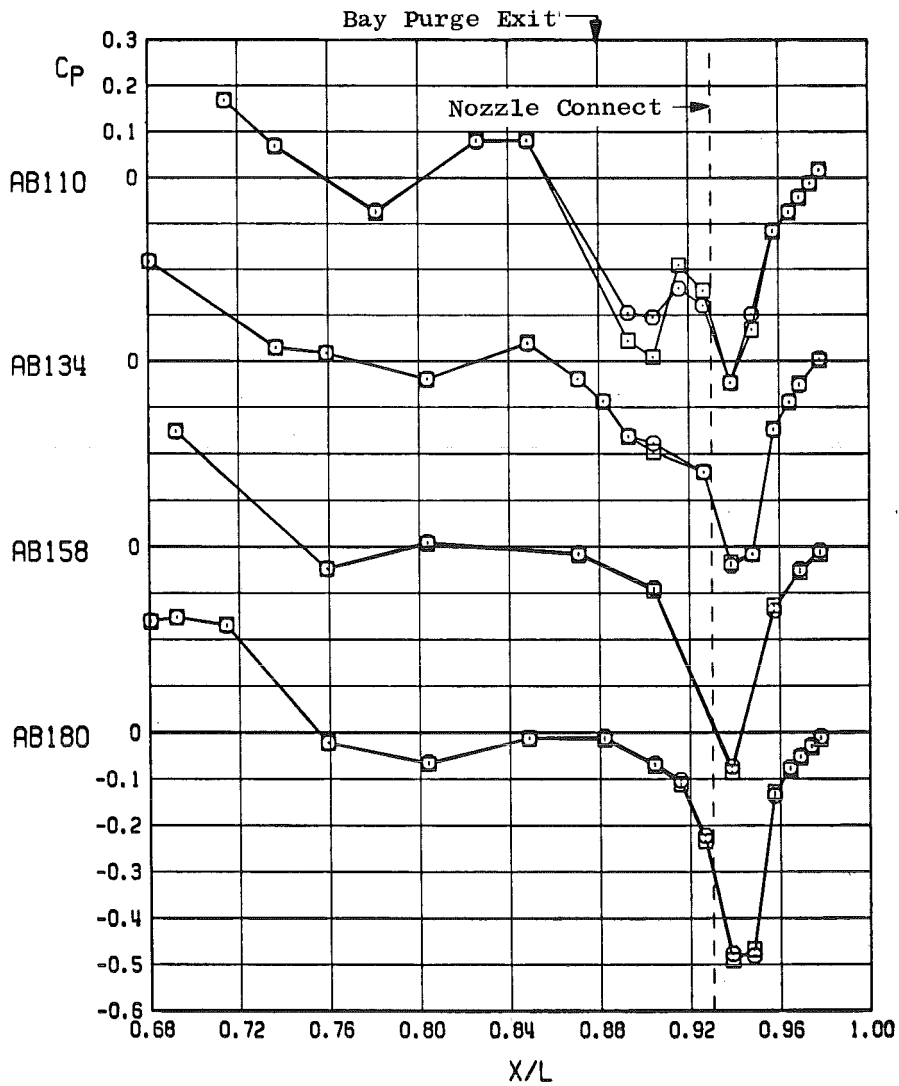
a. Concluded  
Figure 29. Continued.

Sym	Conf	$CA_A$	Bay Purge	RN.PN
○	12	0.00992	On	1903.02
□	21	0.01073	Off	2013.06



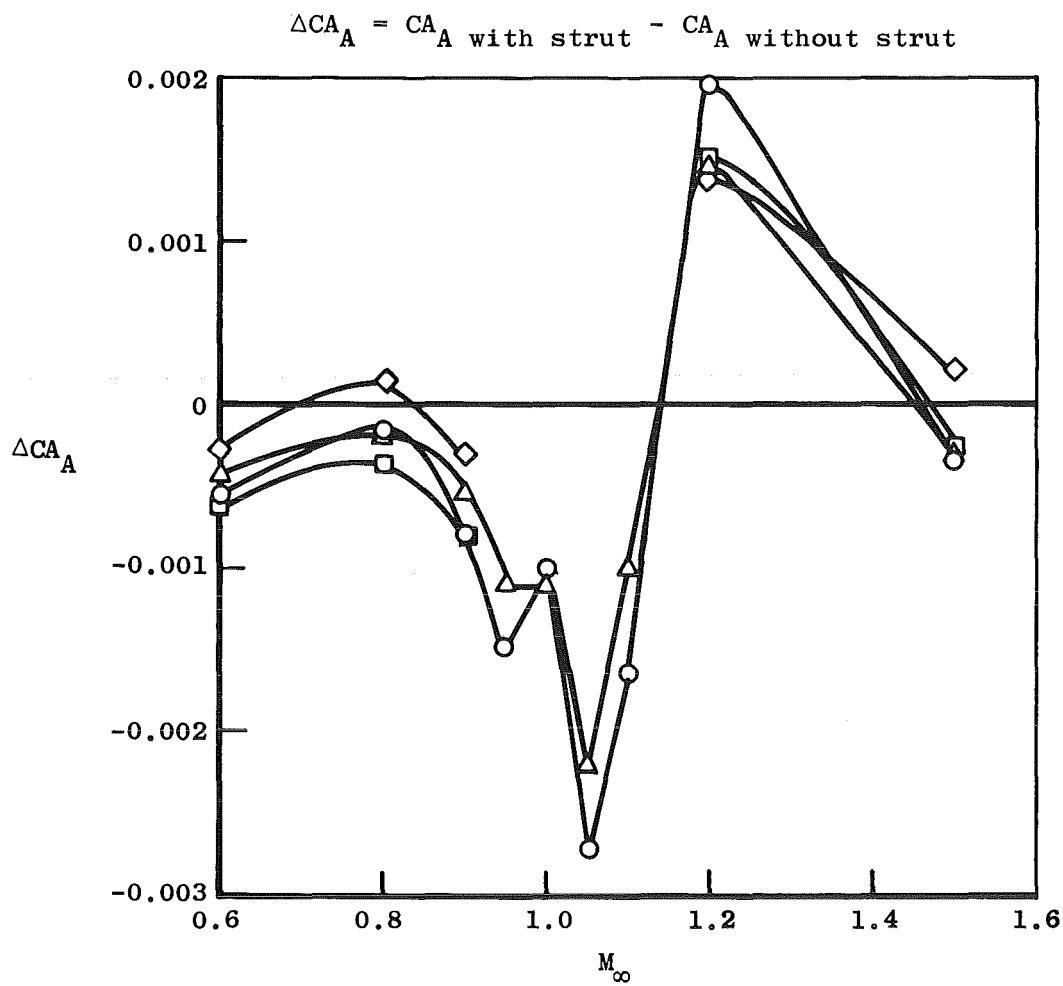
$b_n \alpha = 7 \text{ deg}$   
Figure 29. Continued.

Sym	Conf	$CA_A$	Bay Purge	RN.PN
○	12	0.00992	On	1903.02
□	21	0.01073	Off	2013.06



b. Concluded  
Figure 29. Concluded.

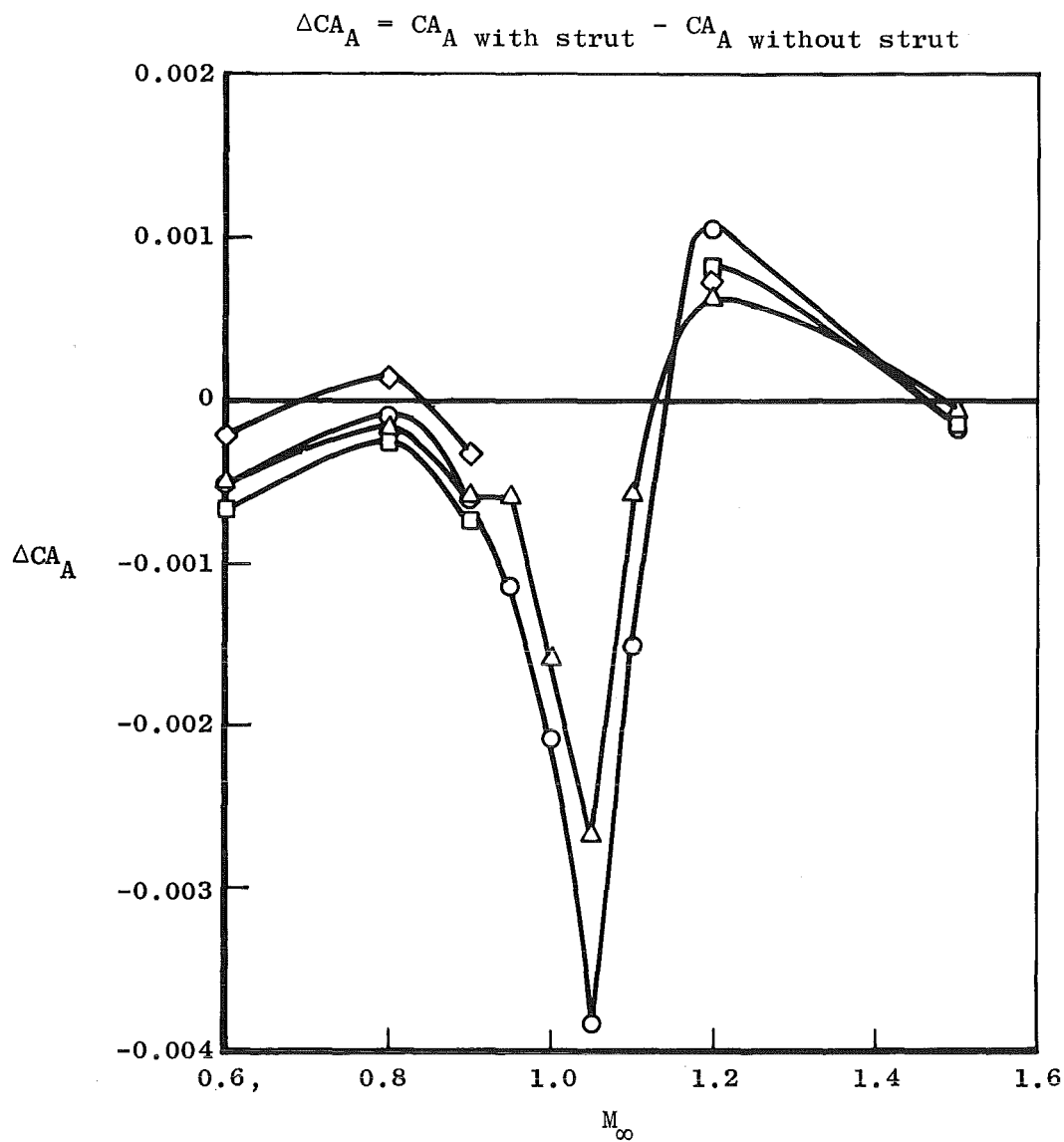
Sym	Nozzle	NPR	Config
○	Cruise 3.4	3.3	5 - 12
□	Part A/B 5.1	4.4	9 - 16
△	Max A/B 6.6	4.8	10 - 17
◇	Max A/B 7.75	6.7	11 - 18



a.  $\alpha = 0$

Figure 30. Strut interference on nozzle-afterbody axial-force coefficient.

<u>Sym</u>	<u>Nozzle</u>	<u>NPR</u>	<u>Config</u>
○	Cruise 3.4	3.3	5 - 12
□	Part A/B 5.1	4.4	9 - 16
△	Max A/B 6.6	4.8	10 - 17
◇	Max A/B 7.75	6.7	11 - 18



b.  $\alpha = 7$  deg  
Figure 30. Concluded.

Sym	Nozzle	NPR	Config
○	Cruise 3.4	3.3	5 - 12
□	Part A/B 5.1	4.4	9 - 16
△	Max A/B 6.6	4.8	10 - 17
◇	Max A/B 7.75	6.7	11 - 18

$$\Delta CN_A = CN_A \text{ with strut} - CN_A \text{ without strut}$$

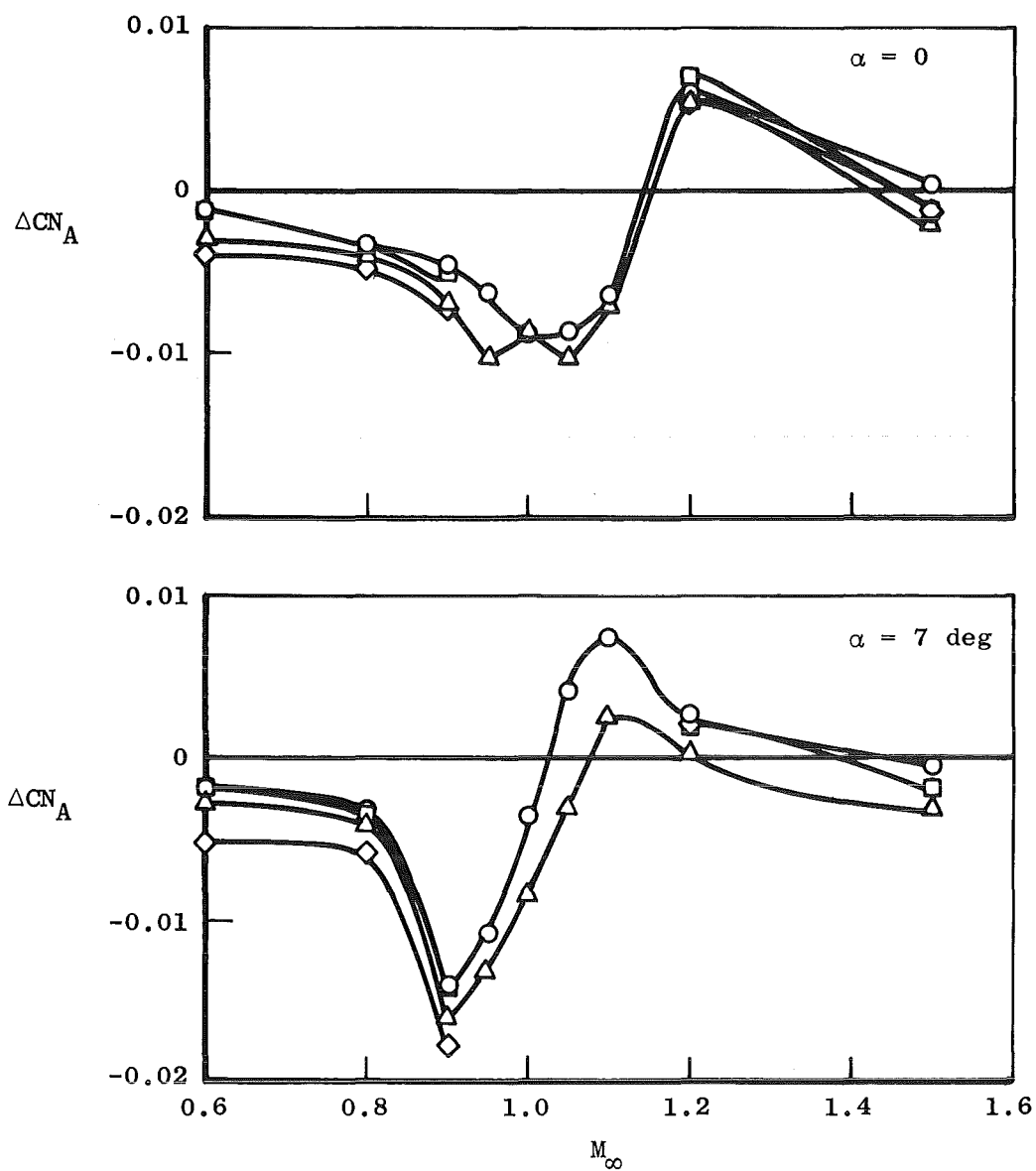
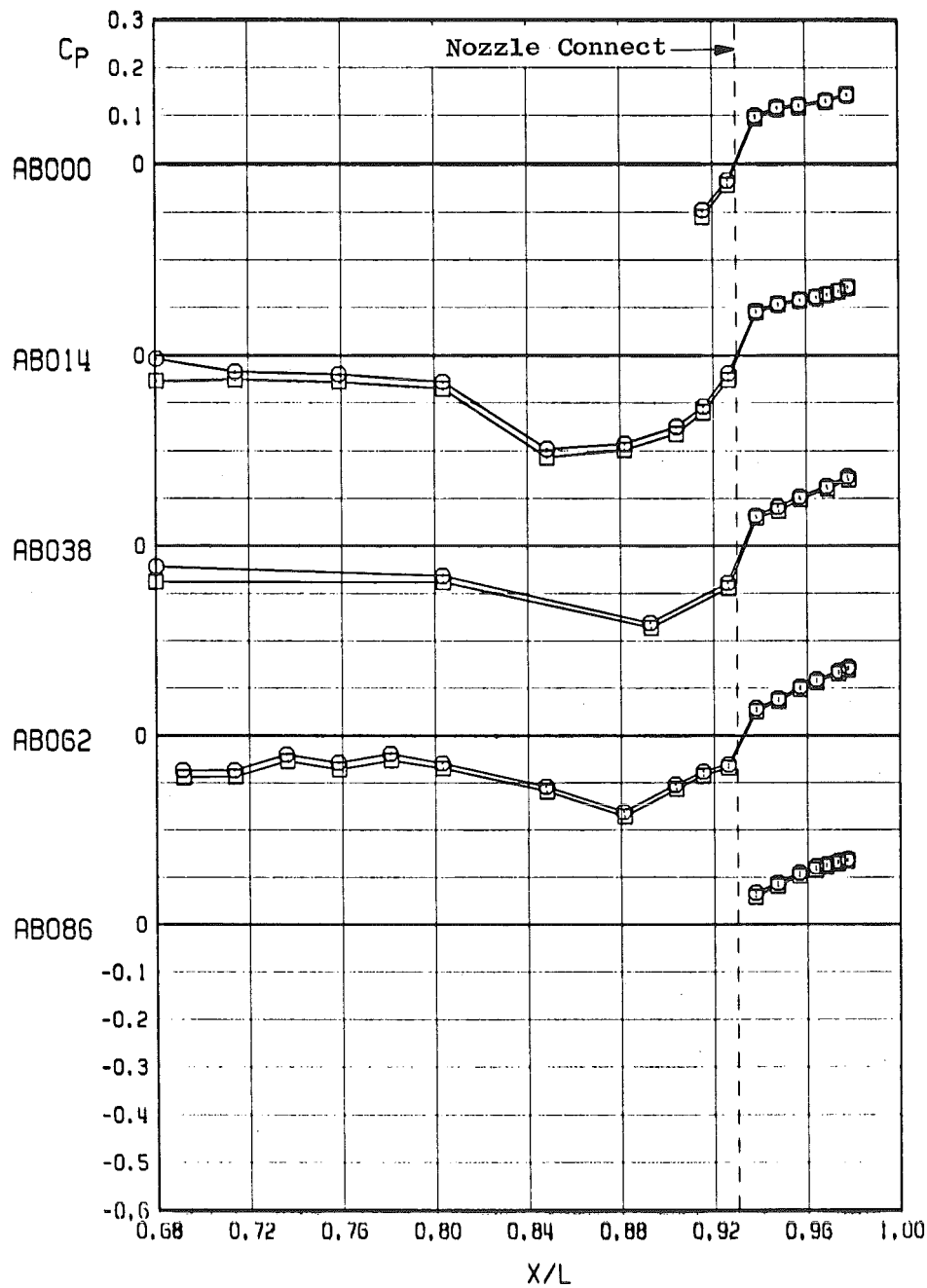


Figure 31. Strut interference on nozzle-afterbody normal-force coefficient.

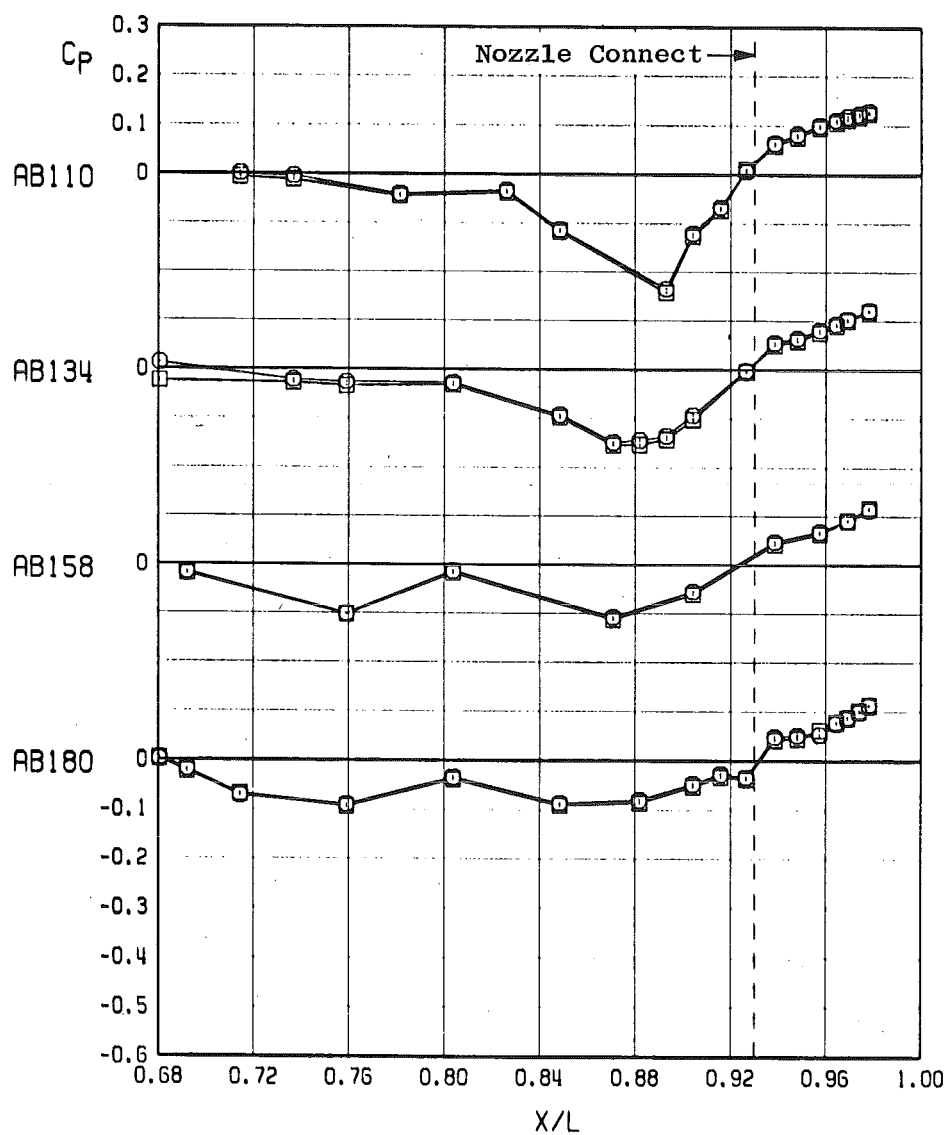
Sym	Conf	$C_{A_A}$	Support	RN.PN
○	10	0.00162	Strut	1774.03
□	17	0.00205	Sting	2027.03



a.  $M_\infty = 0.6$

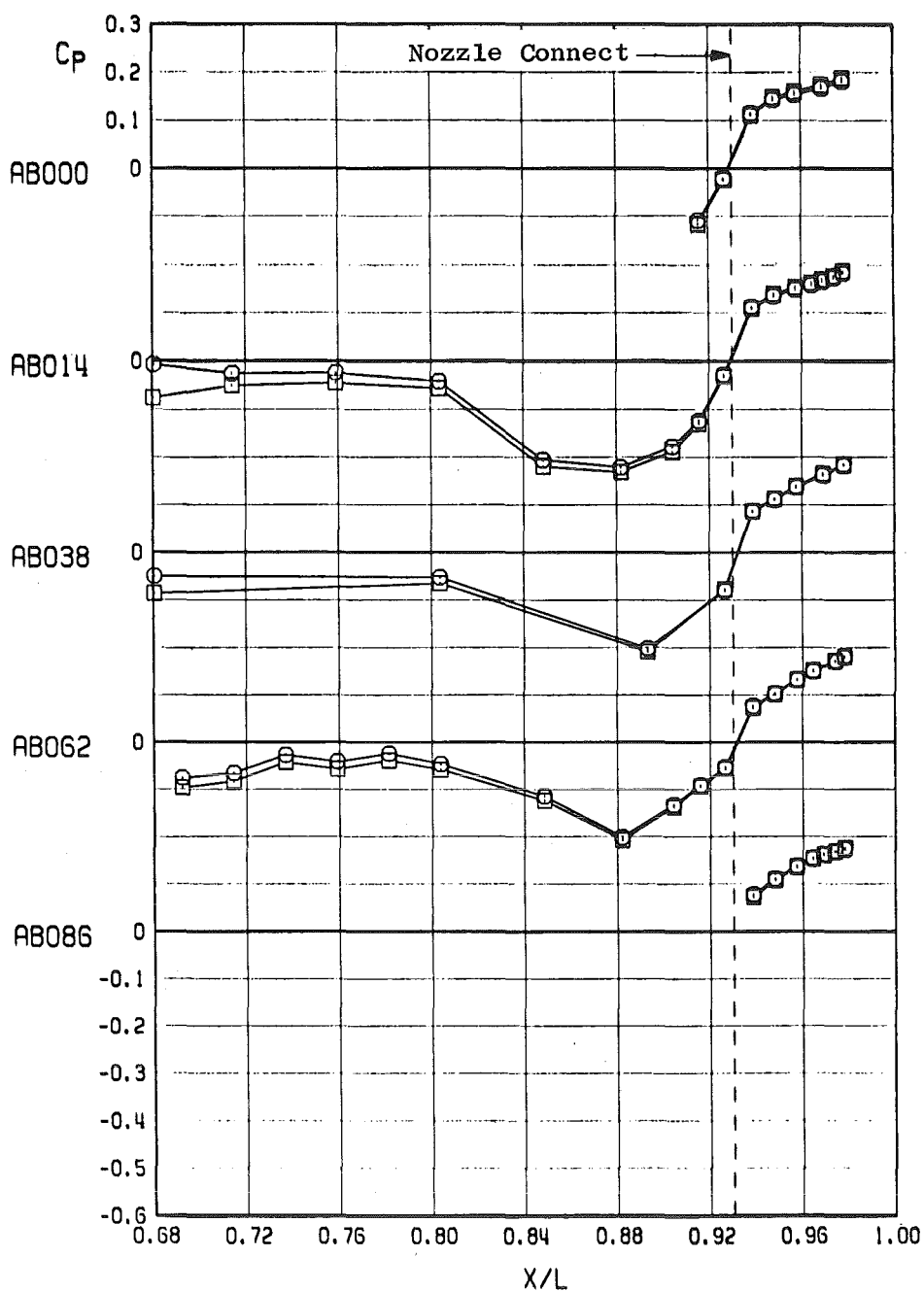
Figure 32. Effect of strut interference on the nozzle-afterbody pressure distributions, max A/B 6.6 nozzle, design NPR,  $\alpha = 0$ ,  $RE \approx 3.4 \times 10^6$ .

Sym	Conf	$CA_A$	Support	RN.PN
○	10	0.00162	Strut	1774.03
□	17	0.00205	Sting	2027.03



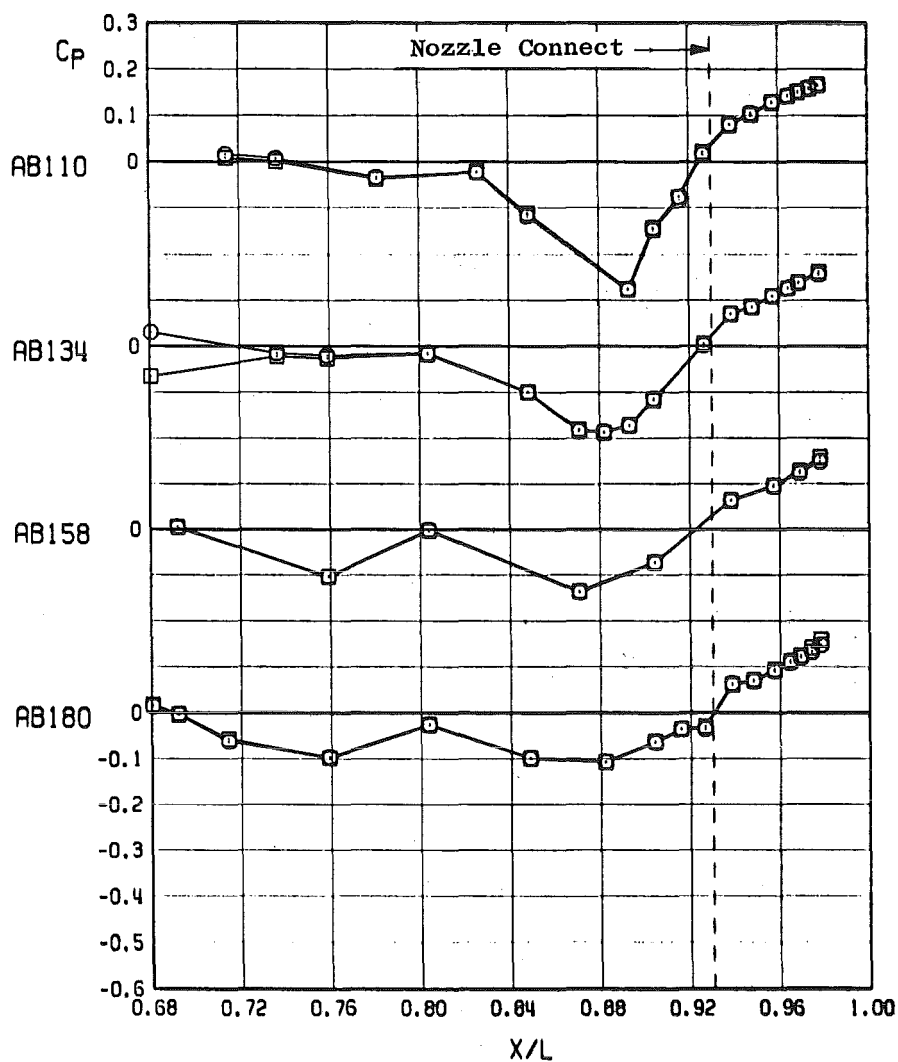
a. Concluded  
Figure 32. Continued.

<u>Sym</u>	<u>Conf</u>	<u>CA<sub>A</sub></u>	<u>Support</u>	<u>RN.PN</u>
○	10	0.00162	Strut	1777.03
□	17	0.00183	Sting	2036.07



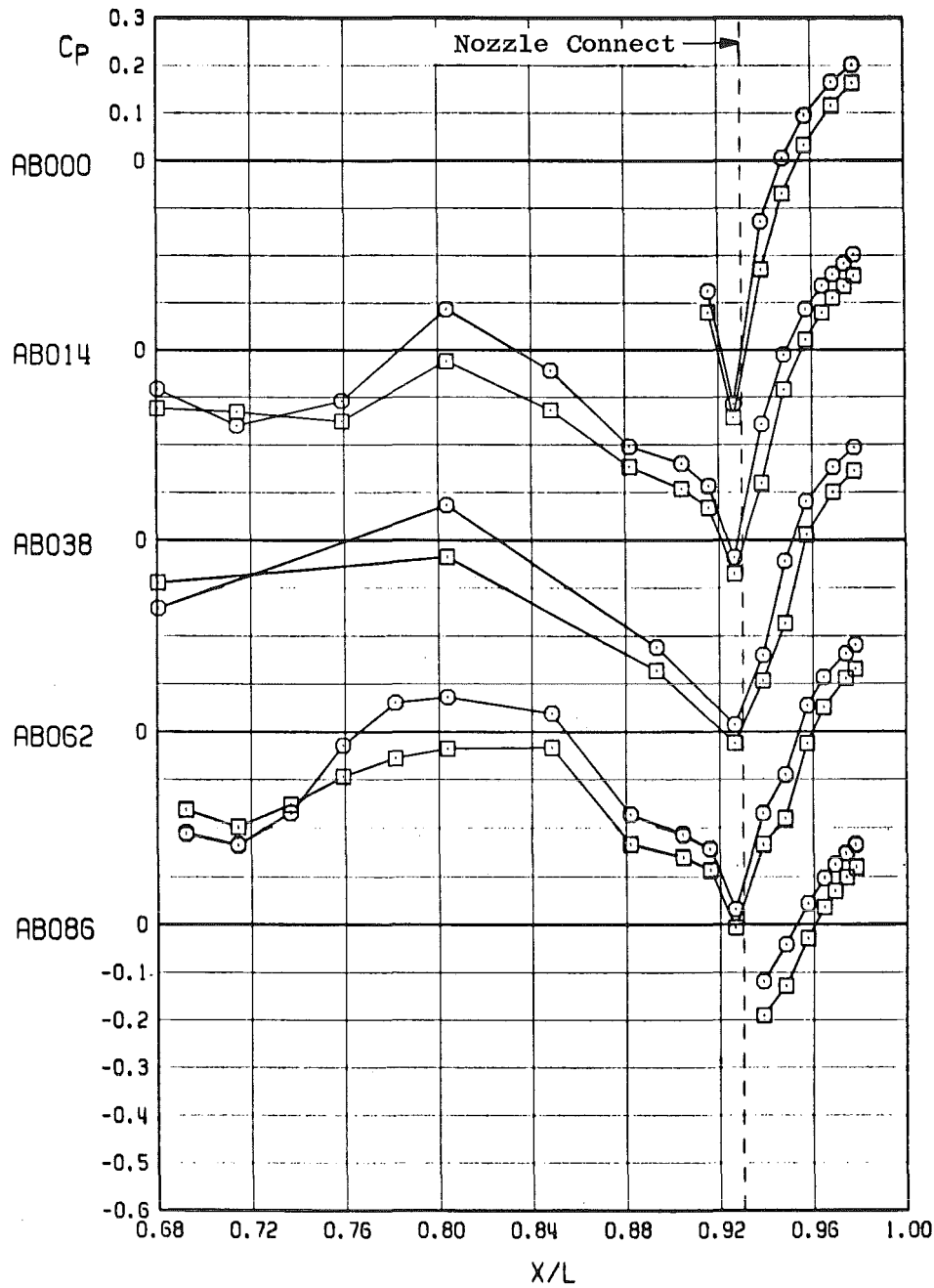
b.  $M_\infty = 0.8$   
Figure 32. Continued.

Sym	Conf	$C_{A_A}$	Support	RN.PN
○	10	0.00162	Strut	1777.03
□	17	0.00183	Sting	2036.07



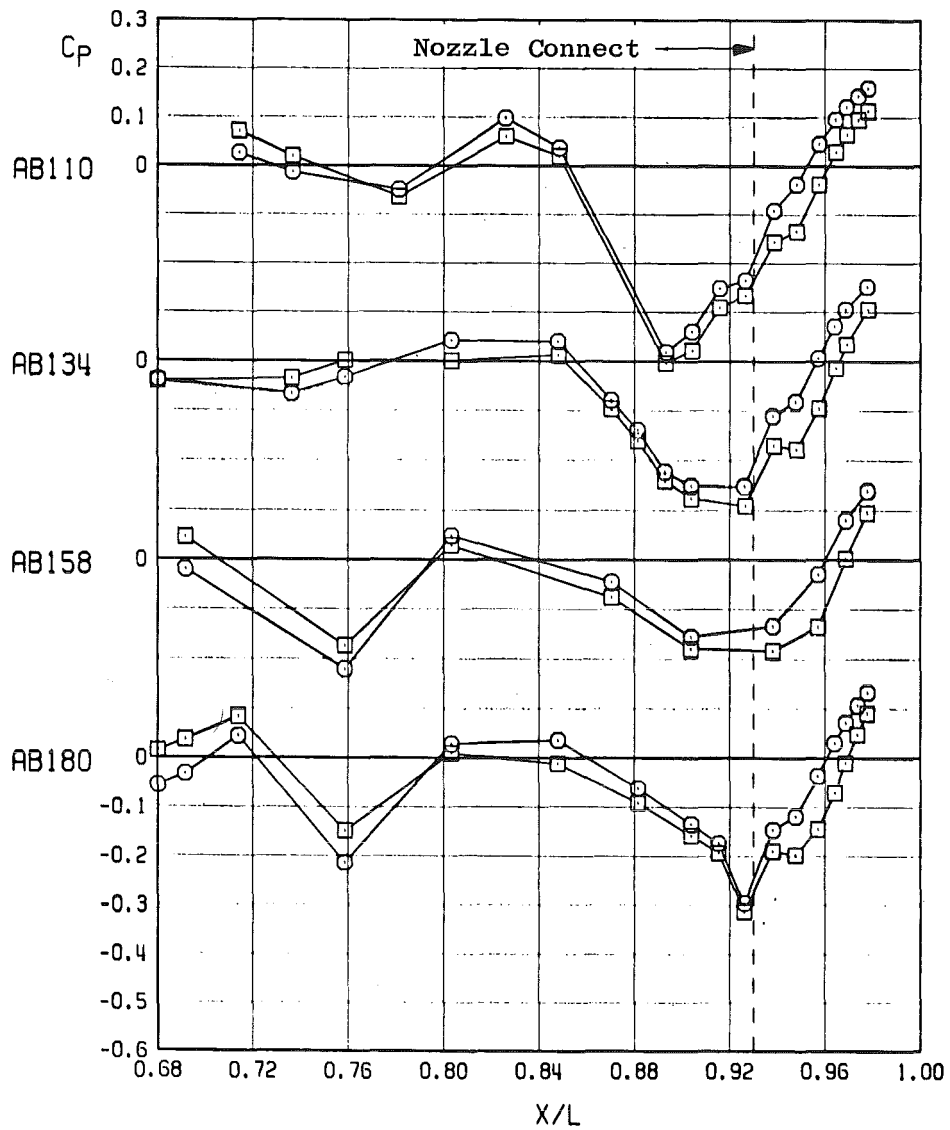
b. Concluded  
Figure 32. Continued.

Sym	Conf	CA A	Support	RN.PN
○	10	0.00510	Strut	1787.03
□	17	0.00732	Sting	2060.01



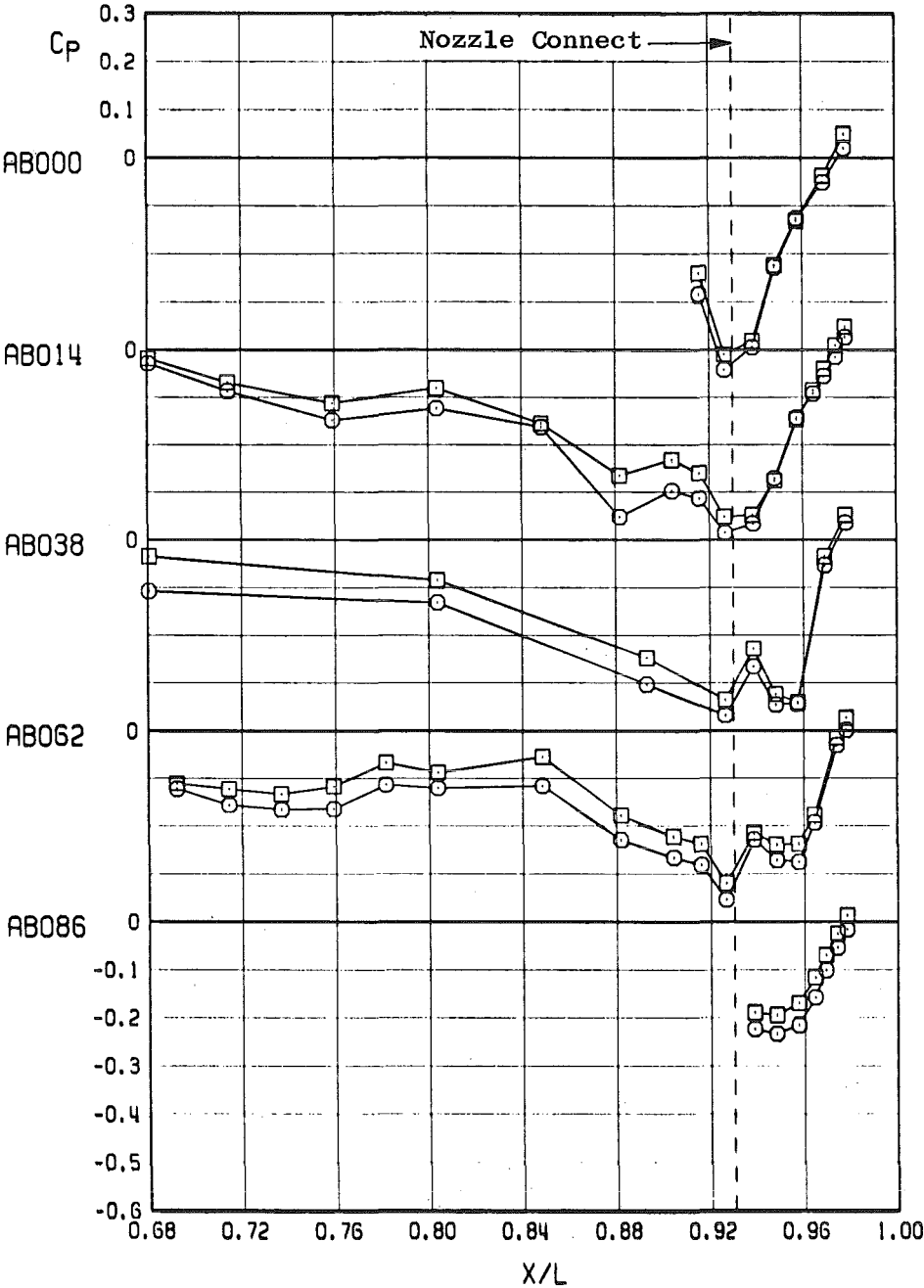
c.  $M_\infty = 1.05$   
Figure 32 Continued.

Sym	Conf	CA <sub>A</sub>	Support	RN.PN
○	10	0.00510	Strut	1787.03
□	17	0.00732	Sting	2060.01



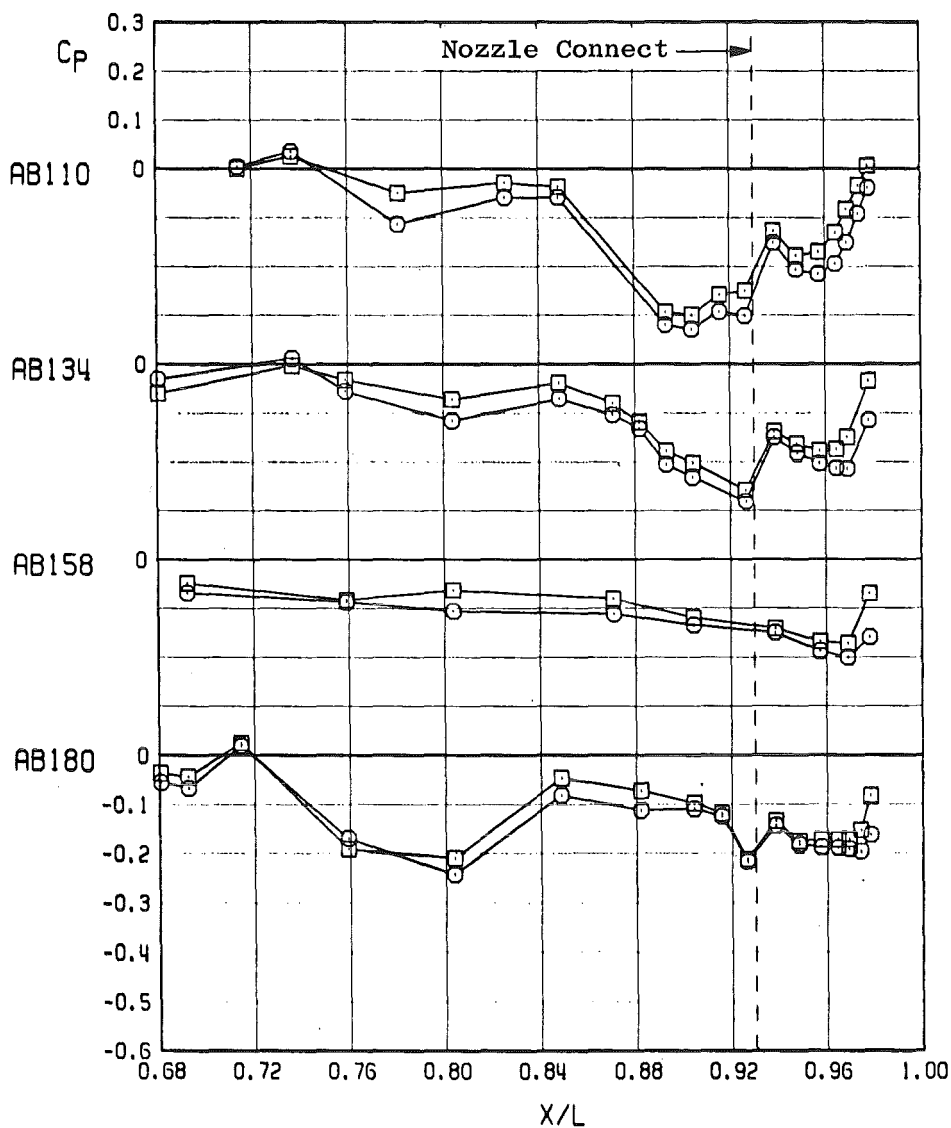
c. Concluded  
Figure 32. Continued.

Sym	Conf	CA <sub>A</sub>	Support	RN.PN
○	10	0.00945	Strut	1793.05
□	17	0.00799	Sting	2077.01



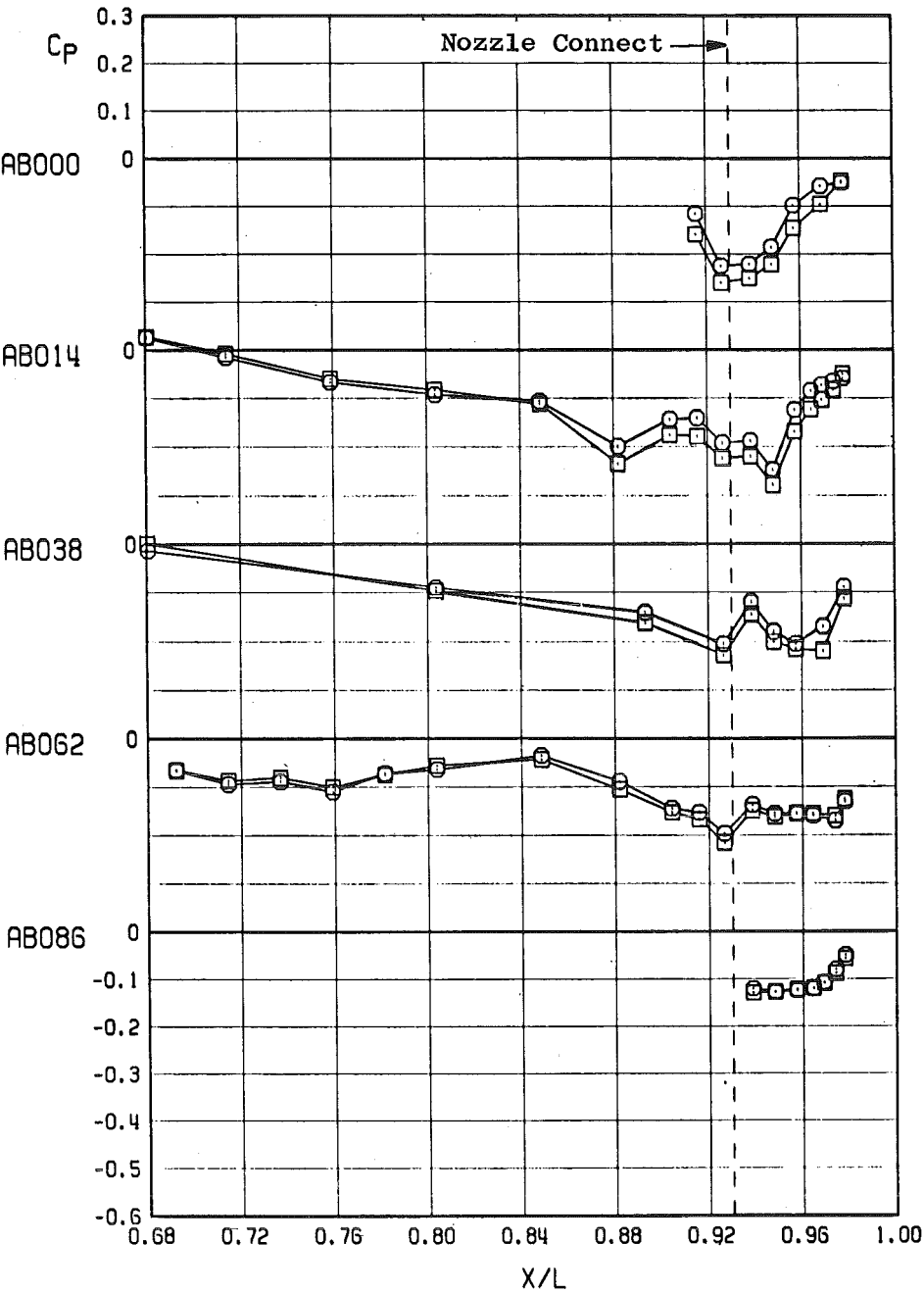
d.  $M_\infty = 1.2$   
Figure 32. Continued.

Sym	Conf	$CA_A$	Support	RN, PN
○	10	0.00945	Strut	1793.05
□	17	0.00799	Sting	2077.01



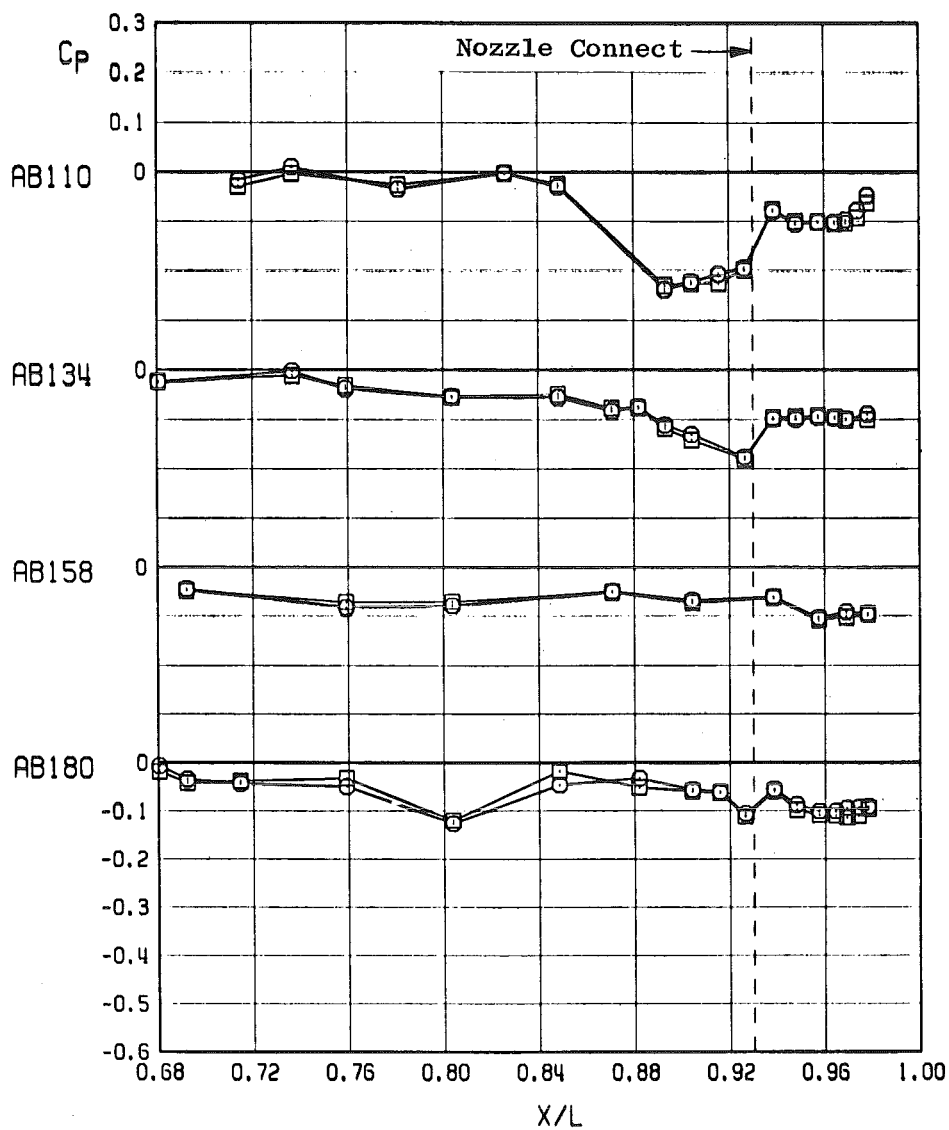
d. Concluded  
Figure 32. Continued.

Sym	Conf	CA <sub>A</sub>	Support	RN.PN
○	10	0.00551	Strut	1796.01
□	17	0.00580	Sting	2089.06



e.  $M_\infty = 1.5$   
Figure 32. Continued.

Sym	Conf	$C_{A_A}$	Support	RN.PN
○	10	0.00551	Strut	1796.01
□	17	0.00580	Sting	2089.06



e. Concluded  
Figure 32. Concluded.

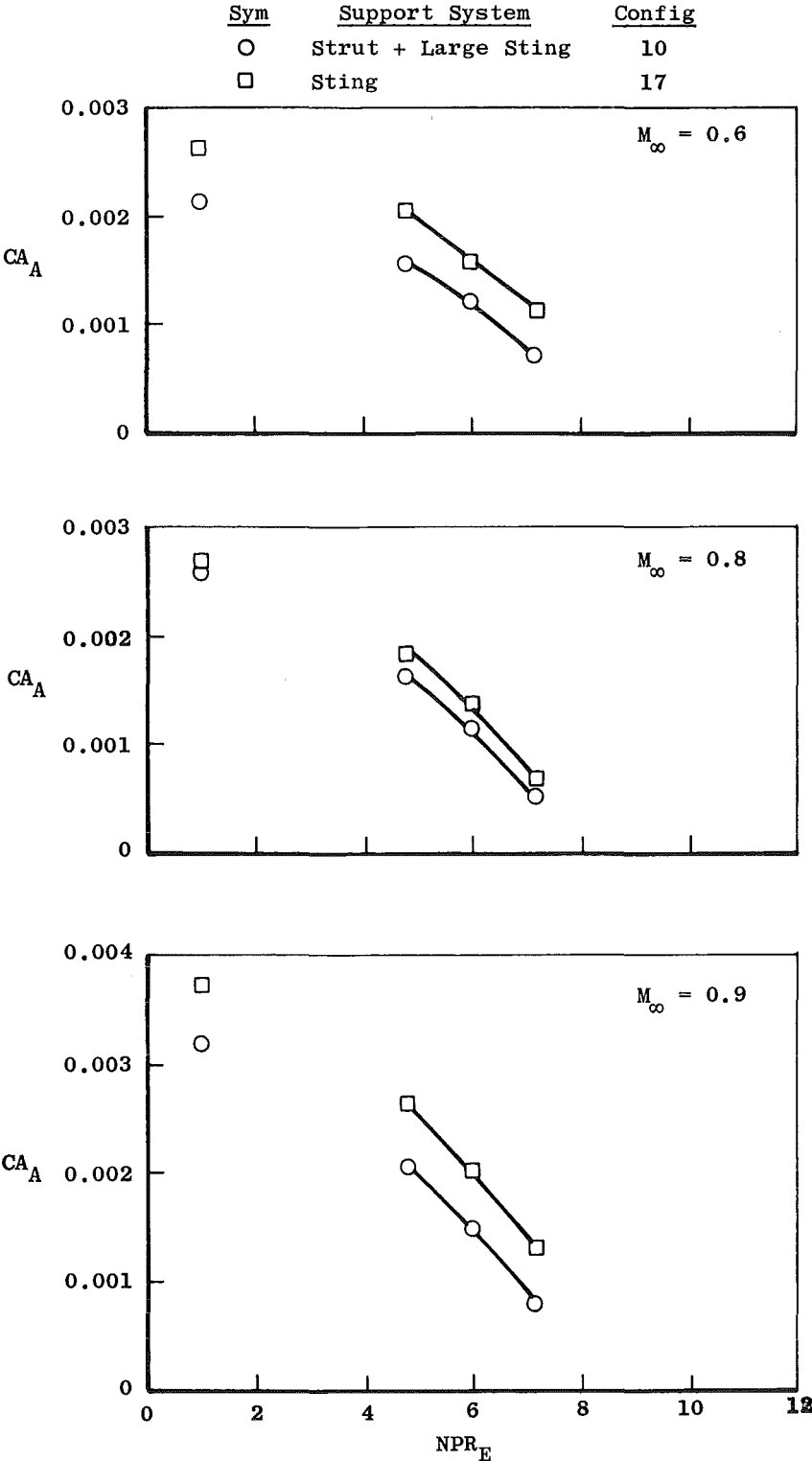


Figure 33. The effect of strut interference on the variation of afterbody axial force with NPR, max A/B 6.6 nozzle,  $\alpha = 0$ .

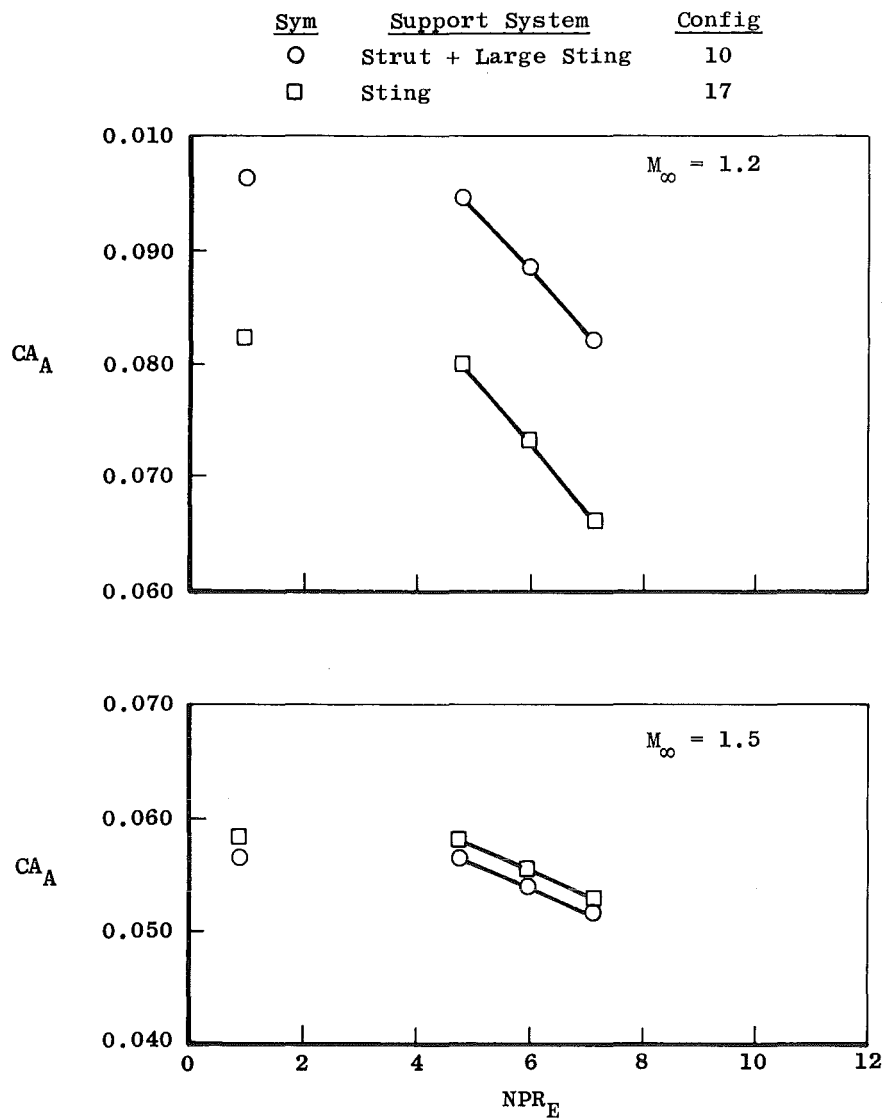
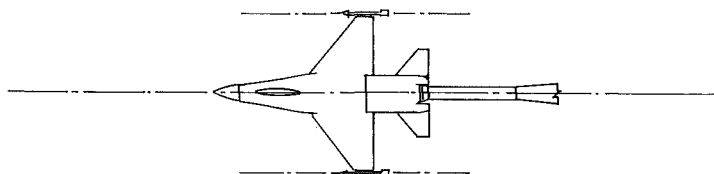
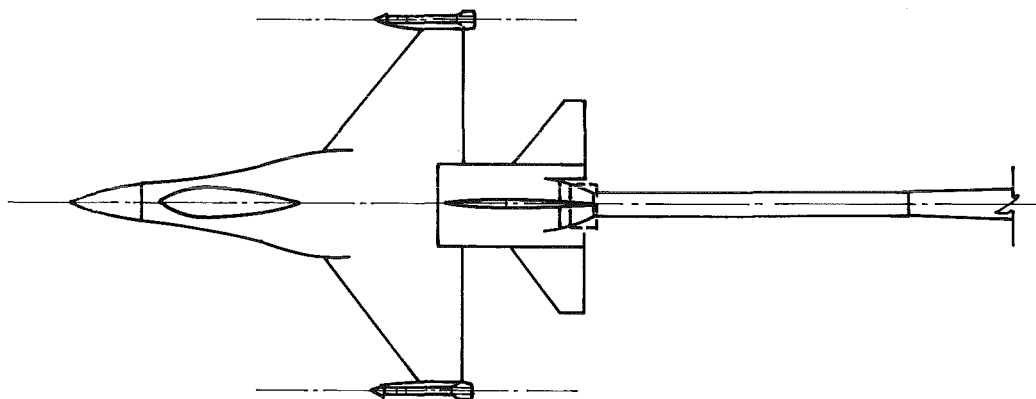


Figure 33. Concluded.



0.11-Scale F-16 Model  
Test Section Blockage Ratio = 0.14 percent

---



0.25-Scale F-16 Model  
Test Section Blockage Ratio = 0.71 percent

---

**Figure 34. Relative size of 0.11-scale and 0.25-scale models  
installed in tunnel 16T.**

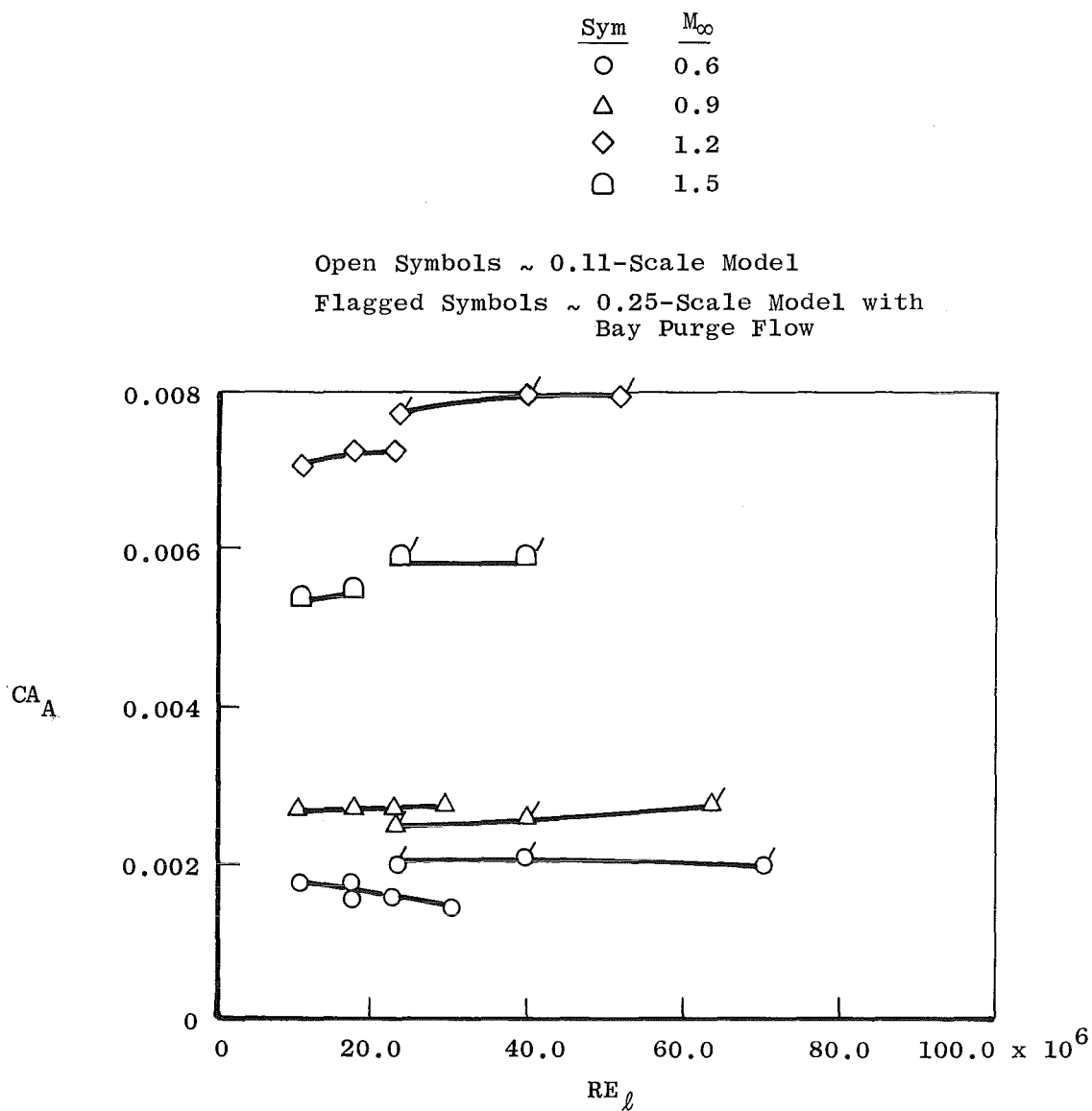
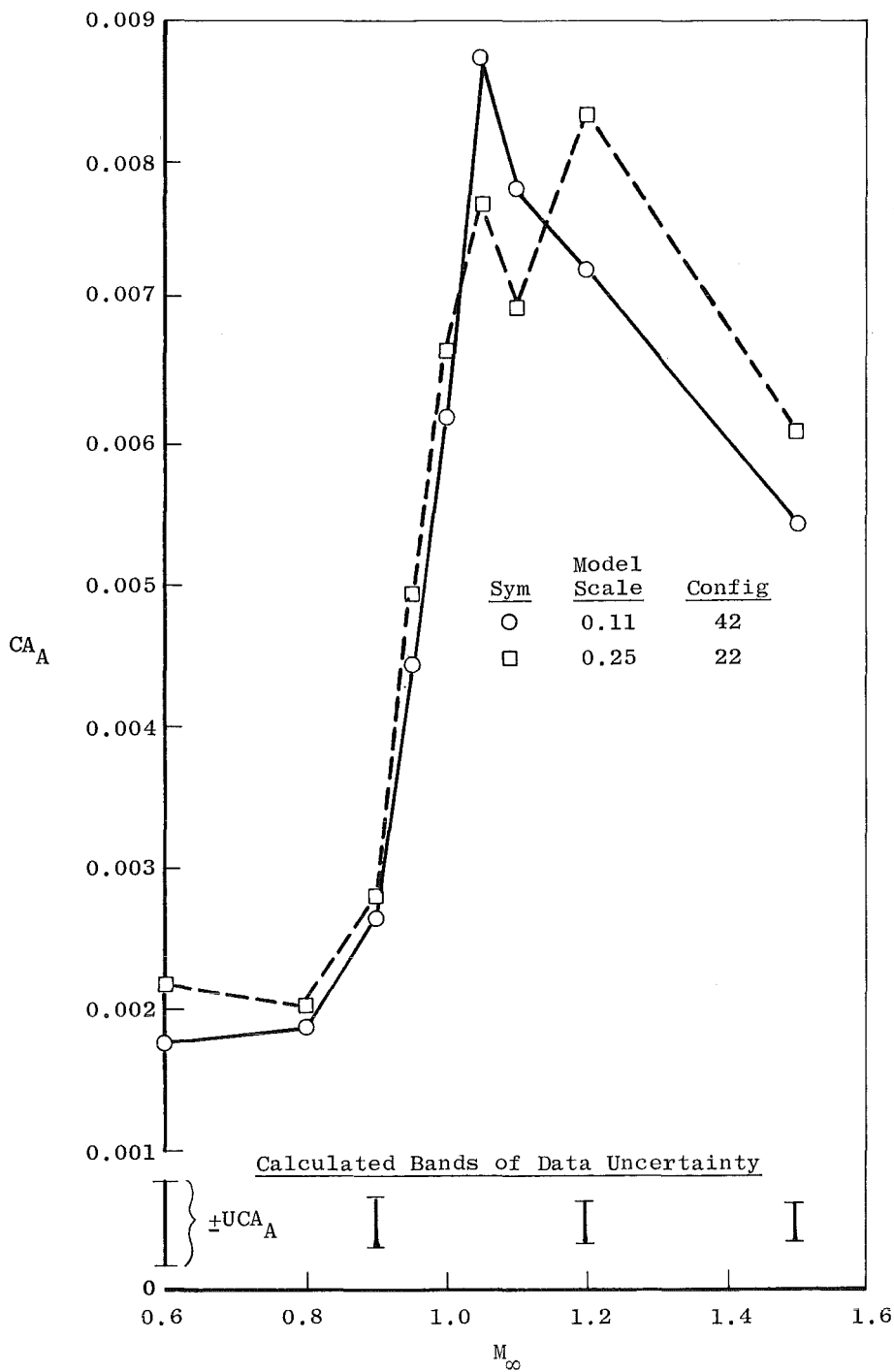
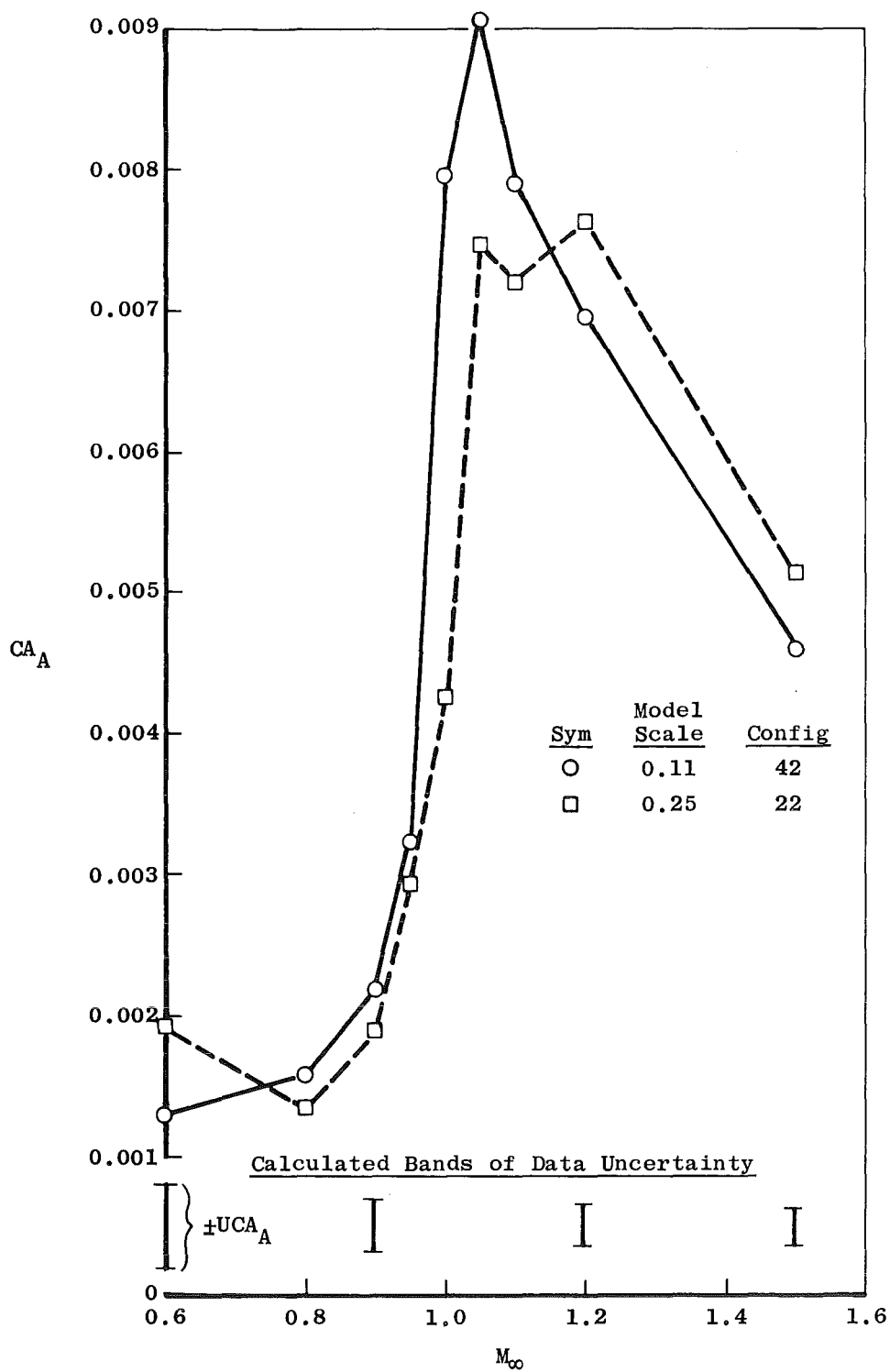


Figure 35. Effect of Reynolds number on axial-force coefficient for the sting-supported F-16 models, max A/B 6.6 nozzle, NPR = 4.8,  $\alpha = 0$ .



a.  $\alpha = 0$

Figure 36. Effect of model scale on the nozzle-afterbody axial-force coefficients, sting support system max A/B 6.6 nozzle, NPR = 4.8,  $Re = 3.4 \times 10^6$ .



b.  $\alpha = 7$  deg  
Figure 36. Concluded.

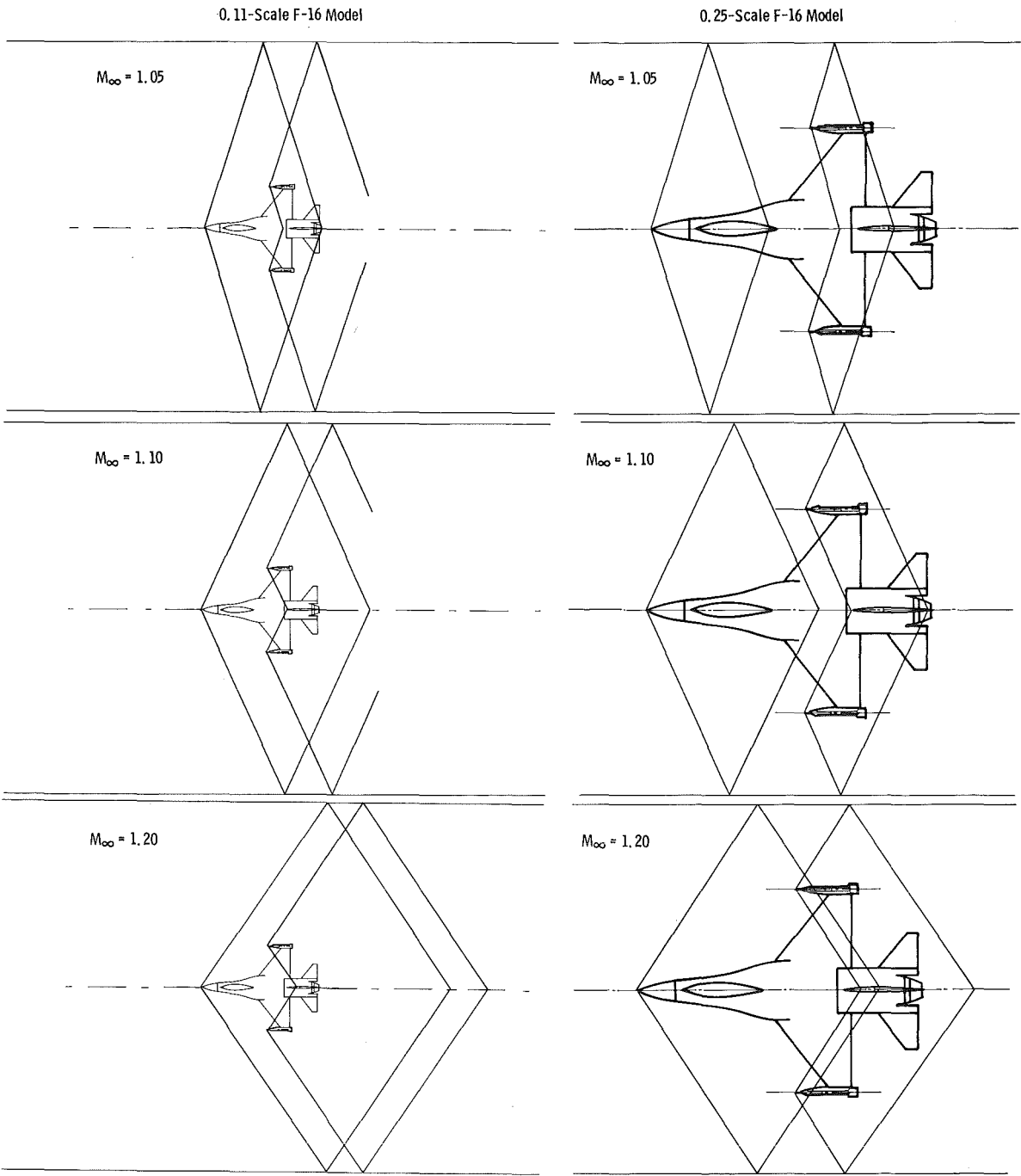


Figure 37. Comparison of primary model shock interactions for the 0.11- and 0.25-scale models.

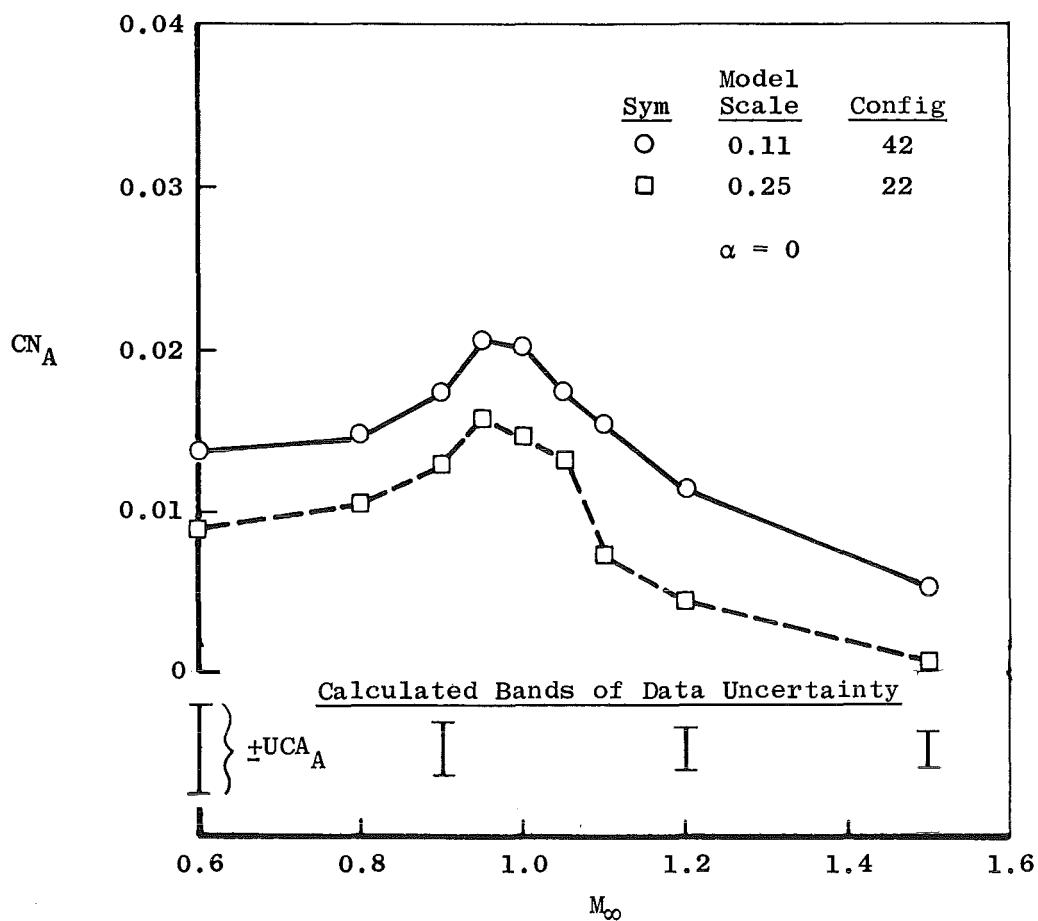
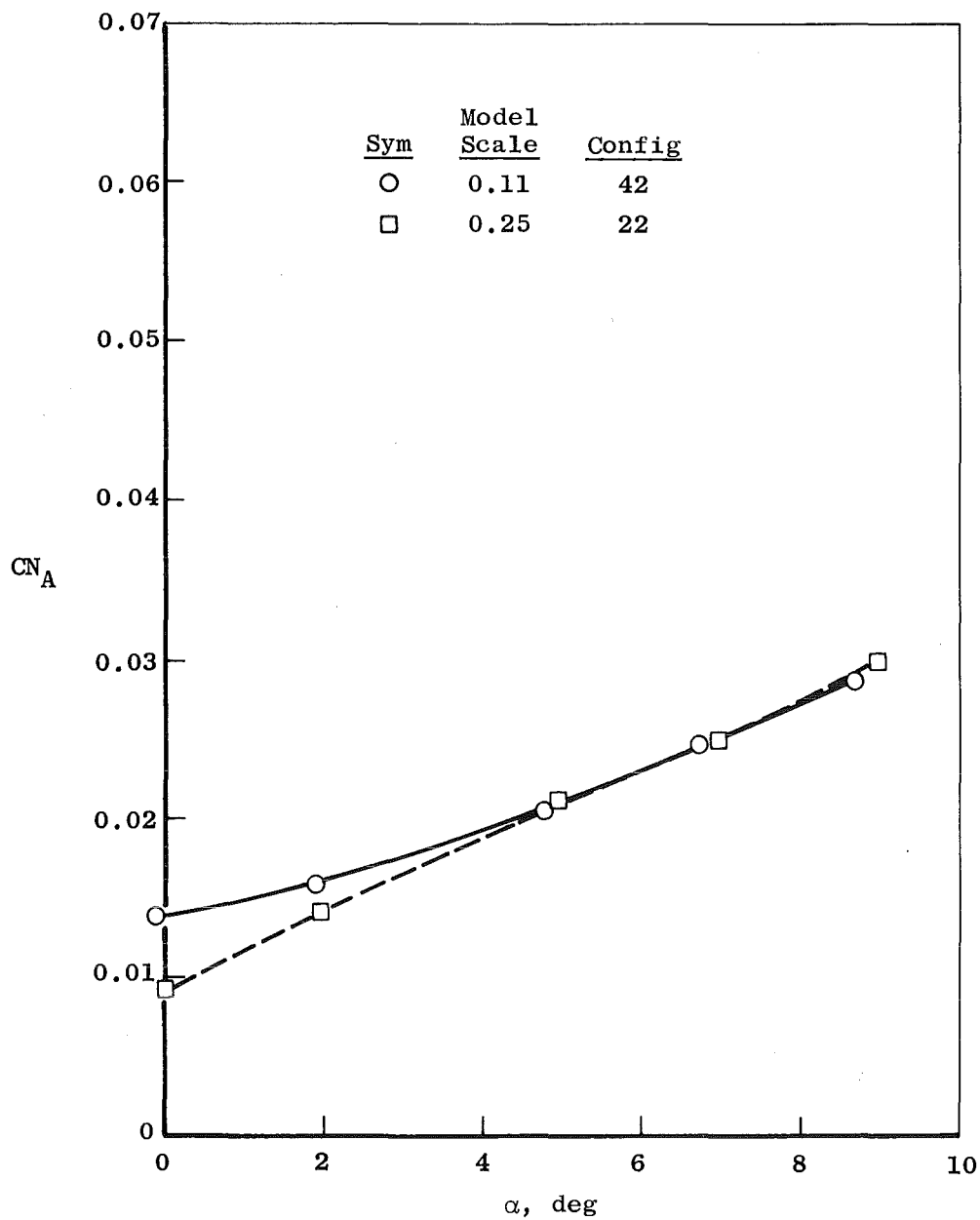
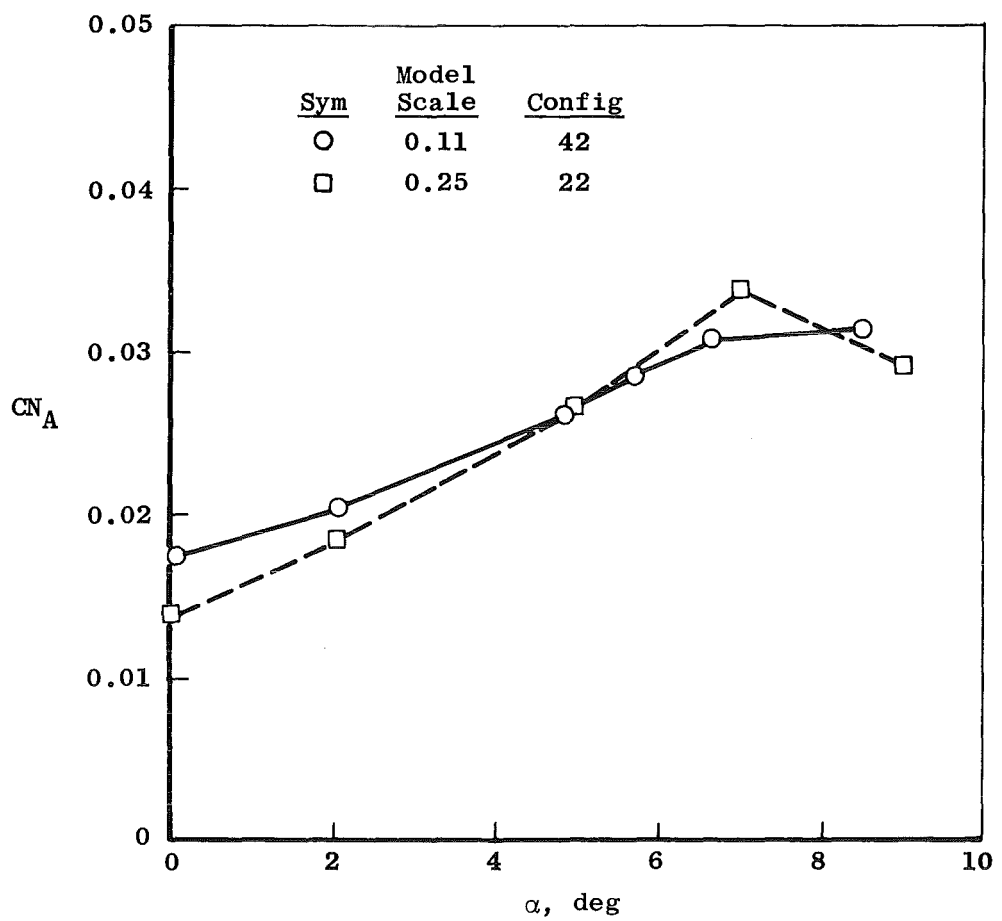


Figure 38. Effect of model scale on the nozzle-afterbody normal-force coefficients, sting support system, max A/B 0.6 nozzle, NPR = 4.8,  $Re = 3.4 \times 10^6$ .

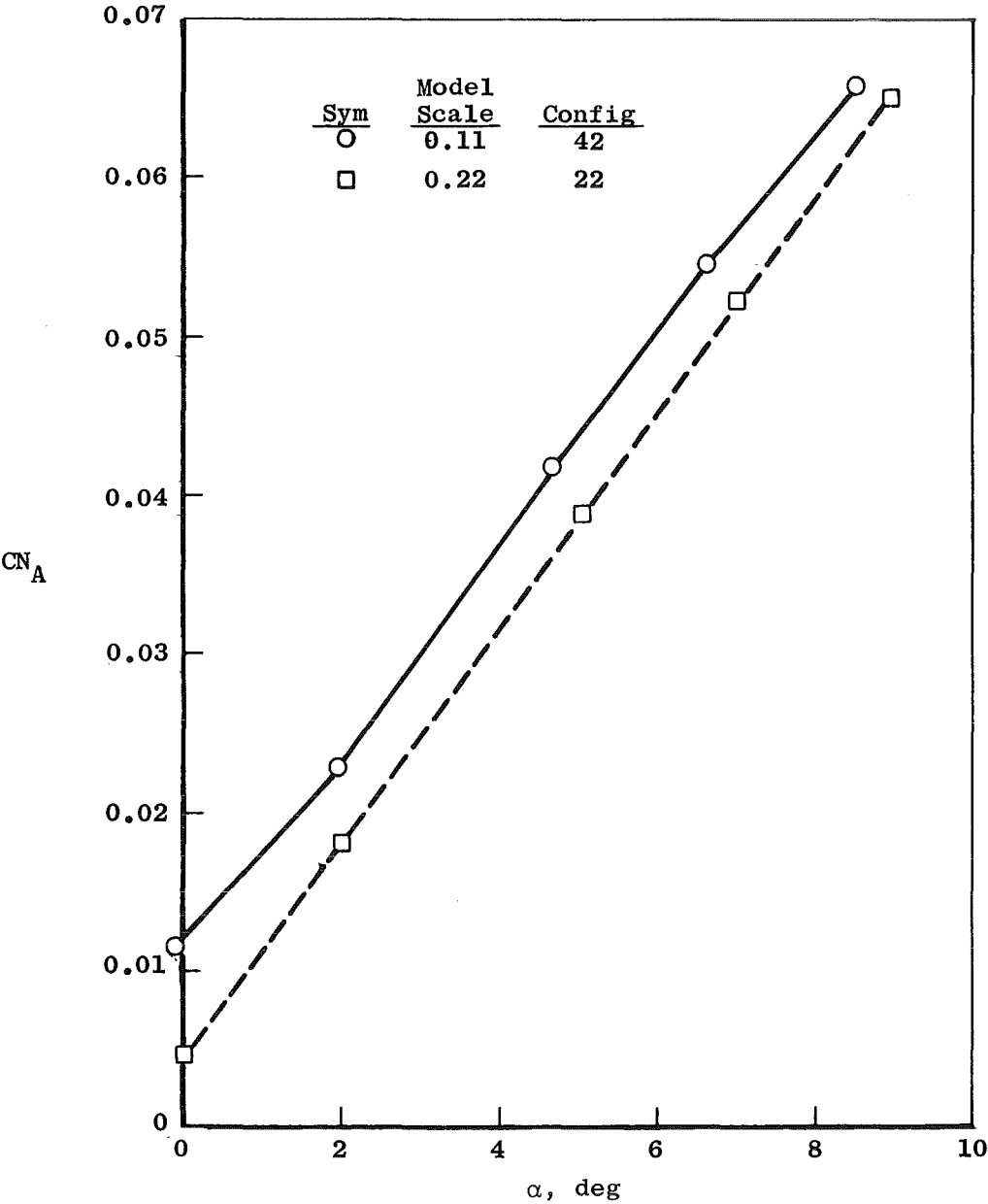


a.  $M_\infty = 0.6$

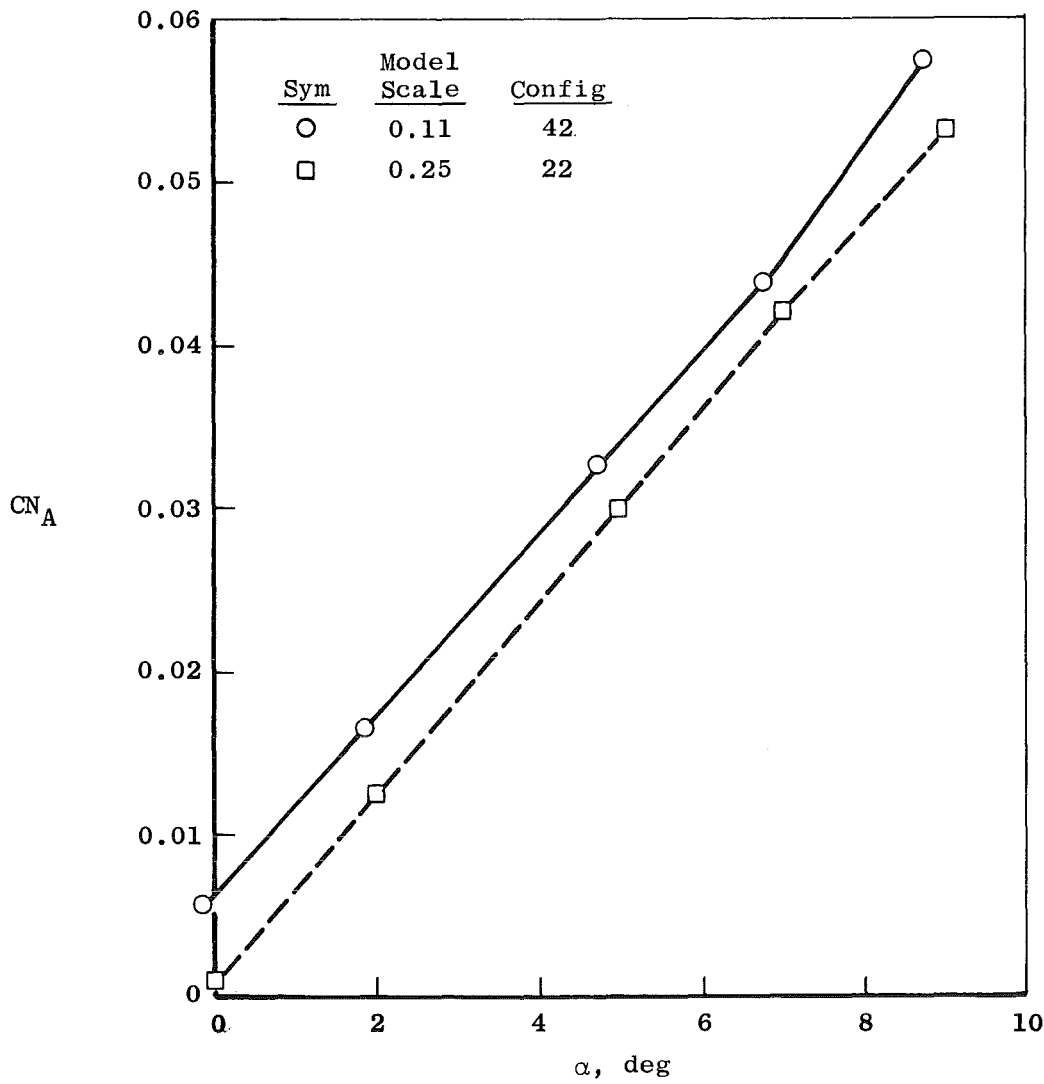
Figure 39. Effect of model scale on the sensitivity of the nozzle-afterbody normal-force coefficient to angle of attack, sting support system, max A/B 6.6 nozzle, NPR = 4.8, RE =  $3.4 \times 10^6$ .



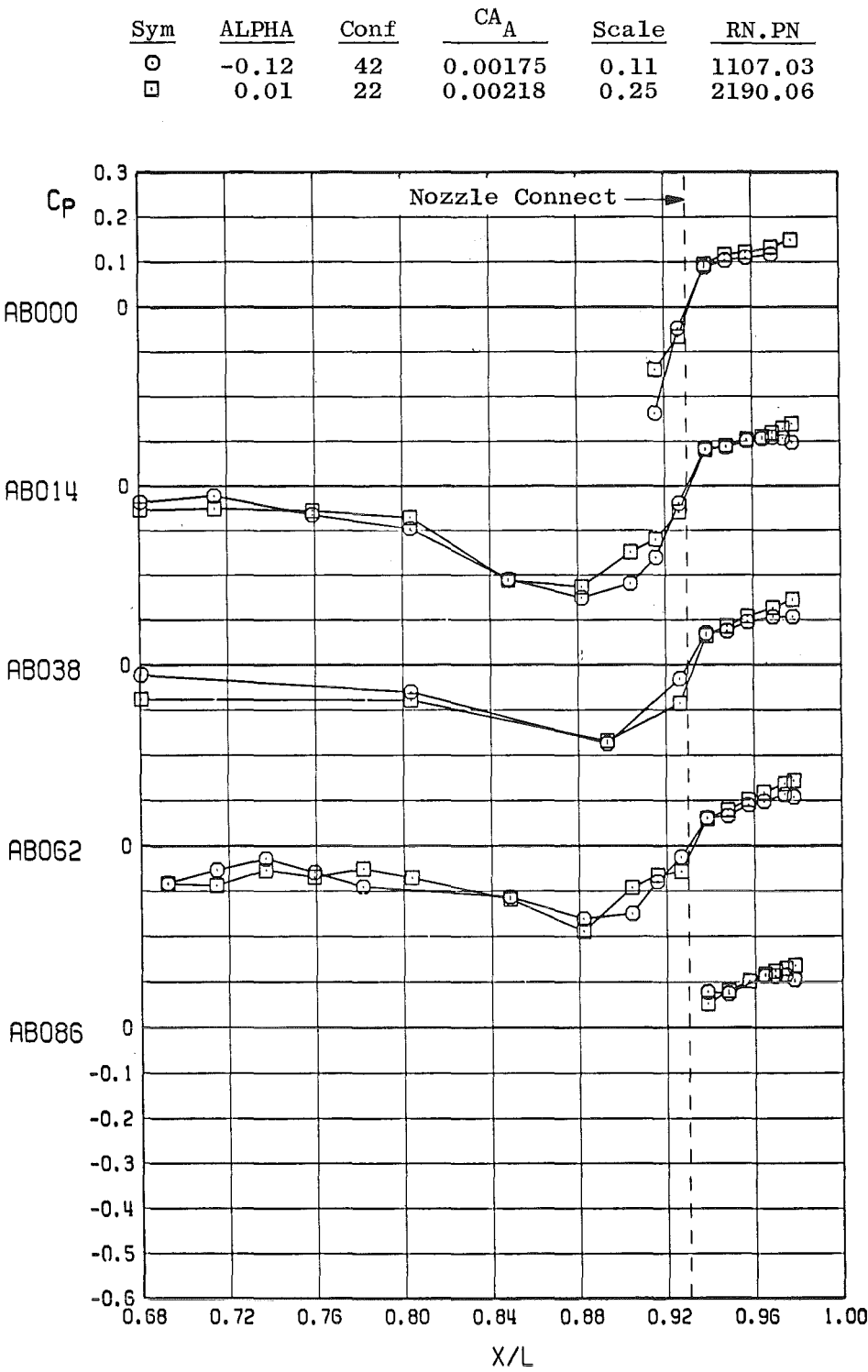
b.  $M_\infty = 0.9$   
Figure 39. Continued.



c.  $M_\infty = 1.2$   
Figure 39. Continued.



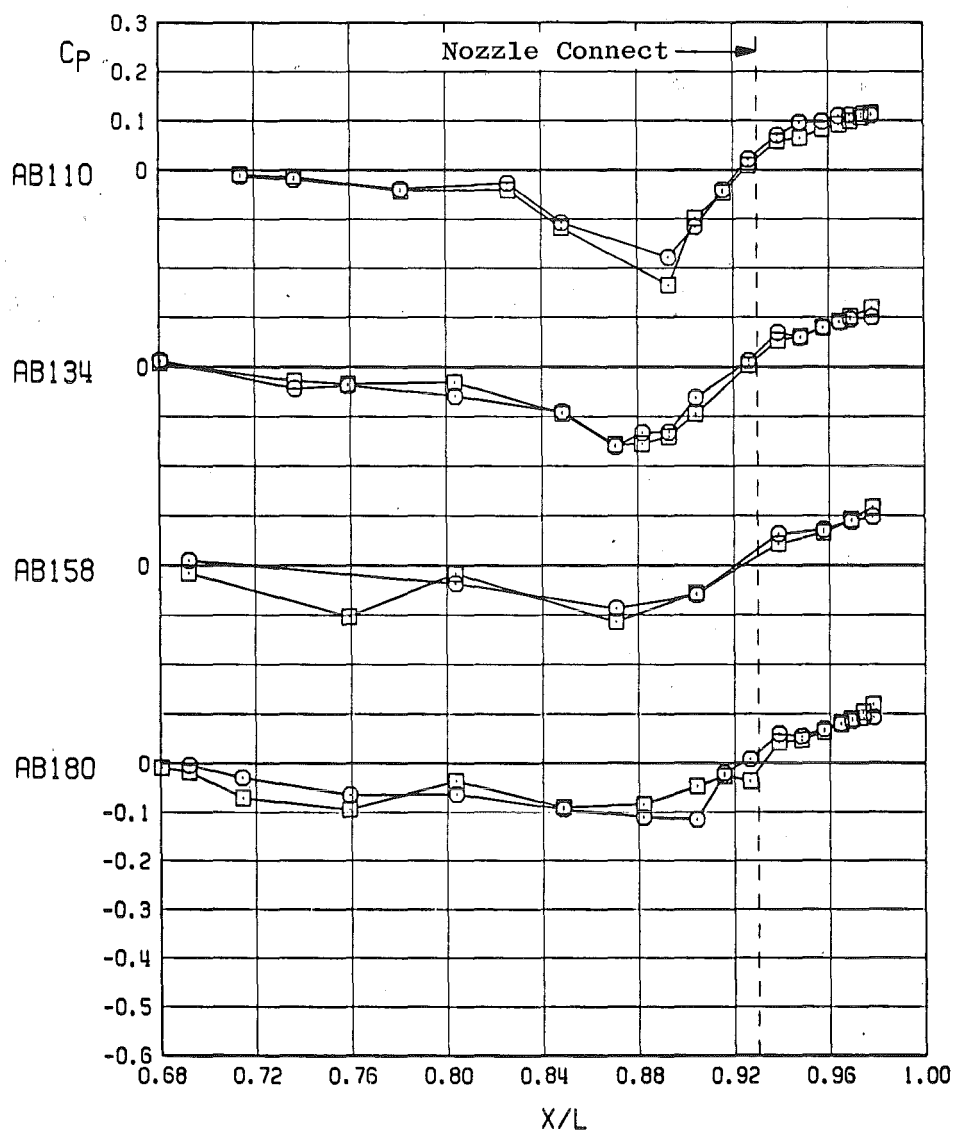
d.  $M_\infty = 1.5$   
Figure 39. Concluded.



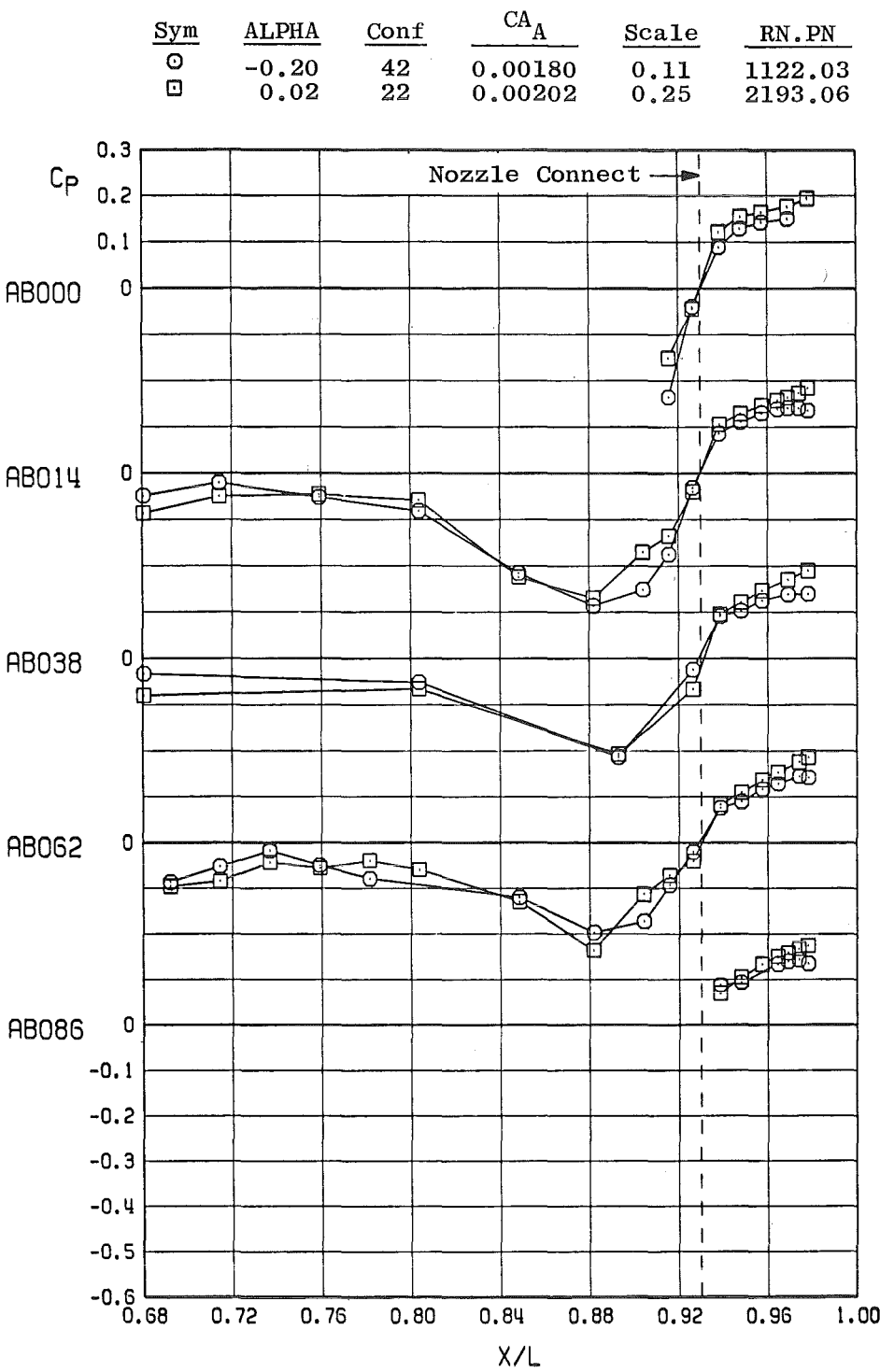
a.  $M_\infty = 0.6$

Figure 40. Effect of model scale on the nozzle-afterbody pressure distributions, sting support system, max A/B 6.6 nozzle, NPR = 4.8,  $Re = 3.4 \times 10^6$ .

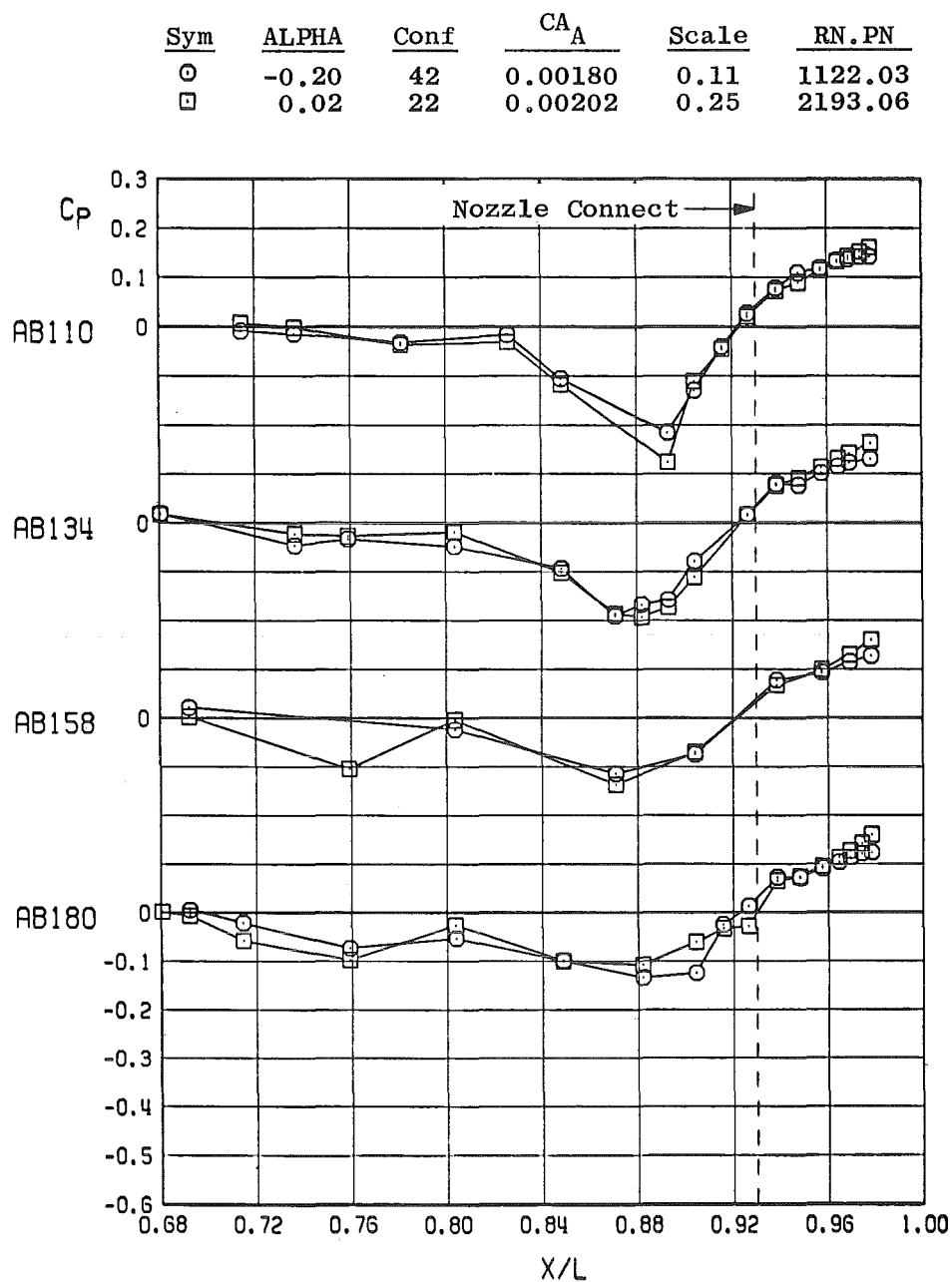
Sym	ALPHA	Conf	$C_{A_A}$	Scale	RN.PN
○	-0.12	42	0.00175	0.11	1107.03
□	0.01	22	0.00218	0.25	2190.06



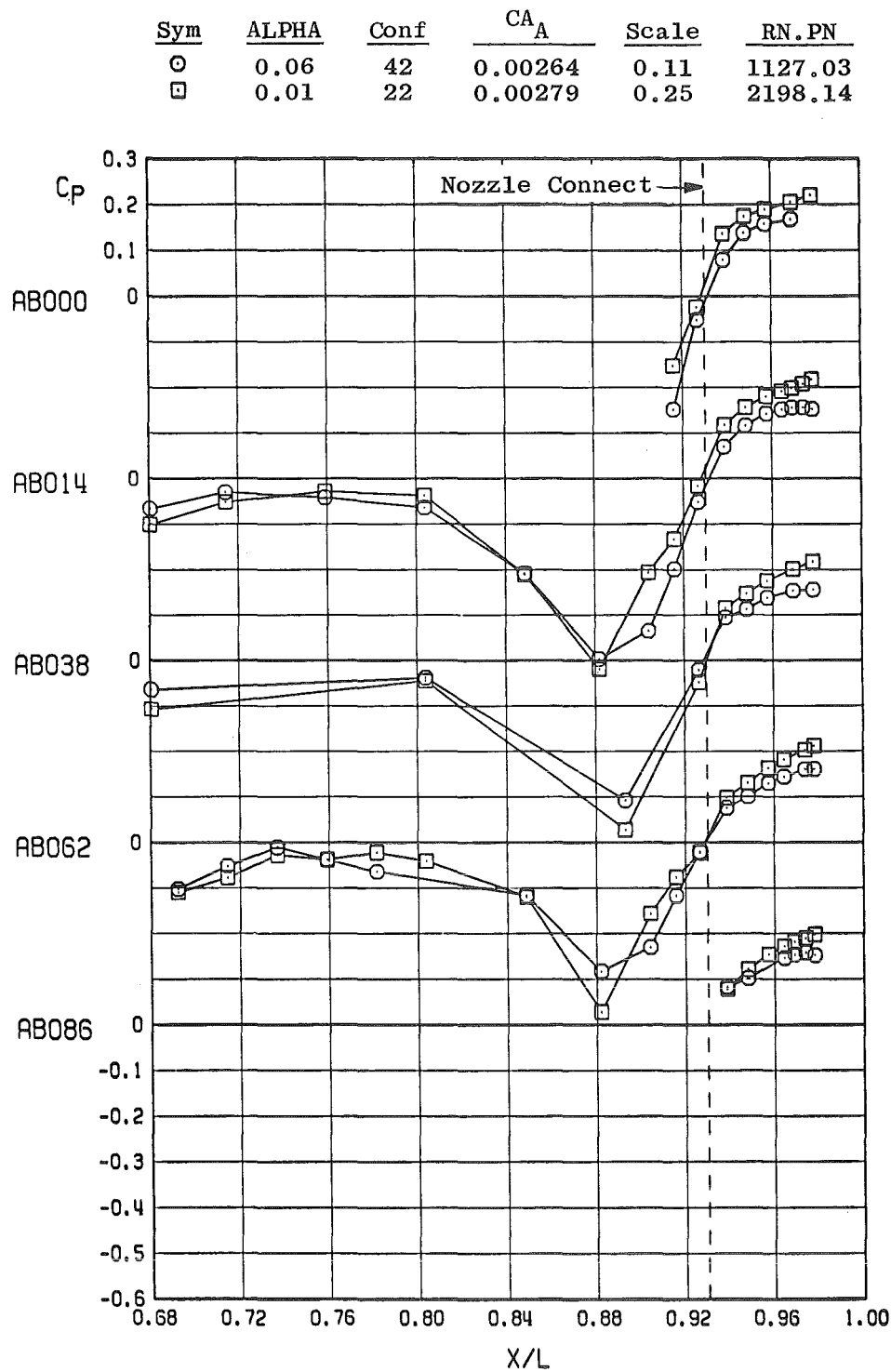
a. Concluded  
Figure 40. Continued.



b.  $M_\infty = 0.8$   
Figure 40. Continued.

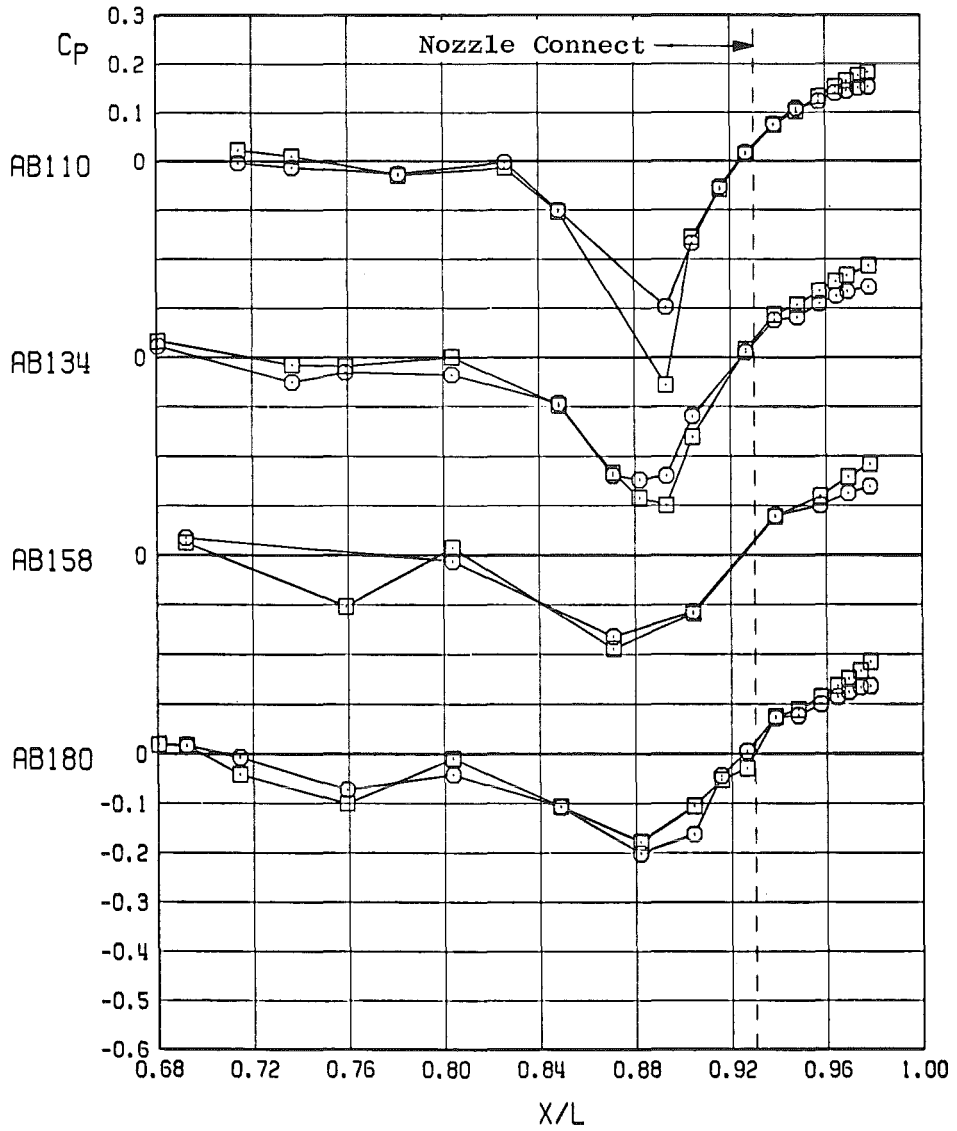


b. Concluded  
Figure 40. Continued.



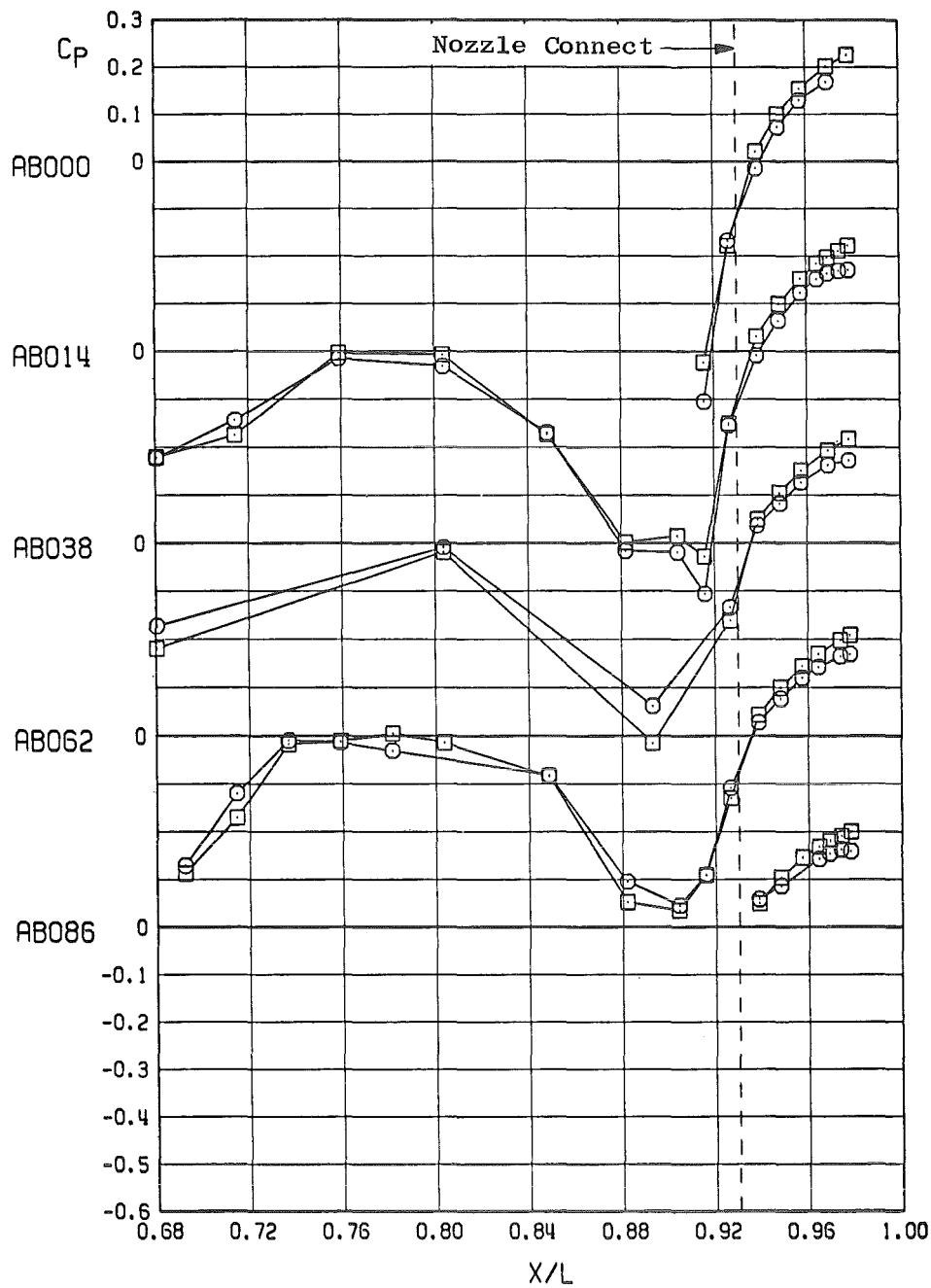
c.  $M_\infty = 0.9$   
Figure 40. Continued.

Sym	ALPHA	Conf	$CA_A$	Scale	RN.PN
○	0.06	42	0.00264	0.11	1127.03
□	0.01	22	0.00279	0.25	2198.14



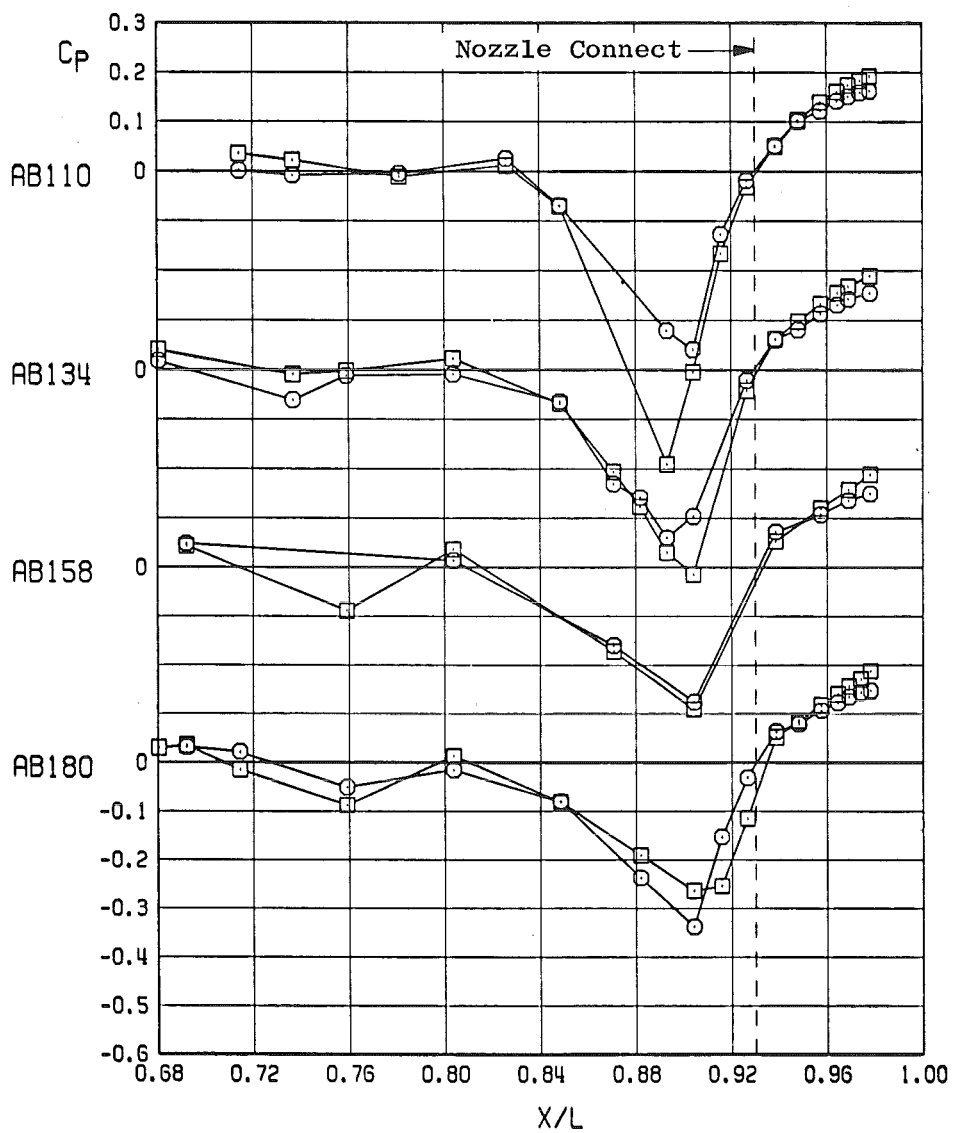
c. Concluded  
Figure 40. Continued.

Sym	ALPHA	Conf	CA <sub>A</sub>	Scale	RN.PN
⊙	0.02	42	0.00442	0.11	1074.03
⊠	0.01	22	0.00494	0.25	2200.11

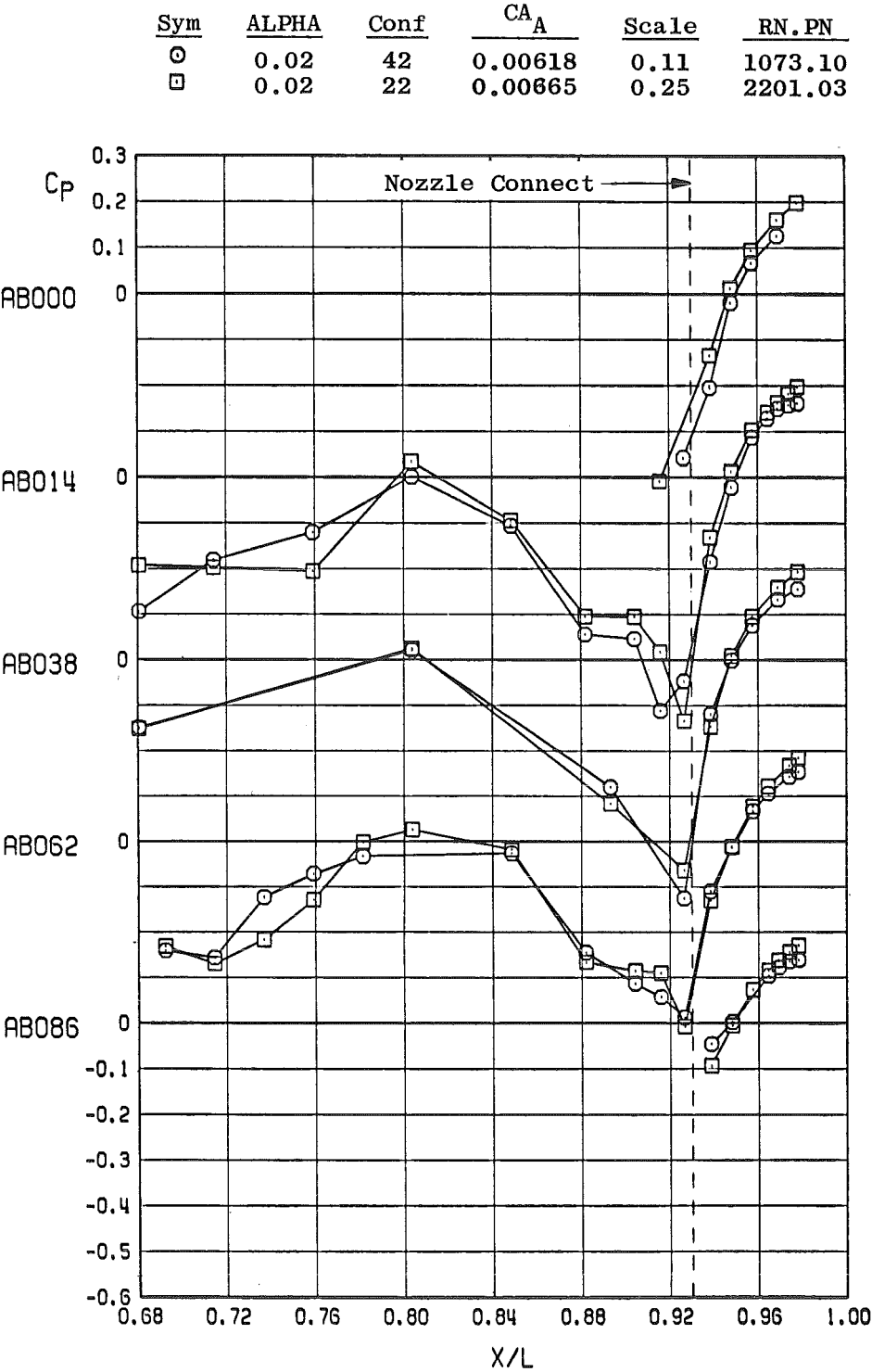


d.  $M_\infty = 0.95$   
Figure 40. Continued.

Sym	ALPHA	Conf	$CA_A$	Scale	RN.PN
○	0.02	42	0.00442	0.11	1074.03
□	0.01	22	0.00494	0.25	2200.11

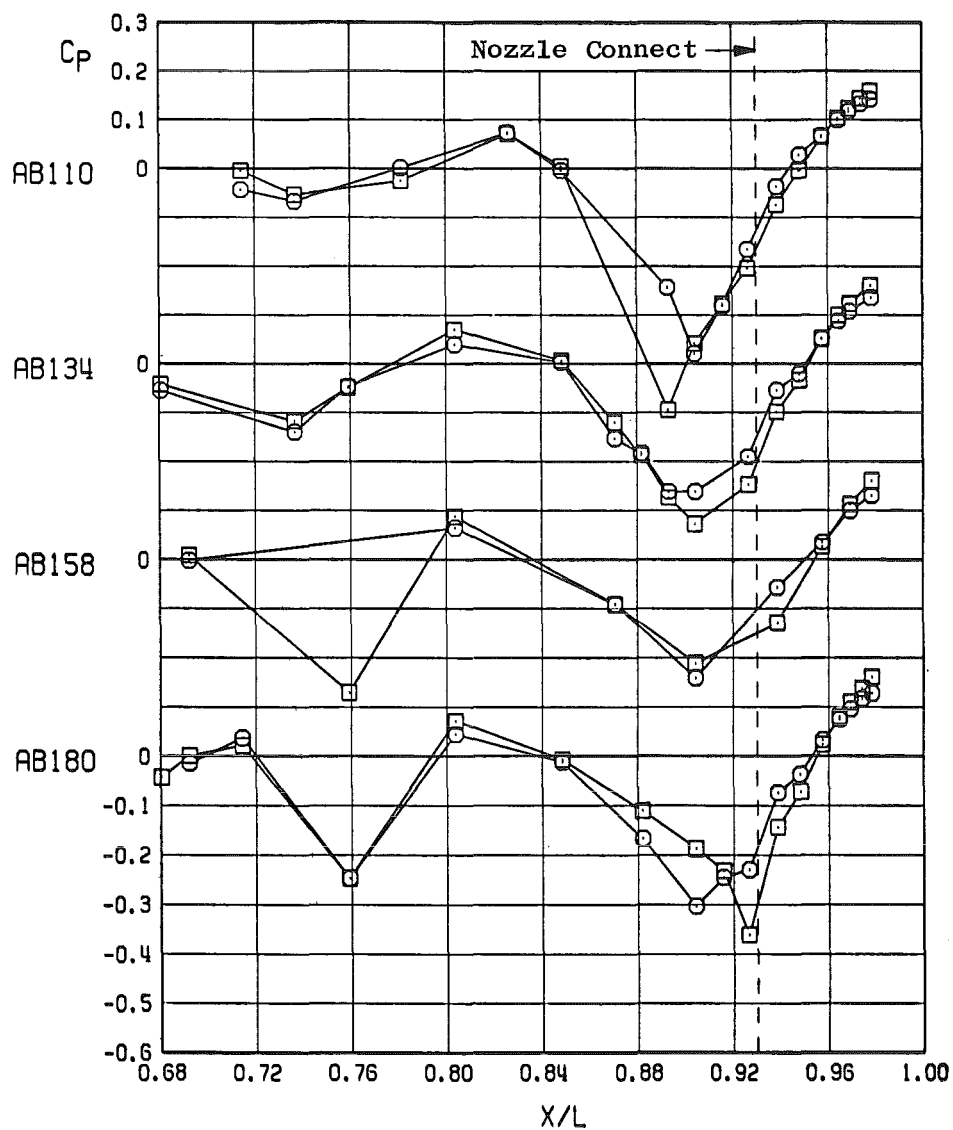


d. Concluded  
Figure 40. Continued.



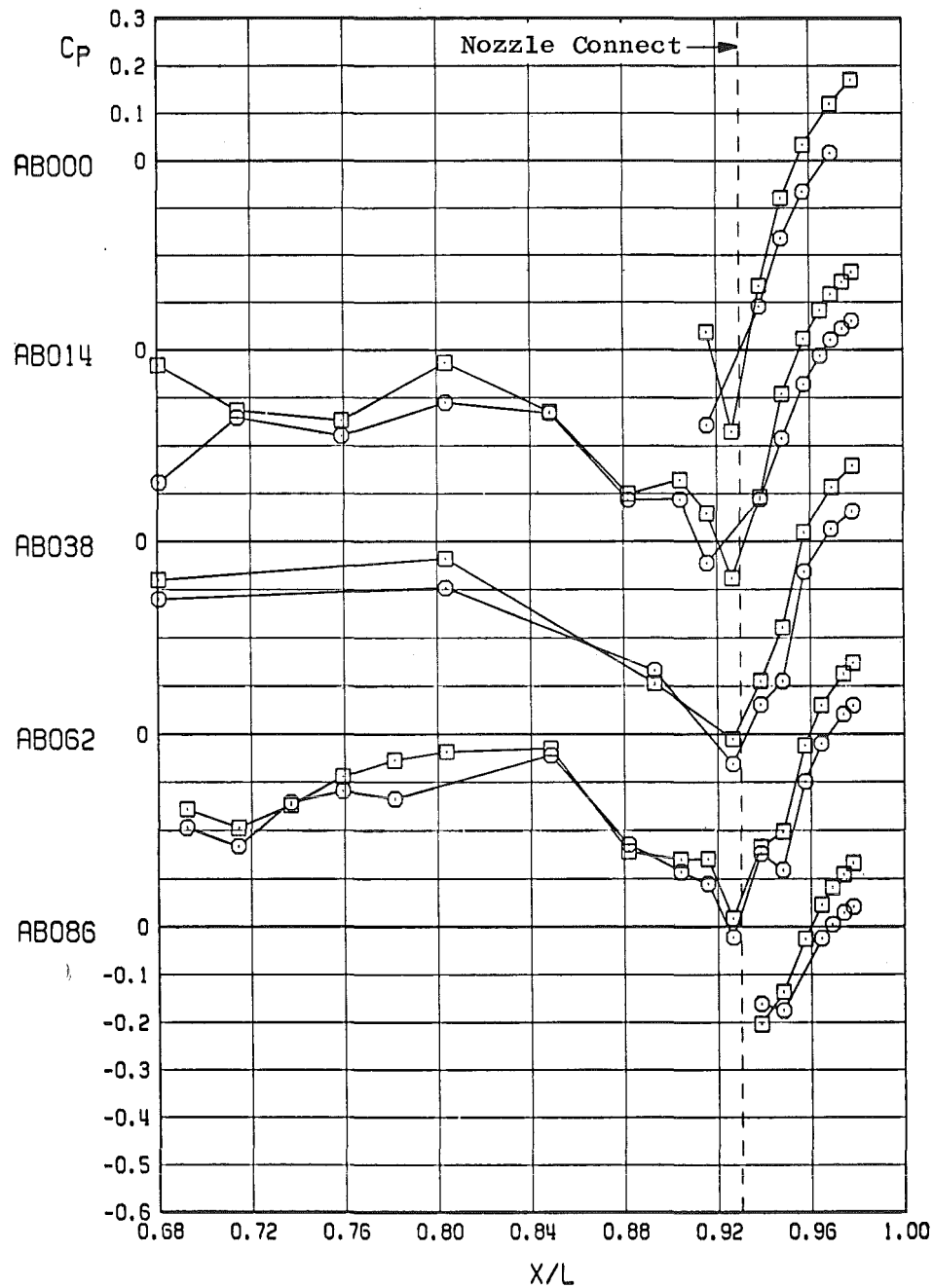
e.  $M_\infty = 1.0$   
Figure 40. Continued.

Sym	ALPHA	Conf	$CA_A$	Scale	RN. PN
○	0.02	42	0.00618	0.11	1073.10
□	0.02	22	0.00665	0.25	2201.03



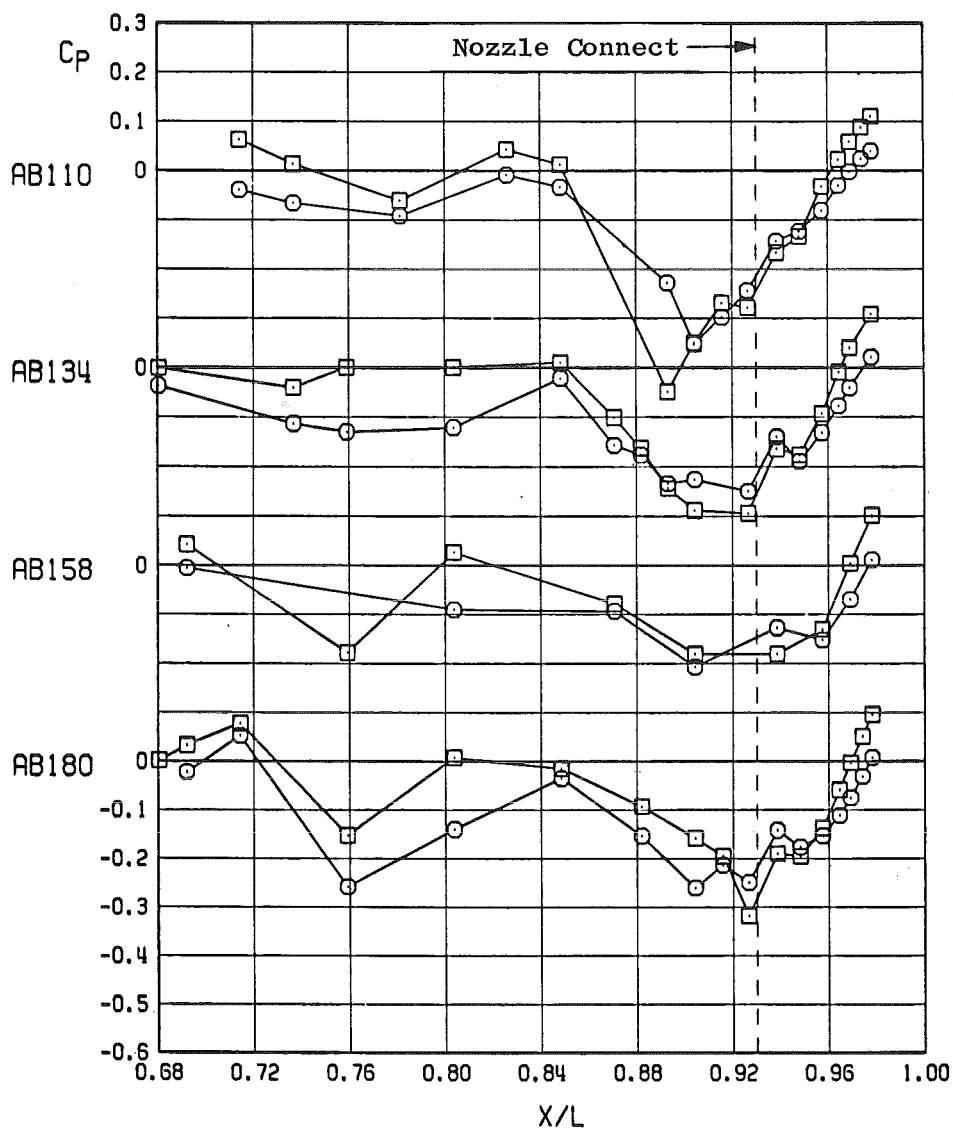
e. Concluded  
Figure 40. Continued.

Sym	ALPHA	Conf	CA <sub>A</sub>	Scale	RN.PN
○	-0.01	42	0.00875	0.11	1072.03
□	-0.00	22	0.00770	0.25	2208.03



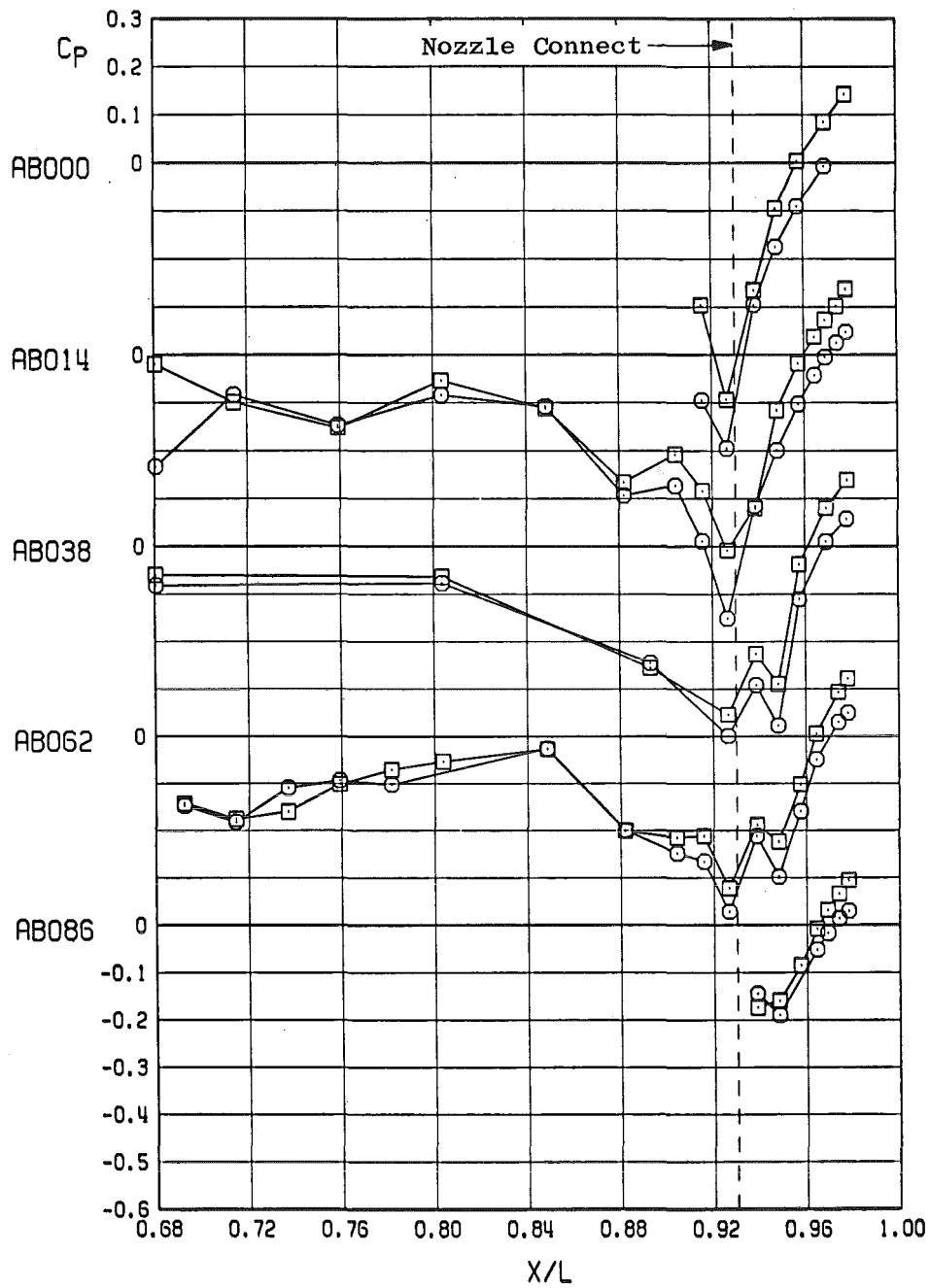
f.  $M_\infty = 1.05$   
Figure 40. Continued.

Sym	ALPHA	Conf	$C_{A_A}$	Scale	RN.PN
○	-0.01	42	0.00875	0.11	1072.03
□	-0.00	22	0.00770	0.25	2208.03



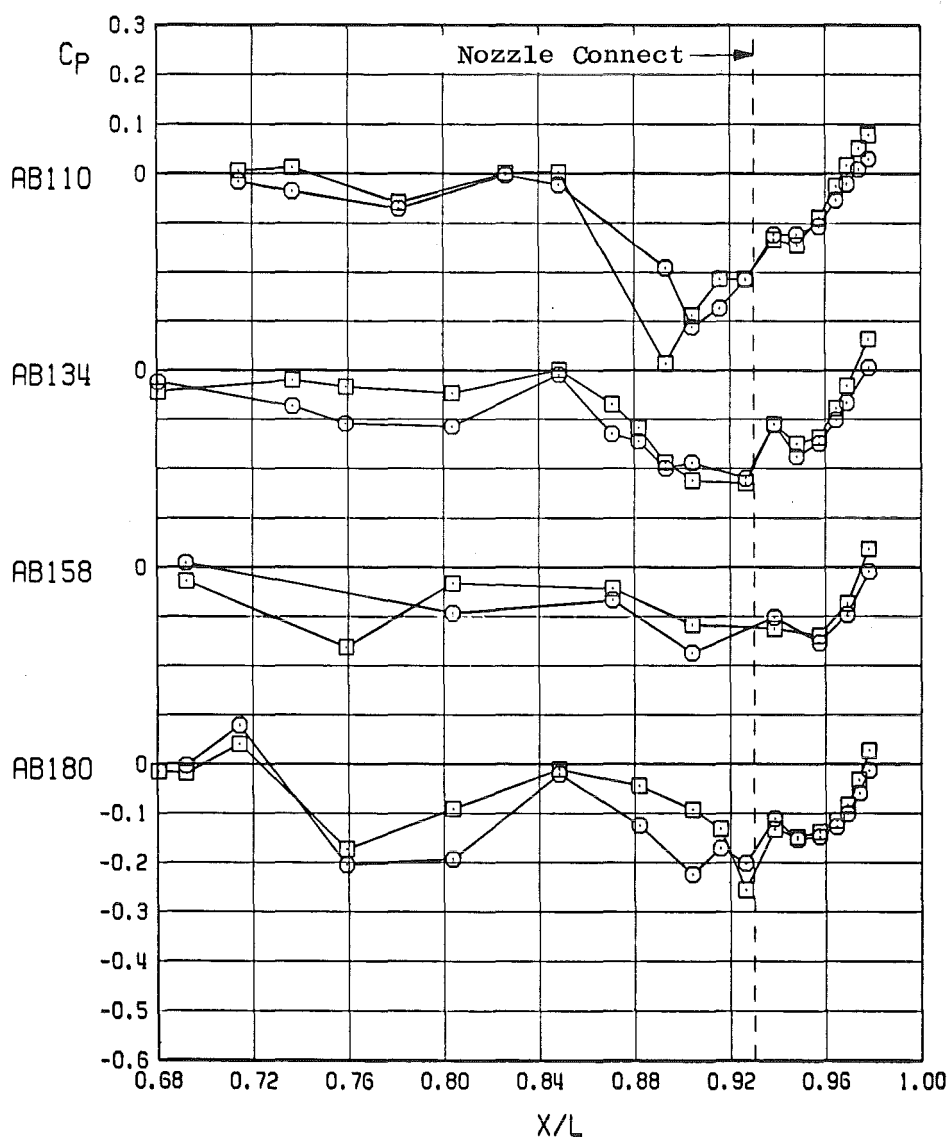
f. Concluded  
Figure 40. Continued.

<u>Sym</u>	<u>ALPHA</u>	<u>Conf</u>	<u>CA<sub>A</sub></u>	<u>Scale</u>	<u>RN.PN</u>
○	0.01	42	0.00781	0.11	1071.03
□	0.01	22	0.00697	0.25	2209.03



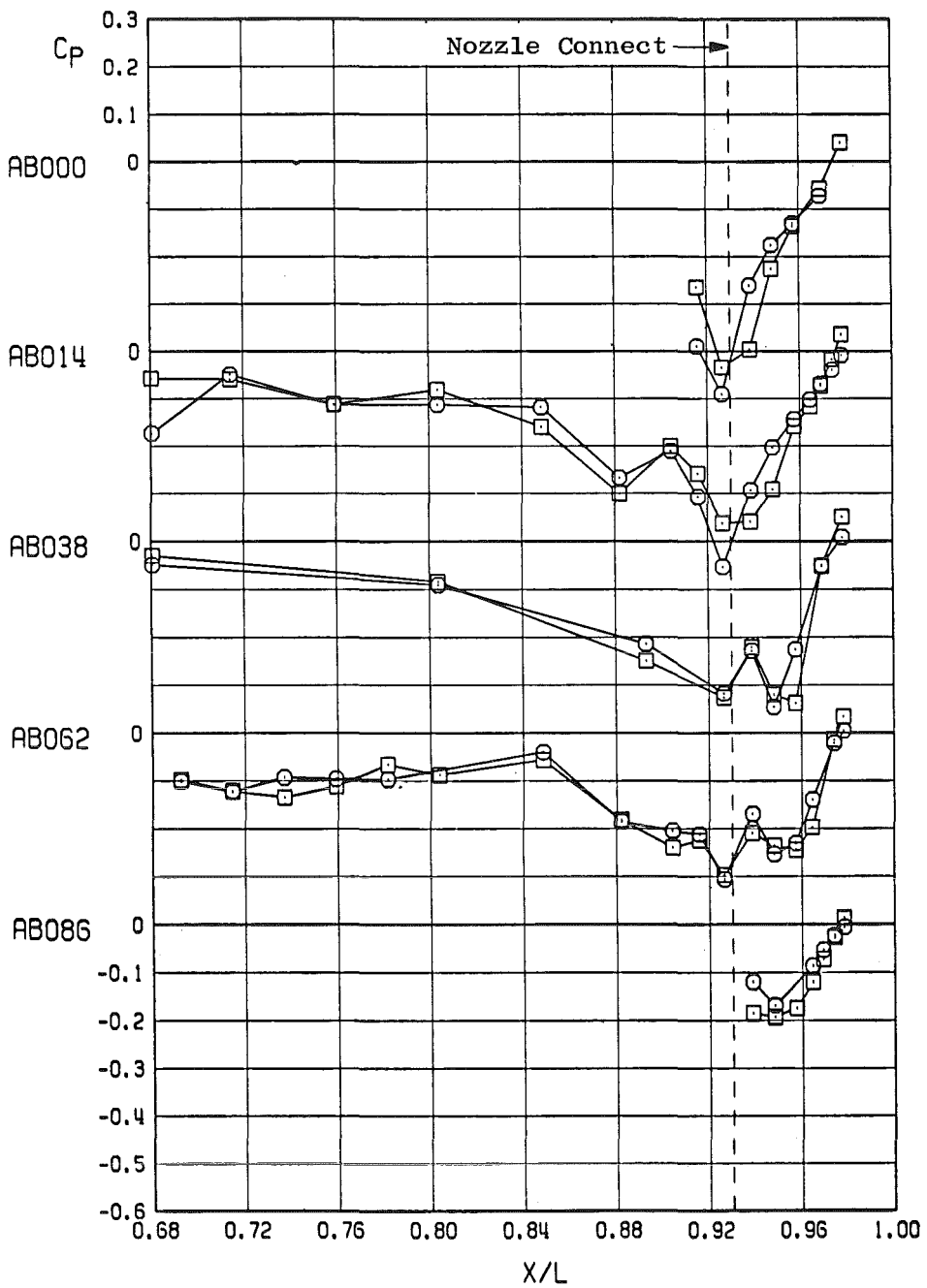
g.  $M_\infty = 1.1$   
Figure 40. Continued.

Sym	ALPHA	Conf	$C_{A_A}$	Scale	RN.PN
○	0.01	42	0.00781	0.11	1071.03
□	0.01	22	0.00697	0.25	2209.03



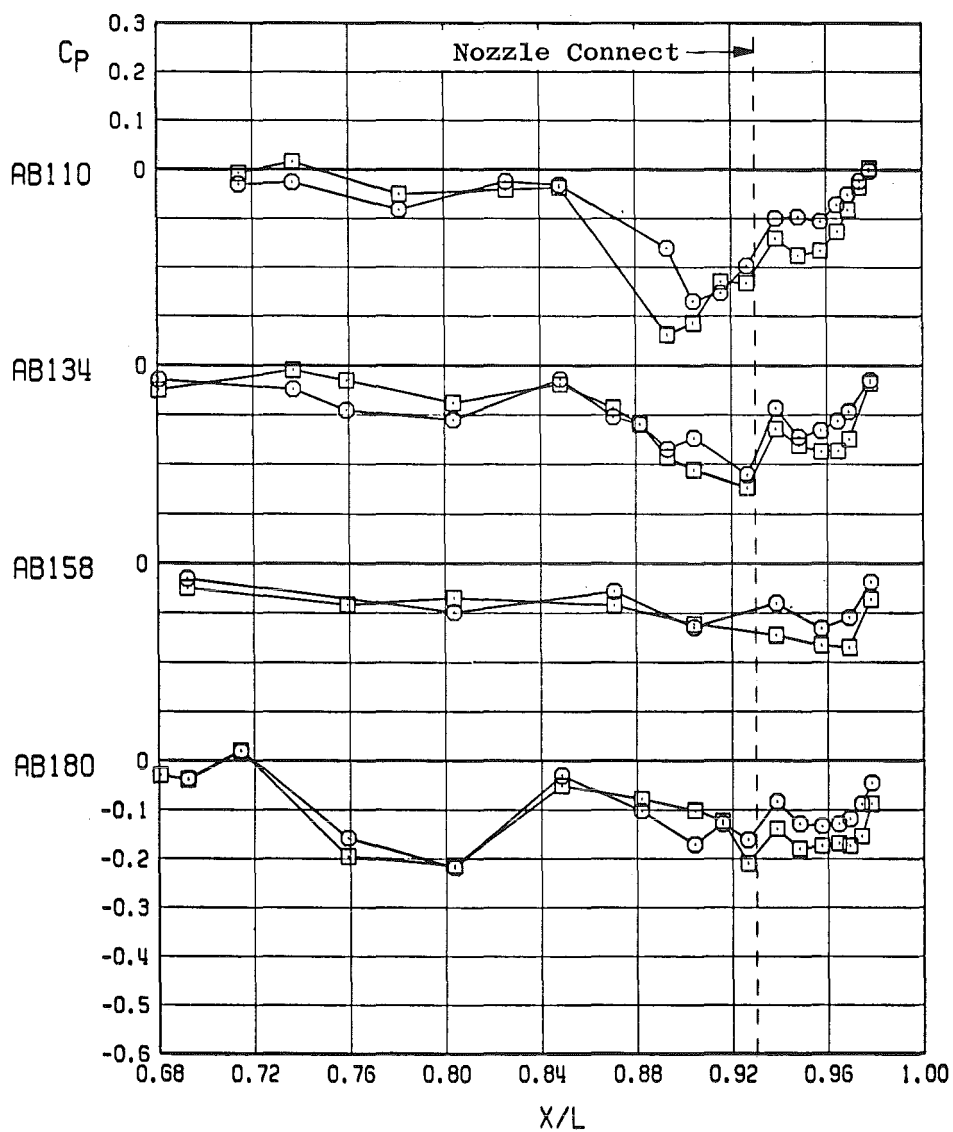
g. Concluded  
Figure 40. Continued.

Sym	ALPHA	Conf	CA <sub>A</sub>	Scale	RN.PN
○	-0.10	42	0.00724	0.11	1051.03
□	0.01	22	0.00834	0.25	2202.06



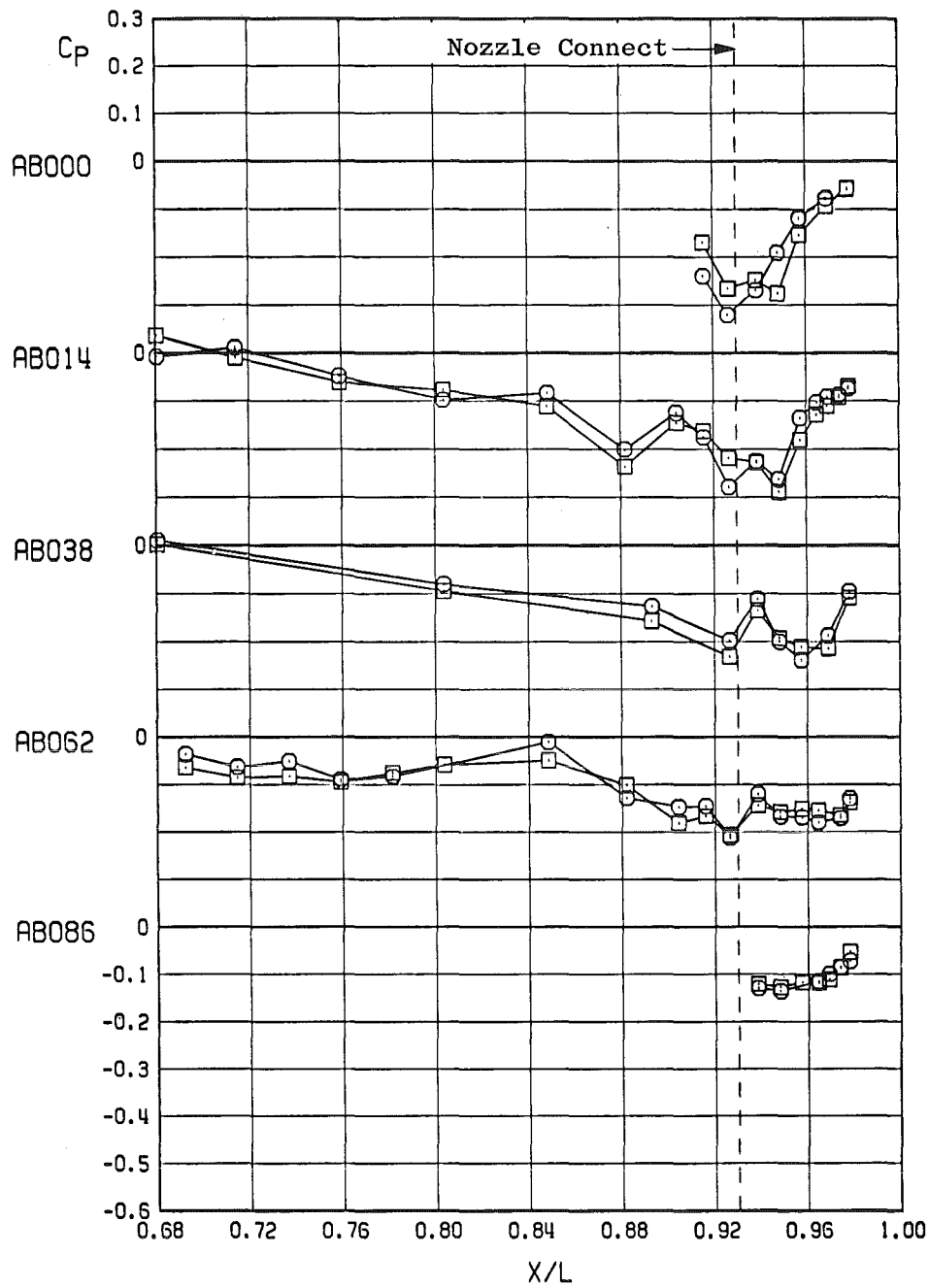
h.  $M_\infty = 1.2$   
Figure 40. Continued.

Sym	ALPHA	Conf	CA <sub>A</sub>	Scale	RN.PN
○	-0.10	42	0.00724	0.11	1051.03
□	0.01	22	0.00834	0.25	2202.06



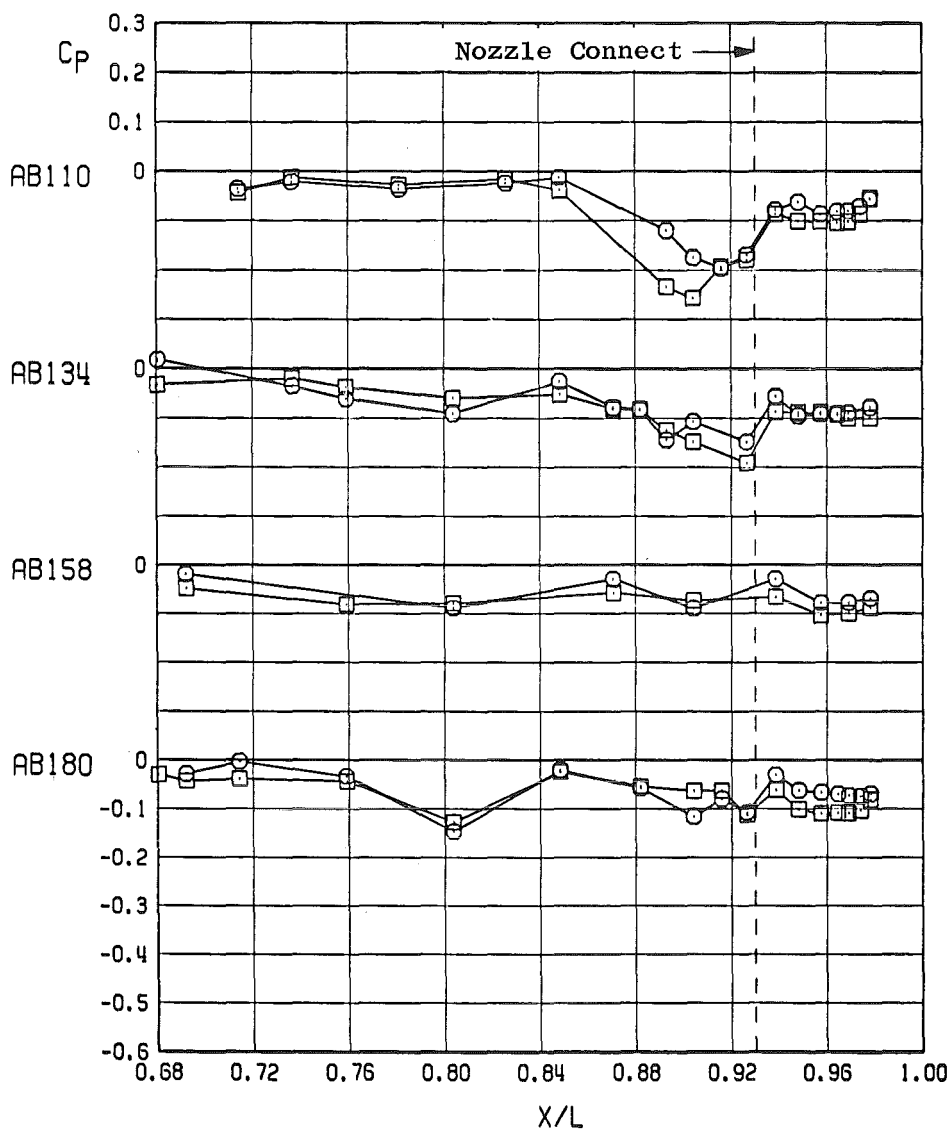
h. Concluded  
Figure 40. Continued.

<u>Sym</u>	<u>ALPHA</u>	<u>Conf</u>	<u>CA<sub>A</sub></u>	<u>Scale</u>	<u>RN.PN</u>
○	-0.14	42	0.00543	0.11	1047.03
□	0.02	22	0.00609	0.25	2214.03



i.  $M_\infty = 1.5$   
Figure 40. Continued.

Sym	ALPHA	Conf	CA <sub>A</sub>	Scale	RN.PN
○	-0.14	42	0.00543	0.11	1047.03
□	0.02	22	0.00609	0.25	2214.03



i. Concluded  
Figure 40. Concluded.

Sym	$M_\infty$	Model Scale	$RE \times 10^{-6}$	Symbols
○	0.6	0.11	2.1	Flagged
□	0.8	0.25	3.4	Plain
△	0.9			
◇	1.2			
◀	1.5			

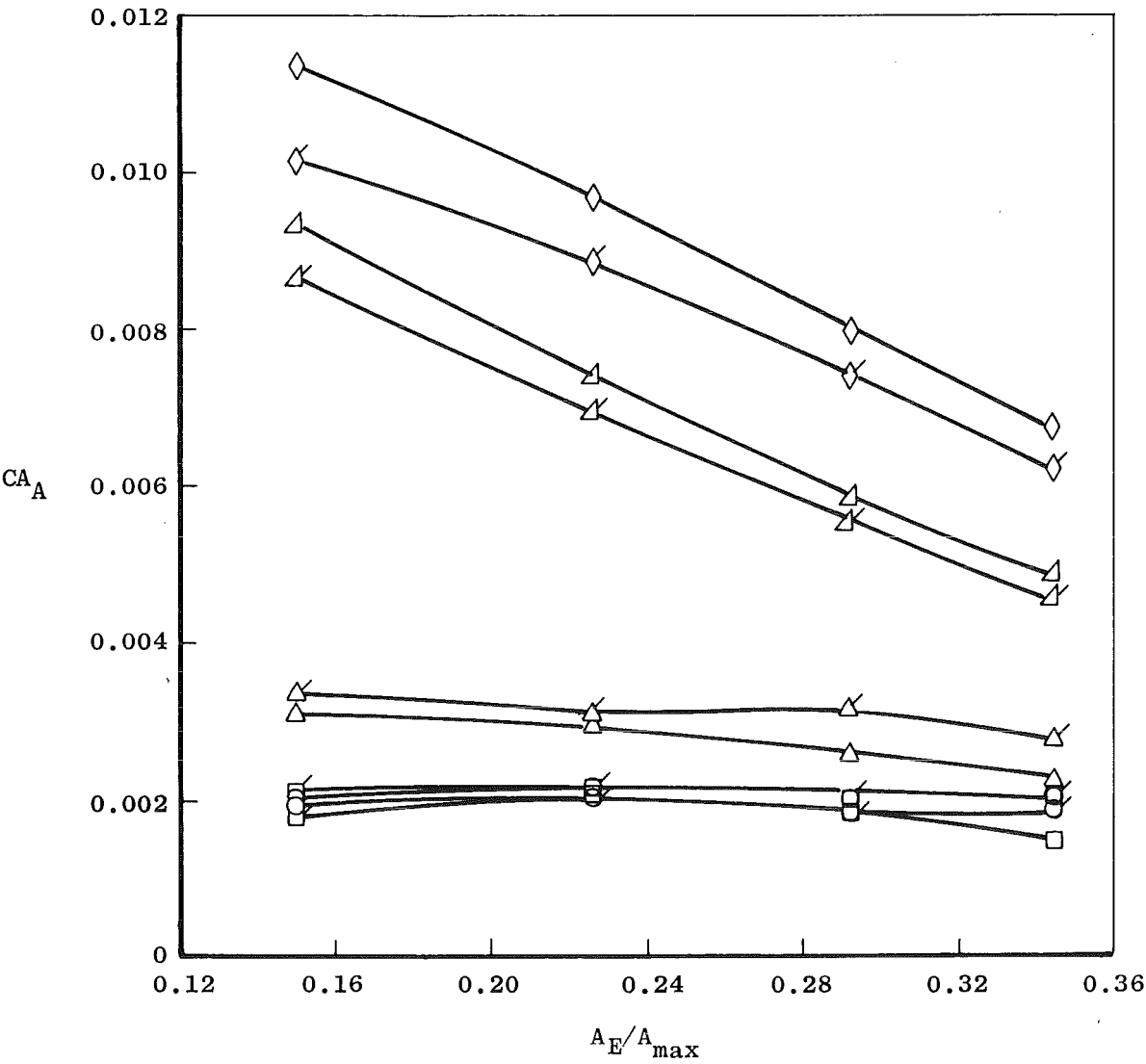


Figure 41. Effect of model scale on the sensitivity of nozzle-afterbody axial-force coefficients to nozzle closure, sting support system, design NPR,  $\alpha = 0$ .

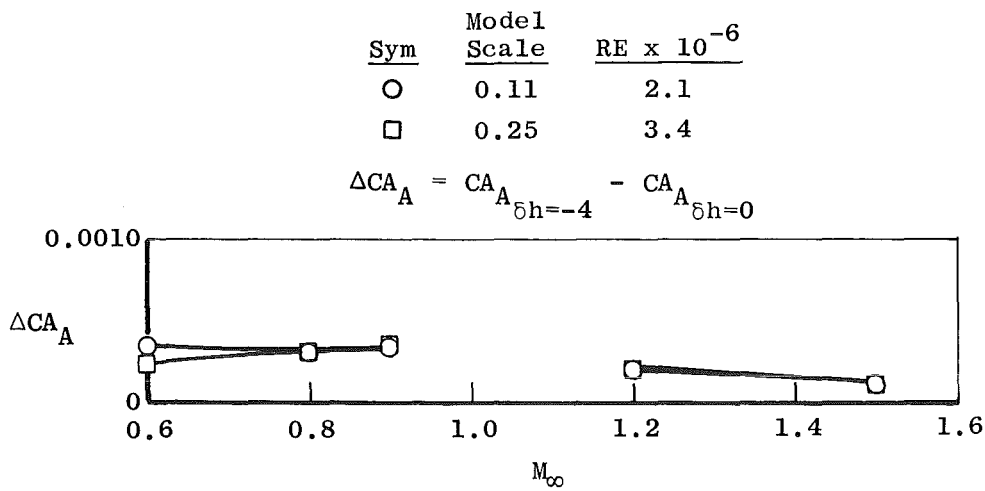
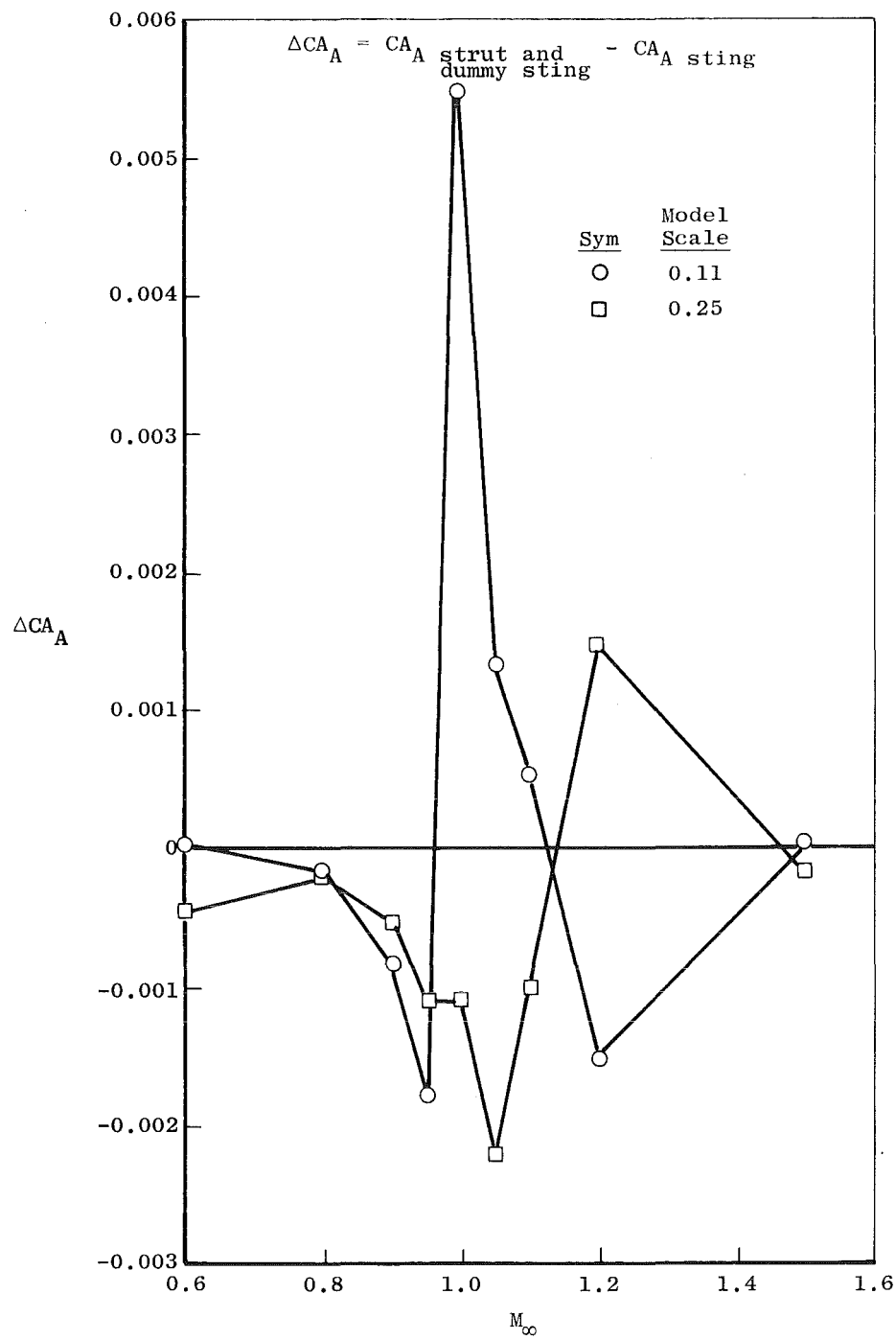
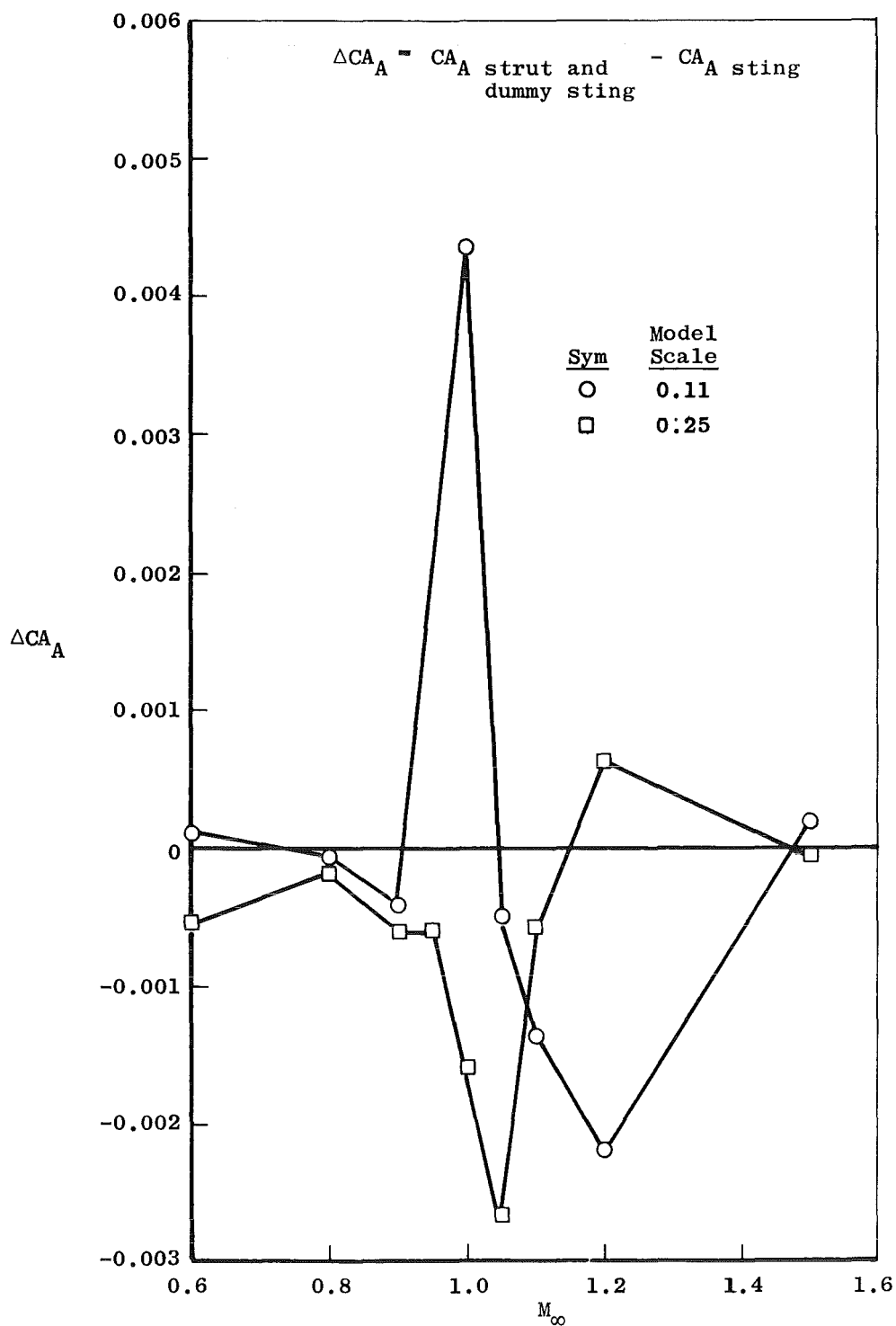


Figure 42. Effect of model scale on the sensitivity of nozzle-afterbody axial-force coefficients to horizontal tail deflection, sting support system, cruise nozzle, NPR = 3.4,  $\alpha = 0$ .



a.  $\alpha = 0$

Figure 43. Comparison of strut interference on nozzle afterbody axial force coefficient from the 0.11 and 0.25 scale models, max A/B 6.6 nozzle, NPR = 4.8.



b.  $\alpha = 7 \text{ deg}$   
Figure 43. Concluded.

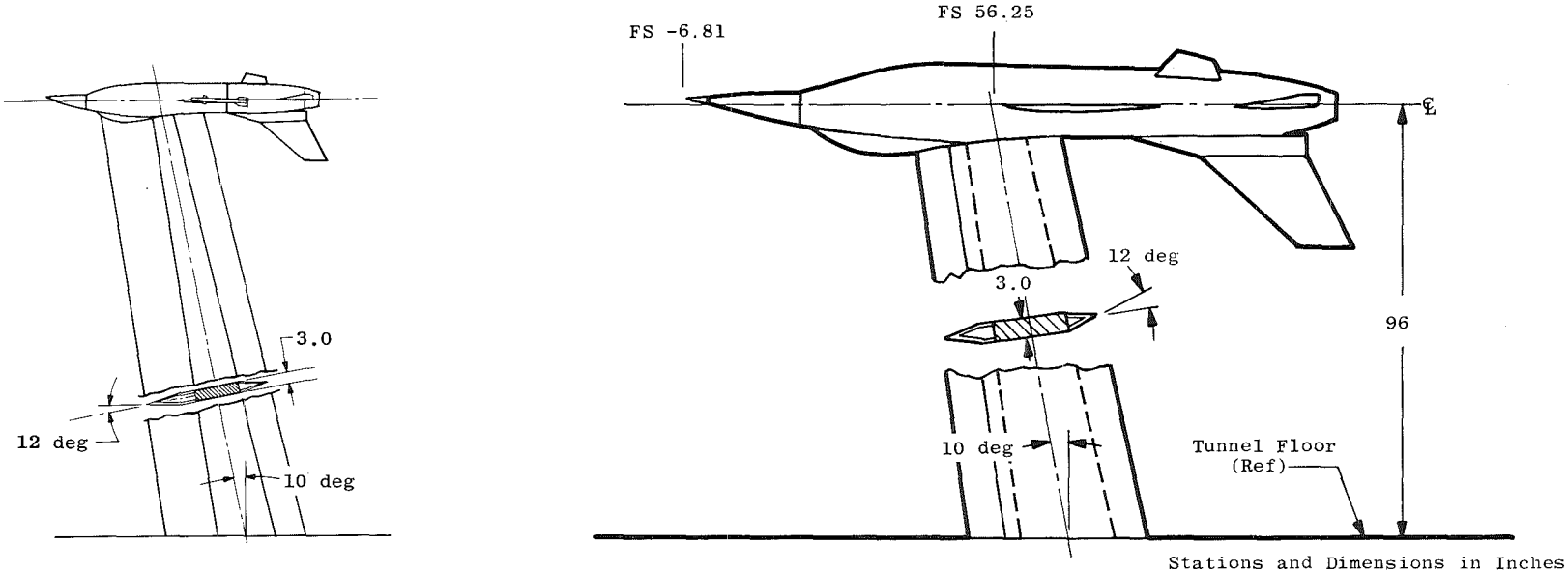


Figure 44. Comparison of strut planforms utilized with the 0.11- and 0.25-scale models.

Table 1. Configuration Identification

Config.	Support System	Dummy Support System	Nozzle Geometry	Run Number Range	Comments
1	Strut	None	Cruise 3.4	1606/01 to 1631/09	
2	↓	↓	Part A/B 5.1	1675/03 to 1690/09	
3			Max A/B 6.6	1634/07 to 1672/12	
4			Max A/B 7.75	1693/03 to 1704/06	
5		Small Sting	Cruise 3.4	1709/03 to 1734/06	
6		↓	Part A/B 5.1	1758/03 to 1769/01	
7		↓	Max A/B 6.6	1737/03 to 1755/12	
9		Large Sting	Part A/B 5.1	1804/03 to 1818/07	
10		↓	Max A/B 6.6	1773/03 to 1801/01	
11	↓	↓	Max A/B 7.75	1821/05 to 1836/01	
12	Small Sting	None	Cruise 3.4	1848/14 to 1985/01	Without Bay Purge
21	Small Sting	↓	Cruise 3.4	1988/03 to 2019/07	
16	Large Sting		Part A/B 5.1	2220/04 to 2323/07	
17	↓		Max A/B 6.6	2023/04 to 2184/03	
18			Max A/B 7.75	2326/01 to 2394/05	
22	↓	↓	Max A/B 6.6	2188/03 to 2216/05 2397/03 to 2416/04	Without Bay Purge

**Table 2. Location of Pressure Instrumentation**  
**a. Forebody Pressure Orifice Designations**

Circumferential Location	Fuselage Station	Data Reduction Name
0°	-6.809	P103
14°	6.473	P104
62°	6.473	P105
110°	6.473	P106
180°	6.473	P107
14°	16.250	P108
62°	16.250	P109
110°	16.250	P110
180°	16.250	P111
14°	28.125	P112
62°	28.125	P113
110°	28.125	P114
180°	28.125	P115
14°	41.249	P116
62°	41.249	P117
110°	41.249	P118
180°	41.249	P119
14°	53.750	P120
62°	53.750	P121
110°	53.750	P122
180°	53.750	P123
14°	74.999	P124
62°	74.999	P125
110°	74.999	P126
180°	74.999	P127
14°	93.751	P128
62°	93.751	P129
110°	93.751	P130
180°	93.751	P131

**b. Afterbody Pressure Orifice Designations**

14°	95.249	P132
38°	95.249	P133
50°	95.249	P134
74°	95.249	P135
77°	95.249	P136
96°	95.249	P137
98°	95.249	P138
122°	95.249	P139
134°	95.249	P140
146°	95.249	P141
180°	95.249	P142
62°	96.876	P143
153°	96.876	P144
180°	96.876	P145
14°	99.999	P203
62°	99.999	P204
105°	99.999	P205
110°	99.999	P206
170°	99.999	P207
180°	99.999	P208

Table 2. Continued  
b. Continued

Circumferential Location	Fuselage Station	Data Reduction Name
26°	103.124	P209
62°	103.124	P210
110°	103.124	P211
134°	103.124	P212
14°	106.250	P213
62°	106.250	P214
70°	106.250	P215
98°	106.250	P216
134°	106.250	P217
158°	106.250	P218
180°	106.250	P219
226°	106.250	P220
62°	109.375	P221
79°	109.375	P222
110°	109.375	P223
14°	112.500	P224
38°	112.500	P225
62°	112.500	P226
134°	112.500	P227
158°	112.500	P228
170°	112.500	P229
180°	112.500	P230
322°	112.500	P231
68°	115.625	P232
74°	114.500	P233
78.5°	115.625	P234
80.5°	114.500	P235
110°	115.625	P236
14°	118.751	P237
62°	118.751	P238
100°	118.751	P239
110°	118.750	P240
134°	118.750	P241
146°	118.750	P242
180°	118.750	P243
26°	121.876	P244
50°	121.876	P245
77°	120.751	P303
83°	120.751	P304
134°	121.876	P305
158°	121.876	P306
170°	121.876	P307
226°	121.876	P308
3°	123.750	P309
14°	123.437	P310
62°	123.437	P311
80.5°	123.750	P313
91.5°	123.750	P315
98°	123.437	P317
110°	123.437	P318
134°	123.437	P319
180°	123.437	P320

**Table 2. Continued**  
**b. Concluded**

Circumferential Location	Fuselage Station	Data Reduction Name
38°	125.001	P322
83°	125.001	P323
134°	125.001	P324
146°	125.001	P325
322°	125.001	P326
14°	126.563	P327
62°	126.563	P328
74°	126.563	P329
83°	125.438	P330
94.5°	126.563	P331
110°	126.563	P332
122°	126.563	P333
134°	126.563	P334
158°	126.563	P335
180°	126.563	P336
226°	126.563	P337
0°	128.187	P338
14°	128.187	P339
50°	128.187	P340
62°	128.187	P341
83°	128.187	P342
95°	128.187	P343
110°	128.187	P344
180°	128.187	P345
0°	129.688	P403
14°	129.688	P404
26°	129.688	P405
38°	129.688	P406
62°	129.688	P407
100°	129.688	P408
110°	129.688	P409
134°	129.688	P410
146°	129.688	P411
170°	129.688	P412
180°	129.688	P413
322°	129.688	P414

**c. Nozzle Pressure Orifice Designations, Flight Simulation Boattails**

0°	131.375	P415
0°	132.701	P416
0°	134.026	P417
0°	135.650	P418
0°	136.906	P419
15°12'	131.375	P420
13°51'	132.701	P421
13°51'	134.026	P422
13°51'	135.000	P423
13°51'	135.650	P424
13°51'	136.325	P425
13°51'	136.906	P426

**Table 2. Continued**  
**c. Concluded**

Circumferential Location	Fuselage Station	Data Reduction Name
39°12'	131.375	P427
37°51'	132.701	P428
37°51'	134.026	P429
37°51'	135.650	P430
37°51'	136.906	P431
63°12'	131.375	P432
61°51'	131.701	P433
61°51'	134.026	P434
61°51'	135.000	P435
61°51'	136.325	P436
61°51'	136.906	P437
87°12'	131.375	P438
85°51'	131.701	P439
85°51'	134.026	P440
85°51'	135.000	P441
85°51'	135.650	P442
85°51'	136.325	P443
85°51'	136.906	P444
111°12'	131.375	P445
109°51'	132.701	P503
109°51'	134.026	P504
109°51'	135.000	P505
109°51'	135.650	P506
109°51'	136.325	P507
109°51'	136.906	P508
135°12'	131.375	P509
133°51'	132.701	P510
133°51'	134.026	P511
133°51'	135.000	P512
133°51'	135.650	P513
133°51'	136.906	P514
159°12'	131.375	P515
157°51'	134.026	P516
157°51'	135.650	P517
157°51'	136.906	P518
183°12'	131.375	P519
181°51'	132.701	P520
181°51'	134.026	P521
181°51'	135.000	P522
181°51'	135.650	P523
181°51'	136.325	P524
181°51'	136.406	P525
-37°51'	131.375	P526
-37°51'	134.026	P527
-37°51'	136.906	P528
-133°51'	131.375	P529
-133°51'	134.026	P530
-133°51'	136.906	P531

**Table 2. Concluded****d. Horizontal Tail Shelf Pressure Orifice Designations, Fuselage Station 131.375**

Circumferential Location	Fuselage Station	Data Reduction Name
84.5°	131.375	P532
86°	131.375	P533
87.5°	131.375	P534
89°	131.375	P535
92°	131.375	P536
93°	131.375	P537

**e. Boom Static and Bay Purge System Pressures**

Tap No.	Circumferential Location	Fuselage Station	Data Reduction Name
	0°	-5.181	P538
	90°	-5.181	P538
	180°	-5.181	P538
	270°	-5.181	P538
BPP1		89.00	P539
BPP2		95.00	P540
BPT1		91.38	P541
BPT2		91.38	P542
BPR1		93.64	P543
BPR2		93.64	P544

**f. Duct Total Pressure and Temperature Rake and Static Pressure Designations**

Support System	Circumferential Location	Fuselage Station	Waterline, in.	Data Reduction Name
Strut	180°	124.492	18.417	PT1
Strut	180°	124.492	18.591	TT1
Strut	180°	124.492	18.801	PT2
Strut	180°	124.492	19.147	PT3
Strut	180°	124.492	19.576	PT4
Strut	180°	124.492	20.074	PT5
Strut	180°	124.492	20.697	PT6
Strut	180°	124.492	21.723	TT2
Strut	180°	124.492	22.750	PT7
Sting	180°	124.492	18.437	PT1
Sting	180°	124.492	18.634	TT1
Sting	180°	124.492	18.830	PT2
Sting	180°	124.492	19.05	TT2
Sting	180°	124.492	19.268	PT3
All	45°	122.492		PS1
All	315°	122.492		PS2

Table 3. Test Condition Matrix

Mach No. Config.	0.6	0.8	0.9	0.95	1.0	1.05	1.1	1.2	1.3	1.4	1.5
	Free-Stream Unit Reynolds Number $\times 10^{-6}$										
1	3.4	3.4	3.4	3.4	3.4	3.4	3.4	3.4	---	---	3.4
2	3.4	3.4	3.4	---	---	---	---	3.4	---	---	3.4
3	3.4	3.4	3.4	3.4	3.4	3.4	3.4	3.4	---	---	3.4
4	3.4	3.4	3.4	---	---	---	---	3.4	---	---	---
5	3.4	3.4	3.4	3.4	3.4	3.4	3.4	3.4	2.6	2.6	3.4
6	3.4	3.4	3.4	---	---	---	---	3.4	---	---	---
7	3.4	3.4	3.4	3.4	3.4	3.4	3.4	3.4	---	---	3.4
9	3.4	3.4	3.4	---	---	---	---	3.4	---	---	3.4
10	3.4	3.4	3.4	3.4	3.4	3.4	3.4	3.4	---	---	3.4
11	3.4	3.4	3.4	---	---	---	---	3.4	---	---	3.4
12	2.0	2.0	2.0	---	---	---	---	2.0	---	---	---
↓	3.4	3.4	3.4	3.4	3.4	3.4	3.4	3.4	3.4	3.4	3.4
16	6.0	5.6	4.8	---	---	---	---	4.4	---	---	---
16	2.0	2.0	2.0	---	---	---	---	2.0	---	---	2.0
17	3.4	3.4	3.4	---	---	---	---	3.4	---	---	3.4
↓	2.0	2.0	2.0	---	---	---	---	2.0	---	---	2.0
18	3.4	3.4	3.4	3.4	3.4	3.4	3.4	3.4	3.4	3.4	3.4
↓	6.0	5.8	5.4	---	---	---	---	4.4	---	---	---
21	3.4	3.4	3.4	3.4	3.4	3.4	3.4	3.4	---	---	3.4
22	2.0	2.0	2.0	---	---	---	---	2.0	---	---	2.0
22	3.4	3.4	3.4	3.4	3.4	3.4	3.4	3.4	---	---	3.4

Table 4. Configuration Identification

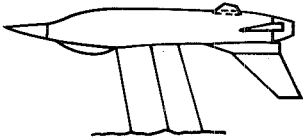
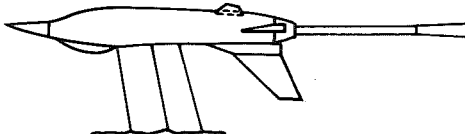
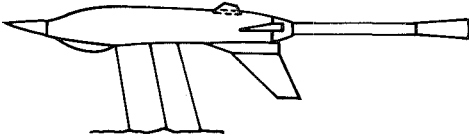
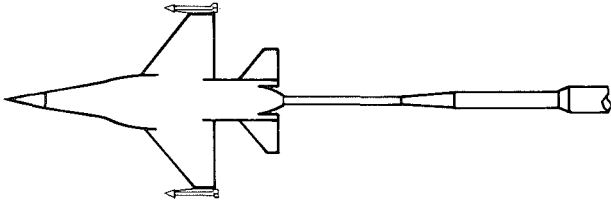
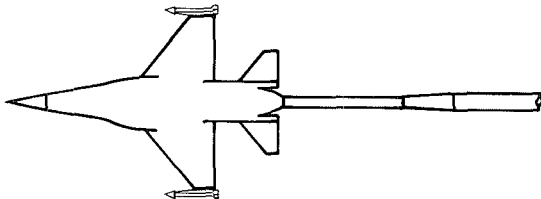
Config	Nozzle	Support System	Dummy Support	Other Config Description	Config	Nozzle	Support System	Dummy Support	Other Config Description
1 2 3 4	Cruise 3.4 Part A/B 5.1 Max A/B 6.6 Max A/B 7.7	Strut ↓	None ↓		5 6 7	Cruise 3.4 Part A/B 5.1 Max A/B 6.6	Strut ↓	Small Sting ↓	
									
Config	Nozzle	Support System	Dummy Support	Other Config Description	Config	Nozzle	Support System	Dummy Support	Other Config Descriptions
9 10 11	Part A/B 5.1 Max A/B 6.6 Max A/B 7.75	Strut ↓	Large Sting ↓		12 21	Cruise 3.4 Cruise 3.4	Small Sting ↓	None ↓	Without Bay Purge
									

Table 4. Concluded

Config	Nozzle	Support System	Dummy Support	Other Config Descriptions					
16	Part A/B 5.1	Large Sting	None	Without Bay Purge					
17	Max A/B 6.6	↓	↓						
18	Max A/B 7.75								
22	Max A/B 6.6	↓	↓						
									

## NOMENCLATURE

ABXXX	Circumferential location of afterbody pressure orifices, deg (see Fig. 14)
ALPHA	Model angle of attack, deg
$A_E$	Model nozzle exit area, in. <sup>2</sup>
$A_e$	Full-scale nozzle exit area, ft <sup>2</sup>
$A_{max}$	Maximum fuselage cross-sectional area, in. <sup>2</sup>
$A_{ref}$	Model wing reference area, 18.75 ft <sup>2</sup>
$A_T$	Nozzle throat area, in. <sup>2</sup>
B.L.	Butt line, in.
$CA_A$	Axial-force coefficient of the complete nozzle and afterbody region of the model, force/ $q_\infty A_{ref}$
CAAB	Axial-force coefficient of the afterbody region of the model, force/ $q_\infty A_{ref}$
CAN	Axial-force coefficient of the nozzle, force/ $q_\infty A_{ref}$
$CN_A$	Normal-force coefficient of the complete nozzle and afterbody region of the model, force/ $q_\infty A_{ref}$
CONF	Configuration
$C_p$	Pressure coefficient, $(p_x - p_\infty)/q_\infty$
DELHR	Horizontal tail deflection angle, positive leading-edge deflection is up, deg
$D_E$	Nozzle exit diameter, in.
$D_S$	Sting diameter at nozzle exit plane, in.
$D_T$	Nozzle throat diameter, in.
F.S.	Fuselage station, in.
L	Model length, 139.97 in.
$M_\infty$	Free-stream Mach number

NPR	Nozzle total pressure to free-stream static pressure ratio
NP <sub>RE</sub>	Effective jet nozzle pressure ratio for an annular jet based on maximum jet diameter (see Section 4.1.5)
PS <sub>i</sub>	Model flow duct static pressure orifice number
PT <sub>i</sub>	Model flow duct total pressure tube number
PT	Free-stream total pressure, psfa
P <sub>i</sub>	Model static pressure orifice number
p <sub>x</sub>	Local static pressure, psfa
p <sub>∞</sub>	Free-stream static pressure, psfa
RN•PN	Data identification number
q <sub>∞</sub>	Free-stream dynamic pressure, psf
RE	Free-stream Reynolds number per foot
RE <sub>ℓ</sub>	Characteristic Reynolds number based on model length
TS	Tunnel station, in.
TT <sub>i</sub>	Model flow duct thermocouple number
X	Axial distance from FS 0
α	Model angle of attack, deg
ΔCA <sub>A</sub>	Incremental value of nozzle-afterbody axial-force coefficient
ΔCN <sub>A</sub>	Incremental value of nozzle-afterbody normal-force coefficient
δ <sub>h</sub>	Horizontal tail deflection, deg
θ	Nozzle divergence angle, deg